



**HUGO MIGUEL  
FILIPE CALISTO**

**Radiómetro por Transpiração Transitória –  
Desenvolvimento de um Sensor de Fluxo de Calor  
para Ambientes de Elevada Agressividade**

**Transient Transpiration Radiometer –  
Development of a Heat Flux Sensor for High  
Aggressivity Environments**

Tese apresentada à Universidade de Aveiro para cumprimento dos requisitos necessários à obtenção do grau de Doutor em Engenharia Mecânica, realizada sob a orientação científica do Doutor Nelson Amadeu Dias Martins, Professor Auxiliar do Departamento de Engenharia Mecânica da Universidade de Aveiro

Apoio financeiro do POCTI no âmbito  
do III Quadro Comunitário de Apoio.

Apoio financeiro da FCT e do FSE no  
âmbito do III Quadro Comunitário de  
Apoio.

Dedico o presente trabalho à minha mãe, Paulina, a quem tudo devo e cujo carinho e apoio são a maior e mais importante constante da minha vida.

Quero também dedicá-lo à memória do meu pai, Miguel, e dos meus avós maternos Madalena e João. Embora já tenham partido, as suas recordações acompanharão sempre o meu caminho.

## **o júri**

presidente

**Prof. Doutor Vasile Staicu**  
Professor Catedrático da Universidade de Aveiro

**Prof. Doutor António Carlos Mendes de Sousa**  
Professor Catedrático da Universidade de Aveiro

**Prof. Doutor Carlos Alberto Nieto de Castro**  
Professor Catedrático da Faculdade de Ciências da Universidade de Lisboa

**Prof. Doutor Tiago Alexandre Abranches Teixeira Lopes Farias**  
Professor Auxiliar com Agregação da Universidade Técnica de Lisboa

**Prof. Doutor Nelson Amadeu Dias Martins**  
Professor Auxiliar da Universidade de Aveiro (Orientador)

## **agradecimentos**

Agradeço ao meu orientador e amigo Prof. Doutor Nelson Martins o apoio manifestados durante o trabalho subjacente à presente dissertação e a oportunidade que me facultou de conciliar a elaboração da mesma com a bolsa que lhe esteve associada. Agradeço a autonomia que me deu para explorar uma diversidade de opções e ferramentas, permitindo-me abordar temas e metodologias que me eram desconhecidas e aprendendo desse modo lições eventualmente mais árduas e penosas mas por isso mesmo mais úteis e duradouras.

Agradeço de forma especial ao Alexandre Pinho da Cruz, ao Bruno Abreu Silva e ao Miguel “Chicco” Silva pelo ânimo e valioso apoio em vertentes particulares das diversas tarefas realizadas, onde a utilidade dos contributos e o saber acumulado apenas foram superados pelo prazer de trabalhar com amigos. Agradeço muito em particular à Bárbara Gabriel não só pelos mesmos motivos como também pelo facto de ter sido um incentivo e uma companhia constantes. Para além de minha prima é, sendo eu filho único, a irmã que não tive.

Não posso deixar de fazer uma menção especial aos meus colegas e amigos Mónica Correia e Filipe Teixeira-Dias pela valiosa ajuda que foram as suas ideias e comentários, somadas à sua disponibilidade e paciência ao servirem de “caixa-de-ressonância” a algumas divagações.

Uma menção especial para o João Alexandre Oliveira, como o próprio escreveu irmão de armas e de vida, amigo inabalável e companheiro de há longos anos nesta viagem.

Não queria de modo algum esquecer todos aqueles que embora sem qualquer envolvimento direto ou indireto com o trabalho propriamente dito me ajudaram e apoiaram com a sua amizade e incentivo ao longo do seu desenrolar. Refiro-me em especial à Patrícia Almeida, mas também ao Marcos Gomes, ao Robertt Valente, ao Ricardo Sousa, ao Victor Neto, ao António Araújo, ao Bruno Lamas, à Sandra Pina, à Susana Olhero, à Joana Neves, à Tânia Barbosa e ao Hugo Coelho.

**palavras-chave**

Medição de Fluxo de Calor, Radiómetro de Transpiração, Fluxo de Calor Convectivo, Fluxo de Calor Radiativo, Partição de Fluxo de Calor, Análise Transitória.

**resumo**

Propõe-se o desenvolvimento de um novo instrumento para medição de fluxos de calor convectivos e radiativos, baseado na operação de um radiómetro de transpiração em regime transitório. Os radiómetros de transpiração atuais baseiam-se em medições de temperatura em regime estacionário num elemento poroso atravessado por um caudal mássico gasoso conhecido. Como consequência da inércia térmica intrinsecamente elevada do elemento sensível poroso, a constante de tempo do instrumento é da ordem dos segundos. O instrumento proposto preservará as vantagens estabelecidas dos radiómetros de transpiração incorporando características adicionais que alargarão a gama de aplicabilidade. As novas características mais importantes serão uma redução significativa do tempo de resposta do instrumento e a possibilidade de medir separadamente as componentes radiativa e convectiva do fluxo de calor. Estes objetivos serão conseguidos através da análise da resposta transitória do instrumento, utilizando-se um caudal pulsado de gás para induzir o comportamento transitório.

**keywords**

Heat Flux Measurement, Transpiration Radiometer, Convective Heat Flux, Radiative Heat Flux, Heat Flux Partitioning, Transient Analysis.

**abstract**

The development of a new instrument for the measurement of convective and radiative is proposed, based on the transient operation of a transpiration radiometer. Current transpiration radiometers rely on steady state temperature measurements in a porous element crossed by a known gas mass flow. As a consequence of the porous sensing element's intrinsically high thermal inertia, the instrument's time constant is in the order of several seconds. The proposed instrument preserves established advantages of transpiration radiometers while incorporating additional features that broaden its applicability range. The most important developments are a significant reduction of the instrument's response time and the possibility of separating and measuring the convective and radiative components of the heat flux. These objectives are achieved through the analysis of the instrument's transient response, a pulsed gas flow being used to induce the transient behavior.

# TABLE OF CONTENTS

LIST OF FIGURES .....	iii
LIST OF TABLES.....	ix
NOMENCLATURE .....	xi
INTRODUCTION .....	1
1.1 Introduction.....	1
1.2 Framework and Relevance .....	3
1.3 Heat Flux Measurement: Literature Review.....	6
1.3.1 Spatial Temperature Gradient Techniques .....	8
1.3.2 Temporal Temperature Change Techniques.....	15
1.3.3 Other Techniques .....	29
1.3.4 Conclusions.....	32
1.4 Objectives and Thesis Contribution.....	33
1.5 Thesis Structure.....	35
ANALYTICAL MODEL FORMULATION AND NUMERICAL SIMULATIONS .....	39
2.1 Introduction.....	39
2.2 Model Requirements and Analytical Approach .....	45
2.2.1 Problem Statement.....	45
2.2.2 Green's Functions Formulation .....	56
2.2.3 Finite Difference Formulation.....	64
2.3 Assumptions and Simplifications.....	70
2.4 Implementation and Results .....	87
2.5 Concluding Remarks.....	106
DIMENSIONING PROCEDURES AND PARAMETRIC STUDIES.....	109
3.1 Introduction.....	109

3.2 Proposed Configuration, Objectives and Approach .....	112
3.3 Dimensioning and Design Procedures.....	119
3.3.1 Basic Assumptions.....	119
3.3.2 Boundary Layer Control, Mass Flow Rate and Compressibility in the Microperforated Plate .....	120
3.3.3 Plate Transmissivity.....	132
3.3.4 Cooling System.....	138
3.4 Parametric Studies.....	143
3.4.1 Variations of Plate Temperatures with Incident Heat Fluxes .....	149
3.4.2 Variations of Plate Temperatures with Transpiration Mass Flows .....	151
3.4.3 External Refrigeration System Temperatures .....	156
3.4.4 Transient Temperature Curves.....	158
3.5 Concluding Remarks.....	163
EXPERIMENTAL STUDY .....	165
4.1 Introduction.....	165
4.2 Integrated Hardware and the Prototype .....	166
4.3 Experimental Results.....	184
4.4 Calibration of the Transient Heat Flux Meter .....	206
4.4.1 Calibration Procedure.....	208
4.5 Concluding Remarks.....	216
GLOBAL CONCLUSIONS AND PROPOSED DEVELOPMENTS .....	217
5.1 Summary .....	217
5.2 Conclusions.....	219
5.3 Future Developments.....	222
REFERENCES .....	225
APPENDIX A – <i>MATHEMATICA</i> CODE.....	243



# LIST OF FIGURES

<b>Figure 1.1</b> - Basic layered gauge principle and thermopile for differential temperature measurement.....	10
<b>Figure 1.2</b> - Thermopile heat flux sensor.....	11
<b>Figure 1.3</b> - Schmidt-Boelter gauge .....	12
<b>Figure 1.4</b> - Basic Gardon gauge configuration.....	14
<b>Figure 1.5</b> - Slug calorimeter .....	17
<b>Figure 1.6</b> - Basic thin film sensor configuration.....	20
<b>Figure 1.7</b> - Convective and radiative heat flux sensor with two sensing elements of different emissivities.....	24
<b>Figure 1.8</b> - Anson-Godridge sensor.....	25
<b>Figure 1.9</b> - Semi-ellipsoidal radiometer.....	26
<b>Figure 1.10</b> - Transpiration radiometer: (a) schematic representation and dimensions, and (b) sensor .....	29
<b>Figure 2.1</b> - Iterative GF calculation methodology .....	64
<b>Figure 2.2</b> - Iterative finite difference calculation methodology.....	71
<b>Figure 2.3</b> - Fluid flow passing from the upstream surface into the perforated pattern.....	75
<b>Figure 2.4</b> - Reynolds vs. Nusselt number relationships.....	81
<b>Figure 2.5</b> - Calculated Reynolds and Nusselt number relationship .....	81
<b>Figure 2.6</b> - Convection heat transfer coefficient as a function of transpiration mass flow.....	82
<b>Figure 2.7</b> - Hexagonal unit cell pattern .....	83
<b>Figure 2.8</b> - ANSYS <i>CFX</i> implementation of radial transient heat conduction in a thin plate.....	94
<b>Figure 2.9</b> - <i>Mathematica</i> implementation of the <i>R01</i> Green's function .....	94
<b>Figure 2.10</b> - Radial temperature profiles using GFSE for Case 1.....	96
<b>Figure 2.11</b> - Comparison of calculated temperatures at $t = 0.2$ s for Case 1.....	96
<b>Figure 2.12</b> - Comparison of calculated temperatures at $t = 0.5$ s for Case 1.....	97
<b>Figure 2.13</b> - Comparison of calculated temperatures at $t = 1$ s for Case 1 .....	97
<b>Figure 2.14</b> - Transient temperature at the centre of the plate for Case 1 .....	98

<b>Figure 2.15</b> – Radial temperature profiles using GFSE for Case 2.....	98
<b>Figure 2.16</b> – Comparison of calculated temperatures at $t = 0.2$ s for Case 2.....	99
<b>Figure 2.17</b> – Comparison of calculated temperatures at $t = 0.5$ s for Case 2.....	99
<b>Figure 2.18</b> – Comparison of calculated temperatures at $t = 1$ s for Case 2 .....	100
<b>Figure 2.19</b> – Transient temperature at the centre of the plate for Case 2 .....	100
<b>Figure 2.20</b> – <i>CFX</i> setup of the small perforated section and illustration of the resulting temperature field.....	103
<b>Figure 2.21</b> – Radial temperature profiles using <i>CFX</i> .....	104
<b>Figure 2.22</b> – Radial temperature profiles using finite differences.....	105
<b>Figure 2.23</b> – Transient temperatures at the centre of the plate .....	105
<b>Figure 3.1</b> – Microperforated plate definition drawing.....	114
<b>Figure 3.2</b> – Non-porous base definition drawing.....	114
<b>Figure 3.3</b> – Cone definition drawing .....	115
<b>Figure 3.4</b> – Porous holder definition drawing.....	115
<b>Figure 3.5</b> – Exploded view of main prototype components .....	116
<b>Figure 3.6</b> – Prototype assembly .....	116
<b>Figure 3.7</b> – Critical transpiration gas (CTG) mass flux as a function of $Re_x$ and for turbulent boundary layers, a laminar boundary layer in a stagnation flow and a laminar boundary layer developing along a flat plate.....	122
<b>Figure 3.8</b> – Critical mass flows as a function of the assumed densities at the porous wall and furnaces temperatures, for the maximum stagnation velocity.....	129
<b>Figure 3.9</b> – Critical mass flows as a function of the assumed densities at the porous wall and stagnation flow velocities, for the maximum densities at the porous wall.....	130
<b>Figure 3.10</b> – Spectral emissive power as a function of temperature and wavelength .	136
<b>Figure 3.11</b> – Plate transmissivity as a function of the hole diameter to spacing ratio of the perforated pattern.....	138
<b>Figure 3.12</b> – SEM image of the irregularity in void geometry and the significant variations in their volume .....	142
<b>Figure 3.13</b> – $60^\circ$ unit cell geometry symmetry (a) and opening (blue), inlet (black), symmetry (red) and wall (green) boundary conditions (b) .....	147
<b>Figure 3.14</b> – Close-up view of the perforated pattern mesh.....	147

<b>Figure 3.15</b> – Basic configuration of the model studying the porous medium interacting with the refrigeration airflow.....	148
<b>Figure 3.16</b> – Plate temperatures as a function of furnace temperature and plate emissivity .....	151
<b>Figure 3.17</b> – Plate temperatures as a function of transpiration mass flows and sensing element emissivities.....	152
<b>Figure 3.18</b> – Percentage of deviation in measured temperatures for different supply temperatures .....	153
<b>Figure 3.19</b> – Average temperatures on the interface between the plate and the porous medium for various transpiration mass flows .....	157
<b>Figure 3.20</b> – Average temperatures on the interface between the plate and the porous medium for various convection heat transfer coefficients.....	157
<b>Figure 3.21</b> – Transient temperature curves at the centre of the plate for various steps in furnace temperature and a constant transpiration mass flow .....	159
<b>Figure 3.22</b> – Transient temperature curves at the centre of the plate for various steps in transpiration mass flow and a constant furnace temperature .....	160
<b>Figure 3.23</b> – Transient temperatures in the plate .....	162
<b>Figure 4.1</b> – Experimental System .....	166
<b>Figure 4.2</b> – Photograph and diagram of the TG measurement and control unit, showing the pressure regulator (a), the rotameter (b) and the manometer (c). .....	168
<b>Figure 4.3</b> – Microperforated plate: early unsuccessful attempt and detailed view of the intended microperforated pattern.....	170
<b>Figure 4.4</b> – Non-oxidized plate sample and oxidized unit mounted on instrument....	170
<b>Figure 4.5</b> – Non-porous base and refrigeration airflow tubing.....	171
<b>Figure 4.6</b> – Non-porous cone for airflow separation.....	171
<b>Figure 4.7</b> – Porous holder .....	172
<b>Figure 4.8</b> – Porosity verification .....	173
<b>Figure 4.9</b> – Thermocouple attachment.....	175
<b>Figure 4.10</b> – Size comparison between the proposed instrument and an earlier, water cooled system .....	176
<b>Figure 4.11</b> – Assembled prototype .....	176
<b>Figure 4.12</b> – Additional tubing shielding .....	177

<b>Figure 4.13</b> – Relationship between furnace set point and cavity temperatures.....	179
<b>Figure 4.14</b> – End of the tubular furnace opposite to the instrument location, with and without the ceramic plug fitted.....	180
<b>Figure 4.15</b> – Transpiration airflow contamination measurement.....	181
<b>Figure 4.16</b> – Transient airflow control setup.....	183
<b>Figure 4.17</b> – Control electrovalve and flow regulators.....	183
<b>Figure 4.18</b> – Sensor 1 cool experiment measured temperatures.....	188
<b>Figure 4.19</b> – Numerical temperatures for the corrected furnace emissivity, various element emissivities and experimentally measured values for the same operational conditions.....	190
<b>Figure 4.20</b> – Closed furnace for 8 hour runs.....	191
<b>Figure 4.21</b> – Data acquisition system real-time interface .....	194
<b>Figure 4.22</b> – Raw data plots .....	195
<b>Figure 4.23</b> – Calculated first derivatives.....	197
<b>Figure 4.24</b> – Sensor 1 linear relationship between mean temperature curve slopes and furnace heat fluxes, in the heating situation.....	201
<b>Figure 4.25</b> – Sensor 1 linear relationship between mean temperature curve slopes and furnace heat fluxes, in the cooling situation .....	201
<b>Figure 4.26</b> – Sensor 2 linear relationship between mean temperature curve slopes and furnace heat fluxes, in the heating situation.....	202
<b>Figure 4.27</b> – Sensor 2 linear relationship between mean temperature curve slopes and furnace heat fluxes, in the cooling situation .....	202
<b>Figure 4.28</b> – Sensor 3 linear relationship between mean temperature curve slopes and furnace heat fluxes, in the heating situation.....	203
<b>Figure 4.29</b> – Sensor 3 linear relationship between mean temperature curve slopes and furnace heat fluxes, in the cooling situation .....	203
<b>Figure 4.30</b> – Sensor 1 linear relationship between heating and cooling temperature curve slopes.....	204
<b>Figure 4.31</b> – Sensor 2 linear relationship between heating and cooling temperature curve slopes.....	205
<b>Figure 4.32</b> – Sensor 3 linear relationship between heating and cooling temperature curve slopes.....	205

<b>Figure 4.33</b> – Comparison of LSE and York-method linear regressions for the heating situation in Sensor 1 .....	212
<b>Figure 4.34</b> – Comparison of LSE and York-method linear regressions for the cooling situation in Sensor 3 .....	212



# LIST OF TABLES

<b>Table 2.1</b> – Internal nodal resistances and volume element for cylindrical coordinates .....	67
<b>Table 2.2</b> – Plate Biot number as a function of the number of holes .....	73
<b>Table 2.3</b> – Plate areas as a function of the number of holes.....	79
<b>Table 2.4</b> – Unit cell parameters .....	84
<b>Table 2.5</b> – One-dimensional initial tests parameters .....	95
<b>Table 3.1</b> –Critical mass flow to choked flow ratios, indicative of the number of holes .....	131
<b>Table 3.2</b> – Emitted radiation parameters.....	136
<b>Table 3.3</b> – Unit cell parameters .....	137
<b>Table 3.4</b> – Maximum admissible temperatures for emission component minimization .....	155
<b>Table 4.1</b> – Furnace axial temperature profiles .....	178
<b>Table 4.2</b> – Furnace set points .....	186
<b>Table 4.3</b> – Furnace set points for transient runs .....	200
<b>Table 4.4</b> – Linear regression results summary .....	213





# NOMENCLATURE

## GREEK LETTERS

$\alpha$	Thermal Diffusivity
$\alpha_{\text{rad}}$	Absortivity
$\beta$	Transient Heat Fluxmeter Calibration Constant
$\gamma$	Specific Heat Ratio
$\Delta$	Difference; Increment
$\varepsilon$	Emissivity
$\zeta$	Element Area Radiative Correction Factor
$\eta$	Element Area Convective Correction Factor
$\lambda$	Wavelength
$\mu$	Dynamic Viscosity
$\xi$	Element Volume Correction Factor
$\rho$	Density
$\rho_{\text{rad}}$	Reflectivity
$\sigma$	Stefan-Boltzmann Constant
$\tau$	Time Constant
$\tau_{\text{rad}}$	Transmissivity
$\varphi$	Angular Coordinate
$\phi$	Porosity
$\psi$	Density Ratio
$\omega$	Uncertainty

## ROMAN LETTERS

A	Area
$c_p$	Specific Heat at Constant Pressure
$c_v$	Specific Heat at Constant Volume
CFD	Computational Fluid Dynamics
CTG	Critical Transpiration Gas
d	Diameter
D	Outer Diameter
e	Hole Spacing; Perforated Pattern Pitch
E	Voltage Output

FS	Full Scale
g	Heat Generation
G, GF	Green's Function
h	Convection Heat Transfer Coefficient
i	Generic Index Number
j	Generic Index Number; Mass Flux (according to context)
k	Thermal Conductivity
L	Distance; Thickness
m	Mass
n	Outward Drawn Normal of Surface; Number (according to context)
N	Number
Nu	Nusselt Number
p	Pressure
Pr	Prandtl Number
q	Heat Flux
r	Radius; Radial Coordinate
$\vec{r}$	Position Vector
R	Gas Constant
Re	Reynolds Number
Reg	Region
$R_{ij}$	Thermal Resistance for node $i, j$
S	Surface
$S_s$	Sensitivity
$S_T$	Seebeck Coefficient
SLPM	Standard Litres per Minute
t	Time
T	Temperature
TG	Transpiration Gas
v	Velocity
V	Volume
x	Cartesian Spatial Coordinate
y	Cartesian Spatial Coordinate
z	Cartesian Spatial Coordinate

## SUBSCRIPTS

abs	Absorbed
app	Apparent
cond	Conductive; Conducted
conv	Convective
corr	Correction; Corrected
em	Emitted
ext	Exterior
f	Fluid
h	Hole
HM	Homogeneous
i	Initial
inc	Incident
o	Out; Outside
p	Pore
rad	Radiation; Radiative
rec	Received
ref	Reference
sur	Surroundings
ST	Steady
tr	Transmitted
w	Wall
$\perp$	Normal (to surface)



# CHAPTER 1

## INTRODUCTION

An introduction to the dissertation is provided, stressing its intended contribution to the field of heat flux measurement, namely the proposition of a new heat flux measurement principle based on a transpiration radiometer's transient response analysis. The relevance of heat flux as a thermodynamic design parameter is discussed. The thesis's contribution, objectives and structure are also discussed and its integration in a continuous line of development is addressed in order to adequately explain the framework in which this work took place. A review of the available methods to measure heat flux, along with a discussion of their relative merits and major advantages and disadvantages, is presented. The contribution of the present work is established and discussed by comparison.

### 1.1 Introduction

The standard interpretation of heat flux defines it as the energy in transit owing to a temperature difference per unit cross-sectional area, normal to the flux direction. Although there are no devices that can measure energy and hence heat or heat flux directly, the effects of energy in transit can be monitored and the heat flux inferred. Heat flux in a thermodynamic system typically varies in both space and time, reflecting the state of the system. Knowledge of heat flux properties in a thermodynamic system enables its assessment in terms of efficiency, safety and availability, embodying an important design, control and diagnostic parameter for most operational thermal systems.

Heat transfer can occur by means of conduction, convection and radiation, either as independent or as combined phenomena. The objective of measuring heat transfer is the quantification of the heat flux. In a solid, heat flux will occur due to conduction alone, but at a solid/fluid interface (a case of practical significance to engineers), the resulting heat transfer will occur owing to at least two of these three modes. Most heat flux sensors measure the total heat flux at the interface or surface, with important consequences when comparisons are made between experimental results and theory or computational fluid dynamics, or correlations of experimental results are

for example used to calibrate a heat flux sensor. The separation of the relative contributions of convection and radiation to the total heat flux, often referred to as heat flux partitioning, is generally the most troublesome issue. A radiation correction can in most cases be easily applied to an experimental configuration, providing the surface temperature and radiative properties of the experimental domain are known [Childs *et al.* 1999]. Extensive studies are available regarding applications where heat flux partitioning must be carried out [Blanchat *et al.* 2009].

Radiation heat flux is an especially important parameter as far as high temperature applications are concerned, namely in systems such as boilers, furnaces or combustion chambers. These systems place severe constraints upon instrumentation due to the harsh physical conditions, in the form of high temperatures and various aggressive processes that include dust, soot or highly reactive chemical species. Such systems are also usually characterized by the occurrence of fouling processes which can severely, if not completely, restrict the application of most types of sensors. As much as possible, they must therefore be robust, reliable and able to avoid or minimize the fouling problem on the sensors themselves.

Physical methods available for the purpose of heat flux measurement are usually based on the monitoring of temperatures. However, while temperature measurements are common and well accepted, heat flux measurements are often given lesser consideration because they are less intuitive: temperature is one of the fundamental properties of a substance and can be determined by human senses, whereas heat flux is a derived quantity that is not easily sensed. How and where the thermal energy goes is often equally (or more) important than temperature levels. Optimizing the thermal energy transfer in many systems is crucial to their performance, rendering sensors that can be used to directly sense heat flux extremely important and fully justifying the line of work that eventually led to the present work.

Most methods for measuring heat flux are based on temperature measurements on or close to the surface of a solid material, usually involving the insertion of a device either onto or into the surface, which can cause both physical and thermal disruptions. As a result, good measurements must aim at minimizing the disruption caused by the presence of the sensor. It is particularly important to understand the thermal disruption caused by the sensor because it cannot be readily visualized and because all heat flux sensors have a temperature change associated to the measurement. Consequently, a wise selection of the sensor type and operating range is important for good heat flux measurements. Of no lesser importance are the reliability and the robustness of the sensor, so these factors should also be considered when selecting a

particular instrument, and must guide the development of any new sensor, as described here.

## 1.2 Framework and Relevance

The desirability for heat flux measurement techniques and instruments as good as possible is rather self evident and is undoubtedly the driving force behind the continuing development both in this field and in others related to it, by taking advantage of the existing instruments, namely diagnostic and control systems.

However, in this particular case, another reason was at least as important and justifies to some extent some of the approaches and decisions that shaped the overall developed work. The present thesis can obviously be taken solely at face value, but it takes a somewhat broader significance when looked upon from the wider point of view of the whole line of work that eventually led to the present transpiration radiometer and that came about through a continuous line of development that can be said to have begun in the early 1990s, as detailed below, and that relies on some principles proposed in the 1970s.

In most studies involving radiometers the output of the instrument has to be obtained in steady-state conditions, for which a variety of theoretical models are available. However, reliable or accurate steady-state data are usually not enough within the framework of advanced diagnostic systems, since for certain measurement applications it is also very important to record dynamic characteristics, such as the transient response of the instrument. If the results are to be obtained in transient conditions, its response time must be considerably shorter. This is one of the main driving forces behind the present work.

The blow-off effect that the transpiration principle implies is central to the desired performance of such an instrument. Indeed, besides having a cooling effect on the sensing element, the transpiration gas is intended both to keep the sensing element clean during operation by deflecting incoming particles and also, just as importantly, to enable the separation of the radiative and convective components of the total heat flux. This can be achieved bearing in mind that the transpiration gas mass flow rate will dictate conditions on the sensing element's surface exposed to the incoming heat flux. A critical transpiration gas mass flow rate will define the following two operating modes:

- For a transpiration gas mass flow greater than the critical value the external stream boundary layer is destroyed and only the radiative component of the total heat flux is received by the sensing element;

- For a transpiration gas mass flow smaller than the critical value the boundary layer is not destroyed and the sensing element receives both to the radiative and the convective components of the total heat flux. This feature enables the separate measurement of the convective and radiative components since the total heat flux is:

$$q_{\text{tot}} = q_{\text{rad}} + q_{\text{conv}} , \quad (1.1)$$

the radiative heat flux being measured directly and the convective heat flux being calculated from the relationship above.

Even from a purely operational point of view, radiation heat flux measurement is arguably the most important part of the problem, since the high temperature levels often found in industrial furnaces dramatically reduce the relative importance of convective heat flux in overall energy balance analyses. Nevertheless, it cannot be ignored since a variety of advanced diagnostic systems rely on total, radiative and convective heat fluxes as input parameters [Calisto *et al.* 2008], although the development of radiometers and total heat flux meters has always been stronger than the development of selective heat flux sensors for industrial applications.

As will be discussed further below, transpiration radiometers are interesting for situations where other techniques are too complex and expensive to be transferred to current industrial applications, mainly due to the high temperature, aggressive environments involved. Previous work along these principles was undertaken in the early 1970s [Moffat *et al.* 1971]. The basic principle already was to blow air through a porous plug (essentially a porous disk mounted on a cylindrical water-cooled copper body) which composed the exposed surface of the gauge.

The air flow had several purposes, the most important of which was to literally blow-off any fluid boundary layer from the surface of the gauge if the flow was sufficiently high, resulting in the elimination of convection. Secondly, the flow provided the temperature difference measured by the gauge, the output signal being proportional to the difference between porous disk and inlet air temperatures. The output signal was monitored by a differential thermocouple, one of the junctions being attached to the back face of the porous disk (on its axis) and the junction set in the transpiration gas stream just behind the disk. The thermal radiation flux was proportional to the signal obtained with the differential thermocouple, *i.e.*, to the temperature difference between the porous medium and the transpiration stream. The porous disk temperature was itself a function of the flow rate and specific heat of the air, as well as of the net radiation heat flux to the disk. The balance between gas cooling and radiation heating



determined the disk temperature, although a calibration procedure was necessary to establish the efficiency of the heat transfer process between the gas and the disk. A second thermocouple could be attached to the disk edge, allowing the use of the instrument as a Gardon gauge if the gas stream was switched off.

Gardon or circular foil gauges were among the first heat flux gauges originally developed to measure thermal radiation flux [Gardon 1953], with their applicability later extended to convection measurements [Gardon 1960]. The Gardon gauge (also known as the asymptotic calorimeter) consists of a hollow cylinder of one material (which acts as a heat sink) with a thin foil of a second material attached to one end. The radial temperature difference between the centre of the disc and its edge is a function of the heat flux to the disk and of the radial temperature profile.

More closely related to the work discussed here was a similar but slightly different radiometer for operation in high-ash boilers [Brajskovic and Afgan 1991, Brajskovic *et al.* 1991]. Basic differences were the fact that instead of going through the plug, the air was directed through slots around a solid plug, and the sensing element was replaced by a Gardon-type heat flux sensor. Indeed, the air flow kept the ash particles from reaching the heat flux gauge and took away the thermal energy as in other transpiration gauges, and heat transfer was radial through the plug as in a circular foil gauge. The heat flux was proportional to the temperature difference measured between the centre and the edge of the plug. Due to their theoretical ability to perform heat flux partitioning and to evaluate deposit thicknesses, these radiometers had the potential to serve as a basis of online furnace and boiler diagnostic systems.

Besides these developments albeit not entirely separate from them, a particular line of development led directly to the work described here. It relied on the same principle of blowing off the convective component of the total heat flux, reverting to the option of having gas crossing the sensitive element [Afgan and Leontiev 1995]. This instrument used a thick (namely when compared with Gardon foils) porous disk as sensing element, replacing the thin net used in earlier instruments. The thicker porous disk had the advantage of collecting the totality of the thermal radiation incident on the surface, no thermal radiation escaping to the inner side of the gauge body due to the non-existent transmissivity of the porous element. In addition, the temperature measurements were made at the front and back surfaces of the porous disk, enabling the determination of the incoming radiation by an energy balance to the porous disk.

The work described here can be said to be in direct continuity from further development of this configuration, namely by the supervisor of this thesis as part of his own PhD, during the course of which a fully operational transpiration heat flux meter

was developed, built and tested in industrial conditions [Martins 1998], its formulation, specifications and performance being discussed in associated publications [Martins *et al.* 1998, Martins *et al.* 2000]. Any of these references makes clear that a rugged and reliable radiometer was obtained, these qualities being extensively proved in full-scale tests carried out in a thermoelectric coal-burning facility. Fouling was indeed shown to be avoided thanks to the transpiration air flow. However, somewhat large response times (up to 5 s) were observed.

While being perfectly adequate for a wide range of applications, namely those in which the instrument was tested, the integration of such an instrument in equipment or systems that exhibit strongly time-dependant behaviours could be hindered by such comparatively high response times. The instrument was also rather bulky, especially due to the necessary water refrigeration system, which could also render it less attractive for some applications. Hardware such as gas turbines (especially for propulsion applications) readily comes to mind as examples of systems that require fast-response instruments, due to the sheer speed at which it operates and which in turn renders slow-responding sensors inappropriate while having restrictions regarding the bulk and weight of all subsystems, including sensors.

The application range of that version of the instrument was subsequently shown to be potentially extended in order to effectively perform heat flux partitioning (which other work suggested by failed to effectively implement) and to obtain a faster response version using a transient operational mode. The path towards these conclusions was similar, since a MSc dissertation was first presented [Hit 2004], having the same supervisor as the one presented here, followed by subsequent publications [Martins *et al.* 2006a, Martins *et al.* 2006b], potential applications in diagnostic systems also being discussed [Calisto *et al.* 2008].

### **1.3 Heat Flux Measurement: Literature Review**

As mentioned earlier, temperature measurements are common and well accepted but heat flux measurements are often given lesser consideration because they are less intuitive. Consequently, sensors that can be used to directly sense heat flux can be extremely important and the present chapter is essentially devoted to the review and discussion of available techniques for thermal radiation and convection flux measurements. If radiation and convection are to be measured separately in situations where both occur simultaneously (arguably the majority of applications), some form of heat flux partitioning must be performed.

There is a large variety of available heat flux measurement techniques, which can be arranged into several categories. One such possible classification broadly divides these techniques into the following four categories:

- **Spatial temperature gradient techniques** – the heat flux across a spatial distance can be determined by measuring temperatures at discrete locations and relating to the temperature gradient and the material properties;
- **Temporal temperature change techniques** – a heat balance is applied to a particular region of the sensor and the temporal measurement of a temperature is related to the heat flux;
- **Energy supply or removal techniques** – a heater or cooler is used to supply or remove energy from a system and a heat balance used to relate the temperature measured to the heat flux;
- **Mass transfer analogy techniques** – measuring mass transfer instead of heat transfer and using an analogy to infer heat transfer.

Due to the often conflicting requirements for sensitivity, robustness, size and cost, any given single heat flux measurement technique is hardly suitable for all applications, the trend being indeed for increased diversity.

As mentioned above, temperature measurements are paramount in most heat flux measurement techniques. A large number of journal articles and chapters in instrumentation books have been written over the years reviewing available heat flux measurement techniques. Some well-established references (in the sense that they have been widely cited) cover general principles [Goldstein 1970, Kostkowski and Burns 1970, Baker and Ryder 1975, Eckert and Goldstein 1976, Thompson and Emrich 1981, Atkinson *et al.* 1983, Goldstein and Chiang 1985, Childs *et al.* 1999] while others focus on specific methods or specific applications, ranging from radiation measurements [Edwards 1970], transient techniques [Scott 1970], high-temperature measurements in gases [Grey 1970], high-speed aerodynamics [Grey 1970, Neumann *et al.* 1988, Neumann 1989], combustion applications [Butler *et al.* 1994, Arai *et al.* 1996, Chander and Ray 2005] to fluidised bed reactors [Saxena *et al.* 1989] and power engineering machines and installations [Jaremkiewicz *et al.* 2009]. An extensive review covering a wide spectrum of methods, with particular emphasis to those oriented to convective heat flux measurement, is available [Diller *et al.* 1993], along with more recent and equally wide-ranging references to which the present review is also indebted [Moffat 1988, Moffat 1990, Moffat 1998, Childs *et al.* 1999].

One unifying factor is that most methods require accurate temperature measurements to be made somewhere as the key to good heat transfer measurements. Many well-established and often cited books and articles have been written covering different aspects of temperature measurement [Baker and Ryder 1975, Eckert and Goldstein 1976, McGee 1988, Childs *et al.* 2000], while others cover specific aspects such as very high temperature measurements [Neuer *et al.* 2001].

### ***1.3.1 Spatial Temperature Gradient Techniques***

#### **Differential Layer and Planar Thermal Gradient Devices**

The simplest heat flux sensor is the so-called layered gauge, consisting of a layer of a material with known thermal conductivity and well-defined thickness, together with two temperature measurement devices located on two opposite faces of the gauge. The gauge is designed so that the heat flux is one-dimensional in the direction defined by the two thermocouples. By measuring the temperature difference under these conditions, all the data required to determine the heat flux are available. Actually, under these specific conditions, Fourier's law can be written as follows, where all the quantities are known with the exception of the heat flux and the temperature distribution is linear:

$$q_x'' = -k \frac{dT}{dx} = -k \frac{T_1 - T_2}{x_1 - x_2} = -\frac{k}{L} \Delta T, \quad (1.2)$$

where  $T_1$  and  $T_2$  are measured temperatures,  $x_1$  and  $x_2$  are measurement locations resulting in sensor thickness  $L$ , which along with thermal conductivity  $k$  are not usually known with sufficient accuracy for any particular sensor to avoid direct calibration of each sensor. The heat transfer rate (in W) is  $q_x = q_x'' A$  and  $A$  is the heat transfer area. An adhesive layer may also be required between the sensor and surface to securely attach the sensor, which adds an additional thermal resistance and increases the thermal disruption. Temperature measurements on the sensor and on the surrounding undisturbed material are recommended to quantify this disruption. A detailed analysis of the performance of this gauge was presented by [Hager 1965]. Similar gauges were later proposed taking advantage from the development of materials science and new production technologies [Godefroy *et al.* 1990, Hager *et al.* 1991].

The selection of a temperature-measuring technique for determining the difference in temperature depends on the need to provide reasonable sensitivity and signal output for the range of heat flux under consideration. The temperature difference can be measured by a variety of methods, most commonly by means of thermocouples.

These have the advantage of generating their own voltage output, which is a function of the temperature difference between their two junctions. They can thus be connected in series to form a thermopile that amplifies the output from a given temperature difference, the voltage output  $E$  being:

$$E = NS_T \Delta T , \quad (1.3)$$

where  $N$  is the number of thermocouple junction pairs and  $S_T$  is the Seebeck coefficient or thermoelectric sensitivity of the junction, calculated as the absolute value of the difference between the Seebeck coefficient of each metal and usually expressed in volts per degree centigrade. The corresponding sensitivity of the heat flux sensor is:

$$S_s = \frac{E}{q''} = \frac{NS_T L}{k} . \quad (1.4)$$

Although sensitivity is determined in practice from a direct calibration, the last member of the previous equation can be used to determine the effects of different parameters for design purposes. The transient response is a function of the separation distance and the material's thermal diffusivity  $\alpha$ . A one-dimensional analysis gave the time required for a 98% response as [Hager 1965]:

$$t = \frac{1.5L^2}{\alpha} . \quad (1.5)$$

From the equations above it can be seen that while sensitivity increases with junction separation  $L$ , the time response increases proportionally to the square of this distance. The use of a thicker layer and/or a lower thermal conductivity material increases the gauge sensitivity since a relatively large temperature difference is obtained, leading to lower heat flux levels. However, these design options also increase the thermal inertia of the gauge and consequently its time response, one of the major drawbacks in the design of these gauges. It should be noted that the temperature difference can be determined by means of thermometers, thermistors, or resistance temperature devices (RTDs), as well as by thermal radiation-based devices and optical methods, besides thermocouples and thermopiles. Thermocouple-based measurement is well known [Heitor and Moreira 1993], but research continues regarding better signal processing procedures, especially in transient measurements [Frankel *et al.* 2008]. The possibility of using intrinsic thermocouples rather than standard soldered ones [Genix *et*

*al.* 2009] or the use of non-standard semiconductor thermoelectric modules, as opposed to conventional thermocouples [Ploteau *et al.* 2007], is also being pursued.

One of the first reported heat flux sensors made use of this technique, with thermometers placed on either side of a cork floor to determine the heat loss in a food processing plant [Hencky 1915]. Some forms of thermopile sensors have found widespread application, leading to commercial production, and several are listed below as examples. There is a variety of gauge configurations, with the basic configuration illustrated in Figure 1.1. The most simple is merely a thermal resistance layer, to which a thermopile with several hundred junctions is fitted over areas in the range of some hundred square centimetres, with the possibility of using flexible material, such as mylar or kapton in order to allow for some surface conformability. Gauges made with these materials lead to uses at relatively low temperatures (around 500°C) and convection heat transfer studies [van Dorth *et al.* 1983], although applications such as fluidised bed combustion chambers [Kumada *et al.* 1990] and fouling in combustion chambers [Marner *et al.* 1989] have been reported. The major limitations of this technique, when thermal radiation has to be measured in high temperature harsh environments, are the problems related with the control of the gauge temperature, the cleanness of the sensing element and the separation of the convection component of the total heat flux.

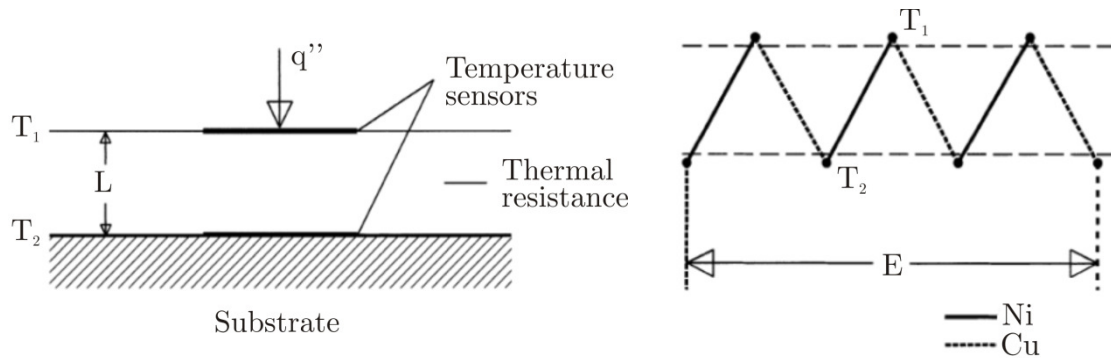


**Figure 1.1** - Basic layered gauge principle and thermopile for differential temperature measurement [Diller *et al.* 1993].

Another successful, widespread and commercially available design using a thermopile consists of thin pieces of two types of metal foil, alternately wrapped around a thin plastic (once again kapton) sheet and welded on either side to form thermocouple junctions, as illustrated in Figure 1.2 [Ortolano and Hines 1983], with a separate thermocouple included to provide a measure of the sensor temperature. Such

sensors are typically limited to measuring temperatures below  $250^{\circ}\text{C}$  and heat fluxes lower than  $100 \text{ kWm}^{-2}$ , with response times of approximately 20 ms. Sensors with higher sensitivity are made with semiconductor thermocouple materials for geothermal applications, with operating temperatures of up to  $1250^{\circ}\text{C}$ .

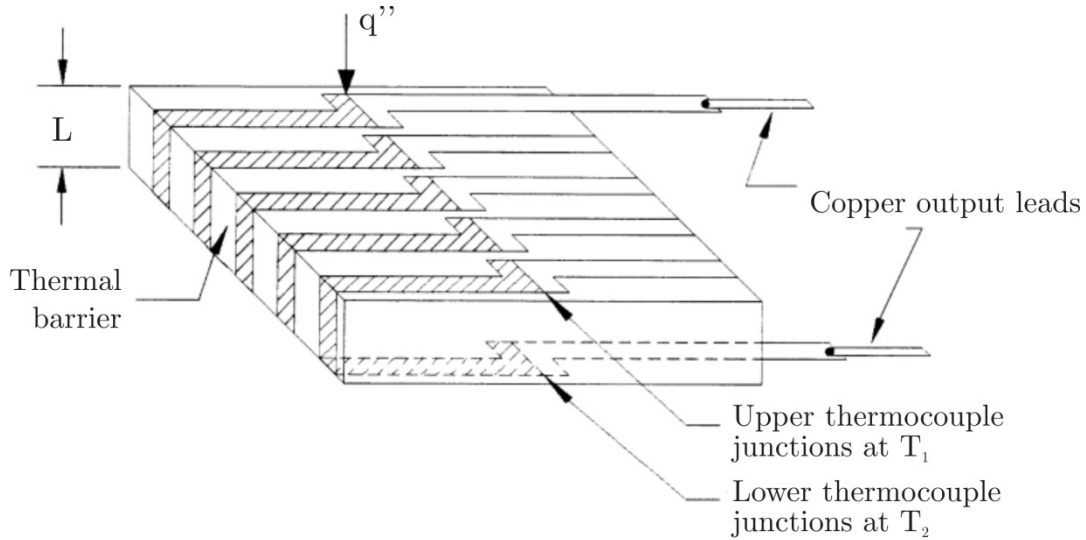


**Figure 1.2** - Thermopile heat flux sensor [Ortolano and Hines 1983].

Different manufacturing techniques (namely thin-film sputtering techniques) result in very thin sensors with low physical and thermal disruption, which when used together with (and for which the use of) high-temperature thermocouples, allow operating temperatures to exceed  $800^{\circ}\text{C}$ , being best suited for heat flux values above  $1 \text{ kWm}^{-2}$ , with no practical upper limit. The sensor's thinness allows the thermal response time to be less than  $10 \mu\text{s}$ , giving a good frequency response, often well above  $1 \text{ kHz}$  [Hager *et al.* 1993, Holmberg and Diller 1995]. A similar sensor design makes use of screen printing techniques of conductive inks and a large number of thermocouple pairs (up to 10,000), yielding sufficiently high sensitivities to measure heat fluxes as low as  $0.1 \text{ Wm}^{-2}$ , thermal time constants of about 1 s and upper temperature limits of approximately  $150^{\circ}\text{C}$  [Terrel 1996]. Sensitivities better than  $40 \text{ mVW}^{-1}\text{cm}^{-2}$  have been obtained with similar sensors [Langley *et al.* 1999], the trend being towards more sensitive sensors with micromachined components [Escriba *et al.* 2005].

Another common technique for measuring the temperature difference across the thermal resistance layer is to wrap wire and then plate one side of it with a different metal (usually wire with copper plating), resulting in a wire-wound sensor looking similar to the sensor shown in Figure 1.2. The difference is that the constantan wire is continuous all around the sensor, so it does not form discrete thermocouple junctions.

Nonetheless, a high sensitivity can be achieved because of the hundreds of windings on the sensors, although at the expense of limited temperatures (up to about  $150^{\circ}\text{C}$ ) and large time constants of around 1 s [van der Graaf 1989]. Plated sensors using ceramic units are available for operation temperatures above  $1000^{\circ}\text{C}$ .

A very popular version of plated wire sensors uses a small anodized piece of aluminium inserted into a water-cooled circular housing, commonly known as the Schmidt-Boelter gauge, illustrated in Figure 1.3 [Kidd and Nelson 1995], available in sizes as small as 1.5 mm diameter which render them highly attractive for aerodynamic testing applications [Neumann 1989]. There is also some ability to contour the surface of the sensor to match a curved model surface for complex shapes. Care must be taken when measuring low heat fluxes with Schmidt-Boelter gauges, although limitations and error avoidance methodologies are well understood [Robertson and Ohlemiller 1995].

A variation on the differential thermopile heat flux sensor concept relies on the thermal gradient being artificially created by a temperature differential on the surface plane of the component. This can be achieved, for example, by using alternate layers of materials of different thermal conductivities or different thicknesses, or by exposing one half of the thermopile junctions to the convective boundary condition fluid [Godefroy *et al.* 1990]. Typically using several hundred thermocouple pairs and aluminium nitride/silicon monoxide vacuum-deposited differential layers, the substantial difference in the thermal conductivity of the two thermal resistance layers generates a sufficiently large thermal gradient in the plane of the thermopile for sensitive measurements.



**Figure 1.3** – Schmidt-Boelter gauge [Hukseflux 2009].



## Gardon gauges

The circular foil gauge was one of the first heat flux gauges originally developed to measure thermal radiation fluxes [Gardon 1953], with its applicability later extended to convection measurements [Gardon 1960]. The Gardon gauge (also known as the asymptotic calorimeter) consists of a hollow cylinder of one material (which acts as a heat sink) with a thin foil of a second material attached to one end. The radial temperature difference between the centre of the disc and its edge is a function of the heat flux to the disk and of the radial temperature profile, measured by means of a thermocouple formed by the junction of a thermoelectrically dissimilar wire connected to the centre of the disc, usually a copper wire connected to a Constantan disc, itself resting on a copper cylinder as illustrated in Figure 1.4. Each gauge must thus be calibrated in order to take into account all the parameters influencing the temperature profile, *e.g.*, heat losses through the thermocouple wires and variable thermal properties of the disk.

For a uniform heat flux, typical of incoming radiation, the centre to edge temperature difference is proportional to the heat flux (neglecting heat losses down the centre wire and assuming that thermal conductivity is constant with temperature), that is:

$$T_0 - T_s = \frac{q'' r^2}{4kL}, \quad (1.6)$$

where  $L$  is the foil thickness and  $r$  the active radius of the foil. The output voltage is proportional to the product of the temperature and the thermoelectric sensitivity of the differential thermocouple. The gauge's time response was demonstrated to be [Gardon 1953, Gardon 1960]:

$$t = \frac{r^2}{4\alpha}, \quad (1.7)$$

where  $\alpha$  is the material's thermal diffusivity.

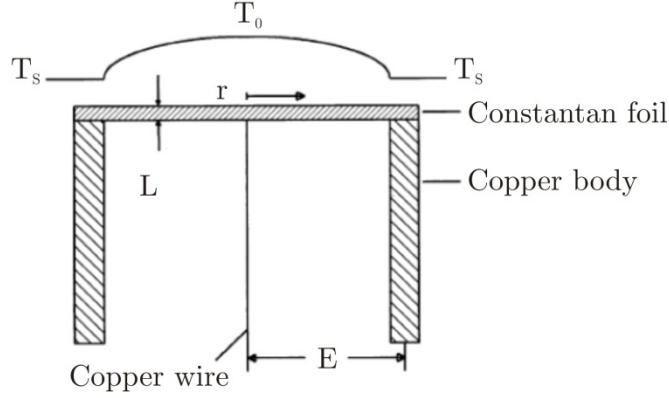


**Figure 1.4** – Basic Gardon gauge configuration [Diller, James *et al.* 1993].

Particular care is required when convection heat fluxes are measured. It has been shown both analytically and experimentally that the output is incorrect for convective heat transfer because of the distortion of the foil's temperature profile from the assumed radially symmetric, parabolic profile of radiation [Kuo and Kulkarni 1991]. Since the amount of error is a function of the gauge geometry, the fluid flow and the heat transfer coefficient, it is difficult to reliably correct. This renders the calibration curves, obtained by means of a thermal radiation heat source, inadequate for convection heat flux measurements, so that correction factors must be considered [Diller *et al.* 1993]. Consequently, great care must be taken to keep the temperature difference across the gauge small if Gardon gauges are used to measure convective heat transfer. The basic Gardon-type gauges have been widely used over time, namely with improved calibration procedures [Ballestrín *et al.* 2006], with recent versions making use of micromachining technologies [Oh *et al.* 2006].

For high temperature and high heat flux operation, some problems have also been reported [Young *et al.* 1984, Englund and Seasholtz 1988, Neumann *et al.* 1988]. In situations such as combustors, water cooling is usually supplied through the body of the sensor to keep the temperature from exceeding material limits. Due to the resulting temperature mismatch between the gauge and surrounding material in which it is mounted, a water-cooled gauge is not recommended for convection heat transfer measurements. It is also important for a water-cooled gauge to ensure that condensation does not occur on the sensor face. Despite the aforementioned limitations, successful high-temperature measurements have been reported using circular foil gauges [Thibault and Hoffman 1979, Shepherd 1985].

Although most heat flux sensors are designed to measure the total heat flux, sensors have been developed to separate convection from radiation (as discussed in further detail below). The most common method is to put a transparent window over

the sensor to eliminate convection to the sensor face. Once the resulting sensor only measures radiation, it is termed a radiometer. The field of view can however be limited in these radiometers and must be included in the interpretation of results. In a dirty environment where the transmission of the window could be degraded, air is usually blown across the face of the window to keep particles away from the sensor.

Gardon gauges have been reported in use for fire spread experiments in the field, measuring both total and radiant heat fluxes emitted from the flame front, a sapphire window attachment being added to the radiant heat flux transducer to eliminate convective heat transfer [Silvani and Morandini 2009], with the usual caveats regarding mixed convective-radiative experiments, which have been widely studied [Kuo and Kulkarni 1991], still applying. As with Schmidt-Boelter gauges, care must be taken when measuring low heat fluxes [Robertson and Ohlemiller 1995]. Both types of gauges are also used as components in hybrid heat flux measurement systems such as the so-called plate thermometer [Ingason and Wickström 2007].

## **Refractive index methods**

A temperature gradient across a transparent medium will cause a local variation in its refractive index. This physical phenomenon can be measured by a number of optical techniques such as schlieren photography, shadowgraph and interferometry. The sensitivity of each method is different, with the schlieren and shadowgraph techniques being appropriate for large thermal gradient applications and interferometry for applications where the thermal gradient is less severe as in, for example, natural convection [Goldstein 1970].

### ***1.3.2 Temporal Temperature Change Techniques***

The basic heat transfer equations can describe the relationship between temperature gradients and surface heat transfer. If the wall material thermal properties are known along with sufficient detail about the temperature history and distribution, heat transfer can be determined as a function of time, after some manipulation, at a location near to or on the surface of interest. Two general types of solutions are used to reduce the temperature history to heat flux. These are commonly designated as the semi-infinite solution and calorimeter methods. Usually involved are surface temperature measurements using thermocouples or RTDs and optical methods that allow for simultaneous measurement of temperatures over the entire surface. All require substantial effort from the user to initiate the test procedure and reduce the data to find heat flux.

A number of techniques are based on these principles, including slug calorimeters, plug gauges, null point calorimeters, coaxial thermocouple gauges, thin-skin and thin-film sensors, and surface temperature monitoring of the whole component.

An important technique for short-duration heat flux tests is to measure the surface temperature history on a test object with a fast-response temperature sensor. For sufficiently short times and a sufficiently thick material, heat transfer can be assumed to be one-dimensional and thermal effects considered not to reach the back surface of the material. The temporal temperature variation

$$\frac{\partial T}{\partial t} = \frac{k}{\rho c_p} \left( \frac{\partial T^2}{\partial x^2} + \frac{\partial T^2}{\partial y^2} + \frac{\partial T^2}{\partial z^2} \right), \quad (1.8)$$

where  $k$  is the thermal conductivity,  $\rho$  is the density and  $c_p$  is the specific heat, becomes a one-dimensional, semi-infinite solution, and for a step change of heat flux at time  $t = 0$  the surface temperature is given by [Diller *et al.* 1993]:

$$T_s - T_i = \frac{2q''\sqrt{t}}{\sqrt{\pi k \rho c_p}}, \quad (1.9)$$

where  $T_i$  is the uniform initial temperature of the substrate and  $T_s$  is the surface temperature as a function of time. Data analysis of the measured temperature record can be performed by several methods, the simplest of which makes use of the analytical solution with each sampled data point to recreate the heat flux signal. The most popular equation for this conversion for uniformly sampled data (*i.e.* uniform time steps) for any time  $t_n$  is [Cook and Felderman 1966]:

$$q''(t_n) = \frac{2\sqrt{k\rho c_p}}{\sqrt{\pi}} \sum_{i=1}^n \frac{T_i - T_{i-1}}{\sqrt{t - t_i} + \sqrt{t - t_{i-1}}}. \quad (1.10)$$

Modifications are also available to provide higher solution stability [Diller and Kidd 1997], as well as numerical solutions to account for changes in property values with varying temperatures [George *et al.* 1991]. Due to the noise amplification inherent in the conversion from temperature to heat flux, analogue methods have been

developed to electronically convert the temperature signal before digitizing the signal [Schultz and Jones 1973].

### Slug calorimeters, plug gauges and null point calorimeters

A typical slug calorimeter comprises a quantity or ‘slug’ of material, thermally insulated from its surroundings, as illustrated in Figure 1.5. A single temperature measurement at the base of the slug is made and is assumed to represent the temperature of the entire slug mass  $m$ , this assumption being valid within a few per cent if the Biot number,  $Bi = hL/k$ , is lower than 0.1, with  $k$  and  $h$  being the conduction and convection heat transfer coefficients, respectively, and  $L$  the depth of the slug. This condition is essentially a classic lumped mass approximation in which the temperature throughout the sensor is assumed to be uniform while changing with time.

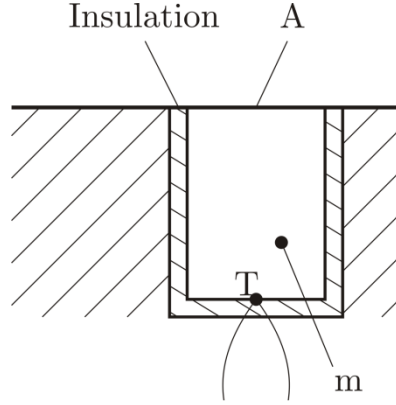


**Figure 1.5** – Slug calorimeter [Diller *et al.* 1993].

When exposed to a fluid at a temperature  $T_f$  and heat transfer coefficient  $h$  over an active area  $A$ , the solution for the temperature change is the following exponential function [ASTM 1988a]:

$$\frac{T - T_f}{T_i - T_f} = e^{-t/\tau}, \quad (1.11)$$

where  $T_i$  is the initial temperature and the time constant  $\tau$  is:

$$\tau = \frac{mc_p}{hA}. \quad (1.12)$$

The time constant can be derived from the temperature response of the system, which can then be used to quantify the heat transfer coefficient  $h$ . Although these calorimeters are simple in principle, it is often difficult to obtain reliable results because of heat losses and non-uniform temperatures. If more accurate results are required, the losses through the insulation layer should be modelled and accounted for by a correction term [Diller *et al.* 1993]:

$$q = \frac{mc_p}{A} \frac{dT}{dt} + q_{loss} = \frac{mc_p}{A} \frac{dT}{dt} + K_{loss} \Delta T, \quad (1.13)$$

where  $\Delta T$  is the temperature difference between the slug calorimeter and the surrounding material. This can be taken as the rise in temperature of the slug, assuming that the surrounding material temperature remains constant for the duration of the data acquisition. The constant  $K_{loss}$  for a given sensor can be determined by calibration and supplied by a laboratory or manufacturer. Slug calorimeters are normally used when the energy input to the surface is fairly constant. They can only produce useful data for short exposures; the duration of use is limited because  $T$  will approach  $T_\infty$  and they must be restored to an initial condition before reuse. It is recommended that a period defined by  $t = L^2/2\alpha$  be allowed prior to logging of data [ASTM 1988a]. Severe disadvantages of this form of device, particularly when measuring large heat fluxes, are the disruption to the thermal boundary layer owing to the thermal discontinuities introduced by the sensor material boundaries and the difficulty of quantifying the heat losses through the insulation layer. It is recommended that the slug itself is manufactured with the same material as the surroundings in order to ensure minimization of non-uniform temperature effects. Despite the aforementioned limitations in terms of experiment time limitations the development of slug calorimeter-based system continues, including as part of calibration facilities and flammability and fire safety studies [Filipczak and Lyon 2002, Filipczak *et al.* 2005].

The plug gauge is a development of the slug calorimeter [Liebert 1994], comprising a slug instrumented with multiple thermocouples to provide the temperature distribution. An annulus is created on the backside of the surface, four thermocouples being attached along the remaining plug to estimate both the temperature gradient and the change in thermal energy content in the plug. This setup gives a better estimate of the heat flux than the slug calorimeter. An additional advantage is that the measurement surface is physically undisturbed.

Null-point calorimeters are a further extension of the slug calorimeter principle, developed to improve plug gauge response times [ASTM 1988b]. They are designed for the measurement of extremely high heat flux levels (over 1000 kWm<sup>-2</sup>). In order to protect the thermocouple and wires, these are mounted in a cavity behind the surface, the temperature measurement location being placed closer to the surface. The heat flux measurement is based on a one-dimensional transient conduction solution and is given, as for a semi-infinite geometry, by Equation 1.10. In order to eliminate the effects of the initial temperature transient on the indicated heat flux, a value of 1.375 is recommended for the ratio of hole diameter to the thermocouple distance from the surface,  $b$  [Kidd 1990b]. Measurements can be taken until the thermal transient reaches the back of the sensor at depth  $L$ , the useful period of measurement being bounded by:

$$\frac{3b^2}{\alpha} < t < \frac{0.3L^2}{\alpha}. \quad (1.14)$$

The term on the right-hand side of the above inequality is associated with an error in the semi-infinite approximation of less than 1% [Kidd 1990b].

### **Coaxial thermocouple gauges**

The principle of the coaxial gauge is to measure the variation in surface temperature directly as a function of time. A thermocouple is formed by a concentric arrangement consisting of a central thermocouple material which is electrically isolated from the outer thermocouple material by an insulating sheath. The thermocouple circuit is completed at the surface by applying a thin layer of one of the thermocouple materials by, for example, vacuum deposition. Alternatively, the thermocouple circuit can be completed by removing the insulation at the tip and soldering or merging the two metals together. The heat flux can be determined from the temporal temperature measurement as for null-point calorimeters. Average coaxial thermocouple material properties can be used for the material properties product,  $\rho c_p k$  [Garcia and de Schor 1990, Kidd 1990a]. Response times are typically 1 ms or less which, although slower than the thin-film sensors, are sufficient for a wide range of applications [Neumann 1989].

### Thin-skin and thin-film devices

This method has been used to study heat transfer in, for example, spacecraft or nuclear warhead re-entry vehicles. In these studies, part of the surface of a model or component is removed and replaced with a thin layer or ‘skin’ of a highly conductive material such as copper, which forms the slug calorimeter [Schultz and Jones 1973].

The assumption in the analysis is that the rate of temperature rise at the rear surface, which can be monitored with thermocouples, is equal to the rate of rise in the mean temperature. Lateral conduction along the skin is ignored. Heat loss from the rear of the skin is assumed to be negligible due to the presence of insulation. Air, which has a relatively low thermal conductivity, can be used for this purpose. Because of advances in thin-film and optical surface temperature measurement, the thin-skin method is considered outdated for most modern aerodynamic testing [Neumann 1989], but is in much use for thermal conductivity measurements [Lourenço *et al.* 2000].

Thin-film sensors are physically small devices applied to the surface of interest and exhibit fast response to thermal conditions because of their small size, as illustrated in Figure 1.6.

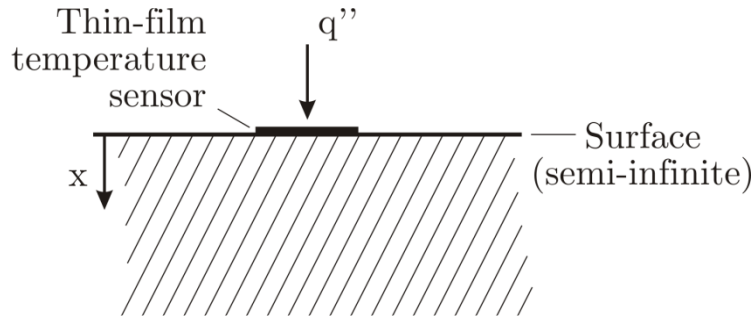


**Figure 1.6** - Basic thin film sensor configuration [Diller *et al.* 1993].

A metallic resistance layer is sputtered, painted and baked, or plated onto the surface. Because the resulting thickness of the sensor is less than  $0.1\text{ }\mu\text{m}$  the response time is a fraction of  $1\text{ }\mu\text{s}$  and there should be no physical or thermal disruption of the measured temperature due to the sensor. The method is used for basic measurements applicable to gas turbine engines, rockets, internal combustion engines and high-speed aerodynamics [Diller *et al.* 1993]. In addition to surface temperature measurement



(single-layer sensors), thin-film sensors can also be used to measure heat flux in layered or composite assemblies.

Sensors of this type were traditionally obtained by vacuum depositing or painting, and sintering on to platinum resistance thermometers an electrically insulating surface, with lead wires obtained in similar fashion. It is not always practicable to manufacture components of an insulating material that will allow the application of thin-film surface sensors for heat transfer studies. One technique to overcome this limitation involves the application of sensors to a polyamide film. An alternative development for use in aggressive environments, such as turbomachinery research, involves the application of vitreous enamel to a component for electrical isolation of the surface sensors [Doorly 1988].

Most thin films produced by a wide variety of methods, either physical or chemical (PVD, CVD, sputtering, *etc.*) for temperature sensor applications, can be used only in very narrow ranges of temperatures, where their components are not subjected to differential thermal expansions, recrystallizations, and grain size modifications [Lourengo *et al.* 1998].

Thin-film sensors have also been combined in a hybrid instrument for solar radiation measurements which relies on them for direct heat flux measurements, which are compared and satisfactorily corroborated by an indirect system, consisting of a CCD camera that uses a water-cooled heat flux sensor as a reference for converting gray-scale levels into heat flux values [Ballestrín and Monterreal 2004].

### **Optical surface monitoring**

Optical methods allow the measurement of the entire temperature field over a section of the surface, with a large amount of data being collected but requiring a more challenging interpretation of data to obtain quantitative heat flux values than with measurements systems that use point sensors.

The most widespread optical temperature measurement method is the use of liquid crystals to record colour change. Of particular relevance to heat transfer studies are the cholesteric (or chiral-nematic) liquid crystals which react to changes in temperature and shear stress by changing colour. These are popularly named

thermochromic liquid crystals. The thermal response of crystals, which is dependent on their viscosity, ranges from 5 ms to a few seconds [Ireland and Jones 1987]. They degrade when exposed to ultraviolet light and are prone to chemical contamination. As a consequence, crystals are encapsulated in polymer spheres, forming a water-based slurry that can be painted or applied with an airbrush to the surface of interest for use over temperature ranges from 5 to 150°C. Setting the lighting for reproducible colour, temperature calibration, image acquisition, and accurately establishing the starting temperature are crucial steps, detailed procedures for accurate measurements having been established [Baughn 1995, Camci 1996, Alekseev 1997]. A complete system typically includes a high-quality video camera, lighting system, calibration system, computer hardware and software for image processing and a liquid crystal kit. Although the basic materials are cheap, the associated equipment is expensive.

The colours can be recorded by means of a video camera and can be stored in terms of the primary colours: red, green and blue. The frames can later be digitally analysed via a computer and frame grabber and the data converted from the RGB system to a hue, saturation and intensity system. Comparison of the hue values with calibration results gives the surface temperature for each pixel location. A video recording of the surface temperature variation in response to a fluid temperature change can be used to determine the surface heat flux and corresponding surface heat transfer coefficient. For semi-infinite conditions, the optically measured variation in temperature with time can be related to the heat transfer coefficient (assumed constant) by solving the following equation:

$$\frac{T - T_i}{T_\infty - T_i} = 1 - e^{\beta^2} \operatorname{erfc}(\beta), \quad (1.15)$$

where

$$\beta = h \sqrt{\frac{t}{\rho c_p k}} \quad (1.16)$$

and  $\text{erfc}(\cdot)$  is the complementary error function available in standard mathematics texts.

Thermographic phosphors emit radiation in the visible spectrum when illuminated with ultraviolet light. The intensity of emission at specific wavelengths can be related to the temperature over a wide range of surface temperatures. A CCD camera is required to record the transient optical images and calibration is challenging, but high-temperature applications are particularly appealing [Bizzak and Chyu 1995]. Infrared thermography is also in widespread use, with a variety of recent references available [Hakenesch 1999, Astarita *et al.* 2000, Astarita *et al.* 2006].

### **Thermal Radiation Methods**

All materials continuously absorb and emit electromagnetic waves or photons by raising or lowering their molecular energy levels. The intensity and wavelengths distribution of emission can be related to the absolute temperature of the material. According to the Stefan-Boltzmann law, radiated heat transfer is proportional to the fourth power of the difference in temperature. Detectors of thermal radiation or radiometers can broadly be grouped according to how the incoming radiation interacts with the detector material. Generally, thermal detectors convert incident radiation into a temperature rise and photon detectors absorb the energy of the incident radiation. Photon detectors were initially more laboratory-bound due to the fact that they were usually more fragile than thermal detectors but they are nevertheless in continuous development because they are inherently adequate to high temperature applications [Bhattacharya *et al.* 2007]. Not all photomultiplication-based instruments are fragile, however, since heavy-duty, rugged versions exist for radiation measurements in industrial burners [Sanz *et al.* 2008].

The advantage of thermal radiation methods is that they are non-contact or non-disruptive. Sensing surfaces are often treated with appropriate coatings in order to establish known, high surface absorptivities/emissivities, enabling thermal radiation measurements. However, some problems arise if these measurements are to be carried out in high temperature, aggressive environments such as those usually found in heavy-duty industrial equipment. Basic problems to be solved are the need to avoid sensing element surface fouling, corrosion problems and contamination of the measurements by the convective component of the total heat flux, not to mention the simple survival of the instrument in such a hostile environment.

In situations where convection and radiation coexist, gauges generally measure the total heat flux. In order to perform heat flux partitioning, gauges are usually designed to measure either radiation or convection, but not both. Arguably the easiest way to measure only radiation is to place a transparent window or lens between the radiation source and the heat flux gauge. A number of devices are based on this approach [McGee 1988], such as pyrometers, bolometers and infrared cameras, representing a well-developed and specialized field. The purpose of this review is not, however, to detail these devices. Incident heat fluxes are typically measured either with gauges using RTDs or thermocouples, or by directly measuring the radiation with photoconductive detectors [Baker and Ryder 1975]. In a different approach, the total heat flux and the convection component can be measured by using two heat flux gauges, one with a high-emissivity coating and the other with a low-emissivity coating, the radiation component being the difference between the measurements of the two gauges. Illustrated in Figure 1.7 is an example of such a sensor [Hukseflux 2009], with one gauge coated with gold and the other with a black absorbent.



**Figure 1.7** – Convective and radiative heat flux sensor with two sensing elements of different emissivities [Hukseflux 2009].

Other variations on the layered gauge principle for high temperature measurements rely on water-cooled configurations, many of which were developed from the latter half of the 1960s to the early 1970s [Anson and Godridge 1967, Schulte and Kohl 1970]. Illustrated in Figure 1.8 is the Anson-Godridge sensor, used to measure the heat flux within an oil-burning boiler. Other similar systems were reported for use as a total heat flux meter in power plant boilers, with an interesting contribution regarding the proposed engineering solutions to permanently install the gauges inside the boiler.

Since the meters are directly installed on the heat exchanger tubes, the heat sink and gauge cooling system are the tubes themselves. A portable version was also proposed, where a heat pipe took the role of the boiler tubes [Neal *et al.* 1980].

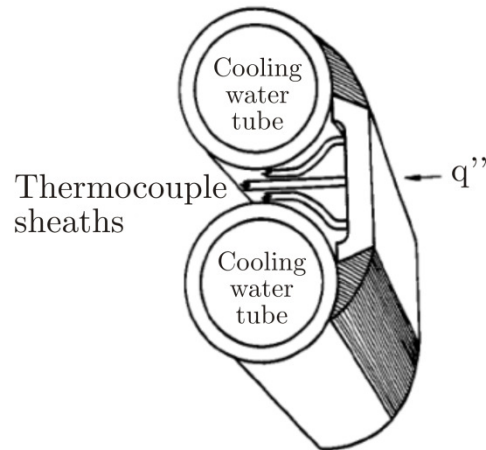


**Figure 1.8** – Anson-Godridge sensor [Anson and Godridge 1967].

Problems arise with the radiation-only devices when the environment of the measurement is dirty enough to leave deposits on the window, which degrades its transmission. The hollow ellipsoidal total radiation flux meter uses a thermopile as the sensing element where all the radiation entering through an inlet small orifice is focused by an ellipsoidal mirror [Chedaille and Braud 1972], the basic sensing element being the layered gauge described above. The ellipsoidal mirror, with a near-unitary reflectivity regardless of wavelength and incident angle, is added in order to focus all the radiation falling on the frontal orifice of the heat flux sensor. A flow of dry nitrogen is injected through small holes placed at the mirror walls in order to avoid the condensation of vapours and the deposition of particles. The sensitivity and response time of this gauge depend essentially on the thermopile used as sensing element. The most important advantage of the ellipsoidal radiometer is its high efficiency in converting thermal radiation into sensible heat (once again regardless of wavelength and direction of incidence), its major drawbacks being the influence of the nitrogen stream on readings, its fragility and the need for periodic calibration which limits its use to laboratory applications. The cleanliness (or lack thereof) of the ellipsoidal mirror and the location of the thermopile give the gauge its high sensitivity and are main factors contributing to its fragility. Any degradation in mirror reflectivity strongly affects the gauge performance and the validity of its calibration curve.

The basic ellipsoidal radiometer has been continuously developed over time, involving improved versions of the instrument itself, its applications in full-scale industrial studies [Hayes *et al.* 2001] and its calibration procedures [Murthy *et al.* 2000, Hayes *et al.* 2001, Murthy *et al.* 2003], with further refinements still taking place and yielding higher sensitivities [Oliveira and Yanagihara 2004, Oliveira and Yanagihara 2008]. This improved version, designated as a semi-ellipsoidal radiometer due to its modified cavity geometry, is illustrated in Figure 1.9.

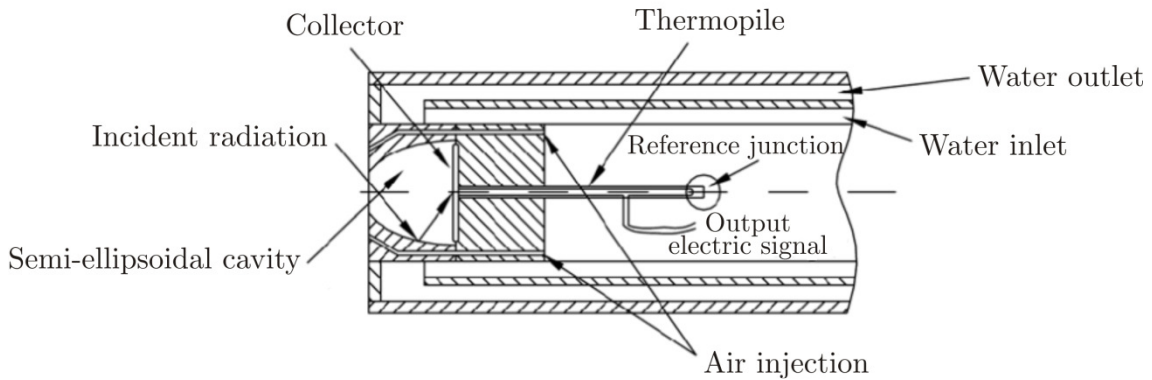


**Figure 1.9** – Semi-ellipsoidal radiometer [Oliveira and Yanagihara 2008].

Other radiometers adequate for application in thermal radiation measurements in full-scale furnaces were proposed. One of them is also a variation of the layered gauge, but in this case the gas screen around the sensing element is present mainly in order to eliminate the convective component of the total heat flux [Ballintijn and Ginsel 1968]. Considering the sensing element type and the described design, relatively good sensitivities can be obtained at the expense of large response times. However, this gauge can distinguish between radiative and total heat flux just by switching the gas screen on or off, thereby performing heat flux partitioning. It also comprises a rugged and simple design, which is an important consideration when industrial uses are foreseen. Its principal problems are the limited ability of the gas screen to avoid fouling and the convective heat flux component, with adverse effects on the gauge accuracy and reliability, and the possible cooling effect of the sensing element due to the gas screen. Despite these limitations, the gauge was successfully used for heat flux studies in industrial furnaces [Hoogendoorn *et al.* 1970].

Another solution developed for measuring radiation heat flux in combusting environments is the transpiration radiometer, this technique having been successfully applied to the measurement of radiative heat loads in gas turbine engines [Atkinson *et*

*al.* 1988] and to the characterization of pool fires [Matthews and Longenbaugh 1989]. The basic principle is to blow air through a porous plug (essentially a thin porous disk mounted on a cylindrical water-cooled copper body) which composes the exposed surface of the gauge, rather than around the sensing element. The air flow has several purposes, the first of which is to literally blow-off any fluid boundary layer from the surface of the gauge if the flow is sufficiently high, resulting in the elimination of convection. Secondly, the flow provides the temperature difference measured by the gauge, the output signal being proportional to the difference between the porous disk and inlet air temperatures. The output signal is monitored by a differential thermocouple, one of the junctions being attached to the back face of the porous disk (on its axis line) and the junction set in the transpiration gas stream just behind the disk. The thermal radiation flux is proportional to the signal obtained with the differential thermocouple, *i.e.*, to the temperature difference between the porous medium and the transpiration stream. The porous disk temperature is itself a function of the flow rate and specific heat of the air, as well as of the net radiation heat flux to the disk. The balance between gas cooling and radiation heating determines the disk temperature, although a calibration procedure is necessary to establish the efficiency of the heat transfer process between the gas and the disk. A second thermocouple can be attached to the disk edge, allowing the use of the instrument as a Gardon gauge if the gas stream is switched off [Moffat *et al.* 1971].

The instrument requires two calibration steps. The first is the determination of the transpiration gas mass flow rate required to eliminate the convective heat flux. The second step is required in order to obtain a correlation between the incident radiation flux and the corresponding output signal, the whole calibration procedure being performed under the same conditions (pressure and external cooling) found during actual measurements. This complex calibration procedure is the gauge's main disadvantage, which is offset by significant advantages such as the possibility of measuring radiation heat fluxes even in the presence of convection or other thermal fluxes governed by external flow aerodynamics. In addition, the gauge is naturally not affected by fouling, since particles are deflected by the transpiration stream and the sensing element has a view angle of virtually  $180^\circ$ .

A similar but slightly different radiometer for operation in high-ash boilers was proposed and studied in detail [Moffat *et al.* 1971, Brajuskovic and Afgan 1991, Brajuskovic *et al.* 1991]. Basic differences are the fact that instead of going through the plug, the air is directed through slots around a solid plug, and the sensing element is replaced by a Gardon-type heat flux sensor. Indeed, the air flow keeps the ash particles from reaching the heat flux gauge and it takes away the thermal energy as in other

transpiration gauges, and heat transfer is radial through the plug as in a circular foil gauge. The heat flux is proportional to the temperature difference measured between the centre and the edge of the plug. This “clean” heat flux gauge can be used with a second gauge that has no air flow, to form a system to measure particle deposition in combustors. As deposition occurs in the “dirty” gauge surface, the heat transfer resistance increases and the measured heat flux drops [Marner *et al.* 1989]. The thickness of the deposit can then be related to the difference in heat transfer between the two gauges. Another fundamental difference is a significantly more powerful screening jet (with a maximum velocity at least twice as high), when compared with the previous solutions. The effect of the screening-gas flow rate level on the calibration curve and response time was investigated, and time constants between 2.3 and 4.6 seconds and an accuracy of plus or minus 10% or better were reported in detailed studies of this gauge [Brajuskovic and Afgan 1991]. Due to their ability to perform heat flux partitioning and to evaluate deposit thicknesses, these radiometers are the basis of online furnace and boiler diagnostic systems [Calisto *et al.* 2008].

The same principle of blowing off the convective component of the total heat flux is used in another heat flux meter (which reverts to the option of having gas crossing the sensitive element) that allows the separate measurement of the convection and radiation components of the total heat flux. Once again, if the transpiration gas flow rate is above a critical flow rate, sufficient for blowing off the boundary layer on the sensing element surface, the sensing element is exposed to the total heat flux, *i.e.*, convection plus radiation heat fluxes. If the transpiration gas mass flow rate is higher than the critical flow rate, the convection heat flux to the sensing element is eliminated and the sensing element only receives the radiation heat flux. With two independent successive measurements, there is the possibility of assessing both the radiation and the convection components of the received heat flux, effectively performing radiation partitioning [Afgan and Leontiev 1995]. This instrument uses a thick (namely when compared with Gardon foils) porous disk as sensing element, replacing the thin net used in earlier instruments [Moffat *et al.* 1971].

The thicker porous disc has the advantage of collecting the totality of the thermal radiation incident on the surface, no thermal radiation escaping to the inner side of the gauge body due to the non-existent transmissivity of the porous element. In addition, temperature measurements are made at the front and back surfaces of the porous disk, enabling the determination of the incoming radiation by an energy balance to the porous disk. This configuration was pursued further, first by obtaining and testing an operational version of the instrument [Martins *et al.* 1998, Martins *et al.* 2000], then by extending its application range in order to effectively perform heat flux



partitioning and to obtain a faster response version using a transient operational mode [Martins *et al.* 2006a, Martins *et al.* 2006b], with work still progressing in this approach as discussed in the following chapters. This transpiration heat flux meter is schematically described and shown in Figure 1.10.

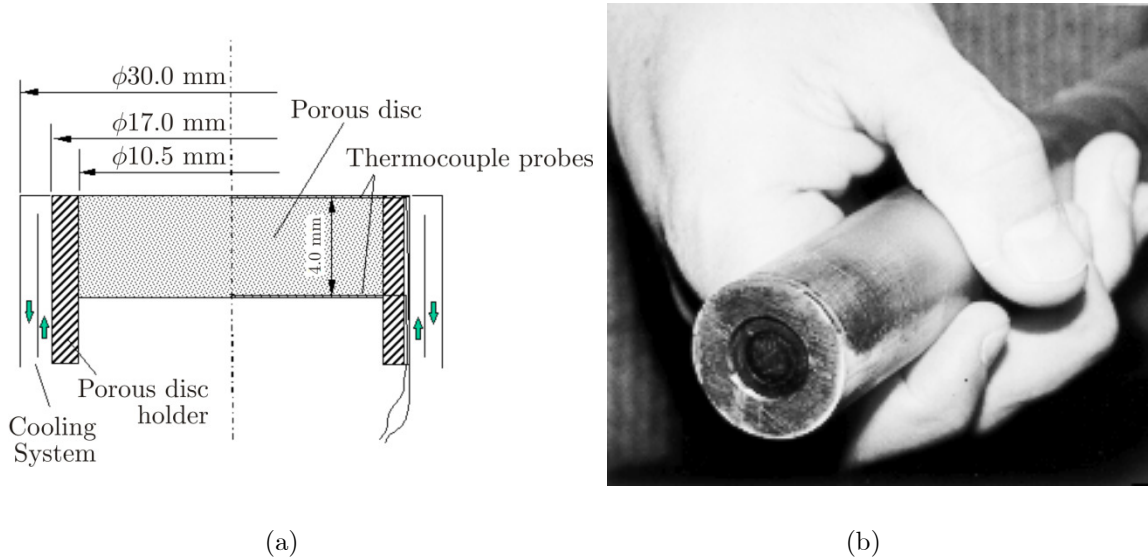


**Figure 1.10** – Transpiration radiometer: (a) schematic representation and dimensions, and (b) sensor [Martins, Carvalho *et al.* 2000].

It should also be noted that despite the importance given to high temperature and high heat flux applications, not all radiometers are developed for such purposes, with an increasing number of references published regarding the development of instruments dealing with solar radiation measurements [Estrada *et al.* 2007] or more specific applications such as heat gains through fenestrations [Marinoski *et al.* 2007].

### 1.3.3 Other Techniques

#### Energy supply/removal or active cooling/heating techniques

Heat flux measurement methods, often referred to as active cooling or active heating, are based on the direct measurement of the energy transfer from or into the sensing element in order to achieve (under steady conditions) a constant temperature or a constant heat flux at its surface. This methodology is akin to other applied in other well-established techniques such as hot wire anemometry or thermal conductivity measurements [Nieto de Castro *et al.* 1991, Beirão *et al.* 2006].

The usual energy exchange method is by means of an electric circuit heater or by dissipation of a pulsed radiation source from a laser, namely because the power is easily measured and controlled. Cooling can be achieved with convective passageways within the device or by means of the Peltier effect [Shewan *et al.* 1989]. Owing to the response time of a typical active heat flux sensor arrangement and of power limitations associated to the electrical heating, these methods are not recommended for either high heat fluxes or for high temperature applications, limiting its applicability in high-temperature industrial furnaces. Active heating methods have also been incorporated on low boundary condition-disruption devices [Saidi and Kim 2004].

A typical sensor design for the measurement of heat transfer into a surface is the use of heater strips exposed to the convective boundary condition but well insulated on the back and sides of the sensor. Electric current is passed through the heater strip material until equilibrium is achieved, monitored by a surface temperature device such as a thermocouple or RTD. A wide variety of such devices has been developed and analysed [Poloniecki *et al.* 1995]. A sandwich construction can be applied to a surface, comprising an insulating layer, a heater, a black background and a liquid crystal layer, in order to obtain local steady state heat transfer values. Commonly used heaters have included thermistors, thin layers of gold, nichrome wires and carbon fibres. The difficulty in applying a uniform layer to a complex geometry can be overcome by means of producing a flexible sandwich which can be stuck to the component of interest. One embodiment of this technique is to use carbon fibres as the heater within an epoxy resin. Thermochromic liquid crystals are applied to the surface to measure the temperature.

Energy supply methods can also be used in a transient mode by applying a known quantity of heat to a surface and by measuring the thermal response. The use of a laser to supply a discrete local heat flux, along with an infrared camera system, has also been employed to determine the local surface temperature distribution due to heating [Porro *et al.* 1991]. A conduction solution using this measured temperature distribution can be used to calculate the heat transfer coefficient.

## Mass transfer analogy techniques

Well-known mathematical similarities between the partial differential equations that govern heat and mass transfer are embodied in the boundary layer relations that rely on the Nusselt, Reynolds, Prandtl, Sherwood and Schmidt adimensional numbers. These can be practically exploited in order to obtain heat transfer measurements from the observations of mass transfer experiments, which have the advantage of being generally much easier to carry out (especially on complex or difficult geometries) than heat transfer experiments and are less prone to experimental error and uncertainty. Additionally, it is much easier to model the equivalent of adiabatic and isothermal boundary conditions.

One of the best-known mass transfer methods is the naphthalene sublimation technique [Goldstein and Cho 1995]. At atmospheric pressure and temperatures, naphthalene ( $C_{10}H_8$ ) sublimates from solid to vapour, *i.e.* without any intermediate liquid phase. This, together with the fact that naphthalene is easily cast and machined, and that its relevant thermophysical properties are well documented, make it an ideal choice. Naphthalene is applied to the surface using casting, machining, spraying or dipping (or a combination of these), the local mass distribution being measured by either weighing or using a surface profile gauge. In order to obtain local rather than surface-average information, the surface is divided into a number of individual segments which are weighed separately. The experiment is run for a long enough period in order to create a reasonable loss of the solid naphthalene, the transferred mass being measured by either weighing or using a surface profile gauge at the completion of the experimental run. Using the appropriate heat and mass transfer relations, the Nusselt number, and hence the convective heat transfer coefficient, can be computed. Albeit useful, the technique does have a number of drawbacks, namely excessive experimental times at low flow velocities and the difficulty of adequately controlling ambient temperature over long periods. The vapour pressure of naphthalene is very sensitive to ambient temperature, so that long experimental times can produce significant experimental errors.

Vapour pressure sensitivity to temperature is also important at high velocities where viscous heating occurs. In high shear flows, naphthalene can be worn-off the

surface by erosion. Long experimental times may cause significant changes in shape in the mass transfer model. The results are by definition time-average values. For wind tunnels, a naphthalene-free air stream should be maintained and variations in air supply temperature minimized. The latent heat of vaporization of naphthalene will cause a drop in the actual surface temperature compared with that of the free stream. It is therefore advisable to measure the temperature of the naphthalene model by thermocouples on the surface. This technique has nonetheless been used to provide accurate and valuable data for applications where conventional heat transfer instrumentation would be more difficult, in particular: external and internal flows, natural convection, fins and heat exchanger geometries, turbulence promoters, impinging jets, rotating surfaces and the cooling of electronic devices [Souza Mendes 1991].

#### ***1.3.4 Conclusions***

An analysis of the main features, advantages and disadvantages of the various methods makes relevant some comparisons with those of the instrument developed and described herein.

Instruments with short response times are typically laboratory-bound and comparatively fragile devices, since their fast responses are often achieved with low thermal inertia components at the expense of robustness. At the opposite side of the spectrum, so to speak, are rugged industrial-grade instruments meant for operation in high-temperature, aggressive environments where fouling may be an issue. These tend to have much larger response times and are usually bulky and require subsystems such as water cooling circuits or must incorporate features such as windows for convection contamination avoidance in the case of radiometers which, in any case, tend to increase overall dimensions, complexity and unit cost. Air-blowing cleaning systems can also be used both for fouling avoidance and for boundary layer blow-off, thus avoiding convection contamination. Furthermore, the implementation of heat flux partitioning requires instruments that are usually more complex, typically having two separate sensing elements, or even two separate instruments for measuring each component of the incident heat flux.

The proposed instrument, while somewhat less robust than earlier transpiration radiometers, was proven to withstand environments with high temperatures and the presence of soot and dust particles. Thanks to its low thermal inertia microperforated sensing element, the designed and proposed instrument allows faster responses than conventional radiometers without significantly compromising its robustness and especially without losing the ability to avoid fouling thanks to its transpiration airflow. Furthermore, faster temperature responses allow a transient operational mode that potentially enables heat flux partitioning implementation, which is aided by the precise airflow control allowed by the instruments precisely defined and comparatively simple geometry. Comparatively diminished dimensions and complexity are achieved using air rather than water refrigeration. This instrument was the subject of a patent application, and the fact that this patent was granted indicates that the issuing organization's own services did not find any instruments with quite the same features as the one under discussion, which validates the intended novelty and contribution of the present document.

## **1.4 Objectives and Thesis Contribution**

The literature review carried out beforehand shows that most of the established methods were developed to be used in clean, well-controlled laboratory environments. In many cases, the proposed techniques are too complex and expensive to be transferred to current industrial applications and have significant limitations when used in high temperature, aggressive environments, leading to a lack of heat flux gauges able to be used in high temperature, aggressive industrial equipment.

From the discussion in the paragraphs above, a clear development line towards a rugged and reliable radiometer becomes apparent, from the basic principle of using a transpiration gas both to eliminate convection by blowing off the boundary layer and to deflect incoming soot particles in order to diminish fouling. A robust operational version had been obtained in earlier work, with adequate performance but much potential for further enhancements, especially as far as bulk and response times were concerned. Its potential for heat flux partitioning was indentified and discussed but not achieved, while other instruments that enable that partition are not suitable for aggressive environments. The next logical step to be taken was thus to attempt:

- A diminution of the sensor's overall dimensions;
- A reduction of the sensor's response time;
- The implementation of heat flux partitioning.

These objectives and contributions of the work described here had however to be achieved without compromising earlier instrument's demonstrated capabilities and advantages.

The problems of the large time constant and of the implementation of a transient operation that would enable an effective heat flux partitioning are related because of the control of allowable thermal levels in the system and of the impact of the transpiration airflow in the temperature fields within the sensing element. The latter's features, notably its morphology and thermal inertia, were also variables to be considered.

Previous instruments were unable to implement heat flux partitioning because of the need to keep temperatures below certain values, especially in order to keep its radiative emission low when compared to incident radiation from the surroundings. This meant that the transpiration airflow could not be switched off for enough time to implement a transient operation mode where the instrument's steady response was anticipated by measuring the slope of the temperature variation curve, which was shown to be proportional to the incident heat flux.

Rather than using the thick (4 mm) porous steel cylinder used in previous instruments, a low thickness (0.1 mm) microperforated plate was used. The microperforated pattern allows a preservation of the transpiration airflow, albeit inducing a transmissivity component in the overall radiative flux balance that must be taken into account. Besides intrinsically lowering the instrument's response time, the new element's much lower thermal inertia leads to much faster temperature curve responses, which in turn allow the switching off of the transpiration airflow for very brief times that nevertheless allow a sufficient temperature increase for curve slope calculation and total heat flux determination.

This means that from an operational point of view the instrument can be thought of mainly as a radiometer, since the default airflow that crosses the sensing element is supercritical, *i.e.* with a mass flux high enough to blow-off the boundary

layer on its outer surface and eliminate convection. That airflow can however be set to subcritical values (or even totally shut-off) several times per second in order to enable total heat flux determination without exceeding maximum allowable temperatures, provided the data acquisition system has enough time resolution for the purpose. If these on-off cycles are short enough, it can be assumed that conditions in the surroundings have not changed significantly and heat flux partitioning is achieved because both components of the total heat flux are measured, radiation directly and convection by difference between successive total flux and radiation measurements. This means that the instrument's basic operation mode makes use of the protection afforded by the transpiration gas while still inducing pulses of calculation-enabling temperature transients.

Overall dimensions are made smaller in part due to the use of the aforementioned low-thickness microperforated plate, but especially by the use of air rather than water refrigeration, enabled by the sensing element's lower thermal inertia.

An instrument embodying all the principles above was designed, after adequate analytical and numerical models were developed and compared, along with further dimensioning procedures and numerical simulations. Several prototypes were built and tested with a data acquisition and processing system designed for the purpose. Detailed calibration procedures were also developed and proposed.

A patent application was prepared and submitted during the development and design process, the issuing organisation (*Instituto Nacional de Propriedade Industrial* – Portuguese National Institute of Industrial Property) having approved the preliminary report, having found no impediments to patentability, and issued a provisional patent application that must be converted into a definitive patent application, pending a decision to carry on by the administration of the University of Aveiro, as patent co-proprietor, to be taken until August 1<sup>st</sup>, 2013 [Calisto and Martins 2012].

## 1.5 Thesis Structure

Chapter 1 provides a brief introduction to the problem of heat flux measurement and the relevance of heat flux as a thermodynamic variable and design parameter. The thesis's contribution, objectives and structure are also discussed and its integration in a

continuous line of research and development is addressed in order to adequately explain the framework in which this work took place. A review of the available methods to measure heat flux, along with a discussion of their relative merits and major advantages and disadvantages, is presented. The contribution of the present work is established and discussed by comparison.

Chapter 2 provides a review of the relevant physical phenomena that must be taken into account during the instrument's development, namely in the definition of both the analytical formulation of its theoretical model and its operational specifications. The integration of the analytical treatment of a large number of small holes with variable physical conditions into a model for heat conduction within the cylindrical element and its interaction with boundary and initial conditions is not straightforward, but is discussed and achieved by treating the cooling effect of the airflow as a heat sink term. Green's functions and finite differences are used with the purpose of obtaining a solution to the boundary value problem resulting from the physical conditions of the sensor, including the system's transient behaviour, its response under various situations being discussed, namely in the simultaneous occurrence of non-uniform initial temperature fields, the presence of heat sink terms and non-homogeneous boundary conditions. Solutions are compared with Computational Fluid Dynamics (CFD) software solutions and the usefulness of the developed models is discussed.

Chapter 3 is a study of dimensional and operational parameters that influence the sensor's performance. Assumptions and simplifications made in the process of developing the analytical model are discussed, along with the instrument's dimensioning and design procedures, taking into account conclusions from the previous chapter and establishing the procedures necessary for carrying out various analytical and numerical parametric studies, namely as far as relevant mass flow values, boundary layer control, compressibility and transmissivity in the microperforated plate, transient effects or the external cooling system are concerned.

Chapter 4 is a detailed discussion of the experimental setup and of equipment selection procedures, along with the presentation and discussion of data acquisition and control setups. The specifications of the various components that were used in the course of the experimental work are presented, while their integration into the data



acquisition and control system are detailed along with implemented methodologies and procedures. Special relevance is given to the data processing flow and operations. Measurements carried out with the discussed setup are described and relevant comparisons with previously developed analytical and numerical models are made against experimental data. Instrument calibration procedures are also proposed, described and discussed.

Chapter 5 lists and discusses the thesis's main conclusions while also presenting proposed developments to be carried-out in the future.



## CHAPTER 2

# ANALYTICAL MODEL FORMULATION AND NUMERICAL SIMULATIONS

An analytical formulation for the proposed instrument is developed from basic principles and assumptions. A low thickness sensing element perforated steel plate is proposed instead of earlier sinterized metal components. The analytical description of small holes with variable physical conditions and their interaction with boundary and initial conditions into a model for heat conduction is not straightforward, rendering necessary simplifications in order to yield a compact and readily understandable model without loss of detail and accuracy.

Possible approaches are presented and compared with numerical simulations performed using Computational Fluid Dynamics (CFD) methods, with emphasis on the element's transient behaviour in situations such as the simultaneous occurrence of non-uniform initial temperature fields, heat sink terms and non-homogeneous boundary conditions. The merits of the proposed approaches are discussed, namely in terms of potentially reduced computational effort when compared to CFD.

### 2.1 Introduction

Underlying the present dissertation is the problem of adequately measuring radiative and convective heat fluxes, either on their own or in combination. Such measurements must in some practical cases be performed in relatively short times, both in order to obtain a fast response for its own sake and to adequately capture possible fast, time-dependant behaviours.

The relative importance of both heat transfer modes may differ, depending on particular conditions of each application, but each mode reflects different characteristics of the respective thermodynamic system, regardless of their relative contribution.

By definition, convective heat transfer depends on the existence of a fluid stream on the heat transfer surface to be considered, its intensity being directly related to local parameters such as boundary layer characteristics, fluid properties or local temperature differences between fluid and wall. Radiative heat transfer not only does not require a physical medium to take place but also has an integral nature (in the sense that it takes into account exchanges with the global system), depending on the radiative properties of the participating surfaces and on the temperature difference between them. Any enclosed fluid may also participate in the radiative transfer balance depending on its radiative properties and temperature. For these reasons, the convective and the radiative heat fluxes may be considered as two different diagnostic parameters, the first reflecting local conditions while the second reflects global or integral conditions.

In order to determine the associated heat flux, a total heat flux measurement problem can thus be divided in two parts, the first one being the identification of the relevant heat transfer modes and the second the analysis of the sensing element response to an energy load. One of the purposes of the instrument to be developed was precisely the differentiation between radiative and convective components of the total heat flux, *i.e.* performing heat flux partitioning.

The study of the relationship between the received heat load and the temperature field in the sensing element under known conditions can then be carried out, the sensor's thermal behaviour depending on the total heat load and not on the associated transfer modes, allowing a separate study of both parts of the overall problem. Radiation heat flux measurement is however the most important part of the problem from an operational point of view, since the high temperature levels usually found in industrial furnaces reduce the relative importance of convective heat flux in the overall energy balance analysis. Nevertheless, convective heat flux cannot be ignored since a variety of diagnostic systems rely on total (rather than merely radiative) heat fluxes as input parameters [Calisto *et al.* 2008].

Broadly speaking, any of the radiative flux measurement techniques and approaches discussed in Chapter 1 could be used. If the environment is clean and convection free, the only additional parameter to account for is typically surface emissivity, since the surface temperature can be known most of the times. The sensing

element surface should therefore be a grey surface with a known emissivity, which must be as high as possible in order to increase the instrument sensitivity.

Obviously, if measurements are carried out in the presence of convective heat fluxes, some precautions are required in order to prevent the radiative component from being contaminated by convective contributions. If the environment is not clean, typically if there is particulate matter in suspension, fouling on the sensing element surface must be prevented since it will affect its radiative properties and render its calibration curves useless.

As mentioned in Chapter 1, a usual technique for the avoidance of the convective component of the total heat flux is the addition of a special transparent window to the gauge, protecting the sensing element from contact with the gas stream. This procedure effectively eliminates the convection component of the total heat flux and an appropriate selection of the window material renders the attenuation of the radiative component negligible, but the instrument view angle is typically reduced.

This is the main reason for the use of a gas screen around the sensing element to avoid fouling on the sensor surface, with air or nitrogen being blown through specific slots around the sensing element or through the element itself if it is porous or perforated. The gas screen's cooling effect on the sensing element not only also affects the sensor's output but can be made a central feature of its operation mode, as discussed below in further detail.

In most studies involving radiometers the output of the instrument has to be obtained in steady state conditions, for which a variety of theoretical models are available. However, reliable steady-state data are usually not enough within the framework of advanced diagnostic systems, since for certain measurement applications it is also very important to record dynamic characteristics such as the transient response of the instrument. If the results are to be obtained in transient conditions, this response time must be considerably shorter.

As explained in Chapter 1, this was one of the main driving forces behind the present work and a suitable theoretical formulation is necessary. Such a formulation was developed by Martins [Martins 1998] in his PhD thesis, leading to an operational heat flux meter, tested in industrial conditions, its formulation, specifications and

performance being discussed in subsequent publications that are evidence of a rugged and reliable radiometer [Martins *et al.* 1998, Martins *et al.* 2000].

Fouling was shown to be avoided thanks to the transpiration air flow, although large response times (up to 5 s) were observed. While adequate for a wide range of applications, the integration of such an instrument in systems that exhibit strongly time-dependant and fast behaviours could be hindered by high response times. The instrument was also bulky due to its refrigeration system. Gas turbines come to mind as examples of systems that require fast-response instruments due to the speed at which they operate and which render slow-responding sensors inappropriate and have restrictions regarding the bulkiness and weight of any subsystem.

Relevant differences exist between the aforementioned instrument and the one developed, designed and discussed here, especially as far as the sensing element is concerned. A relatively thick porous steel cylinder was used in the older version, its high thermal inertia compensated to some extent by the advantage of collecting the totality of the thermal radiation incident on the surface, no thermal radiation escaping to the inner side of the gauge body due to the non-existent transmissivity of the porous element.

The low thickness microperforated (in order to preserve the transpiration airflow) plate proposed in the version discussed here does induce a transmissivity component in the overall radiative flux balance that must be taken into account, but lowers the instrument's response time and makes for much faster temperature curve responses, which in turn allow the switching off of the transpiration airflow for very brief times that nevertheless allow a sufficient temperature increase for curve slope calculation and total heat flux determination.

Differences also exist in terms of the interaction of the sensing element with the transpiration gas, rendering the model based on energy balances inadequate to describe the microperforated plates' behaviour. The presence of a large number of small holes with variable physical conditions (*i.e.* temperatures) must be accounted for in a model for heat conduction within the cylindrical element and its interaction with boundary and initial conditions. This is not straightforward but can be achieved by treating the cooling effect of the airflow as a heat sink term, as described below.

Further refinements were discussed in subsequent articles [Martins *et al.* 1998, Martins *et al.* 2000], namely a fully transient formulation [Martins 1998] that allowed for an extension of the instrument’s application range by opening the way to achieving a faster response and eventually heat flux partitioning.

In the first subsequent experimental approaches, necessary transient behaviours were induced by varying the incident heat flux, exposing and masking the sensing element with a shutter. The transpiration airflow was kept at a steady value while several furnace set points were considered. The exposition of the sensing element to the hot furnace would lead to an increase in temperature and a direct proportionality between the slope of the line tangent to the temperature response curve and the incident heat flux was established, with the same slope being observed in the linear portion of the curve for the same heat fluxes regardless of the initial temperature [Hit 2004]. This meant that it is unnecessary to “wait” for steady-state values and that the transient output of the radiometer can be used to determine the incident heat flux [Martins *et al.* 2006a, Martins *et al.* 2006b]. These conclusions led directly to the work presented in the present document.

A noteworthy difference between the aforementioned experimental studies and the proposed operational mode has to do with how the transient behaviours are induced, since in the present case a pulsed transpiration gas mass flow is to be used, this option holding more promise since on/off control through the use of fast-response electrovalves is easier and faster to implement than the use of a front shutter. The electrovalve typically controls two distinct transpiration mass flow levels: a maximum value that ensures boundary layer blow-off and allows sufficient cooling for the sensing element, and a much lower value that lets some hot gases reach the sensor and that can even be set to a zero value if instrument protection (both in terms of fouling and thermal levels) is not compromised. This does introduce significant differences with the aforementioned earlier studies. In those cases the lower temperature level was reached with the transpiration airflow switched-on but without instrument exposure to the hot source (effectively reproducing a cold experiment, as discussed in Chapter 4), and temperatures only rose when the instrument was placed in the furnace, without variation in the transpiration airflow. This meant that the temperature increase was solely due to the incoming heat flux, no discussion being made in terms of heat flux

partitioning, although the magnitude of the transpiration airflows used and that were also necessary for sensing element thermal protection/refrigeration purposes would correspond to situations where the boundary layer would be blown-off and only radiative heat fluxes would be measured. This would also explain the fact that the slopes of the transient temperature curves were the same in the heating and cooling processes, since the driving force behind them would be the presence or absence of the incoming heat flux, given the constant transpiration airflow [Hit 2004].

The pulsed transpiration mass flow principle means that when the airflow is turned on above a critical value the instrument will behave like a conventional transpiration radiometer. In such conditions the temperature measured by the thermocouple attached to the perforated plate will be a steady-state equilibrium value dictated by the incoming radiation heat flux and the cooling provided by the transpiration airflow. The situation where the airflow is switched-off and the boundary layer will no longer be blown-off, however, will present a dramatic increase in measured temperature that is driven not only by the presence of a convective component in addition to the radiative component that was already present, but also by the absence of transpiration cooling in the sensing element. This process would lead to a steady-state value that would be reached if temperatures were allowed to increase and stabilize, and would indeed be proportional to the total received heat flux. Nevertheless, the slope of the transient temperature curve at the start of the pulse (hence the zero value for time) would still be proportional to the incoming heat flux:

$$q_{\text{total}} = \beta \left. \frac{dT}{dt} \right|_{t=0} . \quad (2.1)$$

The analysis of the transient response is intended precisely to avoid reaching such high temperatures, which would not enable the convenient assumption of a comparatively insignificant plate emission term and most importantly could severely damage components and their weldings and attachments. If the process is carried out in a sufficiently rapid fashion, the radiative component of the heat flux can be treated as constant and the convective component can be estimated. A calibration of the transient



transpiration radiometer would thus involve the determination of the proportionality constant  $\beta$  for various incident heat fluxes.

When the transpiration airflow is reset at its initial mass flux, the transient temperature curve will decrease back towards its initial value dictated by the incident radiative flux but especially by the transpiration airflow, at a rate (*i.e.* slope) that will be a function of the magnitude of both factors and that can also be quantified.

## 2.2 Model Requirements and Analytical Approach

### 2.2.1 Problem Statement

The problem of obtaining a formulation for an instrument sensitive element is essentially one of conduction within the element's solid material, which can be assumed to be homogeneous in terms of composition and properties, with temperature fields resulting from convective, radiative and imposed temperature boundary conditions.

In a solid body in which temperature differences occur, heat flow can be thought of as the rate of energy transfer (in Js<sup>-1</sup>) associated with the vibrational energy of atoms and molecules in the body, and heat flux is the heat flow per unit area at any point of the body. As mentioned earlier it cannot be measured directly but its effects can be observed on the surroundings, as in the melting of ice or the vaporization of water. Inside a solid body, the heat flux can be determined from the temperature distribution only if the relationship between temperature and heat flux is thoroughly understood. In a solid body with a steady temperature gradient, heat flux has a magnitude and a direction and is usually denoted as  $\vec{q}$ . The component of heat flux (in Wm<sup>-2</sup>) for direction  $x$  is for example:

$$q_x = -k \frac{\partial T}{\partial x}, \quad (2.2)$$

where  $k$  is the thermal conductivity in Wm<sup>-1</sup>K<sup>-1</sup> and the negative sign implies that heat always flows in the direction of reducing temperature and  $q_x = \dot{q}_x A$  is the heat rate (in W) and  $A$  is the heat transfer area. In cartesian coordinates the other heat flux components are:

$$q_y'' = -k \frac{\partial T}{\partial y} \text{ and } q_z'' = -k \frac{\partial T}{\partial z}, \quad (2.3)$$

embodying Fourier's law of heat conduction, which applies to bodies that are homogeneous (*i.e.* with the same substance overall), isotropic (heat flow with equal ease in any direction) and of macroscale size.

For a three-dimensional cylindrical system such as the sensor element, the heat diffusion equation is readily available in most of the heat transfer literature references, including the most widespread [Holman 1986, Incropera and DeWitt 1996]. This is adequate for any given solid with heat conduction, and where surface phenomena (*i.e.* convection and radiation) are boundary conditions for the differential equation to be obtained. The form of the heat diffusion equation, when transient conduction and heat generation/sink terms (denoted as  $g$ , in  $\text{Wm}^{-3}$ ) are considered, can be given as:

$$\frac{1}{r} \frac{\partial}{\partial r} \left( kr \frac{\partial T}{\partial r} \right) + \frac{1}{r^2} \frac{\partial}{\partial \varphi} \left( k \frac{\partial T}{\partial \varphi} \right) + \frac{\partial}{\partial z} \left( k \frac{\partial T}{\partial z} \right) + g = \rho c_p \frac{\partial T}{\partial t} \quad (2.4)$$

or, for constant  $k$

$$\frac{\partial^2 T}{\partial r^2} + \frac{1}{r} \frac{\partial T}{\partial r} + \frac{1}{r^2} \frac{\partial^2 T}{\partial \varphi^2} + \frac{\partial^2 T}{\partial z^2} + \frac{g}{k} = \frac{1}{\alpha} \frac{\partial T}{\partial t}. \quad (2.5)$$

Spatial coordinates are  $r$  in the radial direction,  $\varphi$  in the angular or azimuthal direction and  $z$  along the cylindrical axis or cylinder thickness. Density  $\rho$  ( $\text{kgm}^{-3}$ ) and specific heat  $c_p$  ( $\text{Jkg}^{-1}\text{K}^{-1}$ ) can be grouped as the material's thermal diffusivity  $\alpha$ . The aforementioned references do not usually present any form of deduction for this equation, typically restricting themselves to the deduction of the cartesian case and leaving the cylindrical coordinates problem as a mere exercise. The deduction of the appropriate form of the heat equation is nevertheless rather straightforward and useful in the definition of an adequate mathematical model for the sensor, given its cylindrical shape. Some simplifications must be made at this point in order to obtain a viable model for the sensor, as discussed below.

The differential equation of heat conduction does not describe the temperature distribution in a region and will have numerous solutions unless a set of boundary conditions and an initial condition for a time-dependant problem are prescribed. The mathematical form of the solutions to heat conduction equations is determined by the boundary conditions, *i.e.* the value of the temperature (or its derivative) at the boundaries of the heat conducting body. The combination of an energy equation, specific boundary conditions and an initial condition is called a boundary value problem. In this particular case the body has an orthogonal geometry, which means that its boundaries are located where one coordinate is a constant, such as the outer radius of the cylinder.

Initial conditions usually specify a temperature distribution in a medium at the origin of the time coordinate, that is,  $t = 0$ , while boundary conditions describe what physically takes place at the boundaries of the region. The number of boundary conditions for a boundary value problem depends on the form of the energy equation and the geometry of the system under consideration. On a given surface, temperature or heat flux distributions can be specified, or there may be exchanges by convection and/or radiation, the boundary condition being derived by performing an energy balance on the surface. The non-linear radiation term can be troublesome to obtain in some analytical approaches. Boundary conditions are often defined by specifying either temperature or heat flux distributions on surface  $S$  in the well-know forms of:

- Dirichlet (or first kind boundary conditions) in which a temperature distribution is prescribed at the boundary surface, that is:

$$T = f(\vec{r}, t) \text{ on } S$$

where the prescribed surface temperature  $f(\vec{r}, t)$  is in general a function of position and time, and the special case:

$$T = 0 \text{ on } S$$

is called the homogenous boundary condition of the first kind,  $\vec{r}$  being a generic position vector, defined as adequate for each particular application.

- Neumann (or second kind boundary conditions) in which a heat flux distribution is prescribed at the boundary surface, *i.e.*:

$$k \frac{\partial T}{\partial n} = f(\vec{r}, t) \text{ on } S$$

where  $\partial T / \partial n$  is the derivative along the outward drawn normal of the surface and  $f(\vec{r}, t)$  is the prescribed heat flux in  $\text{Wm}^{-2}$ , the special case

$$k \frac{\partial T}{\partial n} = 0 \text{ on } S$$

being called the homogenous boundary condition of the second kind.

- Robin/Fourier (or third kind boundary conditions) in which a heat transfer coefficient is specified and can be obtained by setting radiation and heat supply terms to zero, that is:

$$k \frac{\partial T}{\partial n} + hT = hT_{\infty}(\vec{r}, t) \text{ on } S$$

where for generality ambient temperature  $T_{\infty}(\vec{r}, t)$  is assumed to be a function of position and time. The special case:

$$k \frac{\partial T}{\partial n} + hT = 0 \text{ on } S$$

is called the homogenous boundary condition of the third kind.

Additional boundary conditions (fourth and fifth kinds) can be defined for various physical situations such as interfaces and convection or radiation fluxes, but

these are not always practical to use for analytical purposes since they require the specification of surroundings' (either fluids or surfaces) temperatures.

As mentioned earlier, one of the features of previous versions of the sensor that was felt to be the most perfectible was its response time, which in turn led to the requirement of lowering its thermal inertia. The idea of using a metallic foil much thinner than the original porous steel disc came about naturally as a means of obtaining a much lower thermal inertia, while the option for a microperforated pattern enables a much more precise control of element geometry and physical properties when compared to the porous steel disc, without compromising the transpiration gas flow. This is essential since the transpiration gas pulses are central to the envisioned operational principle, for two main reasons.

On the one hand, various changes in intensity of these pulses' mass flow rate will provide transient temperature variations with varying slopes that can be related to the incident heat fluxes. On the other hand, sufficiently high mass flows will be responsible for enabling the instrument to operate purely as a radiometer, by blowing off the boundary layer on the sensing element's exposed face and thus eliminating the convection heat flux component. As mentioned earlier, this would be done in a periodic fashion in order to allow for the separation of the components of the total heat flux.

It is therefore essential to take into account the effects of the air flow pulse when developing any analytical description of the sensing element being exposed to incident heat fluxes and crossed by a comparatively cold mass flow. It is however obvious that a detailed accounting of a large number of small perforated holes distributed across the metallic element would be rather difficult to implement in purely analytical terms. The cooling effect of the transpiration mass flow and transient effects due to variations in that flow can be more sensibly described through the definition of a heat sink term (*i.e.* a negative generation component) in the basic differential equation.

Assuming that azimuthal symmetry can be considered and that the temperature gradient across the element's thickness must be considered, a more versatile model is obtained and can be readily simplified if this gradient can be ignored, depending on which particular thicknesses are to be considered. In this case, the heat equation:

$$\frac{1}{r} \frac{\partial}{\partial r} \left( r \frac{\partial T}{\partial r} \right) + \frac{1}{r^2} \frac{\partial}{\partial \varphi} \left( \frac{\partial T}{\partial \varphi} \right) + \frac{\partial}{\partial z} \left( \frac{\partial T}{\partial z} \right) + \frac{g}{k} = \frac{1}{\alpha} \frac{\partial T}{\partial t} \quad (2.6)$$

can be simplified to become:

$$\frac{1}{r} \frac{\partial}{\partial r} \left( r \frac{\partial T}{\partial r} \right) + \frac{\partial}{\partial z} \left( \frac{\partial T}{\partial z} \right) + \frac{g}{k} = \frac{1}{\alpha} \frac{\partial T}{\partial t} \quad (2.7)$$

since azimuthal (*i.e.* angular) variations are not to be considered. This is a first-order partial differential equation with respect to time and second-order partial differential equation with respect to the spatial coordinates  $r$  and  $z$ . An initial condition is therefore required for the temporal variation, which can be as simple as a constant initial temperature when time equals zero, or:

$$T(r, z, t = 0) = T_i. \quad (2.8)$$

This condition would correspond to a situation where the sensor was not exposed to any incident heat fluxes or transpiration gas flows, and the temperature over the whole element would be either that of the surroundings or one imposed by an external refrigeration system. Other situations would involve situations where a more complex (in the sense that it would not be constant in space) initial temperature field would be in existence at the moment where any given effect must be evaluated. This could be a situation where an initial equilibrium resulting from incident heat fluxes and the imposed temperature would be disturbed by a variation in the transpiration gas flow.

Boundary conditions must then be specified in spatial terms in order to allow for the solution of the spatial component of the problem. A cylindrical element with radius  $b$  and thickness  $c$  is considered to be exposed to an incident heat flux  $q_{\text{inc}}$  at  $z = c$ . The precise nature of this flux is not known beforehand so it can, as a first approximation, be considered merely as an imposed heat flux rather than being specified as either convection, radiation or combined boundary conditions. At  $z = 0$  the element being heated by heat flux  $q_{\text{inc}}$  will lose heat by an undetermined proportion of

convection and radiation to the tube that supplies the airflow and is assumed to be at a lower temperature. This heat flux is designated  $q_{\text{em}}$ . The outer radial surface at  $r = b$  is maintained at a temperature  $T = T_{\text{ext}}$ .

For generality it can be assumed that both the sink term  $g(r,z,t)$  and the flux boundary conditions  $q_{\text{em}}(r)$  and  $q_{\text{inc}}(r)$  vary with position and time. This spatial variation will be the case to be considered in some situations, while several simplifications can be introduced in other situations, namely time-independent heat fluxes.

The literature states that non-homogenous boundary conditions may give rise to convergence difficulties when the solution is evaluated near the boundary. Thus, whenever possible, it is desirable to transform non-homogenous boundary conditions into homogenous ones [Özisik 1993]. This could be achieved by performing a variable change in the form  $\theta = T - T_{\text{ext}}$  and solving the heat equation for the new variable, the non-homogenous boundary condition  $T - T_{\text{ext}}$  at  $r = b$  being rendered homogeneous in the form  $\theta = 0$  at  $r = b$  and with all remaining boundary conditions and the heat equation adjusted accordingly. This could however render performing surface radiation balances more complicated. In these conditions, the differential conduction equation can be written as:

$$\frac{\partial^2 T}{\partial r^2} + \frac{1}{r} \frac{\partial T}{\partial r} + \frac{\partial^2 T}{\partial z^2} + \frac{1}{k} g(r, z, t) = \frac{1}{\alpha} \frac{\partial T}{\partial t} \quad (2.9)$$

in  $0 \leq r \leq b$  and  $0 \leq z \leq c$  for  $t > 0$  with boundary conditions:

$$\begin{aligned}
\frac{\partial T}{\partial r} &= 0 \text{ at } r = 0 \\
T &= T_{\text{ext}} \text{ at } r = b \\
\frac{\partial T}{\partial z} &= q_{\text{em}} \text{ at } z = 0 \\
\frac{\partial T}{\partial z} &= q_{\text{inc}} \text{ at } z = c \\
T(r, z, t) &= T_{\text{ext}} \text{ at } t = 0
\end{aligned} \tag{2.10}$$

The imposition of an incoming heat flux may be debatable in purely physical terms, since the heat flux at that boundary is the result of the balance between surroundings and gas temperatures on the one hand and the surface temperature on the other, especially when radiation is to be considered.

The assumption of a fixed incoming, radiation-dominated heat flux can be considered reasonable if the contribution of the emission component of the surface balance is kept low when compared to the incident radiation component, which can be achieved if surface temperatures are likewise kept as low as possible. This assumption of an imposed incoming radiation heat flux is furthermore justified by the use of the transpiration principle, which implies that for sufficiently high transpiration mass flows the convective heat transfer is eliminated which, as mentioned in detail later, will correspond to a situation to be encountered for most of the instrument's operation time and will result in a purely radiative boundary condition.

For any given set of conditions in the high-temperature environment, high transpiration gas flows are required in order to lower surface temperatures, diminishing the magnitude of radial flows within the sensing element (overall temperatures being closer to the temperature imposed on the outer radius) and rendering the emission term much less significant. This principle was already applied to nullify these terms in energy balances for sensing elements of previous versions of the instrument [Martins 1998]. High gas flows also have other advantages such as a more effective deflection of incoming soot particles, with the lower temperatures placing less severe thermal



constraints on the outer refrigeration system, and the welding between the thermocouples and the microperforated plate.

It should be noted that the incident heat flux to be considered is not necessarily the overall flux due to the conditions surrounding the outer surface of the element, because of its microperforated pattern and its non-specular surface. While convective exchanges are not significantly altered compared with those for a non-perforated surface, other than by the difference in surface area, radiative exchanges can be substantially different due to transmission and reflection phenomena.

The spectral irradiation  $G_\lambda$  (typically in  $\text{Wm}^{-2}\mu\text{m}^{-1}$ ) that strikes a semitransparent medium surface can be reflected, absorbed or transmitted in diverse proportions, following from a radiation balance that:

$$G_\lambda = G_{\lambda,\text{ref}} + G_{\lambda,\text{abs}} + G_{\lambda,\text{tr}}. \quad (2.11)$$

The determination of these components is in general complex, depending on the upper and lower surface conditions, the wavelength of the radiation and the composition and thickness of the medium, where volumetric effects can strongly influence conditions. If total rather than spectral (*i.e.* integrated over the whole spectrum), hemispherical components are assumed, reflectivity  $\rho_{\text{rad}}$ , absorptivity  $\alpha_{\text{rad}}$  and transmissivity  $\tau_{\text{rad}}$  yield:

$$\rho_{\text{rad}} + \alpha_{\text{rad}} + \tau_{\text{rad}} = 1 \quad (2.12)$$

the subscript “rad” being present to avoid confusions with density  $\rho$  and thermal diffusivity  $\alpha$ .

While most solids are opaque and have zero transmissivity, the microperforated plate has a non-zero value which must be taken into account. From Kirchhoff’s law, it will also be assumed that the total, hemispherical absorptivity of the surface is equal to its total hemispherical emissivity  $\varepsilon$ .

If the temperature of the sensing element surface exposed to the hot surroundings responsible for the incoming radiation is kept low enough to make considering its radiative emission negligible, this means that the  $q_{\text{inc}}$  heat flux considered as a boundary condition can be regarded as the incident radiative (and if present, convective) heat fluxes minus the transmitted and reflected radiative components.

The achievement of low surface temperatures on the sensing element, which given the element's low thickness and consequent lack of thermal gradients along its symmetry axis is the same as keeping the element's temperature low over its whole volume, is therefore important in terms of simplicity of analysis: low surface temperatures ensure that the emission term is negligible when the difference to the surroundings is large, as is typical in boilers and furnaces.

Addressing once more the formulation, in this case the transient heat conduction problem is non-homogenous because of the non-homogeneity of the differential equation (due to the generation term) and/or the boundary conditions.

Heat conduction problems described by non-homogenous partial differential equations and boundary conditions can be handled with more or less difficulty by a variety of techniques, from orthogonal expansion to Laplace transforms or Green's functions (GF) [Carslaw and Jaeger 1959, Arpaci 1966, Özisik 1993]. A homogeneous differential equation is a linear equation where all terms include either the dependent function or one of its derivatives, while a non-homogeneous equation includes a term that is a function of only the independent variable. Similarly, a boundary condition is homogeneous when the dependent variable or its derivatives, or any linear combination of the dependent variable or its derivatives, vanishes at the boundary.

The orthogonal expansion and separation of variables technique is arguably the most common, having extensively been presented and discussed in most of the standard references on heat conduction, with some claiming that it is the proper way of solving this type of heat conduction problems [Arpaci 1966, Özisik 1968]. Its application can be difficult to handle when non-homogenous boundary conditions are present because this presence gives rise to convergence difficulties when the solution is evaluated near the

boundary. So, whenever possible, it is desirable to transform non-homogenous into homogenous boundary conditions.

The non-homogeneous generation term is also typically handled if the problem is split into a set of simpler problems, which can be done if the generation term and the non-homogenous part of the boundary condition do not depend on time [Özisik 1993]. This is usually achieved by splitting the overall problem for the  $T(r, z, t)$  temperature distribution into a steady-state problem that contains the non-homogenous components and is solved for  $T_{\text{ST}}(r, z)$ , and a homogenous transient problem solved for  $T_{\text{HM}}(r, z, t)$ , with the  $T(r, z, t)$  solution for the original problem being given by:

$$T(r, z, t) = T_{\text{ST}} + T_{\text{HM}}(r, z, t) \quad (2.13)$$

This formulation becomes increasingly complex for two- or three-dimensional geometries and with increasing numbers of non-homogeneous boundary conditions. Laplace transforms are also commonly used but present the problem of the existence of an inverse transform not always being guaranteed [Özisik 1993].

An immense number of analytical solutions for conduction heat transfer problems have been accumulated over the years. Even so, in many practical situations the geometry or boundary conditions are such that an analytical solution has not been obtained at all or else involves such a complex solution procedure that numerical evaluation becomes too cumbersome or difficult. As discussed below, in these situations other approaches may be more fruitful, finite-difference methods readily coming to mind as the most common and widespread example, with the basics of the method being readily available even in the most basic heat transfer manuals [Holman 1986, Incropera and DeWitt 1996].

In any case, the difficulty of treating the microperforated patterns as heat sink terms and integrating the presence of this non-homogeneous term must be dealt with, dictating to a large extent the most reasonable options in terms of analytical approach and complexity. The procedure implemented for calculation of the temperature fields using both the GF and finite differences methods nevertheless has some similarities, both approaches being highly structured and methodical processes.

### ***2.2.2 Green's Functions Formulation***

Methods based on the use of Green's Functions (GF) are viable alternatives, being flexible, powerful, and especially well-suited for these particular applications given the fact that the same GF for a given geometry is a building block for determining the temperature distribution for situations such as a space-variable initial temperature distribution and time- and space-variable boundary conditions or volume energy generation/removal [Carslaw and Jaeger 1959, Stakgold 1967, Özisik 1993, Cole *et al.* 2010]. This method can be viewed as a restatement of a boundary value problem into integral form and is useful if the GF is known (or can be found), and if the integral expressions can be evaluated. If these two limitations can be overcome, the GF method offers several other advantages such as systematic solution procedure due to GF libraries being available, saving time and reducing the possibility of error, which is particularly important for two- and three-dimensional geometries. For complex problems in which the heat conduction is caused by several non-homogeneous terms, the effect of each term can be considered separately. The GF method leads to analytical solutions in the form of integrals, the solution taking the form of a superposition (sum) of several integrals, one for each non-homogeneous term in the problem.

Two- and three-dimensional transient GF can be found by simple multiplication of one-dimensional transient GF for the rectangular coordinate system for most boundary conditions, provided that the body is homogeneous and orthogonal. This multiplicative property can result in great simplification in the derivation of the temperature, as well as providing a very compact means of cataloguing the GF in these cases. For cylindrical coordinates, the multiplicative property of the GF applies to certain two-dimensional geometries, which is a further factor of attraction in the particular case under discussion.

Several books give a good overview of the GF method [Carslaw and Jaeger 1959, Stakgold 1967, Özisik 1993, Duffy 2001]. Of special interest is another reference (that has recently been updated in its second edition), presenting an overview of the GF method and giving extensive tables of GF for heat conduction and diffusion. These are organized with a number system for the number of spatial dimensions, the type of coordinate system and the type of boundary conditions, most of the book being devoted

to transient heat conduction and convergence improvement procedures [Cole *et al.* 2010].

Other references have similar objectives to the work presented here, applying GF to heat conduction applications in the context of sensor development applications [Beck and Keltner 1987, Cole 2004], including in full cylindrical geometries, or the behaviour and temperature fields of structures in very high temperature environments, such as fires [Beck and Keltner 1987, Cole 2004, Wang *et al.* 2005, Wang and Tan 2007a, Wang and Tan 2007b].

Most references focus their analyses on very particular applications in which some convenient simplifications can be made, either by considering uniform initial temperature fields, the lack of generation/heat sink terms, homogeneous boundary conditions or steady-state situations. The ultimate aim of the work described here is to establish the formalism necessary to study an azimuthally symmetrical cylindrical geometry in which all these matters must be considered simultaneously, which leads to the matter of establishing the requirements of the model to be developed.

The aforementioned pulsed operation principle dictates that the model must describe the effect of the various mass flows to be considered, especially as far as temperature fields within the disk and its time response are concerned. The latter is fundamental since received heat fluxes were, as mentioned earlier, proven to be directly proportional to the slope of the tangent to the temperature response curve which, in turn, allows an anticipation of the instrument's steady-state values.

Arguably the main conceptual difficulty in the passage from the actual physical system to its analytical description is, in this case, taking into account the microperforated pattern that underlies the transpiration radiometer principle, in order to evaluate the effect of the various mass flows that will cross the plate. As mentioned earlier, the presence of a large number of small holes with variable physical conditions is not straightforward but can be achieved by treating the cooling effect of the airflow as a heat sink term.

The usefulness of GF lies in the fact that once one such function is known the temperature distribution  $T(\vec{r}, t)$  in the medium is readily computed by the Green's

Function Solution Equation (GFSE). In the case of the original three-dimensional transient, non-homogeneous heat conduction and for constant material thermal properties, the solution for  $T(\vec{r}, t)$  is expressed in terms of the three-dimensional GF  $G(\vec{r}, t | \vec{r}', t)$  as:

$$\begin{aligned}
T(\vec{r}, t) = & \int_{Reg} G(\vec{r}, t | \vec{r}', 0) F(\vec{r}') d\vec{v}' \\
& + \frac{\alpha}{k} \int_{\tau=0}^t \int_{Reg} G(\vec{r}, t | \vec{r}', \tau) g(\vec{r}', \tau) d\vec{v}' d\tau \\
& + \alpha \int_{\tau=0}^t \sum_{i=1}^s \int_{S_i} \frac{f_i(\vec{r}_i, \tau)}{k} G(\vec{r}, t | \vec{r}_i, \tau) d\vec{s}_i' d\tau \\
& - \alpha \int_{\tau=0}^t \sum_{j=1}^s \int_{S_j} f_j(\vec{r}_j, \tau) \left. \frac{\partial G}{\partial n_j} \right|_{\vec{r}'=\vec{r}_j} d\vec{s}_j' d\tau
\end{aligned} \tag{2.14}$$

where *Reg* refers to the entire volume of the region considered,  $S_i$  refers to the boundary surfaces of the region *Reg*,  $i = 1, 2, \dots, N$  where boundary conditions of the second through fifth kinds are applied,  $S_j$  refers to the boundary surfaces of the region *Reg*,  $j = 1, 2, \dots, N$  where boundary conditions of the first kind are applied, and  $N$  is the number of continuous boundary surfaces. Differential volume and surface elements in the  $\vec{r}'$  variable are  $d\vec{v}'$ ,  $d\vec{s}_i'$  and  $d\vec{s}_j'$  respectively. The physical significance of the various terms in second member of the equation above is:

- The first term is for the contribution of the initial condition function  $F(\vec{r}')$  on the temperature distribution; that is, GF  $G(\vec{r}, t | \vec{r}', \tau)$  evaluated for  $\tau = 0$  is multiplied by  $F(\vec{r}')$  and integrated over the whole region *Reg*;
- The second term is for the contribution of energy generation  $g(\vec{r}, t)$  on temperature  $T(\vec{r}, t)$ , that is, GF  $G(\vec{r}, t | \vec{r}', \tau)$  multiplied by  $g(\vec{r}, t)$  and integrated over the whole region *Reg* and over the time from  $\tau = 0$  to  $t$ ;
- The third term represents the contribution of the non-homogeneous terms  $f_i(\vec{r}_i, \tau)$  of the boundary conditions on the temperature, for

boundary conditions of the second through the fifth kinds. It consists of the GF evaluated at the boundary, multiplied by  $f_i(\vec{r}_i, \tau)$  and integrated over the whole boundary surface and over the time from  $\tau = 0$  to  $t$ ;

- The last term represents the contribution of the non-homogeneous terms  $f_j(\vec{r}_j, \tau)$  of the boundary conditions on the temperature, for boundary conditions of the first kind. The benefit of rendering homogeneous the imposed temperature condition at  $r = a$  becomes apparent, since this last term would vanish and possible convergence issues near the boundary would be addressed.

As mentioned above, once the GF is known, the temperature distribution  $T(\vec{r}, t)$  in the medium is readily computed. Therefore, the establishment of the proper GF for any given situation is an integral part of the solution methodology using this approach. GF can be obtained by various techniques such as Laplace transforms or the method of images, but the simplest, straightforward and general approach uses the classic separation of variables technique for determining GF [Carslaw and Jaeger 1959, Özisik 1993, Cole *et al.* 2010].

The number of exact solutions in transient heat conduction and diffusion is extremely large and growing. Thus, numbering systems were devised in order to organize them while the numbers themselves can convey explicit meaning and contain a great deal of information. Arguably the most handy system was proposed in 1985 ([Beck and Litkouhi 1985], with further discussion [Beck 1984, Beck 1986]) allowing for a less tedious solution location procedure and a lesser effort in developing new solutions and simplifying the construction of a computer database in the form of the Green's Functions Library [Cole 2000].

The numbering system makes it easier to keep track of the different possible combinations of boundary conditions and the GF associated with them. In cylindrical coordinates with azimuthal symmetry a specific GF is identified by a “number” of the form  $R0JZKL$ , in which  $R$  and  $Z$  represent the coordinate axes, and the letters following each axis name take on values 1 (Dirichlet condition, prescribed temperature), 2 (Neumann condition, prescribed heat flux), or 3 (Robin convective condition) to represent the type of boundary conditions present at the body faces

normal to that axis. Some references also list type 4 (Carslaw condition, thin film with no convection) and 5 (Jaeger condition, thin film with convection) boundary conditions [Cole *et al.* 2010].

Number 0 is also used to denote the lack of a physical boundary: designation *R02* represents a solid cylinder (no physical boundary at  $r = 0$ ) with a boundary condition of type 2 at  $r = a$ . Number *R01Z13* describes a GF for a solid cylinder with the following boundary information: no physical boundary at  $r = 0$ , the curved face at  $r = a$  has a type 1 boundary ( $G = 0$ ), the face at  $z = 0$  has a type 1 boundary and the  $z = L$  face has a type 3 boundary (convection) [Cole 2004, Cole *et al.* 2010]. The numbering system is also able to account for time- and space-variable boundary conditions, initial temperature distributions, interfaces and generation/sink terms [Cole *et al.* 2010].

For the case under discussion the solid cylinder will have a *R01* numbering in the radial direction, illustrating the facts that no physical boundary needs to be specified at the centre of the cylinder (which corresponds to a symmetry situation) and that the external refrigeration system imposes a fixed temperature on the outer radius. Perpendicular to the cylinder's axis are two circular surfaces where heat fluxes occur, leading to a *Z22* designation in the  $z$  direction if the temperature gradient across the cylinder thickness is to be considered.

Of special interest is the fact that multidimensional GFs can be obtained from the multiplication of one-dimensional GF in all cartesian cases and in some cases for cylindrical coordinates, namely if the problem involves only the  $(r, z, t)$  variables (*i.e.* if the problem has azimuthal symmetry), as is the case in the problem under study:

$$G_{RZ} = (G_R)(G_Z) \Leftrightarrow \quad (2.15)$$

$$G_{R01Z22}(r, z, t | r', z', \tau) = G_{R01}(r, t | r', \tau) G_{Z22}(z, t | z', \tau)$$

where the one-dimensional GF will be  $G_{R01}$  and  $G_{Z22}$ , respectively for the radial and  $z$  directions. These are tabulated in several references [Carslaw and Jaeger 1959, Özisik 1993, Cole *et al.* 2010] and can be written as:



$$G_{R01}(r, t | r', \tau) = \frac{1}{\pi a^2} \sum_{i=1}^{\infty} e^{-\beta_i^2 \alpha (t-\tau)/a^2} \frac{J_0(\beta_i r'/a) J_0(\beta_i r/a)}{J_1^2(\beta_i)} \quad (2.16)$$

and

$$G_{Z22}(z, t | z', \tau) = \frac{1}{b} \left[ 1 + 2 \sum_{j=1}^{\infty} e^{-j^2 \pi^2 \alpha (t-\tau)/b^2} \cos\left(\frac{j\pi z}{b}\right) \cos\left(\frac{j\pi z'}{b}\right) \right] \quad (2.17)$$

where  $J_0$  and  $J_1$  are Bessel functions of the first kind and  $\beta_i$  are eigenvalues found from  $J_0(\beta_i) = 0$ .

Both GF expressions above involve infinite series, raising numerical issues associated with the solution of infinite series solutions, which can have slow convergence that render obtaining accurate numerical values difficult and can lead to lengthy computer evaluation time due to the large number of terms to be evaluated. The latter are an issue in heat conduction, especially if many temperature values (in space or time) or high numerical accuracy are needed.

Every infinite series must be truncated to a finite number of terms when evaluated numerically on a computer. The number of terms determines the accuracy of the numerical result but the number of terms required for accurate evaluation can vary with time and location within the body and this non-uniform convergence makes difficult a beforehand estimate of how many terms of the series are necessary. The use of a fixed number of terms, for example for the purpose of evaluating temperature variations over time in several locations, risks poor accuracy in some locations and a waste of computer time in others. Thus, a convergence criterion is needed to choose the number of terms, at any location and time, to provide a predetermined accuracy without wasting computer cycles.

When the series contains an exponential factor the most usual convergence criterion is to specify the maximum allowable absolute value of the time-exponential argument, which decreases monotonically and dominates the convergence behaviour in the aforementioned series. Tracking the value of the argument is a conservative way of

controlling convergence but is possible to apply ahead of time in order to specify the number of necessary series terms. The convergence criterion is to continue to add terms to the series until the argument of the exponential factor exceeds a maximum set value.

Expressions for both  $G_{R01}$  and  $G_{Z22}$  include time-exponential arguments in the form  $e^{-A}$  where  $A$  is either  $\beta^2\alpha(t - \tau)/a^2$  or  $j^2\pi^2\alpha(t - \tau)/b^2$ . Their presence multiplying by all other terms in each series causes rapid numerical convergence of the series for large Fourier numbers (or dimensionless times)  $Fo = \alpha(t - \tau)/a^2$  and  $\alpha(t - \tau)/b^2$ . The convergence criterion can be used to determine the number of series terms needed for accurate evaluation of temperatures, terms being added until  $A > K_{\max}$ , where  $K_{\max}$  is the maximum allowable absolute value of the exponential argument. This determines the size of the exponential factor and controls the convergence speed.

Consider the example of  $G_{Z22}$ , dimensionless times are usually considered large if  $\alpha t/b^2 > 0.025$  for this type of GF [Cole *et al.* 2010]. The exponential term will be smaller than 0.001 when the absolute value of the argument is greater than  $K_{\max} = 6.9$ , *i.e.*:

$$\frac{\beta_m^2 \alpha t}{b^2} > 6.9. \quad (2.18)$$

In this case  $\beta_m = j\pi$ , so the above relation yields  $N_{\max} = 9$  for  $Fo = 0.001$ , meaning that only eight terms of the infinite series are necessary to make the exponential factor smaller than 0.001. If  $\alpha t/b^2 = 0.025$  only five terms are necessary, and for “large” values of  $\alpha t/b^2$  (such as 0.17 or larger) only the first term is necessary [Cole *et al.* 2010].

It should be noted that the GF method, as discussed above, yields analytical expressions for temperatures over times and locations for a given set of initial conditions, sink terms and boundary conditions, that can be expressed in numerical terms if necessary values such as temperatures, coordinates or times are supplied. In order to perform the computations required by the Green’s Function Solution Equation (GFSE), analytical forms of the initial temperature field, the sink term and the

boundary conditions in terms of time and spatial coordinates are necessary so that they can be used as input in the GFSE for performing integrations.

While the GF formulation is potentially extremely useful, it does have some limitations that must be kept in mind, namely when variable boundary conditions or source/sink terms are to be considered. Such a situation would lead to the use of analytical functions of time and spatial variables that would require updating as necessary, since in the case under discussion the sink term will be constant neither in time nor in location. Its magnitude is a function of the difference between local and transpiration flow temperatures (even if the latter is assumed to be constant). This means that for arbitrarily short times solutions will probably be fairly accurate. Nonetheless, their accuracy will diminish if the sink term is not updated. This difficulty can be overcome by applying GFSE in an incremental approach, implementing an iterative calculation procedure that can be described as follows:

1. Adequate GFs are selected;
2. A grid of points is defined for calculation purposes in spatial coordinates;
3. Boundary conditions are specified;
4. An initial temperature field is specified as an analytical function of space coordinates and time  $t$ ;
5. The grid and the initial temperature field are used for computing an initial sink term, based on the temperature difference between the solid and the transpiration airflow and features such as hole diameter and plate thickness. Once again an analytical function of space coordinates and time  $t$  is sought;
6. A number of summation terms is specified;
7. A timestep is selected;
8. Temperatures as a function of initial temperature fields and sink terms are computed for  $t = \text{timestep}$ ;
9. Updated analytical temperature fields and sink term functions, or if necessary/applicable boundary conditions, are obtained from calculated point temperature and coordinates.

The process is repeated until either a maximum number of iterations (*i.e.* a total time) are performed or some other termination criterion is met, such as minimum temperature variations between iterations, as shown in Figure 2.1.

This iterative process and updating of boundary and sink terms is not encountered in most literature references given the fact that those applications deal with constant boundary and source/sink terms, the case of successive heating and cooling cycles being the only notable exception [Talati and Jalalifar 2009]. The reasonability of such an approach must therefore be carefully considered, especially when intrinsically iterative methods such as transient finite differences can be considered as alternatives, as discussed below.

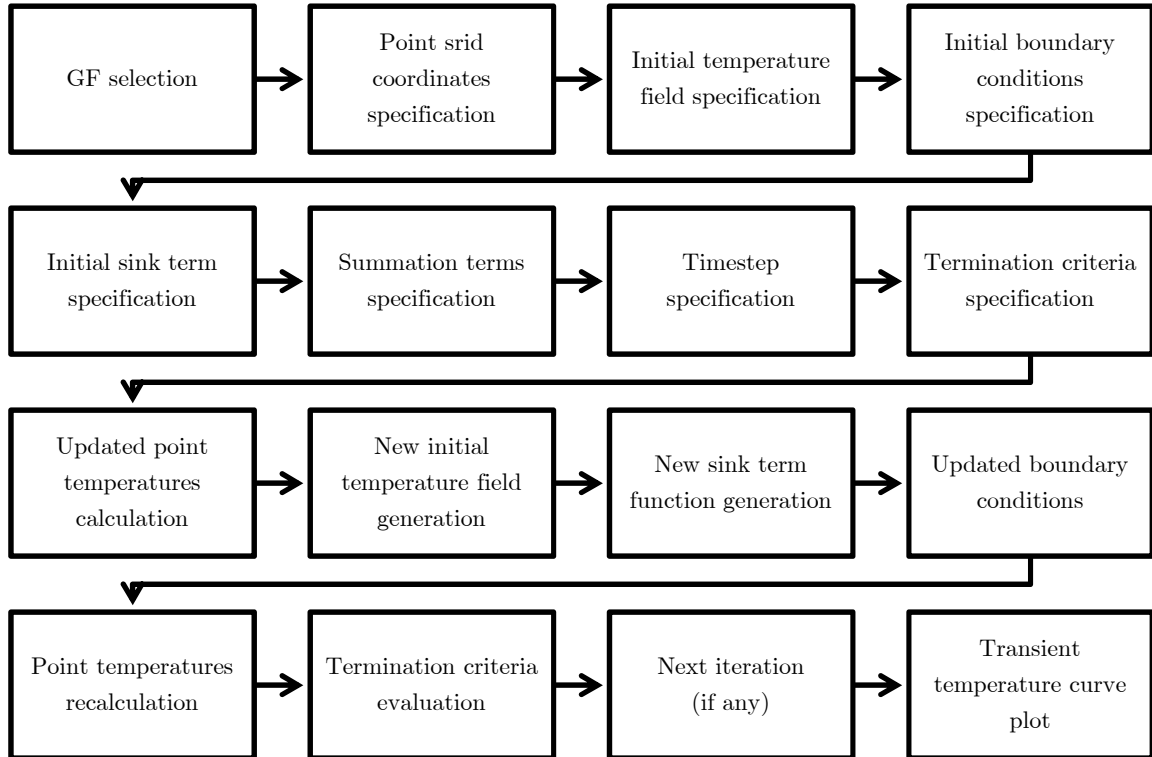


**Figure 2.1** – Iterative GF calculation methodology.

### 2.2.3 Finite Difference Formulation

A typical finite difference formulation typically involves the approximation of differential increments in temperature and space coordinates, once an adequate element grid of nodes has been defined. This numerical approach replaces the continuous

temperature distribution by fictitious heat conducting rods connecting nodal points where heat flux balances are established and where heat generation terms can be considered.

For multidimensional transient problems approaches such as Heisler charts or products solutions are adequate in some cases, especially for regular-shaped solids. Unfortunately many geometric shapes of interest do not fall into these categories, and boundary conditions may vary with time, rendering a mathematical solution potentially impossible and a computational numerical technique necessary. Such problems can be set up using the resistance concept for describing heat transfer between nodes.

The thermal resistance concept is widely used and can be thought of as the ratio between a driving potential and the corresponding heat transfer rate. The thermal resistance for conduction is usually given as:

$$R_{t,\text{cond}} = \frac{L}{kA}, \quad (2.19)$$

where  $L$  is the spatial distance,  $A$  the area and  $k$  the thermal conductivity, while for convection the following expression is used:

$$R_{t,\text{conv}} = \frac{1}{hA}, \quad (2.20)$$

where  $h$  is the convection heat transfer coefficient.

Radiation is a somewhat more complex matter. While the radiation heat flux from hot surroundings to a colder surface is usually written as:

$$q_{\text{rad}} = \varepsilon \sigma A (T_{\text{sur}}^4 - T_{\text{s}}^4), \quad (2.21)$$

where  $\varepsilon$  is the surface emissivity and  $\sigma$  is the Stefan-Boltzmann constant, it can also be expressed as:

$$q_{\text{rad}} = h_r A (T_{\text{sur}} - T_s), \quad (2.22)$$

with a radiation heat transfer coefficient in the form:

$$h_r = \varepsilon \sigma \left[ (T_{\text{sur}} + T_s) (T_{\text{sur}}^2 + T_s^2) \right]. \quad (2.23)$$

Here the radiative transfer is modelled in a manner similar to convection in the sense that it is linearized, making the heat exchange proportional to a temperature difference rather than to the difference between two temperatures to the fourth power. It should however be noted that  $h_r$  strongly depends on temperature while the temperature dependence of the convection heat transfer coefficient  $h$  is generally weak. A thermal resistance for radiation can nevertheless be written as:

$$R_{\text{t,rad}} = \frac{1}{h_r A} \quad (2.24)$$

Designating a node of interest with the subscript  $i$  and adjoining nodes with subscript  $j$ , the steady-state input to node  $i$  will be zero, that is:

$$q_i + \sum_j \frac{T_j - T_i}{R_{ij}} = 0, \quad (2.25)$$

where  $q_i$  is the heat delivered to node  $i$  by heat generation, radiation, *etc.*, while  $R_{ij}$  can take the form of convection boundaries, internal conduction, *etc.*

The specification of volume element  $\Delta V$  and internal nodal resistances is straightforward for cartesian coordinates, especially when the grid consists of equally-spaced increments  $\Delta x$ ,  $\Delta y$  and  $\Delta z$ . For the case under consideration, with its cylindrical coordinate system, internal nodal resistances and volume element  $\Delta V$  can be summarized as listed in Table 2.1:

**Table 2.1** - Internal nodal resistances and volume element for cylindrical coordinates.

Nomenclature for increments	$r, m; \varphi, n; z, p$
Volume element $\Delta V$	$r_m \Delta r \Delta \varphi \Delta z$
$R_{m+}$	$\frac{\Delta r}{k(r_m + \Delta r/2) \Delta \varphi \Delta z}$
$R_{m-}$	$\frac{\Delta r}{k(r_m - \Delta r/2) \Delta \varphi \Delta z}$
$R_{n+}$	$\frac{r_m \Delta \varphi}{k \Delta r \Delta z}$
$R_{n-}$	$\frac{r_m \Delta \varphi}{k \Delta r \Delta z}$
$R_{p+}$	$\frac{\Delta z}{k r_m \Delta r \Delta \varphi}$
$R_{p-}$	$\frac{\Delta z}{k r_m \Delta r \Delta \varphi}$

Once steady-state problems are set up, a system of equations is constructed and can be solved for nodal temperatures using matrix inversion techniques or, more typically when the number of nodes becomes larger, Gauss-Seidel iterations applied by solving for temperature  $T_i$  in terms of the resistances and temperatures of adjoining nodes  $T_j$  as:

$$T_i = \frac{q_i + \sum_j (T_j / R_{ij})}{\sum_j (1/R_{ij})}. \quad (2.26)$$

The procedure usually involves the specification of an initial set of values for  $T_i$  obtained by any adequate method, which are then used to recalculate nodal temperatures. The process continues until temperature variations between iterations are arbitrarily small.

When the problem of interest is transient, the net energy transfer into the node must be evidenced as an increase in internal energy of the node, which when expressed

in terms of specific heat and temperature leads to an approximation for its rate of change in time from instant  $t$  to  $t+1$  as:

$$\frac{\Delta E}{\Delta t} = \rho c_p \Delta V \frac{T_i^{t+1} - T_i^t}{\Delta t} \quad (2.27)$$

where  $\Delta V$  is the volume element. Designating the thermal capacity as:

$$C_i = \rho_i c_{p_i} \Delta V_i \quad (2.28)$$

the general resistance-capacity formulation for the energy balance on a node is

$$q_i + \sum_j \frac{T_j^t - T_i^t}{R_{ij}} = C_i \frac{T_i^{t+1} - T_i^t}{\Delta t}. \quad (2.29)$$

Such formulations can be developed on the basis of a forward-difference technique, in that the temperature of a node at a future time increment is expressed in terms of the surrounding nodal temperatures at the beginning of the time increment. In this case the expressions are called explicit formulations because it is possible to write nodal temperatures explicitly in terms of the previous nodal temperatures. In this formulation, the calculation proceeds directly from one time increment to the next until the temperature distribution is calculated at the desired final state.

The difference equation may also be formulated by computing the space derivatives in terms of the temperatures at the  $t+1$  increment. Such an arrangement is called a backward-difference formulation because the time derivative moves backward from the times for heat conduction into the node. This backward-difference formulation does not permit the explicit calculation of  $T^{t+1}$  in terms of  $T^t$ . Rather, a whole set of equations must be written for the entire nodal system and solved simultaneously to determine temperatures  $T^{t+1}$ , so the backward-difference method produces an implicit formulation for the future temperatures in the transient analysis.



The advantage of an explicit forward-difference procedure is the direct calculation of future nodal temperatures. However, the stability of this calculation is governed by the selection of the values of space and time increments. On the one hand, a selection of a small value of space increment automatically forces the selection of some maximum value of time increment. On the other hand, no such restriction is imposed on the solution of the equations which are obtained from the implicit formulation. This means that larger time increments can be selected to speed up the calculation. The obvious disadvantage of the implicit method is the larger number of calculations for each time step. For problems involving a large number of nodes, however, the implicit method may result in less total computer time expended for the final solution because very small time increments may have to be imposed in the explicit method from stability requirements. Much larger time increments can be employed with the implicit method to speed the solution.

The time increment necessary to ensure stability is usually given as [Holman 1986]:

$$\Delta t \leq \min \left\{ \frac{C_i}{\sum_j (1/R_{ij})} \right\} \quad (2.30)$$

while the following expression is useful for alleviating potential problems of round-off errors in computer solutions when small thermal resistances are employed:

$$T_i^{t+1} = \frac{\Delta t}{C_i} \left[ q_i + \sum_j \frac{T_j^t - T_i^t}{R_{ij}} \right] + T_i^t. \quad (2.31)$$

As mentioned above, heat generation (or heat sinks, as needed in the present case) and radiation phenomena can be accounted for with term  $q_i$ , while convection boundaries are treated in the same way as internal conduction. Given the method's iterative approach, it is always possible to update sink terms, convection and radiation between iterations, adjusting their magnitude with the nodal temperatures calculated in

all iterations. This is especially relevant concerning radiation, given its strongly non-linear nature.

Regarding the implementation of finite differences, the iterative calculation procedure that can be described as follows:

1. A grid of points is defined for calculation purposes in spatial coordinates;
2. Nodal resistances, element volumes, sink terms and thermal capacities are calculated;
3. An initial temperature field is specified as nodal temperatures;
4. The stability criterion is applied in order to determine the minimum time increment;
5. New nodal temperatures are computed for  $t = \Delta t_{\min}$ ;
6. Updated sink terms and radiation resistances obtained if necessary;
7. The process is repeated until either a maximum number of iterations (*i.e.* a total time) are performed or some other termination criterion is met, such as minimum temperature variations between iterations.

This process can be summarized as illustrated in Figure 2.2.

When the transpiration airflow is reset at its initial mass flow, the transient temperature curve will decrease back towards its initial value dictated by the incident radiative flux but especially by the transpiration airflow, at a rate (*i.e.* slope) that will be a function of the magnitude of both factors and that can also be quantified.

## 2.3 Assumptions and Simplifications

A proper methodology needed to be established in order to implement both the GF method and the finite difference approach. Despite the fact that the GF library lists a number of readily available analytical formulations, these must nevertheless be adequately used by setting up a solution to the conduction problem under study, and all necessary operations must be performed in order to obtain temperature values for all locations and times of interest.

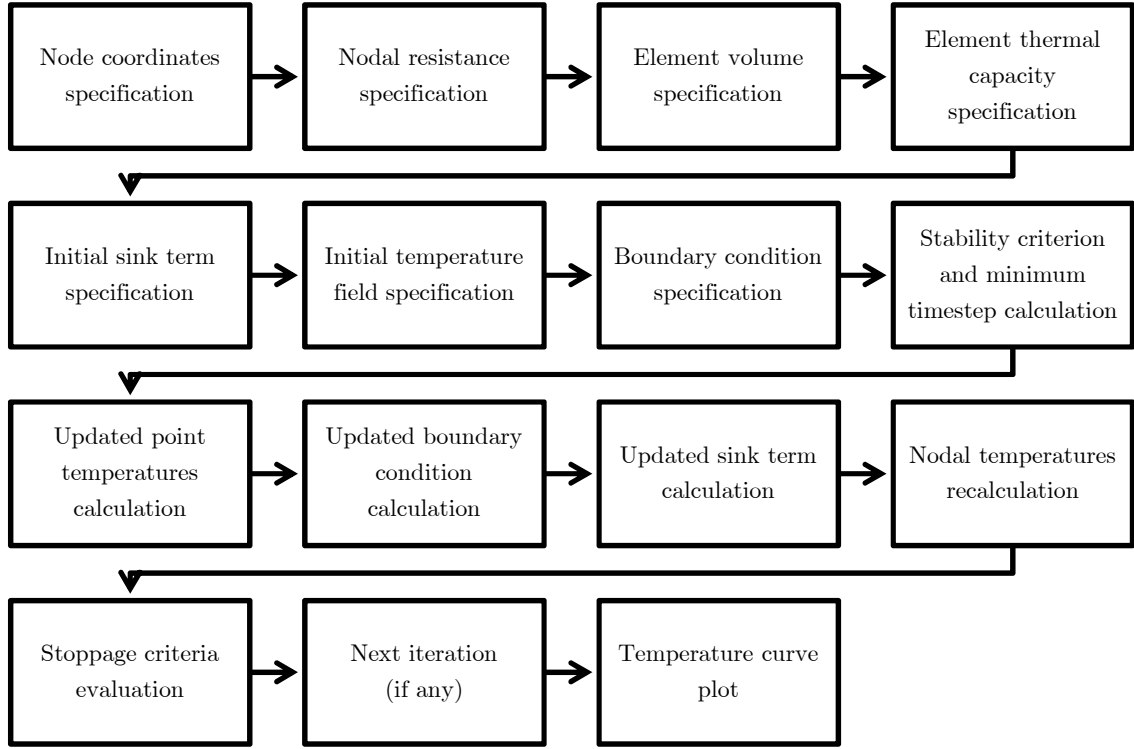


**Figure 2.2** – Iterative finite difference calculation methodology.

In order to use both the GF method and finite differences as a basis for the study and development of a heat flux meter, it was felt necessary to gain more precise insight into their results in an incremental fashion. This was done by comparing results of both approaches with those obtained with equivalent CFD simulations of the same physical problem, including heat sink terms, radiation and convection.

At this point the question of whether a one-dimensional approach was adequate in describing the problem needed to be addressed, in order to proceed with parametric studies. As mentioned earlier an assumption of azimuthal symmetry is reasonable for the case under discussion, given its geometry and boundary conditions. Thus, a fully three-dimensional approach would be unnecessary, but more importantly the sensing element's small thickness (much smaller than its diameter) could render conduction one-dimensional in radial direction and lead to a much simpler approach by ignoring temperature gradients along the element's thickness.

This was exactly the basis for the analytical model developed for Gardon gauges [Gardon 1953]. Their sensing elements typically have thicknesses ranging from as low as 0.05 to 0.2 mm (hence the frequently used designation of “thin foil”). Given the fact

that some of the robustness of earlier transpiration radiometers was to be retained, and besides dimensioning considerations discussed in some detail in Chapter 3, a thickness value of around 0.1 mm was considered adequate. Other applications of microperforated steel plates were found (including, oddly enough, *espresso* machine filters) with thicknesses around the same value that exhibited satisfactory mechanical resistance.

As discussed below in Chapter 3, common manufacturing processes such as photoetching place a limitation on the range of hole diameter to plate thickness ratio, rendering impractical holes with diameters smaller than the plate thickness. For the intended range of sensing element diameters (around 10 mm), hundreds of 0.1 mm holes can nevertheless be fitted in order to preserve the transpiration principle, and the question of whether a one-dimensional approximation to the behaviour of the sensing element can be settled by examining the plate's Biot number. Biot numbers are usually calculated as:

$$\text{Bi} = \frac{hL_c}{k} \quad (2.32)$$

where  $h$  is the convection heat transfer coefficient,  $k$  is the thermal conductivity and  $L_c$  is a characteristic length that is often indicated as a solid's volume to surface area ratio but can also be, for simple geometries, a radius or a thickness. For lumped analysis validity purposes the criterion is usually to regard it as valid when  $\text{Bi} < 0.1$ .

While thermal conductivity is at most dependent on temperature, the convection heat transfer coefficient is strongly dependent on the airflow velocity on the surface. In order to roughly evaluate which Biot numbers are to be expected, thermal conductivity is assumed to be on the lower side of the range of values for stainless steel (typically ranging between 13 and 19 WK<sup>-1</sup>m<sup>-1</sup>), while for simplicity in a rough approach convection coefficients can be assumed to be those of air in forced convection found in standard textbook tables (up to 200 WK<sup>-1</sup>m<sup>-2</sup>), although as discussed in detail below the determination of convection coefficients is a much more complicated matter and will be performed with adequate care later on. Suffice to say for the moment that

actual convection coefficients for the application under discussion will be typically higher than those used for these Biot number calculations.

If a Biot number is calculated based on plate thickness (0.1 mm) and radius (4.75 mm, as will be explained in Chapter 3) as characteristic lengths, Biot numbers would be  $Bi = 0.0015$  and  $Bi = 0.076$  respectively. An  $L_c$  characteristic length can more properly be defined and used to calculate a solid's volume to surface area ratio. If a 9.5 mm total diameter, 0.1 mm hole diameters and 0.1 mm plate thickness are used, the following Biot numbers are obtained as a function of the number of holes:

**Table 2.2** – Plate Biot number as a function of the number of holes.

Number of Holes	250	500	750	1000
Biot Number	0.00071	0.00067	0.00064	0.00061

These are hardly surprising considering the plate's very low thickness and can arguably be even lower if effects that have to do with convection enhancing phenomena are considered, as will be discussed in further detail below.

All Biot numbers in Table 2.2 are below the conventional  $Bi < 0.1$  limit where lumped analysis is deemed reasonable but values for the radial direction are without surprise larger than those for thickness, where the very low Biot number values indicate negligible temperature gradients, make a one-dimensional approximation reasonable and greatly simplify obtaining accurate models for describing the sensing element's behaviour and testing and verifying results for both approaches.

The selection of an adequate value for the convection coefficient is of the utmost importance while being somewhat more complicated than apparent at first sight and certainly not as simple as used values tabulated in textbooks.

Standard heat transfer references often list relationships meant to be used for developing or fully developed flows. If heating is occurring at the surface of a tube through which a fluid is flowing, Nusselt numbers and heat transfer coefficients are highest at the inlet, where boundary layer thicknesses are smallest, and decrease gradually towards fully developed values. These effects are usually described by

defining an entry length, defined as the distance from the entrance where relevant variables reach within 2% of their fully developed values. Laminar flows show strong dependency on the Reynolds number and lead to entry length values as high as 115 times the diameter, while turbulent flows entry lengths' are much shorter and less dependent on Reynolds numbers. However, in many flows of practical interest entrance effects only become insignificant beyond lengths higher than 10 diameters. Furthermore, Nusselt numbers for uniform surface temperatures and uniform heat flux conditions are nearly identical in the entrance regions [Çengel 2006].

Given the plate's very low thickness, the lateral areas of individual holes are very low, so that the relationships for entry regions have a limited applicability even if several hundreds of holes are to be considered. These small lateral areas also raise the question of determining the precise nature of the convection interaction of the transpiration airflow with the perforated plate. Since the transpiration airflow is expected to be colder than the surroundings and the plate, heat will be removed by convection not only in the microperforated pattern but also (and potentially mostly) on the windward face of the perforated plate, on which the incoming transpiration airflow impinges. The magnitude of this heat transfer will be a function of the surface areas and the local temperature difference between the air and each surface, besides the local convective heat transfer coefficient that can be influenced by geometry and flow conditions.

While single hole relationships are useful and important in understanding the nature of the convective interaction between the airflow impinging on a perforated surface and the holes themselves [Sparrow and Gurdal 1981, Cho *et al.* 1997], other parameters have greater importance as far as perforated patterns are concerned. The matter of considering a repetitive pattern is nevertheless fundamental since this regular geometry gives rise to a symmetry pattern whereby each hole is surrounded by a region where symmetry surfaces exist as its boundaries. Within each such unit cell, the heat transfer and fluid flow characteristics are identical to those of all the other cells that blanket the surface, so that measurements for a single cell yield information for the entire surface [Sparrow and Ortiz 1982], as can be seen from the illustration in Figure 2.3.

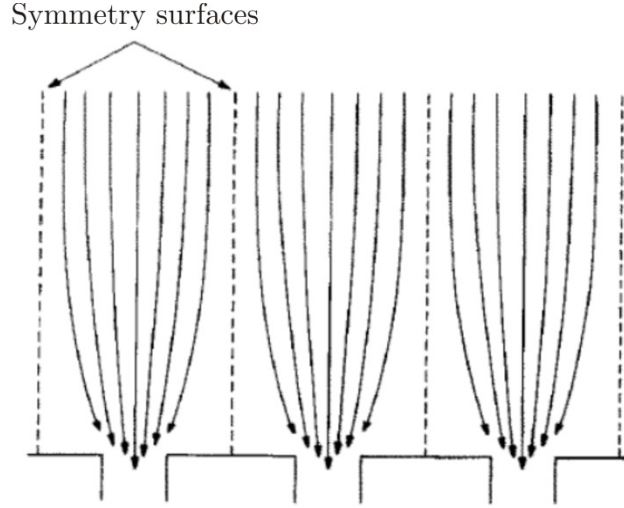


**Figure 2.3** – Fluid flow passing from the upstream surface into the perforated pattern [Sparrow and Ortiz 1982].

Although it was found that the influence of the hole length-to-diameter ratio has significance, it was shown that the appropriate heat transfer area for the determination of the heat-transfer coefficient is essentially that of the hole-approach flow [Andrews *et al.* 1991]. Various studies showed that correlations for Nusselt and Reynolds numbers using a convection coefficient based solely on the hole internal surface area did not adequately correlate the experimental results, indicating that internal hole heat transfer was not the dominant physical process. The use of the hole approach surface area to define convective heat transfer coefficient resulted in a good correlation of the results, indicating that the hole approach convective heat transfer was the dominant heat transfer process [Andrews *et al.* 1988].

The importance of the hole spacing-to-diameter ratio is therefore fundamental in the determination of heat transfer coefficients since it influences the acceleration of the airflow when transitioning from its incoming bulk velocity to the faster flowing airflow towards and inside the holes. Correlations for a variety of situations and geometries have been developed, typically relying on experimental results and considering a large variety of Reynolds numbers, up to 20,000 [Sparrow and Ortiz 1982, Dorignac *et al.* 2005, Fenot *et al.* 2005].

As discussed in further detail in Chapter 3, a 2.5 spacing-to-diameter ratio was eventually selected due to boundary layer control and radiation transmissivity considerations. This led to a perforated pattern with 0.1 mm holes with a 0.25 mm

spacing, and interestingly some of the correlations mentioned above are available for the exact 2.5 spacing-to-diameter ratios of interest in the present work [Sparrow and Ortiz 1982], although this was actually only realised after the dimensioning procedures discussed in Chapter 3 were carried out and components had been manufactured according to those specifications.

While these correlations were admittedly obtained with somewhat larger holes than those under discussion (with diameters ranging from 1 to 10 mm), the fact that the diameters to be considered here are smaller is not expected to significantly invalidate such relationships since recent experimental results show that airflow characteristics in microtubes (*i.e.* for somewhat lower diameters than those considered here), namely heat transfer correlations for laminar and turbulent flows, are the same as for larger tubes if the higher velocities related to smaller diameter and possible compressibility phenomena are duly taken into account [Yang *et al.* 2012].

The aforementioned correlations propose Nusselt numbers based on different assumptions regarding characteristic lengths. An earlier study proposes that the Nusselt number can be determined as [Sparrow and Ortiz 1982]:

$$\text{Nu} = 0.881 \text{Re}^{0.486} \text{Pr}^{1/3} \quad (2.33)$$

with Pr being the Prandtl number (which for air is approximately 0.7) and defining the Reynolds number Re as a function of density  $\rho$ , air velocity  $v$ , hole diameter  $d$  and dynamic viscosity  $\mu$ :

$$\text{Re} = \frac{\rho v d}{\mu} \quad (2.34)$$

and writing the Nusselt number as:

$$\text{Nu} = \frac{hA}{ek} \quad (2.35)$$



where  $h$  is the convection coefficient,  $k$  is the thermal conductivity of air,  $A$  is the area of the surface that participates in the heat transfer process (*i.e.* the unit cell area minus that of the holes) and  $e$  is the hole spacing. This means that this Nusselt number is based on a characteristic length that is the ratio of geometric features rather than an individual constant of the pattern, and that different characteristic lengths are used in the Reynolds and Nusselt numbers.

Other studies extended the work presented in the earlier reference mainly by using a larger variety of spacing-to-diameter ratios (from 1.7 up to 9.6), using an alternative formulation for the Nusselt and Reynolds numbers based on the same characteristic length  $A/e$  and expressing the Nusselt number as a function of the Reynolds number and unit cell parameters, yielding in each hole:

$$\text{Re}_h = \frac{\rho v d}{e \mu} \quad (2.36)$$

and

$$\text{Nu} = 1.202 \left( \frac{e}{\sqrt{A}} \right)^{1.979} \left( \frac{e}{d} \right)^{0.163} \text{Re}_h^{0.409}, \quad (2.37)$$

with results within 10% of all experimental measurements [Dorignac *et al.* 2005]. The earlier formulation was used mainly for compactness.

These formulations allow the calculation of a convection heat transfer coefficient to be used both in a volumetric heat sink term and in the convective boundary encountered on the windward side of the plate, in terms of an incoming air mass flow. This in turn enables the study of the effect of varying mass flows passing through the perforated pattern, of which the convection coefficient will be a function.

It is therefore necessary to obtain a relationship between the incoming transpiration mass flows, which can be characterized in terms of their pressures, densities, temperatures and velocities, and the velocities in the holes and resulting Reynolds and Nusselt numbers and therefore convection coefficients. All this for any

given perforated pattern, especially as far as its hole diameter-to-spacing ratio is concerned since it dictates heat transfer areas.

At this point it is reasonable to assume that all the incoming compressed air passes through the holes in the perforated pattern, although in practice some leakage is expected at the fringe of the plate if some less than perfect welding is present. Nevertheless, this assumed mass continuity can be expressed as:

$$\dot{m}_1 = \dot{m}_2, \quad (2.38)$$

where  $\dot{m}_1$  is the mass flow in the compressed air feed tube and  $\dot{m}_2$  is the sum of mass flows in the  $N$  holes of the pattern, *i.e.*:

$$\rho_1 v_1 \frac{\pi d_1^2}{4} = N \rho_2 v_2 \frac{\pi d_2^2}{4} \quad (2.39)$$

where  $\rho$ ,  $v$  and  $d$  are densities, velocities and diameters, respectively. This equation can be simplified and rearranged by multiplying and dividing each side of the equation by the relevant dynamic viscosity, obtaining the following relationship where Reynolds numbers are made to appear:

$$\mu_1 d_1 \text{Re}_1 = N \mu_2 d_2 \text{Re}_2. \quad (2.40)$$

Given the fact that the plate is a rather poor heat exchanger due to its low thickness and relatively low surface area, and that relatively high mass flows are to be used in order to ensure boundary layer blow-off, the bulk of the transpiration airflow is not expected to heat up significantly, even when considering a temperature increase due to compression in the holes. This means that viscosity variations due to temperature differences are assumed to not be significant and allow writing the Reynolds number in the holes as:

$$\text{Re}_h = \text{Re}_2 = \frac{\text{Re}_1 d_1}{N d_2}. \quad (2.41)$$

Once Reynolds numbers for the holes are known, the Nusselt number correlations above can be used to compute various convection coefficients, as intended. A certain incoming mass flow is a function of the tube area, the airflow velocity and its pressure, and it is always possible to obtain a desired mass flow by any combination of such parameters. In practice, constraints are usually posed in terms of a fixed feed line diameter (and therefore flow area) and a compressed air supply pressure. Operational parameters are described in detail in Chapter 3, when the dimensioning of the perforated plate and the setting of operation conditions are discussed. Within the framework of developing an adequate formulation for the sensing element such detail is unnecessary and some parameters were fixed, namely the compressed airflow cross section and the supply pressure.

Given the plate's very low thickness, the question of whether to consider the lateral area of the holes in the perforated pattern for convective heat transfer purposes could be thought of as secondary, but that assumption does require some careful consideration. The plate's effective frontal area can be calculated as the difference between its actual frontal area and the area of each hole multiplied by the number of holes, while the total hole lateral area is the perimeter of each hole multiplied by the number of holes and the plate thickness. If a plate diameter of 9.5 mm and a 0.1 mm hole diameter equal to the plate thickness, the area ratio can be calculated as shown in Table 2.3.

**Table 2.3** – Plate areas as a function of the number of holes.

Number of holes	250	500	750	1000
Effective frontal area [m <sup>2</sup> ]	$6.89 \times 10^{-5}$	$6.70 \times 10^{-5}$	$6.50 \times 10^{-5}$	$6.30 \times 10^{-5}$
Hole lateral area [m <sup>2</sup> ]	$7.85 \times 10^{-6}$	$1.57 \times 10^{-5}$	$2.36 \times 10^{-5}$	$3.14 \times 10^{-5}$
Area ratio	8.77	4.26	2.76	2.00
Total area [m <sup>2</sup> ]	$7.68 \times 10^{-5}$	$8.27 \times 10^{-5}$	$8.86 \times 10^{-5}$	$9.44 \times 10^{-5}$

While the frontal area of the plate is obviously higher than the sum of the lateral areas of the holes, the contribution of the latter naturally rises as their number increases. When the number of holes is in the order of a thousand, as will happen in

the prototype, the frontal area of the plate is still double that of the holes, but it was felt necessary to take the hole area into account by adding it to the frontal area when used in the aforementioned relationships for the determination of the convective coefficient.

As the diameter of the compressed air supply, the same value as earlier was used, *i.e.* 9.5 mm, while a supply pressure of 5 bar was specified since it is the standard supply pressure at the laboratory where the experimental work was to be conducted, and a supply temperature of 25°C was also assumed. Likewise, using the aforementioned assumption that the bulk of the airflow will not heat up significantly in contact with the plate, Prandtl numbers and air thermal conductivities were taken to be those at 25°C.

Convective heat transfer coefficients could thus be calculated as a function of incoming air mass flows, representing the actual physical situation to be encountered by the prototype when in operation. It should be noted that the aforementioned correlations for Nusselt numbers use the full area of the unit cell rather than a value that subtracts the frontal area of the holes. However, this correction was considered relevant when using the correlation, so that the total area values in Table 2.3 were used in the calculations. The fact that the correlations were obtained for a range of spacing-to-diameter ratios (2.0 and 2.5 for the version used) means that for a given plate frontal area a large number of holes is necessary to fulfil the ratio requirement, meaning that the areas for small numbers of holes were not used because they would potentially translate a situation outside the bounds of the correlations' validity. Furthermore, as discussed in Chapter 3, a low number of holes in the pattern would lead to poor flow uniformity and low transmissivity that could have detrimental effects on the sensing element's intended performance. Values for 1000 holes are for the moment sufficiently representative for model development purposes.

Illustrated in Figure 2.4 is the Nusselt number as a function of the Reynolds number, using both of the aforementioned relationships, *i.e.* the earlier one embodied in the upper curve of black circles [Sparrow and Ortiz 1982] compared to values resulting from the application of the latter work [Dorignac *et al.* 2005], for hole diameter between 1 and 15 mm and hole spacing/diameter ratios ranging from 1.7 to 9.6.

The plot in Figure 2.5 illustrates the same numbers calculated using the values and assumptions discussed above. The graphic in Figure 2.6 illustrates the relationship between incoming mass airflow and the convection heat transfer coefficient on the plate, where as expected the power function adjusted from calculated values, *i.e.*:

$$h = 45654\dot{m}^{0.486}. \quad (2.42)$$

The same 0.486 exponent as in Equation 2.33 is displayed.

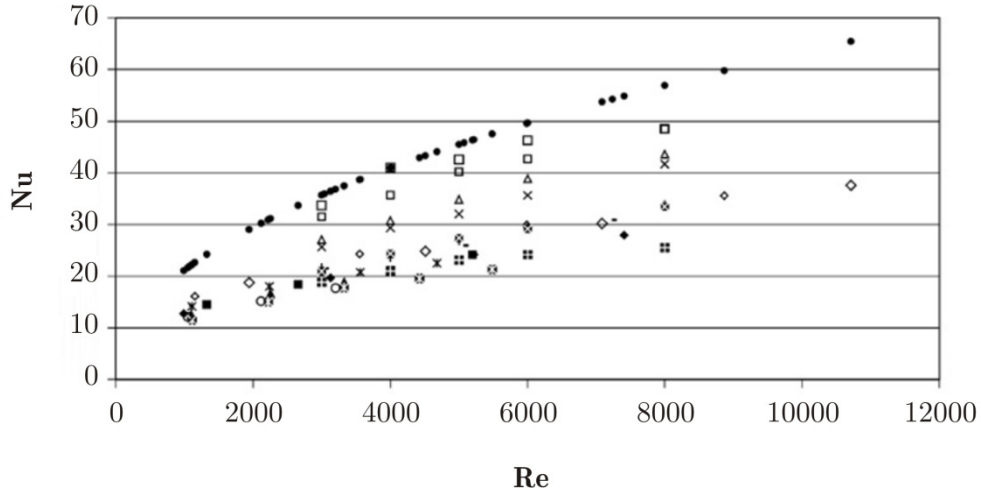


**Figure 2.4** – Reynolds vs. Nusselt number relationships [Dorignac, Vullierme et al. 2005].

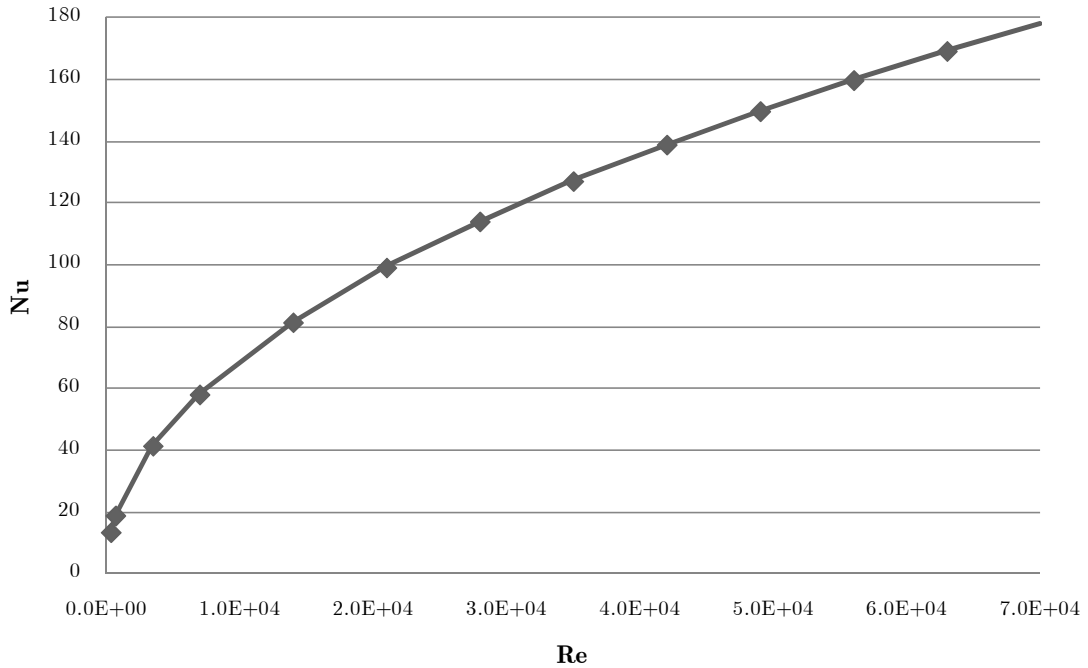


**Figure 2.5** – Calculated Reynolds and Nusselt number relationship.

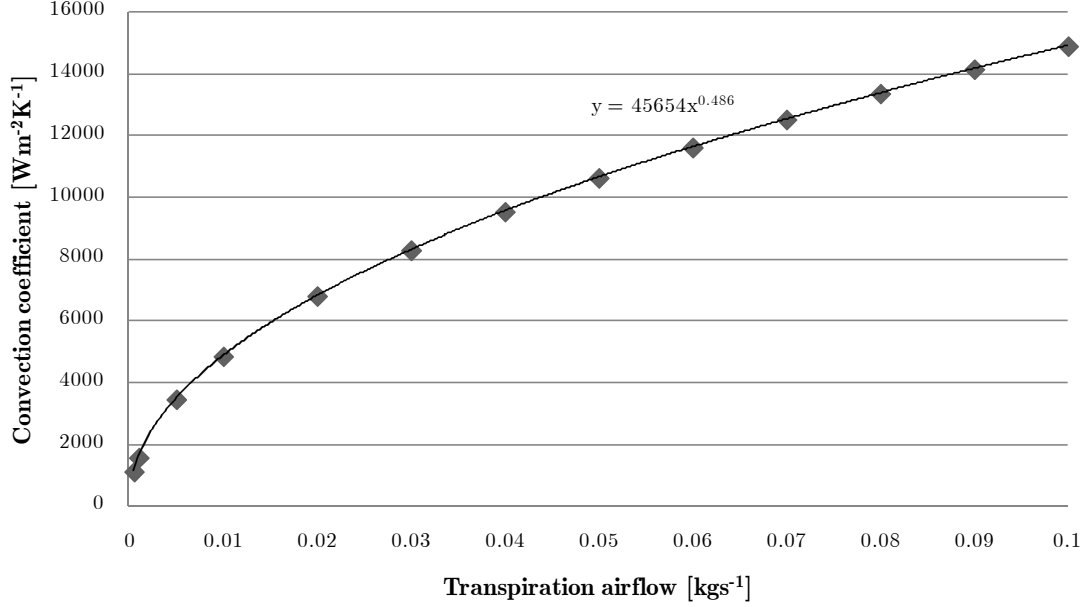


**Figure 2.6** – Convection heat transfer coefficient as a function of transpiration mass flow.

Although different criteria were used in the definition of which particular area should be used, Nusselt numbers are approximately the same for the same Reynolds numbers, although the calculated values lie mostly outside the range of Reynolds numbers shown from the references. This is not necessarily surprising given the fact that somewhat a smaller perforated pattern is considered here, so that the Reynolds number will be higher for similar total mass flows.

Within the framework under discussion and for the same reason encountered in the field of mechanics of materials, a 60° staggered pattern (also known as a hexagonal pattern given the fact that any node is surrounded by six others in a hexagonal arrangement) was used in preference to a square pattern since it guarantees an isotropic distribution in the plane of the plate, while for instance a square pattern would lead to an orthotropic behaviour [Dowling 1999]. While the earlier of the references cited when calculating convection coefficients relied on the 60° staggered pattern [Sparrow and Ortiz 1982], the other also studied the square pattern [Dorignac *et al.* 2005]. Illustrated in Figure 2.7 is the hexagonal pattern of unit cells considered in the earlier study, showing the unit cell's pitch (the same as spacing  $e$  considered in the present work) and diameter.

The same pattern was used in the remainder of the work described here but in a different fashion for plate transmissivity calculations. The pattern can also be thought of as an equilateral triangle with a hole at each vertex, and area calculations using triangular elements are slightly more simple than for hexagons, while the holes merely dictate a need to divide their perimeter, each hole having only one sixth of its perimeter and area within a particular cell, the same as saying that a single hole in the pattern belongs to six different units.

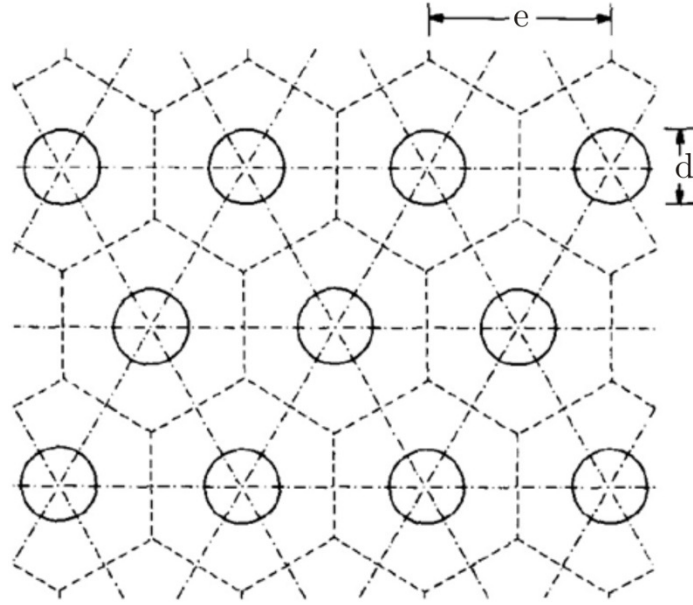


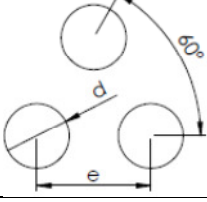
**Figure 2.7** – Hexagonal unit cell pattern [Sparrow and Ortiz 1982].

Such considerations are relevant in terms of finite differences in order to compute element surface areas sink terms for heat transfer. The thermal resistance formulations in Equations 2.29 to 2.34 require element areas for conductive, convective and radiative heat transfer, and plate thickness  $L$ , hole diameters  $d$  and their spacing  $e$  dictate unit cell volumes and heat transfer areas, as summarized in Table 2.4.

Regarding the specification of element areas in the resistance formulations, it is proposed to consider the upper surface of the element for radiative heat transfer, while for convective transfer, given the plate's very low thickness, the area to be considered will be that of the lower surface of the element plus the lateral area of the holes. This effectively means that the volumetric heat sink term is converted into a superficial resistance term that no longer needs to be taken into account in term  $q_i$  of Equations 2.35, 2.36, 2.39 and 2.41. This only occurs for this very particular situation where a

thin plate is being considered and a convection coefficient was determined for the whole of the perforated pattern.

**Table 2.4** – Unit Cell Parameters.

<b>Unit Cell</b>	
<b>Element Frontal Area</b>	$\frac{e^2}{2} \sin(60)$
<b>Unit Cell Volume</b>	$\frac{e^2}{2} \sin(60)L$
<b>Effective Frontal Heat Transfer Area</b>	$\frac{e^2}{2} \sin(60) - \frac{\pi d^2}{8}$
<b>Effective Volume</b>	$\left( \frac{e^2}{2} \sin(60) - \frac{\pi d^2}{8} \right) L$
<b>Hole Lateral Heat Transfer Area</b>	$\pi L \frac{d}{2}$
<b>Overall Convective Transfer Area</b>	$\frac{e^2}{2} \sin(60) - \frac{\pi d^2}{8} + \pi L \frac{d}{2}$

If the assumption of the same convection coefficient for the windward face of the elements and for the interior of the holes was not considered reasonable, as could be the case for a much thicker plate, a volumetric sink term (in  $\text{Wm}^{-3}$ ) could nevertheless be readily calculated from a properly calculated convection coefficient by specifying an interfacial area density  $D_{\text{sink}}$  (in  $\text{m}^{-1}$ ) for each particular unit cell, as the ratio between the area for convective heat transfer within the holes in that cell ( $\text{m}^2$ ) and the unit cell volume ( $\text{m}^3$ ). This density parameter would be constant for each particular unit cell and the same throughout the total volume of the component, unless specified otherwise. Once a thickness and the unit cell parameters were selected, the interfacial area density could be defined and allow the calculation of the area over which the convective heat sink would take effect using relationship:

$$A_{\text{sink}} = D_{\text{sink}} \Delta V \quad (2.43)$$



where  $\Delta V$  is the element volume. The volumetric convective heat sink can be defined using Newton's law of cooling in the form:

$$-g_{\text{sink}} = h(T_{\text{node}} - T_{\text{air}})D_{\text{sink}} \quad (2.44)$$

where  $h$  is the convection coefficient for the airflow through the holes,  $T_{\text{node}}$  is the nodal temperature and  $T_{\text{air}}$  is the temperature of the airflow.

It should be kept in mind that the sink term above merely describes the amount of heat that is removed from the plate by convection due to the temperature difference between the transpiration airflow and the perforated pattern, but that the magnitude of the temperatures in the plate is ultimately dictated not only by convection but also by the radiative interaction between the sensing element's surface and its hot surroundings, via the radiative source's area and emissivity and the element's own reflectivity, emissivity and transmissivity.

Rather than introducing the relevant element areas explicitly in the resistance formulations using the cumbersome relationships listed in Table 2.5, these can be used to specify element area and volume correction factors to the frontal area  $A$ . This is done both for the element radiative heat transfer areas in the form:

$$\zeta_{\text{corr}} A = A_{\text{rad}} , \quad (2.45)$$

where  $A$  the element frontal area. Likewise, a correction factor can be defined for the convective exchange in the form:

$$\eta_{\text{corr}} A = A_{\text{conv}} , \quad (2.46)$$

while a corrected volume for element heat capacity correction can also be defined as:

$$\xi_{\text{corr}} \Delta V = \Delta V_{\text{corr}} , \quad (2.47)$$

where  $\Delta V$  is the element volume. This value is expected to be the same as for the radiative heat transfer area correction factor given the fact that the corrected volume is merely the effective (*i.e.* corrected) area multiplied by the plate thickness.

Once the unit cell parameters are set, the correction factors can be determined from the relationships in Table 2.4. Using the aforementioned values of 0.1 mm for the hole diameter and plate thickness and of 0.25 mm for the hole spacing, the correction factors become:

$$\zeta_{\text{corr}} = \frac{A_{\text{rad}}}{A} = 0.8549 \quad (2.48)$$

$$\eta_{\text{corr}} = \frac{A_{\text{conv}}}{A} = 1.4353 \quad (2.49)$$

$$\xi_{\text{corr}} = \frac{\Delta V_{\text{rad}}}{\Delta V} = 0.8549 \quad (2.50)$$

As expected the correction factors for the radiation area and the volume are the same and take into account the diminution in frontal area and volume due to the holes, yielding values lower than unity, while the correction factor for convection is higher because of the sum of the lateral area of the holes to the effective frontal area, as was previously discussed and is shown in Table 2.4.

It should be noted that this definition of a radiative transfer area where a difference between blockage and opening areas is implied is essentially the same as taking into account a transmissivity term, which means that the application of this radiative area correction factor inherently takes into account this radiative property of the element that is extended to the total area of the plate.

The discussion above is furthermore useful in another situation, which has to do with the boundary layer blow-off phenomenon. If the transpiration mass flows are insufficient to eliminate the boundary layer on the side of the plate exposed to the high temperature surroundings, some convection heat transfer will take place and the same area considered for radiative heat exchange must be considered for this convective transfer, effectively introducing another resistance at each computational node. This

effect was duly taken into account when comparing situations where relatively low transpiration mass flows were used.

## 2.4 Implementation and Results

Calculations with the GF and finite differences methods were implemented using Wolfram *Mathematica* 8, while CFD simulations were performed using ANSYS, namely its *CFX* module.

The purpose of such comparisons warrants some further discussion as far as their motivation is concerned. It could be argued that the commercial CFD software could be used with confidence given its established reputation in a wide range of applications and previous experience, even as far as the author and supervisor of the present document are concerned, and that the complexities related to the development of the aforementioned analytical and numerical approaches would thus be rendered unnecessary. Operational prototypes could thus be designed and built, their performance and output being subsequently compared with the CFD model and its results, without bothering with complex analytical formulations.

The use of the CFD software was always intended for design purposes, not only regarding the sensing element itself but especially when considering the overall instrument as a system consisting of various components, rather than merely as a sensing element.

This does not mean that proper analytical and numerical methodologies would not be useful, going beyond a mere unwillingness to use a commercial tool without a more detailed theoretical understanding of the underlying phenomena.

While undoubtedly more detailed in terms of the range of phenomena and models than can be implemented and studied, CFD software does require the specification of particular geometric features of the systems to be studied, as for instance the diameter and pitch of a particular perforated plate. This is typically done either directly in a CAD module of the CFD package or by importing the necessary files from dedicated CAD software, after which the finite element mesh is created for computation purposes.

Parametric studies of geometry changes can thus be rendered somewhat cumbersome in terms of methodology due to this need for creating new geometry files. Furthermore, precisely because CFD software typically implements a variety of physical models in great detail, simulations can take significant amounts of time to run.

The methodologies proposed and discussed above can potentially reduce the computational effort involved, at least for the type of geometry of interest, since parametric tests regarding various perforation parameters can be conducted merely by adjusting the unit cell parameters listed in Table 2.4, while various operational conditions can be simulated by specifying relevant temperatures in the boundary conditions and airflows or calculating convection coefficients using the correlation of Equation 2.42, rather than creating new CAD geometries to be imported and meshed into the CFD software. Relevant information about the behaviour of the sensing element such as temperature spatial distributions, transient variations or time constants  $\tau$ , can thus be obtained at a fraction of the computational effort.

The choice for *Mathematica* came naturally since it is the foremost computational software program used in scientific and engineering technical computing, including relevant features such as mathematical function libraries (such as the Bessel functions and their zeros for  $G_{r01}$  calculation), support for symbolic computation and numeric and symbolic tools for calculus, two- and three-dimensional data and function visualization tools, solvers for various differential equation types and a programming language supporting procedural, functional and object oriented constructs.

On the other hand, the choice for ANSYS is equally self-evident, given its pre-eminence as a numerical simulation and analysis tool, namely in terms of CFD and especially now that *CFX* and *Fluent* are both available within a common package. All relevant phenomena within the framework of the present discussion, such as fluid flow, heat sink terms, convection and radiation heat transfer between hot gases and solid surfaces or conduction heat transfer within a solid, could thus be studied.

Besides the conduction equations within the solids and the fundamental single-phase fluid flow Navier-Stokes equations employed in standard computational fluid dynamics software, the other models implemented in *CFX* are radiation and turbulence models.

Given the low optical thickness of the envisaged application, the selected radiation simulation technique was the Discrete Transfer model [Shah 1979]. This model is based on tracing the domain by multiple rays leaving from the bounding surfaces and depends upon the discretization of the equation of transfer along rays. The path along a ray is discretized by using the sections formed from breaking the path at element boundaries and the physical quantities in each element are assumed to be uniform. These rays have to be traced through the domain in the same way that the photons would be tracked in the Monte Carlo model, rendering the model description for both Monte Carlo and Discrete Transfer models more or less identical. For the results to be accurate the elements must be chosen so that the radiation field is reasonably homogeneous inside them. This means, for example, that they must be small enough that the scattering optical depth is less than unity across each element. The Discrete Transfer model was found to be more computationally efficient than the Monte Carlo technique and was thus used.

Regarding turbulence, one of the most prominent turbulence models, the  $k$ - $\varepsilon$  ( $k$ -epsilon) model, has been implemented in most general purpose CFD codes and is considered to be the industry standard model. It uses Reynolds Averaged Navier-Stokes equations and has proven to be stable and numerically robust and has a well established regime of predictive capability. For general purpose simulations, the  $k$ - $\varepsilon$  model offers a good compromise in terms of accuracy and robustness.

Within *CFX*, the  $k$ - $\varepsilon$  turbulence model uses the scalable wall-function approach to improve robustness and accuracy when the near-wall mesh is very fine. The scalable wall functions allow solution on arbitrarily fine near wall grids, which is a significant improvement over standard wall functions.

The wall function method uses empirical formulas that impose suitable conditions near to the wall without resolving the boundary layer, thus saving computational resources. All turbulence models in *CFX* are suitable for a wall function method. Scalable wall functions overcome one of the major drawbacks of the standard wall function approach in that they can be applied on arbitrarily fine meshes. If the boundary layer is not fully resolved, the logarithmic wall function approximation to model the boundary layer is relied upon without affecting the validity of the scalable

wall function approach. If the details of the boundary layer are not sought then it may not be worth fully resolving it.

All simulations and calculations were carried out on a computer equipped with an Intel Core i7 processor at 2.93 GHz clock frequency and 4 MB of RAM, on a Windows 7 64-bit operating system.

Once possible approaches to the problem at hand are identified and reasonable assumptions and simplifications are made, the various options can be put to the test through an incrementally more detailed procedure.

The analysis of the various possible Biot numbers indicates that a radial one-dimensional approach is reasonable given the plate's low thermal gradients along its thickness, greatly simplifying the formulation of the problem both for Green's functions and finite differences.

As mentioned earlier, a comparison of results with equivalent CFD simulations was always intended as means of validating their accuracy. Implied is also the comparison between both of the approaches discussed before, if only to rule out the use of one in detriment of the other if large discrepancies are verified or if significant differences in computational effort become apparent.

A one-dimensional finite differences approach to the problem takes the form of a radial problem where a single element is considered along the plate thickness (*i.e.* the  $z$  direction) and with the same height as the plate itself. The one-dimensional, radial nature of the problem leads to thinking of the elements as a succession of annular regions and setting  $\Delta\varphi = 2\pi$ , which leads to an isotropic behaviour as far as the angular coordinate is concerned, the question of how many elements to consider in the radial direction remaining.

Convective and radiative boundaries are treated as thermal resistances, with the temperature imposed by an external refrigeration system specified on the outermost node. Generation/sink terms are considered into the  $q_i$  term of the finite difference formulation but, as discussed earlier, the plate's low thickness enables the treatment of heat removed from the element in the holes of the perforated pattern in a convective resistance term where it is considered along with the convection on the element's (and

thus the plate's) windward face. The discussion above retains the possibility of using a volumetric sink term and the finite difference code developed for simulation purposes (see Appendix A) can be readily adapted to take into account a variable sink term, which indeed remains built into the formulation (albeit as a constant) and will be used in the first simple simulations, where various heat sink terms will be considered for comparison with the GF and CFD approaches.

These initial simulations are intended to gain confidence in the approaches in situations where anomalous results would be sufficiently clear to stand out and simple to analyze. The relative merits of the possible approaches can also be compared with ease and decisions regarding their implementation taken with more confidence.

Regarding the use of the GF approach in a one-dimensional radial approach with an imposed temperature  $T_{\text{ext}}$  on the outer radius  $a$ , the aforementioned one-dimensional  $G_{R01}$  function is necessary, that is:

$$G_{R01}(r, t | r', \tau) = \frac{1}{\pi a^2} \sum_{i=1}^{\infty} e^{-\beta_i^2 \alpha(t-\tau)/a^2} \frac{J_0(\beta_i r'/a) J_0(\beta_i r/a)}{J_1^2(\beta_i)}, \quad (2.51)$$

where  $J_0$  and  $J_1$  are Bessel functions of the first kind. Note that the formulation would be written in the same manner if a long cylinder where the effect of conditions on its extremities would be insignificant was considered. This function is inserted into the GFSE (Equation 2.14) in the form:

$$\begin{aligned} T(r, t) = & \int_{r'=0}^a G_{R01}(r, t | r', 0) F(r', 0) 2\pi r' dr' \\ & + \frac{\alpha}{k} \int_{\tau=0}^t \int_{r'=0}^a G_{R01}(r, t | r', 0) g(r', \tau) 2\pi r' dr' d\tau \\ & - \alpha \int_{\tau=0}^t T_{\text{ext}} \left. \frac{\partial G_{R01}}{\partial n'} \right|_{r'=a} 2\pi a d\tau \end{aligned} \quad (2.52)$$

If a uniform initial temperature field  $T_i$  is assumed, the first integral in Equation 2.52 becomes:

$$T_i \int_{r'=0}^a G_{R01}(r, t | r', 0) 2\pi r' dr' . \quad (2.53)$$

Likewise, for a uniform generation/sink term  $g_i$ , the second integral in Equation 2.52 can be written as:

$$g_i \frac{\alpha}{k} \int_{\tau=0}^t \int_{r'=0}^a G_{R01}(r, t | r', 0) 2\pi r' dr' d\tau . \quad (2.54)$$

The derivative of  $G_{R01}$  is:

$$\left. \frac{\partial G_{R01}}{\partial n'} \right|_{r'=a} = \frac{1}{\pi a^3} \sum_{i=1}^{\infty} e^{-\beta_i^2 \alpha(t-\tau)/a^2} \frac{\beta_i J_0(\beta_i r/a)}{J_1(\beta_i)}, \quad (2.55)$$

so that the GFSE becomes:

$$\begin{aligned} T(r, t) = & \frac{1}{\pi a^2} \int_{r'=0}^a G_{R01} \sum_{i=1}^{\infty} e^{-\beta_i^2 \alpha(t-\tau)/a^2} \frac{J_0(\beta_i r'/a) J_0(\beta_i r/a)}{J_1^2(\beta_i)} F(r', 0) 2\pi r' dr' \\ & + \frac{\alpha}{k} \frac{1}{\pi a^2} \int_{\tau=0}^t \int_{r'=0}^a G_{R01} \sum_{i=1}^{\infty} e^{-\beta_i^2 \alpha(t-\tau)/a^2} \frac{J_0(\beta_i r'/a) J_0(\beta_i r/a)}{J_1^2(\beta_i)} g(r', \tau) 2\pi r' dr' d\tau \\ & - \alpha T_{\text{ext}} \frac{1}{\pi a^3} \int_{\tau=0}^t \sum_{i=1}^{\infty} e^{-\beta_i^2 \alpha(t-\tau)/a^2} \frac{\beta_i J_0(\beta_i r/a)}{J_1(\beta_i)} 2\pi a d\tau \end{aligned} \quad (2.56)$$

As mentioned before, the implementation of the GFSE in this form can be problematic due to numerical convergence issues arising from the non-homogeneous  $T_{\text{ext}}$  boundary condition imposed on the outer diameter, so as suggested in references. Thus, an alternative solution was tested, where the contribution of the non-homogeneous boundary, *i.e.* the third term on the second member of Equation 2.56, is given as [Cole *et al.* 2010]:



$$T_{\text{ext}} \left( 1 - \frac{1}{\pi a^2} \right) \int_{r'=0}^a \sum_{i=1}^{\infty} e^{-\beta_i^2 \alpha(t-\tau)/a^2} \frac{J_0(\beta_i r'/a) J_0(\beta_i r/a)}{J_1^2(\beta_i)} 2\pi r' dr'. \quad (2.57)$$

A converged solution employing fewer than 50 terms in the series was found using the alternative solution, while for 1000 terms the slower version employing the non-homogeneous condition still had not converged. The alternative solution was therefore employed in the following calculations.

A simple one-dimensional radial case can thus be studied using both the GF formulation and the finite difference method, and the same study can be easily implemented in CFD software, with all the necessary flexibility in terms of geometry creation and boundary condition specification, as illustrated in Figure 2.8.

Figure 2.9 illustrates one of the reasons of the choice of *Mathematica* as the software for implementing Green's functions. The ease of specification of integrals, sums and Bessel functions necessary to the calculations is readily apparent.

As a starting point for the comparative study, a simple radial conduction case was considered, with adiabatic tops as far as the thin plate is concerned, no nodal balances due to convection or radiation having to be performed in finite differences and no need to perform updating procedures discussed earlier and summarized in Figure 2.1 needing to be considered for the GF solution. For simplicity, no variations in material properties were considered, although this will not be the case later. Properties were assumed to be those of stainless steel at ambient temperatures, in all three methods.

From the variety of tests carried out, two are described and their conditions summarized in Table 2.5. As discussed earlier, the negative heat generation term can be thought of as heat sink that will lead to an amount of heat to be removed from the plate by convection due to the temperature difference between the transpiration airflow and the perforated pattern, but that the magnitude of the temperatures in the plate are ultimately dictated not only by convection but also by the radiative interaction between the sensing element's surface and its hot surroundings, via the radiative source's area and emissivity and the element's own reflectivity, emissivity and transmissivity.

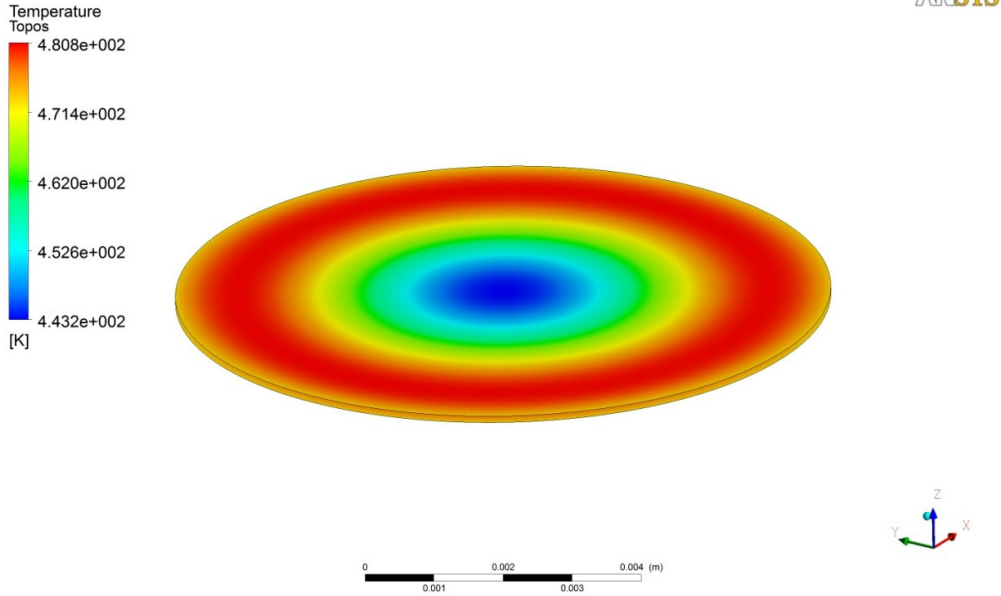


Figure 2.8 – ANSYS CFX implementation of radial transient heat conduction in a thin plate.

```

Clear[nLim, β, α, a, τ, t, G, k, initial, sink, Ta, gLi, gL, dgLra, dgLra, templ, temp2]
nLim = 500;
β[n_] = BesselJZero[0, n];
α[n_] = BesselJ[1, β[n]];
a = 0.005;
τ = 0;
t = τ;
G = 4 * 10-6;
k = 1;
initial = 273;
sink = 0;
Ta = 373;

gLi[xlinha_] := 1 / (Pi * a2) * Sum[ e-(β[n])2 * a * t / a2 * BesselJ[0, β[n] * xlinha] * BesselJ[0, β[n] * x] / (α[n]2], {n, 1, nLim}

gL[xlinha_, τ_] := 1 / (Pi * a2) * Sum[ e-(β[n])2 * a * (t - τ) / a2 * BesselJ[0, β[n] * xlinha] * BesselJ[0, β[n] * x] / (α[n]2], {n, 1, nLim}

dgLra[xlinha_] := 1 / (Pi * a2) * Sum[ e-(β[n])2 * a * t / a2 * BesselJ[0, β[n] * xlinha] * BesselJ[0, β[n] * x] / (α[n]2], {n, 1, nLim}

templ[t_] = ∫0a gLi[xlinha] * initial * 2 * Pi * xlinha dxlinha - G / k * ∫0t ( ∫0a gL[xlinha, τ] * sink * 2 * Pi * xlinha dxlinha ) dτ - Ta * ∫0a dgLra[xlinha] * 2 * Pi * xlinha dxlinha;

Plot[templ[t], {t, 0, 20}, AxesOrigin -> {0, 270}, GridLines -> Automatic, GridLinesStyle -> Directive[Orange, Dashed]]
sdata = Table[templ[i], {i, 20}]
ListPlot[sdata, PlotStyle -> {PointSize[Medium], Red}]
templ[20]

G * dgLra[τ_] = 1 / (Pi * a3) * Sum[ e-(β[n])2 * a * (t - τ) / a2 * β[n] * BesselJ[0, β[n] * x] / α[n], {n, 1, nLim}

temp2[t_] = ∫0a gLi[xlinha] * initial * 2 * Pi * xlinha dxlinha - G / k * ∫0t ( ∫0a gL[xlinha, τ] * sink * 2 * Pi * xlinha dxlinha ) dτ - (-Ta) * G * ∫0t dgLra[τ] * 2 * Pi * a dτ + G

```

Figure 2.9 – Mathematica implementation of the R01 Green's function.

**Table 2.5** – One-dimensional initial tests parameters.

Case	1	2
Initial Temperature [K]	273	1273
Outer Radius Temperature [K]	473	1273
Heat Generation [ $\text{Wm}^{-3}$ ]	$500 \times 10^6$	$-250 \times 10^6$

Transient temperature curves at the centre of the plate (the region where the thermocouple will be installed in the prototype) were determined along with radial temperature distributions as a function of time at several timesteps. Regarding the implementation of GF, this was done by plotting the  $T(r,t)$  distribution both as a function of radius  $r$  and time  $t$ .

Radial temperature distributions in the plate for Case 1 (see Table 2.5) obtained using GFSE are shown in Figures 2.10 for times 0.2, 0.5 and 1 s, as well as for fully converged steady-state conditions. Shown in Figures 2.11 to 2.13 are comparisons of values calculated by all three methods at the same instants, while Figure 2.14 shows the transient temperature variation at the centre of the plate calculated by the three methods. Figures 2.15 to 2.19 illustrate the same phenomena for Case 2 (see Table 2.5).

All graphs illustrate the very small differences observed between any of the three approaches, and these results are from simulations obtained after mesh refinement procedures were carried out both in *CFX* and for finite differences on one hand, and an increase in the number of terms in the sums of the GFSE was found not to have a significant impact on result, on the other.

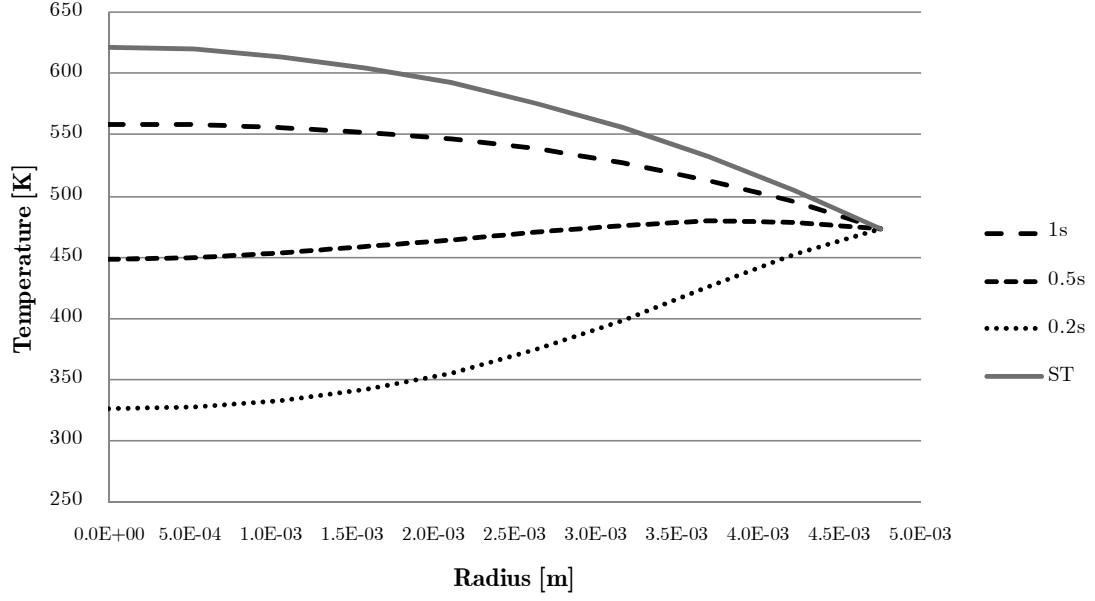


**Figure 2.10** – Radial temperature profiles using GFSE for Case 1 (see Table 2.5).

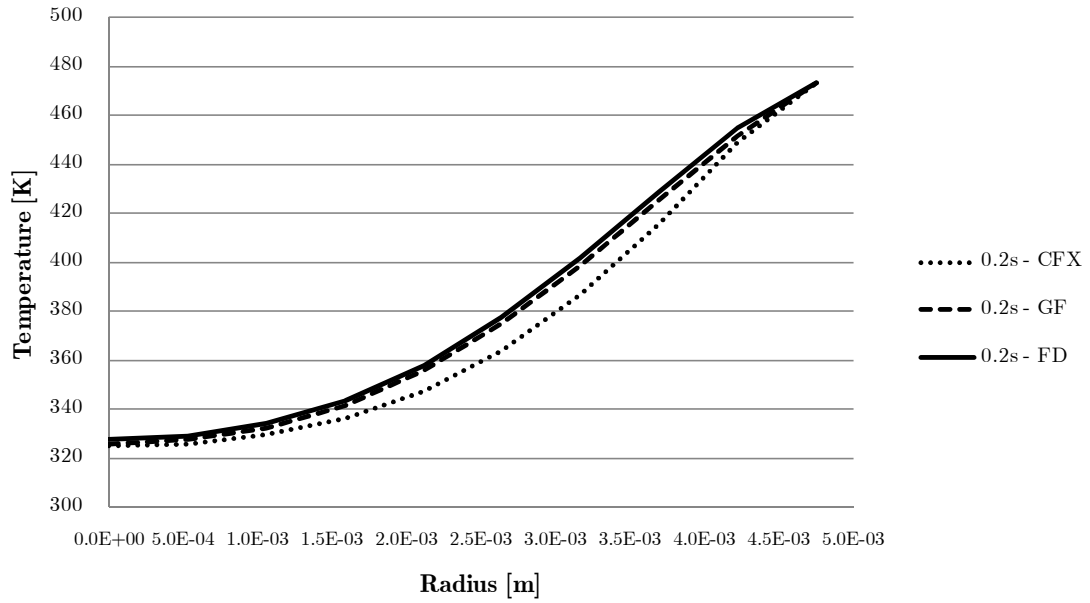


**Figure 2.11** – Comparison of calculated temperatures at  $t = 0.2$  s for Case 1 (see Table 2.5).

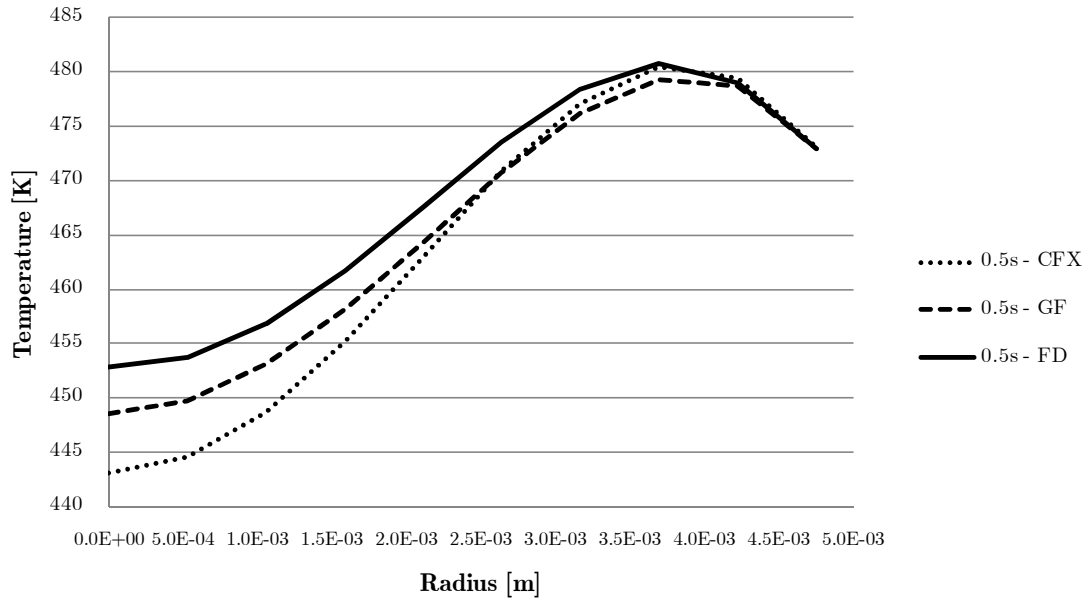


**Figure 2.12** – Comparison of calculated temperatures at  $t = 0.5$  s for Case 1 (see Table 2.5).

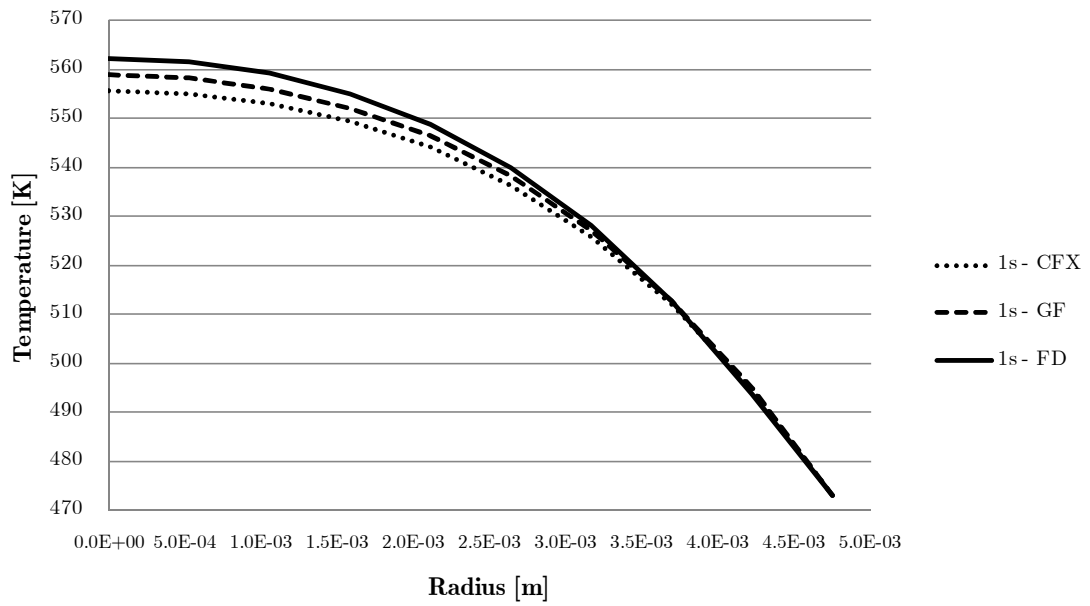


**Figure 2.13** – Comparison of calculated temperatures at  $t = 1$  s for Case 1 (see Table 2.5).

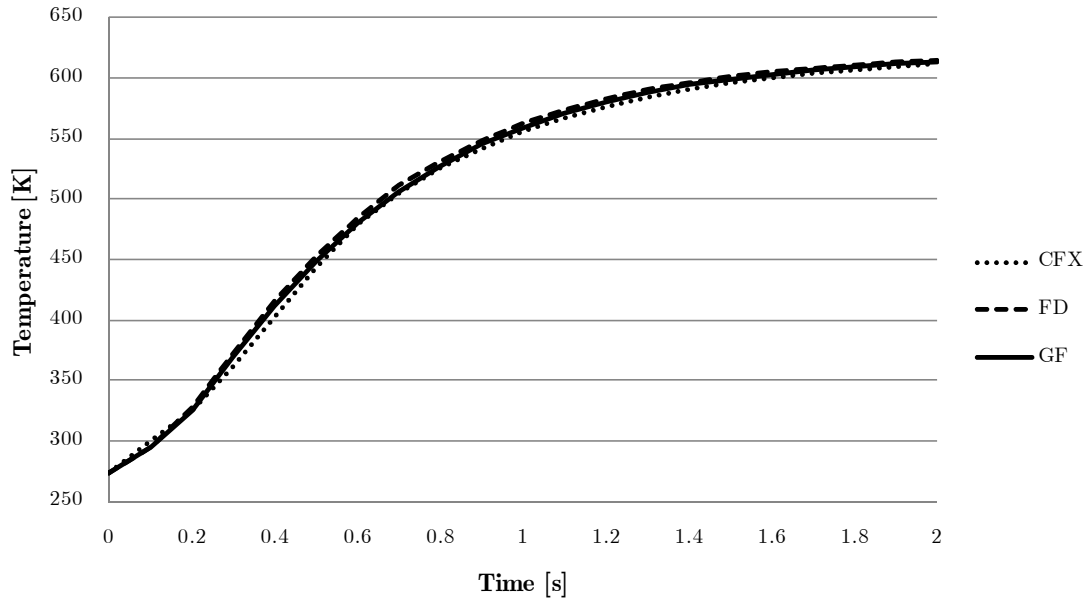


**Figure 2.14** – Transient temperature at the centre of the plate for Case 1 (see Table 2.5).

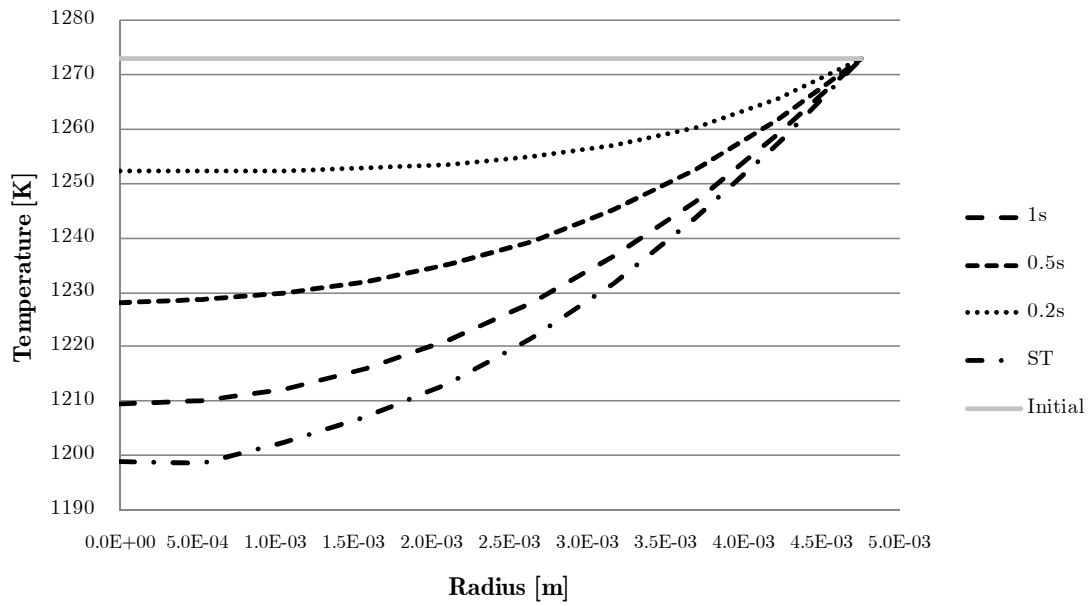


**Figure 2.15** – Radial temperature profiles using GFSE for Case 2 (see Table 2.5).

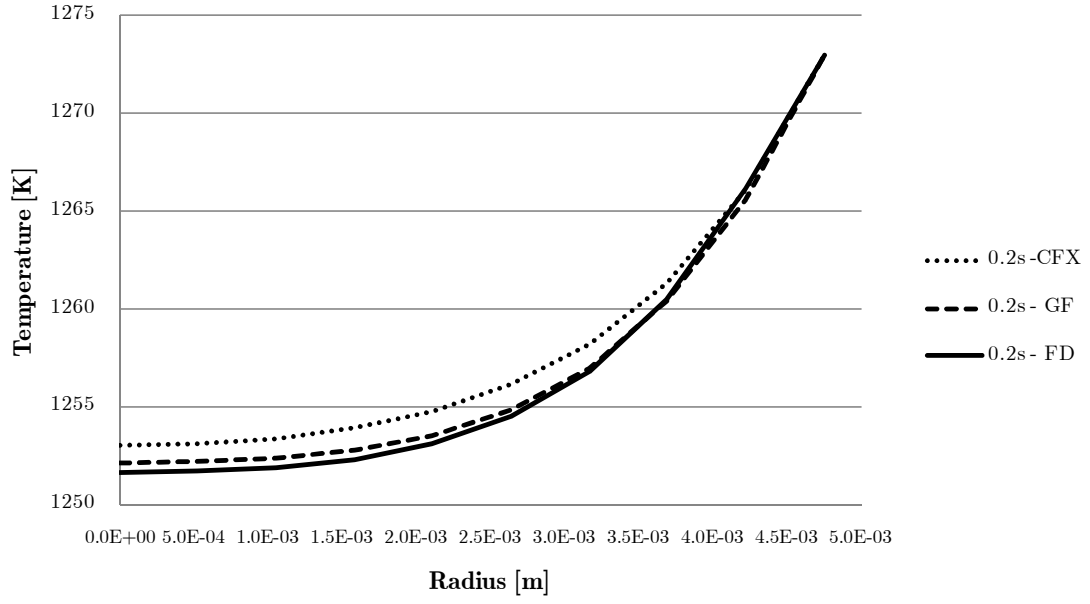


**Figure 2.16** – Comparison of calculated temperatures at  $t = 0.2$  s for Case 2 (see Table 2.5).

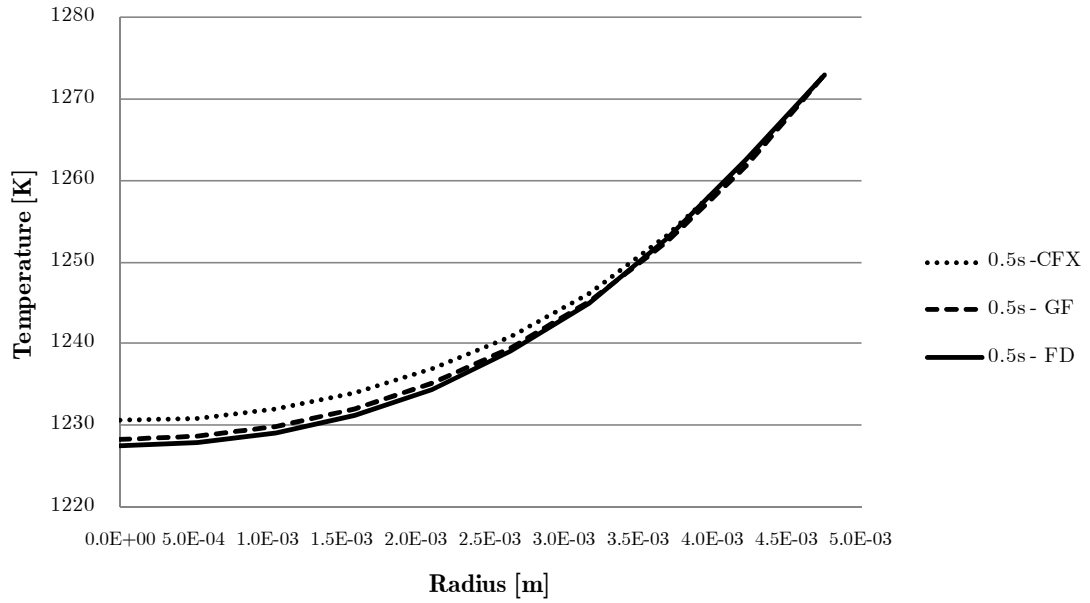


**Figure 2.17** – Comparison of calculated temperatures at  $t = 0.5$  s for Case 2 (see Table 2.5).

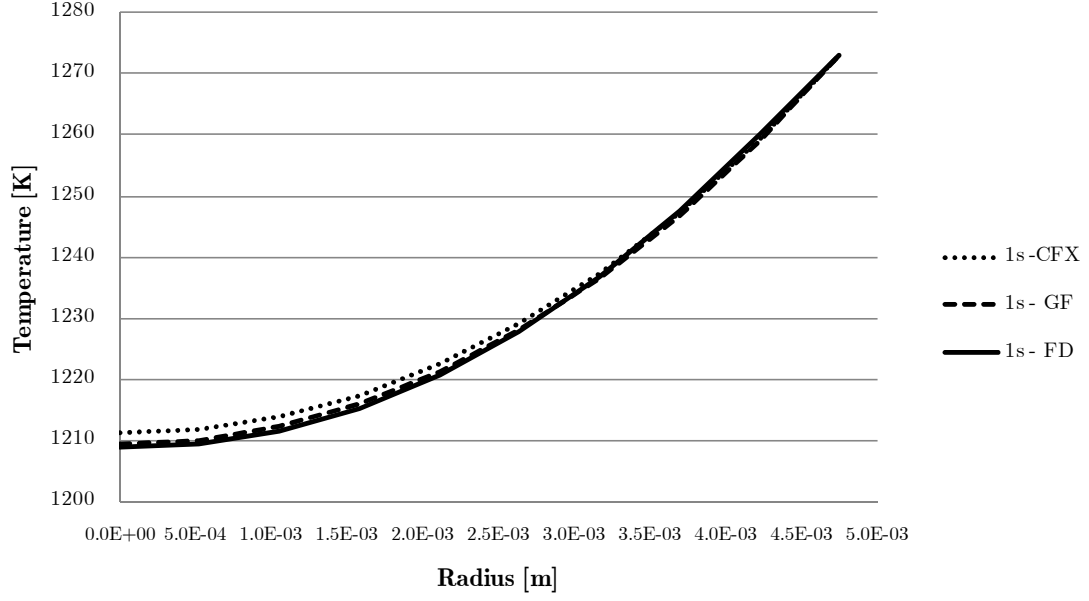


**Figure 2.18** – Comparison of calculated temperatures at  $t = 1$  s for Case 2 (see Table 2.5).

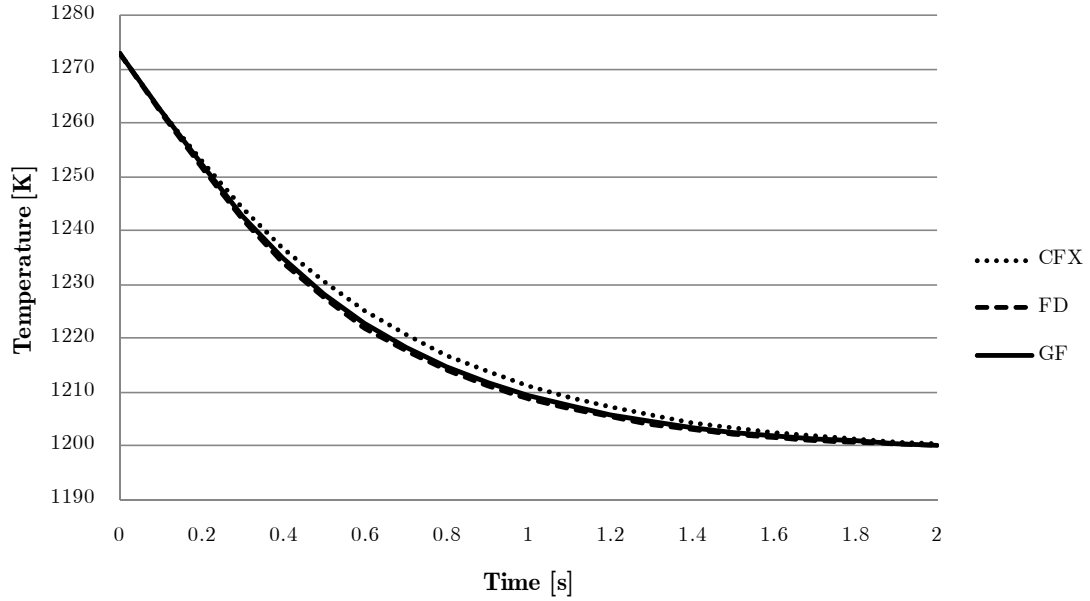


**Figure 2.19** – Transient temperature at the centre of the plate for Case 2 (see Table 2.5).

The results in Figures 2.10 to 2.19 illustrate the basic soundness of both developed models when compared with well-established commercial simulation software, at least for these fairly simple first tests. It should be noticed that in these simple simulations no energy balances are performed other than those (implied by the methods) of conduction along the radial coordinate, so none of the update procedures



summarized in Figure 2.1 need to be considered for the GF solution, the same happening as far as the imposition of fixed generation/sink terms is concerned. The question of comparing the accuracy of the GF method results with those of the finite differences approach makes sense and its usefulness cannot be questioned from the point of view of obtaining analytical insight into the problem. Its separation of effects caused by initial temperature fields, generation terms and boundary conditions is especially relevant. In these conditions, where the element's thermal behaviour is entirely dictated by the initial temperature field and constant boundary temperatures and generation terms, the GF method can be looked upon as an exact analytical solution where no manipulations are necessary besides the integrations and sums described in Equations 2.52 to 2.57. From this point of view and only for these particular conditions, the GF method can be regarded as an analytical benchmark for the numerical *CFX* and finite differences methods.

As mentioned earlier, the GF method may become inaccurate if variations in boundary conditions fail to be taken into account. In the absence of explicit analytical descriptions of these variations, some form of updating procedure is necessary. New analytical functions for all necessary parameters can be obtained at time intervals short enough to ensure that no relevant transient variations are missed, based on energy balances at a number of spatial points in space sufficient to ensure that spatial accuracy is retained. The functions obtained in this manner are used as the initial temperature fields, generation/sink terms and boundary conditions for the subsequent time iteration.

In so doing the GF method becomes a sort of hybrid, with an analytical basis but requiring iterative numerical procedures to recalculate boundary conditions in order to maintain its accuracy. Furthermore, most practical situations, and certainly the one under discussion in the present document, will need to take into account variations in the intensity of generation/sink terms and of boundary conditions such as the radiative and convective exchanges with surroundings, even if the overall system is one-dimensional along its radius, as assumed here.

Numerical methods such as finite differences or finite elements are intrinsically iterative (even in steady-state formulations and, inherently more so, in transient approaches) and their formulation explicitly considers the diversity of heat transfer

modes that can take place at the boundaries as discussed earlier for finite differences, where various resistance terms were defined for each phenomenon.

Although elegant in formal terms, computationally powerful in some situations and always useful as a fully analytical approach, the iterative procedure for GF is less interesting than the inherently iterative transient finite differences approach, which thus becomes more economical in computational terms, if less compact in the description of the problem when compared with an analytical approach.

From the point of view taken in this document, GFSE is first and foremost a powerful analytical tool that in this particular case is less flexible and more cumbersome to implement than an intrinsically numerical and iterative finite differences approach. The latter method will therefore be used in more detailed comparisons with the commercial CFD software. These will consider the actual geometry of the components, namely its perforated pattern, by relying on the relationships obtained above for convection heat transfer coefficients as a function of transpiration airflows, as well as on the correction factors for convective and radiative heat transfer areas and element volumes. The variations of material properties with temperature will also be considered.

The two purely numerical methods were tested for situations where radiation and convection are present, in order to compare results from the purpose-developed finite difference model with those of the commercial software. The same thin plate as before was used, but with air at a given temperature on one side, and surroundings with a predefined temperature and no convection on the other, allowing the study of conditions more closely akin to those of the perforated plate to be studied subsequently. Purely convective and radiative boundaries were first studied separately and later combined, and good concordance between the results obtained from *CFX* and finite differences was apparent.

The transient transpiration principle to be used in practice was also tested by using results from simulations at a given transpiration airflow level as initial values for subsequent simulations where the airflow is diminished or eliminated. This process only requires the necessary adjustments in terms of boundary conditions, especially as far as

the convection coefficient is concerned, since no significant airflow will be considered and values for natural convection can be used.

A final test was performed before moving on to the simulation of the full scale system, which can be thought of as a simpler version of the perforated plate simulations that must later be studied.

In terms of *CFX*, the setup is merely a small circular section of the perforated plate with the same perforation patterns as the definitive plate and similar to those discussed above. This plate is exposed to radiation from the furnace on one side while being cooled by a transpiration airflow crossing it from the other, with an imposed temperature at the outer radius. A comparison is intended with the numerical model relying on finite differences that was developed and discussed above, including the correlations for the convection coefficient and the area correction factors. While not expected to be as accurate as the CFD simulation, since it does not take into account all the complex behaviours, such as turbulence, that occur in the interaction between the perforated plate and both its hot surroundings and its cooling transpiration airflow, the model is nevertheless expected to provide reasonable values for the transient temperature fields within the element. This simplified setup also allows for much faster simulations. Temperature results are shown in Figure 2.20.

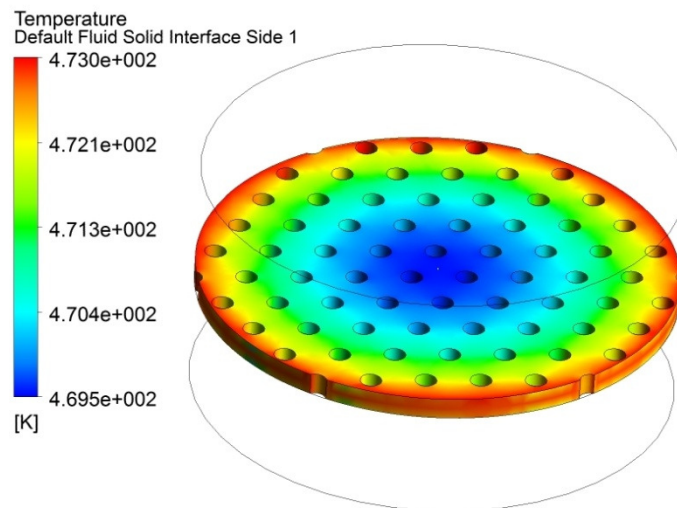


**Figure 2.20** – *CFX* setup of the small perforated section and illustration of the resulting temperature field.

As before, radial temperature profiles at various timesteps were obtained, for various radiation source temperatures and several different mass flows. An example is illustrated in Figures 2.21 and 2.22 for a mass flow of  $0.001 \text{ kgs}^{-1}$  at 298 K, a radiative source at 1023 K and an imposed temperature at the outer radius of 473 K, which is also the plate uniform initial temperature.

An interesting feature of the *CFX* curves is the slight “wobble” that occurs in the radial temperature profiles and that is due to the fact that the curve along the radial direction where values were sampled passes close to the holes, although not intersecting them. This effect is obviously absent from the finite differences curves.

The curve behaviours are similar and a comparison of the scales of the graphs of Figures 2.21 and 2.22 shows that calculated values for the two methods differ in less than 10% in all cases. Figure 2.23 likewise illustrates the transient temperature curves at the centre of the plate, with 10% error bars placed on the finite differences results curve emphasizing the difference between calculated values.

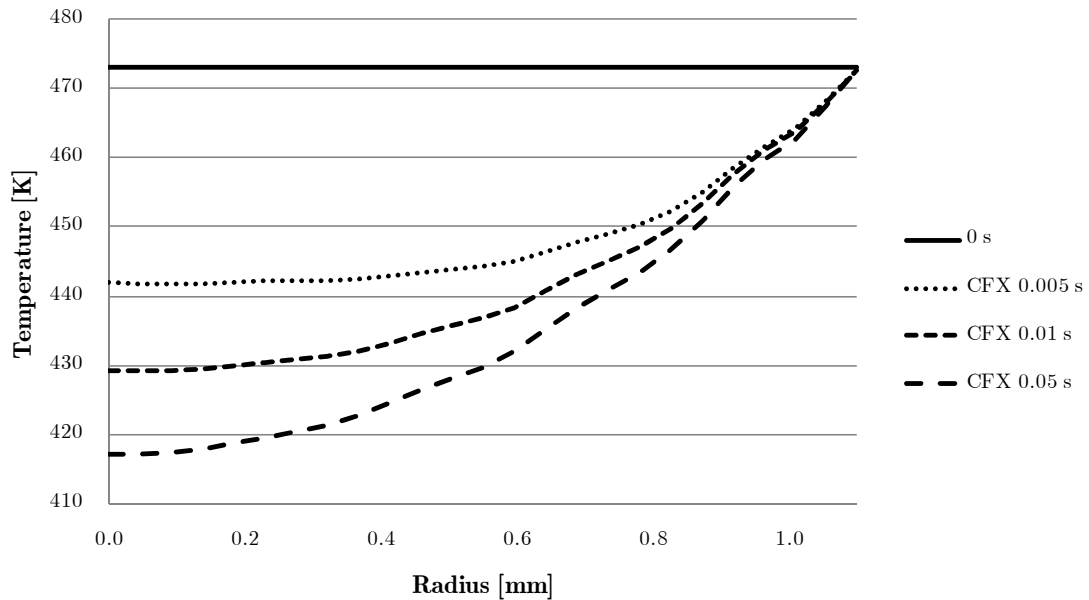


**Figure 2.21** – Radial temperature profiles using *CFX*.

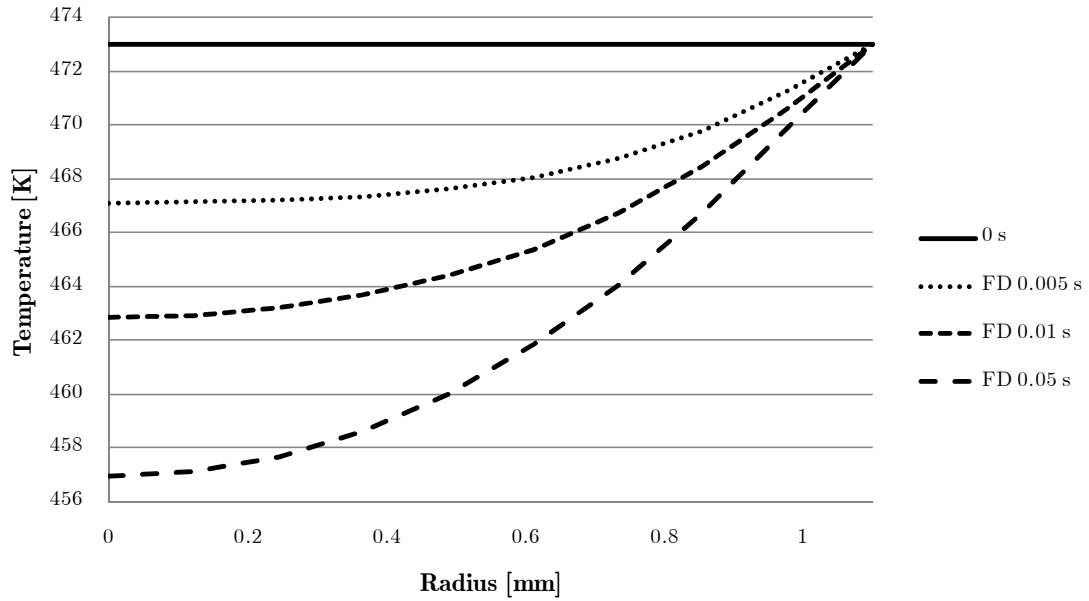


**Figure 2.22** – Radial temperature profiles using finite differences.

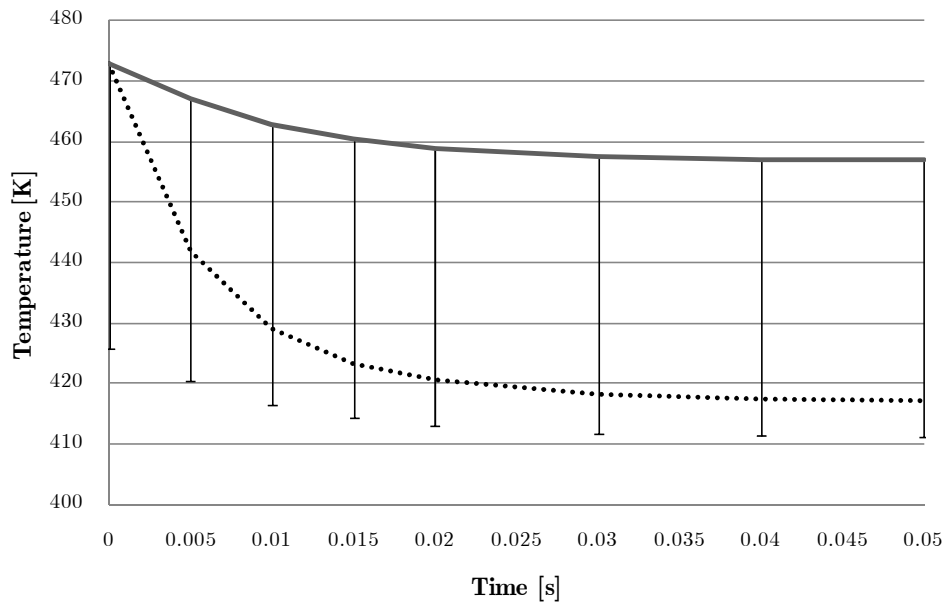


**Figure 2.23** – Transient temperatures at the centre of the plate.

The results from these studies show that the finite differences model is able to process the same physical problem as the commercial CFD software and that the correlation obtained for the convection coefficient provides accurate values. The CFD software does have a much greater flexibility in handling more complex geometries, and implements more detailed physical models that better describe the overall thermal and

fluid dynamics behaviour of the system, rendering it more attractive for subsequent simulations.

Differences in temperature values calculated with each model were typically between 5 and 8%, no value greater than 10% being observed which, in itself, is a rather satisfactory value considering that the finite differences model is much less powerful than a full-scale commercial CFD software.

While the pure conduction tests discussed when comparing the GF, finite differences and *CFX* did not present particular difficulties regarding the presence of non-linear phenomena such as radiation, differences were to be expected for the simulation where their occurrence might be problematic and lead to deviations in comparative results. The comparison of an explicit method (such as finite differences as implemented here) with the implicit methods on which *CFX* relies, compounded by local heterogeneities such as the microperforated pattern, was expected to lead to even greater differences. From this viewpoint, the obtained results are satisfactory given the simplicity of the approach and the assumptions and simplifications made.

Insight about the various occurring physical phenomena was nevertheless gained from the development and testing of the GF and finite differences models and confidence in the results of the CFD software was enhanced by the comparisons that were carried out, building on previous experience with such software.

## 2.5 Concluding Remarks

The present chapter was devoted to the description of the instrument's working principle and to possible formulations for the study of the sensing element's behaviour.

The problem requirements were first of all discussed and subsequent simplifications were implemented as necessary and once their reasonability was established. Among these requirements, the need to take into account a non-homogeneous transient problem was foremost, especially given the presence of the interaction between a perforated plate being heated by radiation and a colder transpiration airflow crossing the pattern of holes, leading to the analytical treatment of such an interaction as a heat sink term.

The GF method was recognized as being well suited to the task of providing an analytical solution to the heat diffusion equation within the three-dimensional cylindrical system embodied by the sensor element, and a proper methodology was established in order to implement the GF method and solve the conduction problem in order to obtain temperature values for all locations and instants of interest, for a variety of cases. Concurrently, a finite differences approach was also found to be adequate for the same purpose, with added benefits in terms of implementation in conditions where boundary conditions require updating in space and time.

In order to describe the phenomena that needed to be integrated into the model, relationships were obtained for convection heat transfer coefficients as a function of transpiration airflows, together with correction factors intended to take into account the perforation parameters of the sensing element. Given the latter's low thickness and after studying the areas involved in convective and radiative heat transfer processes, a decision was taken to treat the heat transfer in the holes together with convection in the windward face of the plate. Nevertheless, the formulation necessary to deal with a volumetric generation/sink term was obtained and discussed, and remains built into the formulation for use in a different set of assumptions if necessary.

A comparison of results of both approaches with those of equivalent CFD simulations of the same physical problems showed good approximation and simultaneously provided both increased confidence in the results provided by the GFSE and validation for the simulations to be carried out for dimensioning purposes using CFD software.

The use of the CFD software was always intended for design purposes, not only regarding the sensing element itself but especially when considering the overall instrument as a system consisting of various components, rather than merely as a sensing element. The methodologies proposed and discussed showed reduced simulation times and overall computational effort for the type of geometry of interest, parametric tests regarding physical parameters of the sensing element and operational conditions such as airflows can be conducted merely by adjusting unit cell parameters or relevant temperatures, airflows and convection coefficients using the developed correlations. Relevant information about the sensing element's behaviour regarding temperature

spatial distributions, transient variations or its time constant  $\tau$  for various conditions can thus be obtained at a fraction of the computational effort of CFD simulations.

Likewise, relevant phenomena such as those arising from the pulsed transpiration airflows to be employed in practice can be implemented with reasonable results at a fraction of the computational effort required for CFD simulations.

These numerical results, along with the insight gained into the physical processes at work within and around the sensing element, are felt to fully justify the effort that was put into the development of the analytical and numerical methods proposed, implemented and discussed in the present chapter. This is especially relevant regarding the finite differences approach that was extended with good results to a domain of application, *i.e.* the transient interaction between a transpiration airflow and a perforated plate exposed to convective and radiative boundary conditions that was not encountered in any bibliographical reference, although others unknown applications of the sort obviously cannot be ruled out.



## CHAPTER 3

# DIMENSIONING PROCEDURES AND PARAMETRIC STUDIES

The overall configuration of the system is studied, together with dimensional and operational parameters that influence sensor performance. Assumptions and simplifications made in the process of developing the analytical model are discussed, along with the instrument's dimensioning and design procedures, taking into account conclusions from the previous chapter and establishing the procedures necessary for carrying out various analytical and numerical parametric studies as far as relevant mass flow values, boundary layer control, compressibility and transmissivity in the microperforated plate, transient effects or the cooling system are concerned.

### 3.1 Introduction

The ultimate goal of the work described here is an instrument for the measurement of convective and radiative heat fluxes which would overcome drawbacks noted in conventional heat flux meters (or at least in existing transpiration radiometers such as the one from which the present work originated) by having several desirable advantages that cannot be found in conventional instruments, namely:

- A more compact configuration and a less complex system by the use of air cooling both in a microperforated low-thickness sensing element and in a porous holder/outer casing;
- A significantly reduced response time obtained through a lower overall thermal inertia and the implementation of the transient response analysis;
- An effective heat flux partitioning (*i.e.* splitting the total heat flux into the radiative and convective components thereof) achieved through a pulsed airflow operation mode.

The proposed sensing element is to have a much lower thermal inertia than those of earlier instruments and exhibit faster temperature variations in time, while being much more efficiently refrigerated, thus reducing cooling requirements. This makes the avoidance of excessive temperatures within the system much easier, renders using air cooling a viable option and has several interesting consequences, such as:

- Lesser refrigeration needs allow the use of a much less complicated and more compact refrigeration system when compared with conventional transpiration radiometers, which use water refrigeration systems that require more parts in more complex configurations and, consequently, added manufacturing, assembly and maintenance complexities;
- A faster response using an operational mode where transient behaviours are induced by variations in the transpiration airflow can be defined. It was proven earlier [Hit 2004, Martins *et al.* 2006a, Martins *et al.* 2006b] that the slope of the line tangent to the temperature response curve is directly proportional to the total heat flux received by a porous disc, making it unnecessary to “wait” for steady-state values and using the transient output of the radiometer to determine the incident heat flux. The necessary transient behaviour is induced by using a pulsed transpiration gas mass flow;
- The transient behaviour induced by using a pulsed transpiration gas mass flow may also enable the implementation of heat flux partitioning, since the airflow can be made subcritical for short time periods in order to measure the total heat flux rather than only the radiative component, temperature levels being nevertheless kept within acceptable levels. This ability has not been achieved by earlier instruments.

The proposed microperforated plate maintains established advantages of transpiration radiometers such as their protection from fouling by soot particles and their ability to withstand high temperature and heat flux environments, provided by the preservation of the air mass flow on which the transpiration radiometer principle is based

The pulsed operation principle dictates that the effect of the various mass flows to be considered must be described, especially as far as temperature fields within the disk, time responses and heat flux partitioning are concerned. Received heat fluxes were

proven to be directly proportional to the slope of the tangent to the temperature response curve, which in turn allows an anticipation of the instrument's steady-state values. The faster response of the proposed instrument enables its integration in strongly time-dependant systems, and its reduced bulk and weight are useful in systems where such restrictions may apply.

The main conceptual difficulty in the passage from the actual physical system to its analytical or numerical description is taking into account the microperforated pattern that underlies the transpiration radiometer principle, in order to evaluate the effect of the various mass flows that will cross the plate. This difficulty is evident in any kind of analytical approach, so that some simplifications had to be made. As described earlier, a description of the cooling effect of the airflow was achieved by treating it as a heat sink term integrated both in a Green's functions formulation and a finite difference scheme, used for the purpose of obtaining a solutions to the boundary value problem resulting from the physical conditions of the sensor, and comparisons with CFD simulations confirmed the soundness of the approach.

Treating the presence of a large number of small holes with variable physical conditions is not straightforward. As far as the use of CFD tools is concerned, numerous small features usually involve more geometrically complex models and typically require additional mesh refinements for adequate accuracy, and compromises must be reached regarding these requirements versus computational times and necessary computer resources. However, previous experience with CFD tools was extant and the comparisons made with GFSE and finite difference calculations described in the Chapter 2 justified their use for more detailed simulations, especially those intended to study features that could not be taken into account, as the microperforated pattern, or parts of the system that are not central to the discussion and that for that reason were not considered in the analytical model, such as the external refrigeration system.

Thus, much of the overall design relies both on standard fluid mechanics and heat transfer analytical tools, as well as on CFD. The selection of physical and operational parameters, as well as performance analysis of the proposed heat flux measurement instrument, also relies on CFD, along with various analytical principles described in detail below.

### 3.2 Proposed Configuration, Objectives and Approach

The proposed microperforated sensing element, central to the intended instrument performance, was discussed above and especially in Chapter 2 but must itself be analysed in terms of the temperature fields developed within it, not only when interacting with high-temperature environments and external cooling systems, but especially in interaction with various transpiration mass flows and taking into account phenomena such as gas compressibility and transmissivity to the incident radiation.

Decisions needed to be taken beforehand regarding the overall configuration of the instrument, especially concerning how necessary airflows are handled and the external refrigeration system's features and dimensioning. Given the stated objective of using a less cumbersome (both in terms of dimensions and complexity) solution than water cooling (which led to more parts in more complex configurations, with added manufacturing, assembly and maintenance complexity), compressed air is the most obvious alternative. Although any suitable cooling gas can be used, air is the most straightforward choice, considering its availability and cost effectiveness. Nevertheless, the question of how to make this airflow interact with the rest of the system remained. This was addressed by using a refrigeration airflow (separate from the aforementioned transpiration airflow) that interacts with a porous steel part that serves both as a sensing element holder and as an outer casing for the overall system. This porous part makes use of the large specific area (defined as the ratio between the surface area available for heat transfer and the volume) of the porous parts to effectively interact with the stream of cooling air and render a proper design and dimensioning process necessary.

Even if the airflows come from the same compressed air source or circuit, they must be somehow separated in order to adequately play their roles. This can be achieved by placing a solid component within the porous outer casing, that should be as thin as possible in order not to unduly increase overall thermal inertia while being sufficiently sturdy to withstand the pressures of the compressed air flows and the stresses of the welding process to which it will be subjected during prototype construction. This component can take the form of a hollow cone placed within the sensor casing, below the microperforated plate.

The porous holder must be placed atop and joined to a non-porous base that houses the refrigeration airflow tube and the conical component. The refrigeration airflow enters the non-porous base tangentially in order to provide it with a swirl component and therefore to increase its residence time in the space between the cone and the porous holder, when compared to a situation where its injection would be made along the part's revolution axis, *i.e.* parallel to the transpiration airflow. All joints between the porous holder, the non-porous base and the cone must necessarily be airtight and be achieved with welding or brazing.

Temperature measurements in the microperforated plate are made using a 0.25 mm diameter thermocouple that is passed inside the conical element through a sealed hole in its lower tube, and is then connected by laser welding to the centre of the microperforated plate using a slightly larger central hole for guidance. The plate is then attached (*e.g.* brazed) to the porous holder in order to guarantee air tightness around its rim. This assembly dispenses with moving parts.

Once the compressed air tubes are connected to supply lines and the thermocouple is connected to a data acquisition system, which also controls an electrovalve that regulates the pulsed transpiration airflow using the associated software, the instrument is ready to measure heat fluxes.

Illustrated in Figures 3.1 to 3.4 is the proposed overall configuration of the system (definition drawings of each of the various components). The dimensions that are shown were specified once the dimensioning procedures described in this chapter were complete and prospective providers for the parts were consulted, since some adjustments required by the manufacturing processes had to be made. An exploded and an assembly view are also provided in Figures 3.5 and 3.6 respectively.

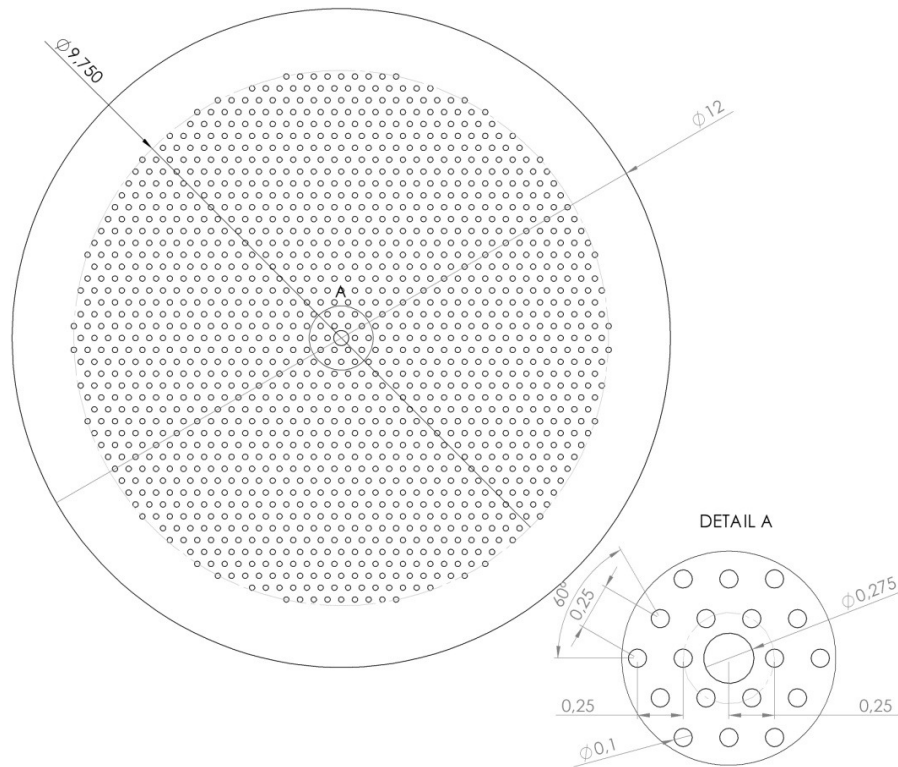


**Figure 3.1** – Microperforated plate definition drawing.

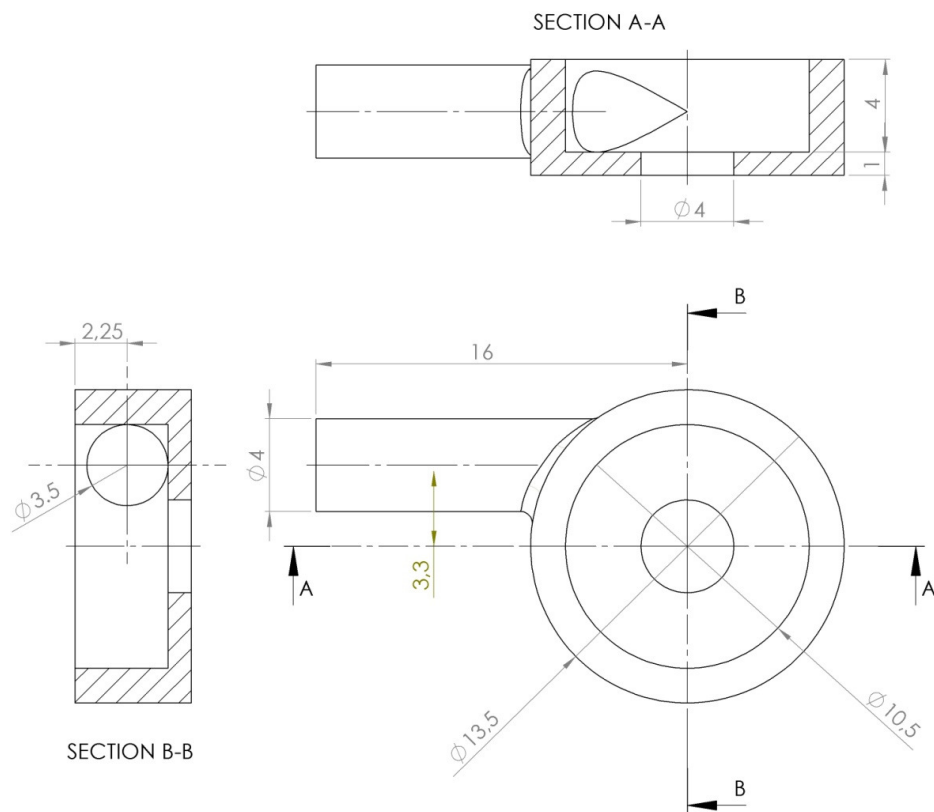


**Figure 3.2** – Non-porous base definition drawing.

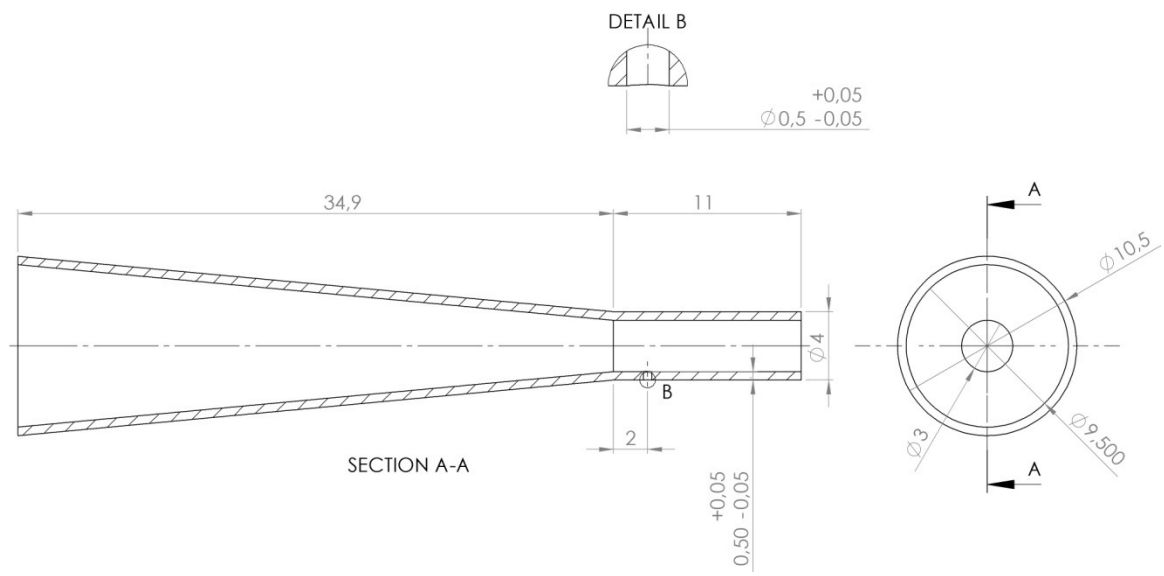


**Figure 3.3** – Cone definition drawing.

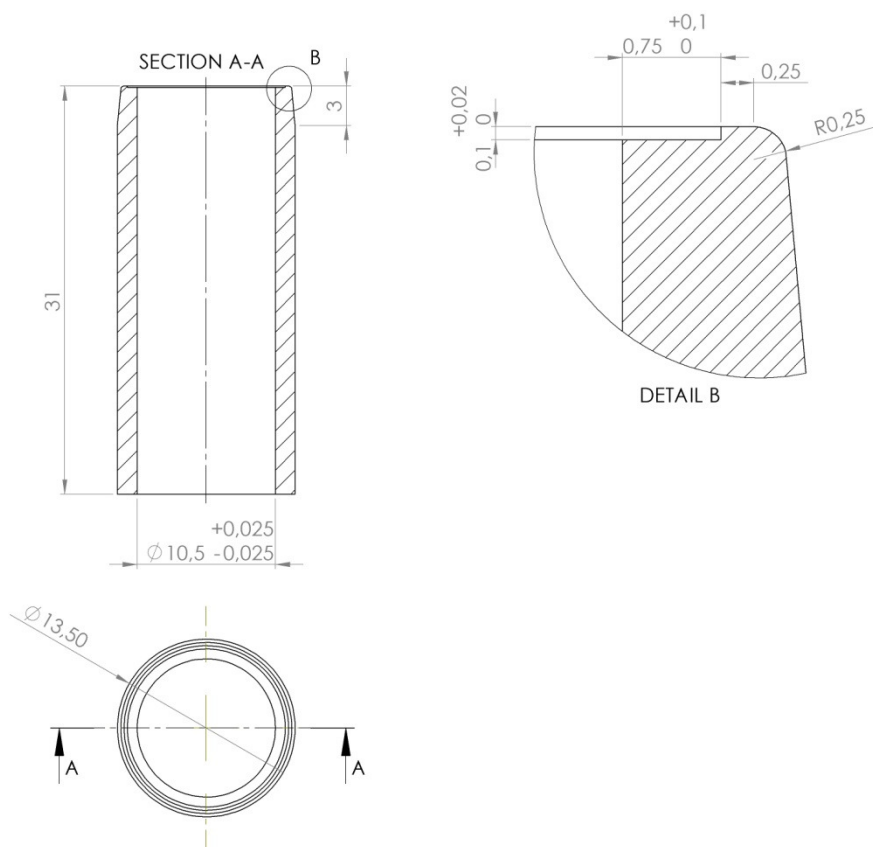


**Figure 3.4** – Porous holder definition drawing.

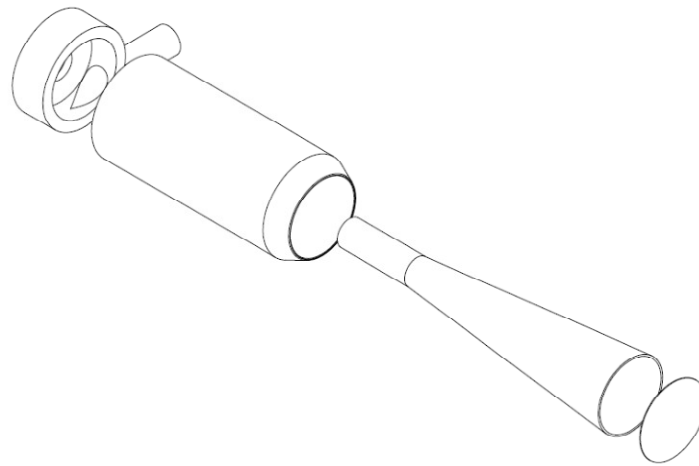


**Figure 3.5** – Exploded view of main prototype components.

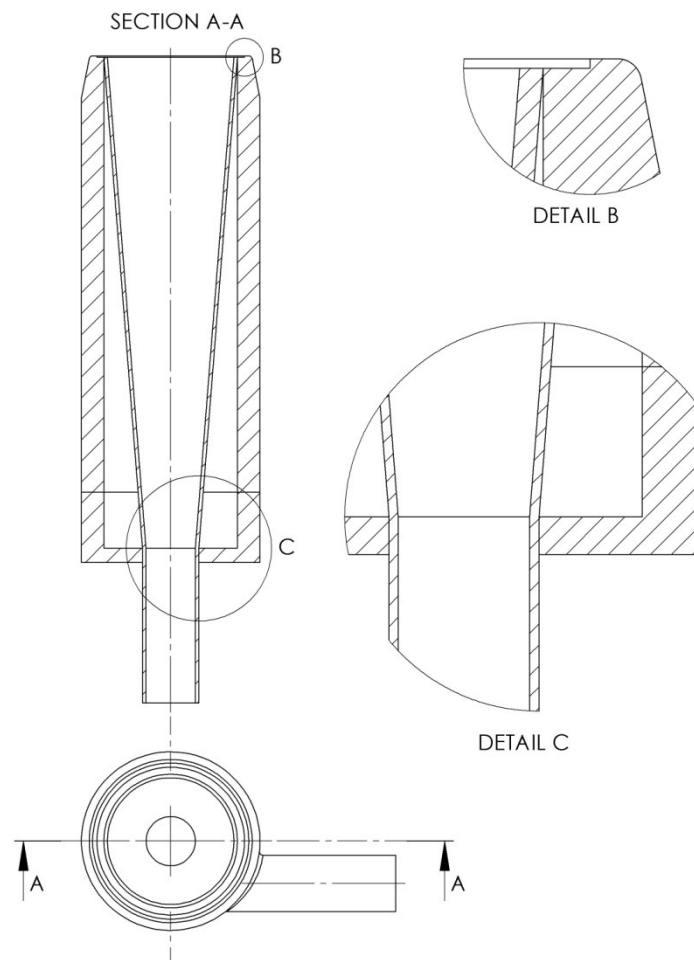


**Figure 3.6** – Prototype assembly.



In order to produce viable instrument prototypes, the plate's overall physical parameters, such as its diameter, thickness and material, must therefore be defined. Its perforated pattern must also be defined in terms of diameter, spacing and placement. Given the fact that the proposed instrument is essentially (despite all aforementioned differences with conventional versions) a transpiration heat flux meter, conditions for the implementation of the boundary layer blow-off principle must be ensured, as this requirement has a direct impact on the definition of a proper perforated pattern. This meant that analytical models that describe boundary layer blow-off for various situations were examined and used to determine necessary gas mass flows, regardless of particular features of the perforated plate.

Once the necessary compressed air mass flows are determined, the matter of passing them through a microperforated pattern also raises the question of knowing whether the considerable difference in diameter between the feed line tubes and the plate holes, along with pressure differences between both sides of the plate, can give rise to compressibility and choked flow conditions that can place an upper limit to the passable mass flow through each hole and therefore through the overall perforated pattern, that must be dimensioned accordingly.

However, the selection of perforated pattern parameters must consider one other phenomenon, namely a radiation transmissivity term that was absent in the sensing elements of earlier instruments because of their opacity. This led to the need to adequately describe and calculate the transmissivity of a perforated thin plate, to specify a maximum acceptable value (since it cannot be avoided) and to adjust the perforation parameters accordingly. Care must be taken to avoid possible undesirable effects such as extraordinary transmission phenomena. This makes necessary some further caution regarding the interaction between incident radiation (namely as far as its wavelength is concerned) and the holes of the microperforated pattern.

The procedures described above result in the definition of the geometric and dimensional features of the various system components, together with its physical properties. Nonetheless, other studies remain to be carried out, namely as far as operational parameters or transient effects are concerned. Parameters such as the magnitude of the transpiration and refrigeration airflows or external medium

temperatures, as well as their relationships with temperatures developed within the sensing element, must be carefully addressed.

For any given set of conditions in the high-temperature environment, considerable transpiration gas flows are required in order to provide enough refrigeration to keep temperature fields in the sensing element within acceptable limits and to lower surface temperatures, diminishing the magnitude of radial flows within the microperforated plate (overall temperatures being closer to the temperature imposed on the outer radius) and rendering the emission term much less significant. This principle was already applied to nullify these terms in energy balances for sensing elements of previous instruments [Martins 1998].

High gas flows also have other advantages such as a more effective deflection of incoming soot particles, while the lower temperatures place less severe constraints on the outer refrigeration system. In earlier transpiration instruments, large airflows were indispensable at all times in order to provide refrigeration, which meant that convection measurements were never performed because the airflow could not be interrupted, in order to impede the hot gases from making contact with the sensor surface. Typical airflows ranged from 10 to 60 SLPM (Standard Litres per Minute) while in the work described here significantly lower values are expected thanks to much-reduced refrigeration needs. In order to always be able to blow-off the boundary layer, this value is nevertheless strongly overdimensioned.

What happens within the sensing element when the pulsed operation results in subcritical mass flow values is also of particular relevance, given the transpiration airflow's refrigeration role. Care must be taken in order to ensure that excessive temperatures are not reached during those situations. Such transient effects must be studied and anticipated beforehand. This means that while the transpiration airflow must be known with precision in order to quantify its effect in terms of time-varying temperature fields in the sensing element and of boundary layer blow-off, the refrigeration airflow can, if necessary, be set at a maximum value, regardless of other considerations.

### 3.3 Dimensioning and Design Procedures

#### 3.3.1 *Basic Assumptions*

The proposed changes discussed earlier in terms of overall configuration, operation mode and physical features do not make reasonable a direct transposition of the specifications of components of earlier instruments. This does not mean that some items do not have similar dimensions between instruments, even if these can in some cases be somewhat arbitrarily imposed, the most obvious example probably being the sensing element's frontal area. The earlier instruments mentioned before used a sensing element with a diameter of 10 mm and a thickness of 4 mm [Martins 1998]. Besides allowing some form of comparison, this diameter results in a manageable part that allows for the intended reduction in both overall dimensions and thermal inertia, and was thus specified as a basic parameter.

As already mentioned, an example of application of low thickness microperforated plates was found in *espresso* machine filters that were around 0.1 mm in thickness. These samples showed adequate thermal behaviour and good mechanical resistance. Thus, the idea to use similar components for the instrument's sensing element was naturally considered. A survey of providers, manufacturing technologies and prices for obtaining the plates resulted in the selection of photo-etched rather than micro-machined components. This technique is very useful in obtaining the required components effectively but has the limitation that holes with diameters smaller than the plate thickness are extremely difficult to obtain, thus placing limits on hole diameter to plate thickness ratios.

All other component dimensions were thus specified using the referred diameter and thickness values as starting points, although some had to be subsequently slightly adjusted due either to the dimensioning procedures and numerical studies discussed below, or to limitations imposed by the various manufacturing processes. Some of these occurred while some components were already under production but no significant changes were required, the only noteworthy one being the change in effective diameter of the microperforated pattern that came about due to a need to increase the cone wall thickness when it was no longer possible to adjust the porous holder's inside diameter. This meant that the porous holder has an internal diameter of 10.5 mm, the cone wall

is 0.5 mm in thickness and thus has an internal diameter of 9.5 mm rather than the intended 10 mm. The microperforated pattern was extended to a diameter of 9.75 mm in order to ensure it covers as much area as possible by overlapping the top of the cone.

### ***3.3.2 Boundary Layer Control, Mass Flow Rate and Compressibility in the Microperforated Plate***

A central aspect of the proposed heat flux measurement method is the possibility of enabling an effective heat flux partitioning which, as discussed earlier, requires the elimination of the boundary layer on top of the sensing element. The transpiration cooling principle of blowing a gas stream through a porous wall is especially useful bearing in mind that the perforated plate is merely a particularly well-ordered porous medium. If the blowing gas mass flow is sufficiently high, the aerodynamic and thermal boundary layers developing on the porous surface are destroyed and the convective heat transfer from the main stream to the considered surface is eliminated.

The effect of a transpiration cross stream on the Nusselt number for a laminar boundary layer developing on porous wall is well established, relationships for the limiting conditions of a main stream parallel and perpendicular to a flat plate [Hartnett and Eckert 1957], as well as for turbulent boundary layers being available [Kutateladze and Leontiev 1964, Leontiev 1966]. Subsequent work focused mainly on empirical and numerical studies, with a particular emphasis on the latter [Tedeschi *et al.* 1995, Franca *et al.* 1998].

The critical transpiration gas (CTG) mass flow rate required to promote the destruction of the boundary layer over the porous disc is a basic parameter to be defined for the proposed heat flux sensor. In the definition of the CTG mass flow rate it is necessary to consider the laminar or turbulent nature of the mainstream flow (*i.e.* on the furnace side), its velocity and temperature, the density  $\psi$  between the TG and the main stream gas, as well as the local geometry. The local Reynolds number  $Re_x$  defines the boundary layer nature, while the density difference is defined mainly by temperature differences, the influence of the geometry being introduced through an appropriated choice of Nusselt number correlation.

A variety of expressions is available for mass flows (typically given in  $\text{kg s}^{-1}$ ) or mass fluxes (in  $\text{kg s}^{-1}\text{m}^{-2}$ ) in various situations, namely laminar or turbulent flows over flat plates or stagnation situations. A comparative study of these various transpiration mass flow or flux relationships is available, with some very useful conclusions [Martins 1998]. This comparison was conducted for the purpose of determining not only the critical blow-off mass flow or flux for any given situation, but also in order to study its sensitivity to various parameters. For the blow-off a laminar boundary layer, the following relationship is valid for  $0.7 < \text{Pr} < 1$  [Hartnett and Eckert 1957]:

$$j_{\text{w,cr}} = C \frac{\rho_0 v_0}{\psi \sqrt{\text{Re}_x}}, \quad (3.1)$$

where  $C = 0.62$  for laminar flow over a flat plate and  $C = 2.35$  for laminar stagnation plane flow, while the air density ratio is:

$$\psi = \frac{\rho_0}{\rho_w}, \quad (3.2)$$

$\rho_0$  and  $\rho_w$  being the air densities for the main stream and at the porous wall, respectively. For a turbulent boundary layer and  $\psi < 1$ , the following equation was previously proposed [Martins 1998]:

$$j_{\text{w,cr}} = 0.02888 \frac{1}{1 - \psi} \left[ \ln \left( \frac{1 + \sqrt{1 - \psi}}{1 - \sqrt{1 - \psi}} \right) \right]^2 \left( 1 + 1.32 \text{Re}_x^{-0.112} \right) \rho_0 v_0 \text{Re}_x^{-1/5}. \quad (3.3)$$

It was found that the sensitivity of the critical mass flux relatively to the density ratio is higher for the laminar boundary layer. This is important information given the fact that the main stream temperature is not necessarily known. Another conclusion was that for  $\text{Re}_x > 10^5$  the limiting critical mass flux is always given by the law for a turbulent boundary layer, regardless of the value of the density ratio.

For  $Re_x < 10^5$  the value of the limiting flux is not so clear and actually depends on the effective transition  $Re_x$ , that is the laminar or turbulent nature of the boundary layer, the density ratio  $\psi$  and the main stream flow direction relatively to the sensor surface (parallel or stagnation flow). The mass flux values necessary for boundary layer blow-off are also higher than for  $Re_x > 10^5$ , as illustrated in Fig. 3.7, where the CTG mass flux as a function of  $Re_x$  and  $\psi$  is plotted. Once it is not possible to predict the Reynolds number for which transition occurs, the relations for the turbulent boundary layer were plotted for the whole Reynolds number range [Martins 1998]:

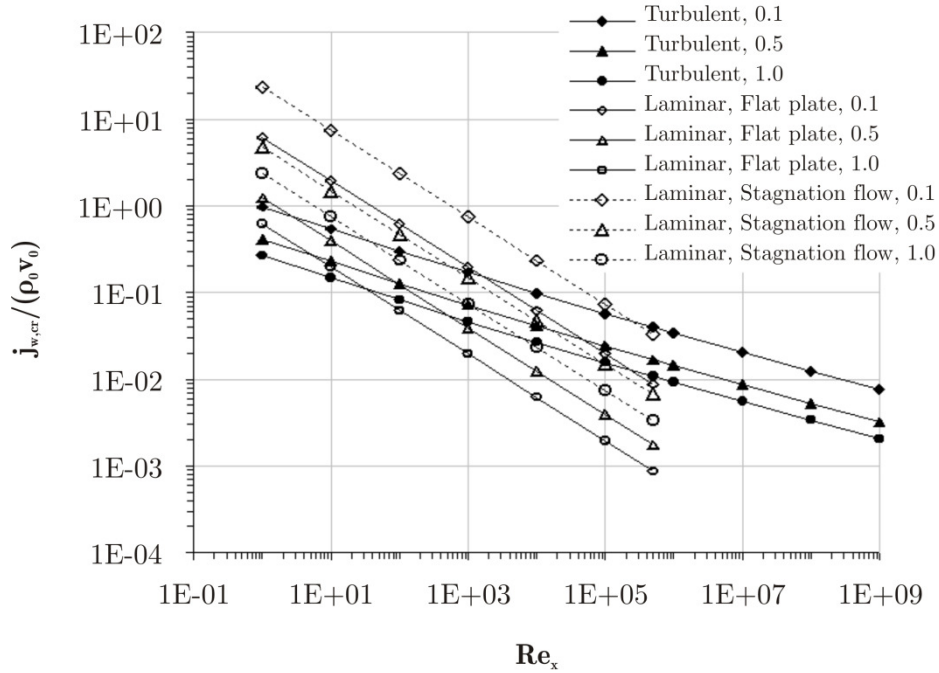


**Figure 3.7** – Critical transpiration gas (CTG) mass flux as a function of  $Re_x$  and  $\psi$  for turbulent boundary layers, a laminar boundary layer in a stagnation flow and a laminar boundary layer developing along a flat plate [Martins 1998].

It can be observed that the critical mass flux is given in an adimensional form where mass flux  $j$ , with units in kilograms per second per square meter, is divided by the main stream velocity and density. Results in Figure 3.7 mean that in order to always guarantee an effective blow-off, the relationship valid for laminar boundary layer on a stagnation plane flow valid for  $0.7 < Pr < 1.0$  can be used for CTG calculation, that is:

$$j_{w,cr} = 2.35 \frac{\rho_0 v_0}{\psi \sqrt{\text{Re}_x}} \quad (3.4)$$

The Reynolds number for the main stream must also be specified for the stagnation flow situation:

$$\text{Re} = \frac{\rho v L}{\mu}. \quad (3.5)$$

The characteristic length  $L$  was considered to be the same as the perforated plate's diameter which, in effect, corresponds to a situation where a nozzle would be blowing straight at the perforated plate. Although arguably unrealistic, this assumption is helpful in the specification of an assuredly critical transpiration flow. The density can be calculated as before, while the dynamic viscosity of the fluid can be found from the standard power law:

$$\frac{\mu}{\mu_0} = \left( \frac{T}{T_0} \right)^n, \quad (3.6)$$

where  $n = 0.7$  for air and  $\mu_0$  is a known dynamic viscosity at temperature  $T_0$ , usually  $1.71 \times 10^{-5} \text{ Nsm}^{-2}$  at 273 K [White 1998]. It should also be noted that the fluid density and velocity used in the calculation of the main stream Reynolds number are the same used in the determination of the critical transpiration mass flow.

The calculation of the CTG does not take into account any parameters related to the porous medium being crossed by the transpiration airflow. Previous transpiration radiometers used large mass flows in order to ensure boundary layer blow-off while providing additional refrigeration to keep temperature fields in the sensing element within acceptable bounds and to minimize the surface radiation emission [Martins 1998]. This means that a sensing element with a much lower thermal inertia could fulfil such requirements while relying on either smaller transpiration airflows or less bulky refrigeration systems than previous instruments. In any case, once a CTG value is

obtained, the question remains about how it will interact with the porous element it is crossing in thermal and dynamic terms.

The fact that the sensing element being studied is a thin plate with a microperforated array of small holes also raises questions about the behaviour of the transpiration airflow when transitioning from the feed tube to the plate itself, since the large difference in flow areas raises possible compressibility issues that may result in choked flow conditions and inhibit mass flow increases that could be necessary in order to ensure boundary layer blow-off. Furthermore, given the fact that the transpiration and refrigeration airflows are provided by compressed air at several times the atmospheric pressure, sonic flow is likely to occur since pressure ratios as low as 2:1 may be sufficient for its occurrence.

For given stagnation conditions, the maximum possible mass flow passes through a duct when its throat is at the critical or sonic condition. The duct is said to be choked and can carry no additional mass flow unless the throat is widened. Compressible flow theory available in any of the standard textbooks states that for isentropic flow through a duct (a common and convenient assumption) the maximum mass flow possible is proportional to the throat area and stagnation pressure, and inversely proportional to the square root of the stagnation temperature, which for air ( $\gamma = c_p/c_v = 1.4$ ) reduces to [White 1998]:

$$\dot{m}_{\max} = \frac{0.6847 p_0 A^*}{\sqrt{R T_0}} \quad (3.7)$$

stagnation temperatures and pressures being respectively

$$T_0 = T_1 + \frac{v_1^2}{2c_p} \quad (3.8)$$

and

$$p_0 = p_1 + \left(1 + 0.2 \text{Ma}_1^2\right)^{3.5}, \quad (3.9)$$



with subscript 1 indicating a point immediately upstream from the perforated plate.

The calculation of the Mach number of the incoming compressed air is obviously dependent on its velocity, which is a function of the gas mass flow that circulates in the feed line. While the velocity is merely the ratio of the mass flow rate and the flow area, the Mach number must be determined in order to compute the stagnation pressure, and can be calculated as the ratio between this velocity and the local speed of sound  $a$ :

$$\text{Ma} = \frac{v}{a}, \quad (3.10)$$

which in turn can be calculated as:

$$a = \sqrt{\gamma R T}, \quad (3.11)$$

where, as mentioned earlier,  $\gamma$  is the specific-heat ratio for air,  $R$  is the ideal gas constant and  $T$  the temperature.

At this point the calculations to be performed are dimensioning procedures for the perforated plate that must enable it to perform as intended for most foreseeable situations. As far as its function is concerned, as the sensing element of an instrument that is first and foremost a radiometer regardless of other possible features such as heat flux partitioning, this means that boundary layer blow-off must be ensured over a wide range of conditions, including the less favourable.

Given the instrument's intended function as a radiometer, care must be taken to ensure some certainty that the blow-off process is effective, and this can be achieved in several ways. The use of the relationship valid for laminar boundary layer on a stagnation plane flow provides the highest critical flow estimate for a given Reynolds number, while considering the density  $\rho_w$  at the porous wall to that of the compressed air flow that crosses the plate, although the actual value is smaller and could readily be estimated using well-established relationships for the pressure loss through the perforated pattern and the related density variations [Kolodzie and Van Winkle 1957, Fried and Idelchik 1989, Ishizuka et al. 2005].

Considering the density  $\rho_w$  at the porous wall as being equal to that of the compressed air flow that crosses the plate will lead to overestimated transpiration airflows and will actually increase the calculated critical mass flow for higher supply pressures, which is obviously counterintuitive. This assumption is merely intended to ensure boundary layer blow-off for any conditions and does not mean that such overestimated airflows will necessarily be used in normal operational conditions, where the mass flow to be used will probably be considerably smaller.

Moreover, the nature of the airflow on the furnace side must also be taken into account, since stagnation flows are not necessarily the most common in normal conditions, nor is their magnitude similar in terms of velocity to those used to compute the maximum values to be handled by the perforated plate. Nevertheless, the capability to work in extreme conditions remains built into the system.

The critical transpiration mass flow will thus be a function of conditions on the side of the compressed air fed to the system, namely its pressure, temperature and geometry (*i.e.* tubing diameters that influence mass flow), and conditions in the main stream such as the flow direction, velocity, temperature and pressure. While in some applications it may be assumed that the main stream is at atmospheric pressure, in others, such as gas turbines, that assumption may not be valid. In this particular case, given the fact that the experimental work to be carried out would take place in a furnace open to the atmosphere, the pressure was set at  $1,013 \times 10^5$  Pa (*i.e.* 1 atm) for all calculations and simulations, air density in the main stream being a function of temperature.

In the case under discussion the flow will not be passed through a single duct but rather through a pattern of small holes. This means that the microperforated plate must be dimensioned in such a way that it enables the passage of the required mass flow even if conditions become sonic at the level of the small holes. The calculation of the maximum mass flow permissible in the small holes can then be compared with the critical transpiration gas mass flow in order to determine the minimum number of holes necessary to accommodate the necessary gas flow, bearing in mind that a greater number of holes of the same diameter will diminish the mass flow through each of them by dividing the incoming total flow, so that a greater total flow can be circulated.

In terms of transpiration airflow handling, the perforated plate will thus be considered adequately dimensioned when the number of holes of a certain diameter is sufficient to accommodate the largest considered mass flow, which is in turn dictated by boundary layer blow-off requirements, and this maximum mass flow is ensured even if choked flow conditions are present in the perforated pattern. Other considerations that have to do with the interaction between the perforated pattern and incoming radiation are addressed in detail later on.

Under the aforementioned assumptions, the critical transpiration mass flow (in  $\text{kg s}^{-1}$ ) will increase with increasing density  $\rho_w$  at the porous wall, and will obviously be higher for increasing main stream stagnation flow velocities, Equation 3.4 showing a direct proportionality between the critical mass flow value and the stream velocity, that is tempered by the inverse proportionality between the critical mass flow and the square root of the Reynolds number.

It should be remembered that stagnation flows on the perforated plate are assumed and that reasonable velocities must be specified for these flows, which likewise require the definition of representative furnace temperatures, namely in order to calculate air densities, viscosities and Reynolds numbers on the “hot” side of the plate, assumed to be at one atmosphere in pressure as mentioned above. Conversely, while the temperature of the incoming transpiration airflow can safely be assumed to be constant at  $25^\circ\text{C}$ , possible variations in pressure must be taken into account because they do occur in practice and influence the density of the compressed air flow which, as discussed, will be considered equal to that of the air near the porous wall.

With all these values, density ratios  $\psi$  and critical mass fluxes and flows can be calculated as described by Equations 3.2 and 3.4. Assumed furnace temperatures were considered in increments of  $250^\circ\text{C}$  from  $500$  to  $1500^\circ\text{C}$ , stagnation flow velocities were set at 1, 2, 5, 10  $\text{ms}^{-1}$  and then in increments of 10 up to 50  $\text{ms}^{-1}$ , while the range of values considered for the compressed air pressure ranged from 2 to 8 bar, at 0.5 bar increments.

Considering the aforementioned formulae and the assumptions listed above, the highest critical mass fluxes naturally occur for the highest value of density  $\rho_w$  at the porous wall for each considered temperature, for the highest values of stagnation flow

velocities and for the highest temperatures considered in the furnaces, since these minimize the density ratio  $\psi$  for any fixed supply pressure and therefore maximize the critical mass flow, as illustrated in Figures 3.8 and 3.9. One of the interesting results from the numerical simulations of the perforated plate being crossed by varying gas mass flows, described in further detail below, is the conclusion that densities at the plate wall, averaged over its entire area since local variations result from the holes, can be thirty times or more smaller than the density of the incoming compressed air flow, illustrating the large degree of overdimensioning present in these considerations.

These critical mass flows are processed and fed from the compressed air system but given the large pressure differences with the atmospheric pressure in the furnace the possibility of choked flow in the holes of the microperforated pattern must be taken into account. Equations 3.7 to 3.11 allow the calculation of the maximum mass flow that can be accommodated by a hole of a certain diameter. The calculation of the choked mass flows allows an analysis of the number of necessary holes of a certain diameter, but other factors must be kept in mind, namely the need to ensure as uniform a flow as possible on the outer surface of the plate and the fact that the radiation transmissivity of the plate is a direct function of the perforated and non-perforated areas of the plate, as discussed below.

For small hole diameters the choked flow value will naturally be very low, so the criterion selected for dimensioning the perforated plate was to study the number of holes of a certain diameter necessary to accommodate the highest critical mass flow rate encountered in the previous step of the process, this value occurring for a stagnation velocity of  $50 \text{ ms}^{-1}$  and for the maximum density considered at the porous wall, that is the density corresponding to the compressed air flow at 8 bar for each of the temperatures of interest. As mentioned earlier, the assumption of such values does not mean that such overestimated airflows will necessarily be used in normal operational conditions, where the mass flow to be used will probably be considerably smaller and relatively small mass flows will ensure boundary layer blow-off.

Once values for both the critical transpiration mass flows necessary to ensure boundary layer blow-off and the mass flow that can be passed in a given hole at choked flow conditions are available, the number of necessary holes can be thought of as

merely the ratio between the critical mass flow and the choked flow in each hole of the pattern, since it is assumed that all the incoming compressed air is passed through the perforated pattern, although this may not be the case if a faulty welding process is applied to the edge of the plates when they are attached to the porous holder. These areas are obviously not only a function of the number of holes and their number but also of their spacing, so that the numbers of holes obtained here must be considered along with the intended values for plate transmissivity. Furthermore, the ability to accommodate the necessary number of holes with a specified spacing on a plate with a pre-determined diameter and therefore frontal area must obviously be checked, ensured and adjusted if necessary.

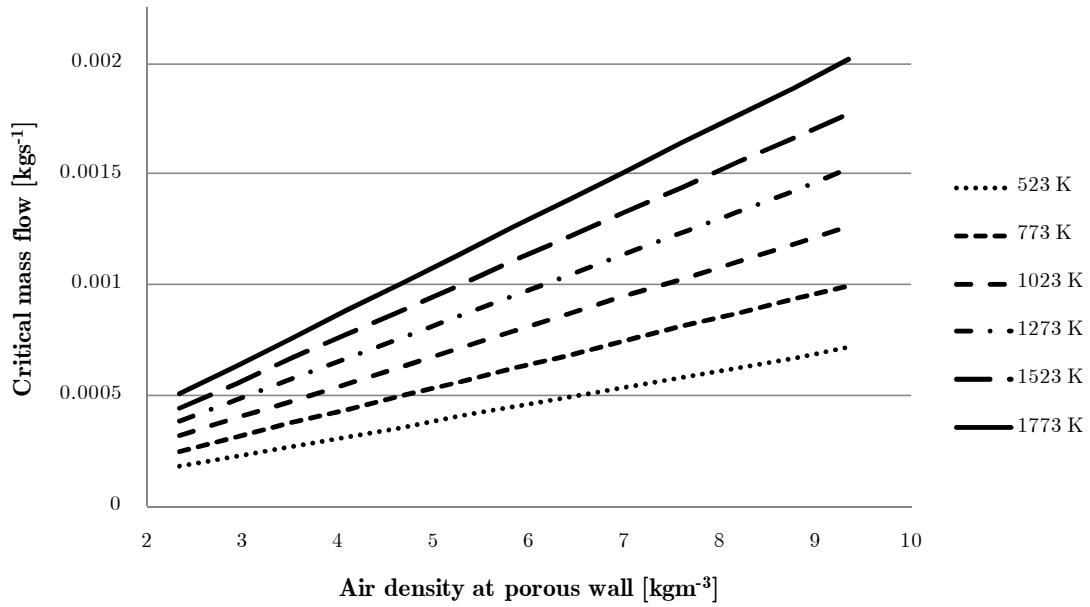


**Figure 3.8** – Critical mass flows as a function of the assumed densities at the porous wall and furnaces temperatures, for the maximum stagnation velocity.

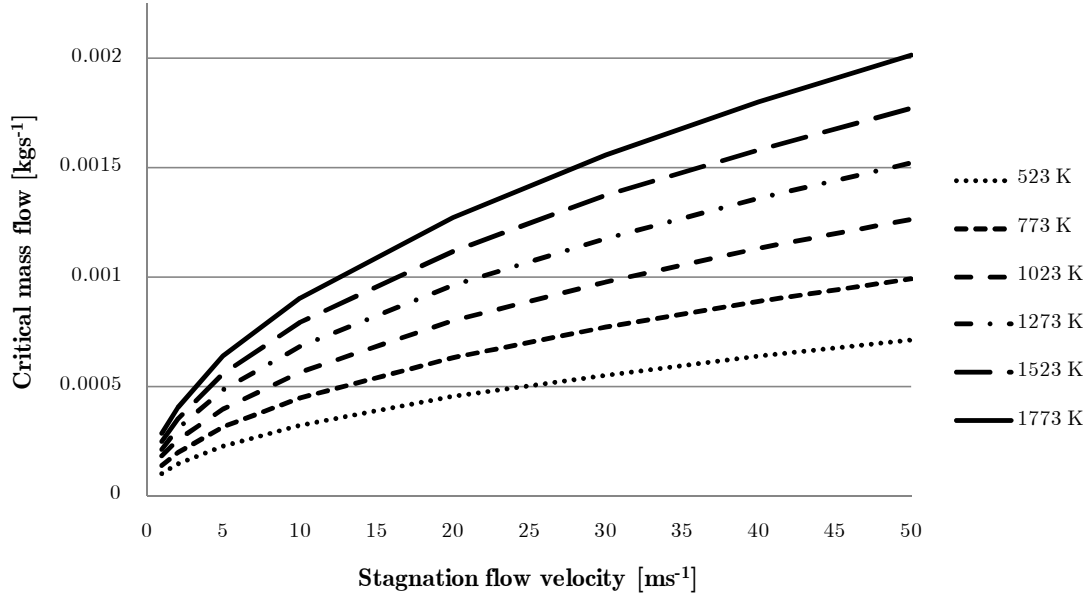


**Figure 3.9** – Critical mass flows as a function of the assumed densities at the porous wall and stagnation flow velocities, for the maximum densities at the porous wall.

Choked flows in the holes are determined from Equation 3.7, which requires a knowledge of conditions upstream of the plate in terms of temperature, pressure and flow velocity, so that Mach number and stagnation temperatures and pressures, can be calculated using Equations 3.8 to 3.11. Pressures and temperatures are the same as considered before, while flow velocities and Mach numbers upstream of the plate are calculated considering the feed line diameter and from the maximum critical mass flow at each temperature, that is the critical value occurring for the highest density at the porous plate and highest stagnation external flow, as mentioned above.

Once these values are available, the necessary number of holes in the pattern can be calculated as the ratio between the maximum critical mass flow to be accommodated at a given temperature and the choked mass flow for a specified hole diameter, as listed in Table 3.1.

**Table 3.1** – Critical mass flow to choked flow ratios, indicative of the number of holes.

$d^*$ [mm]	Critical mass flow to choked flow ratios					
	523 K	773 K	1023 K	1273 K	1523 K	1773 K
0.005	194.22	270.72	343.53	413.68	481.78	548.22
0.1	48.56	67.68	85.88	103.42	120.45	137.06
0.5	1.94	2.71	3.44	4.14	4.82	5.48
1	0.49	0.68	0.86	1.03	1.20	1.37

From the values in Table 3.1 it is visible that a single 1 mm hole would be able to accommodate almost any possible critical mass flow under discussion, while for the intended hole diameter of 0.1 mm the number of necessary holes to handle the maximum critical mass flow is merely 138. If all 138 holes were placed tangent to each other along the diameter of the plate, a total diameter of 13.8 mm would be obtained, which proves that it is a simple matter to place the necessary number of holes in the specified plate diameter. Additionally, other considerations regarding the specification of the perforation pattern parameters have more to do with plate transmissivity and flow uniformity issues rather than with boundary layer blow-off and compressibility problems in the holes leading to insufficient transpiration mass flows. This also means that the number of holes calculated from plate transmissivity and flow uniformity criteria will lead to a safely overdimensioned number of holes as far as transpiration requirements as concerned.

As mentioned earlier mass flows are heavily overestimated merely for dimensioning purposes, and actual operational mass flows are expected to be much smaller, but another related matter should be kept in mind.

The use of comparatively high transpiration mass flows is fundamental from the point of view of the measurement principle and the analytical approaches discussed in the previous chapter, since these large airflows are the only way of achieving the low surface temperatures that enable the assumption of a negligible emission component in the radiative balance between the plate's surface and the hot surroundings encountered, for instance, in furnaces.

Given the fact that the aforementioned CTG airflows are largely overdimensioned, the operational use of similar values will ensure both the intended boundary layer blow-off and the low surface temperatures. As discussed in Chapter 4, the maximum mass flows achievable in a measurable manner (*i.e.* using mass flow meters rather than simply connecting compressed air lines at the maximum pressure setting) in the laboratories where the experimental studies took place are indeed similar in magnitude to the maximum values discussed above, although slightly smaller but certainly sufficient to ensure both intended objectives.

Another interesting effect to be considered is a lessening of the importance of the external refrigeration system. The contact area between the porous medium and the rim of the plate was maximized to a reasonable extent without leading to unduly large diameters atop the instrument, nevertheless remaining rather small. The bulk of the plate's refrigeration needs, if only for radiative emission minimization, will undoubtedly be met by the transpiration airflow given its magnitude and its direct contact with a massive portion of the plate's mass and volume. This also means that the fail-safe position of the valves controlling the transpiration airflow must be such that the airflow is on in the absence of control signal in the valve, which must thus be a normally-open valve.

### ***3.3.3 Plate Transmissivity***

Besides boundary layer control and compressibility issues, other considerations must be made regarding the use of the microperforated plate, since the presence of the pattern of holes has other implications.

While the option of using a thin perforated plate rather than a comparatively thick sinterized porous cylinder as the sensing element is rather naturally intuitive from the strict point of view of its thermal inertia, it does entail a need to carefully consider some factors that could otherwise be ignored. Especially relevant is the issue of the element's transmissivity, since the combination of the low thickness and the perforated pattern renders it non-opaque, such an effect being visible (although at a different wavelength than the ones at which the element is expected to perform) even when such the plate is held at arm's length.



The behaviour of a solid element exposed to incident radiation is a complex phenomenon even in cases when no perforation is present, since solids can exhibit various degrees of emissivity, reflectivity and transmittance that can be characterized with varying levels of accuracy and complexity. The problem is compounded by the presence of any degree of porosity that implies some convection and alters the radiative and conductive behaviours. This additional complexity should be taken into account even in cases when no perforation is apparent through the whole thickness of the element, since phenomena such as internal reflection, reemission and scattering can occur within the cavities of the porous medium and the interfaces between phases.

There are numerous references that deal with various aspects of porous media, including their thermal behaviour, and increasingly with media with very small (*i.e.* nanoscale) and ordered porosities [Wehrspohn 2005]. Of interest within the framework of the present work is also the existence of transient effects of radiative transfer in semitransparent materials [Siegel 1998].

An accurate evaluation of the medium's thermal behaviour is of critical importance for its use as a sensing element but such an analysis is potentially difficult due to the aforementioned internal reflection, reemission and scattering phenomena. These are potentially very difficult to analyse. Thus, a variety of techniques are available in order to simplify the task, often involving the determination of a single effective thermal conductivity for the simpler case of a single solid material and only one gas. Some involve detailed calculations of radiative balances within the cavities [Tsai and Strieder 1986] but most are based on averaging techniques that treat the highly heterogeneous phases (each of which can be either opaque, transparent or semi-transparent) as one or several homogeneous materials [Travkin and Catton 2001], relying on known morphology data and yielding average values for the various materials, that enable much simpler heat transfer calculations.

The thin perforated plate is a very particular case of porous medium, for several reasons, and is fortunately a much simpler situation than those mentioned above. In all relevant situations but especially given the plate's low thickness and the related small diameter and spacing of the microperforated patterns, special care must be applied when studying periodic structures exposed to electromagnetic radiation, due to the possible occurrence of unforeseen and usually unfamiliar phenomena, such as the

phenomenon of greatly enhanced transmission of light through a subwavelength aperture in an otherwise opaque metallic film patterned with a regularly repeating periodic structure, such as the microperforation under discussion.

This phenomenon is designated as Extraordinary Optical Transmission (EOT). When light of a certain wavelength falls on a subwavelength aperture, it is diffracted isotropically and evenly in all directions, with minimal far-field transmission. This is the understanding from classical aperture theory as first described [Bethe 1944] and later corrected [Bouwkamp 1950]. In EOT however, the regularly repeating structure enables a much higher transmission efficiency to occur, up to several orders of magnitude higher than that predicted by classical aperture theory [Ebbesen *et al.* 1998, Martín-Moreno *et al.* 2001], this effect being widely studied and exploited when such amplifications are sought [Chao-Chun 1973, Letrou and Gheudin 1992, Green and Yi 2004, Canpean and Astilean 2009].

It is therefore necessary to make sure that no such effects are to be expected when defining the microperforated pattern that is intended to interact with incoming thermal radiation. The latter is usually defined as the emission of electromagnetic waves from all matter that has a temperature greater than absolute zero. Moreover, in the scope of this document it is conventionally defined as ranging from about 0.1  $\mu\text{m}$  to several hundred microns, covering the infrared, visible and near-ultraviolet portions of the electromagnetic spectrum.

The sensor prototype will be tested in a blackbody furnace which can be set to temperatures up to 1500°C. Thus, in order to verify whether EOT phenomena can be expected, the wavelength range of the radiation produced in the furnace must be determined.

According to Wien's displacement law, there is an inverse relationship between the wavelength of the peak of the emission of a black body and its temperature when expressed as a function of the wavelength, that is:

$$\lambda_{\max} T = C_3, \quad (3.12)$$

where  $C_3 = 2897.8 \text{ K}\mu\text{m}$ . This means that if furnace temperatures from 750 to 1500°C are considered, emission maxima will range from 2.83 to 1.63  $\mu\text{m}$ , while spectral emissive power as a function of temperature and wavelength can be calculated using Planck's distribution:

$$E_{\lambda,b}(\lambda, b) = \frac{2hc_0^2}{\lambda^5 \left[ \exp\left(\frac{hc_0}{\lambda kT}\right) - 1 \right]} = \frac{C_1}{\lambda^5 \left[ \exp\left(C_2/\lambda T\right) - 1 \right]} \quad (3.13)$$

where  $h$  and  $k$  are the universal Planck and Boltzmann constants respectively,  $c_0$  is the speed of light in vacuum and with  $C_1 = 3.742 \times 10^8 \text{ W}\mu\text{m}^4\text{m}^{-2}$  and  $C_2 = 1.439 \times 10^4 \text{ K}\mu\text{m}$ , as illustrated in Figure 3.10.

As discussed earlier the envisaged plate thickness values for the present application were around 0.1 mm, with limitations on hole diameter to plate thickness ratios imposed by the manufacturing processes. Given the results in Table 3.1, it is visible that the avoidance of EOT phenomena in subwavelength apertures is straightforward, since hole diameters are significantly larger than incoming radiation wavelengths. The wavelength band where 80% of emitted radiation at the considered temperatures occurs (*i.e.* excluding the lower and upper 10% of the total range) can also be calculated using the blackbody radiation functions, as summarized in Table 3.2.

The hole diameter-to-plate thickness ratio limitation must be combined with the geometric analysis of the transmissivity in order to establish proper dimensions for the microperforated pattern to be obtained, bearing in mind the fact that transmissivity should be kept as low as possible when other radiative heat exchange parameters such as absorption and reflection are constant, in order to maximize the amount of heat absorbed by the plate and transformed into a measurable temperature increase for transient analysis.

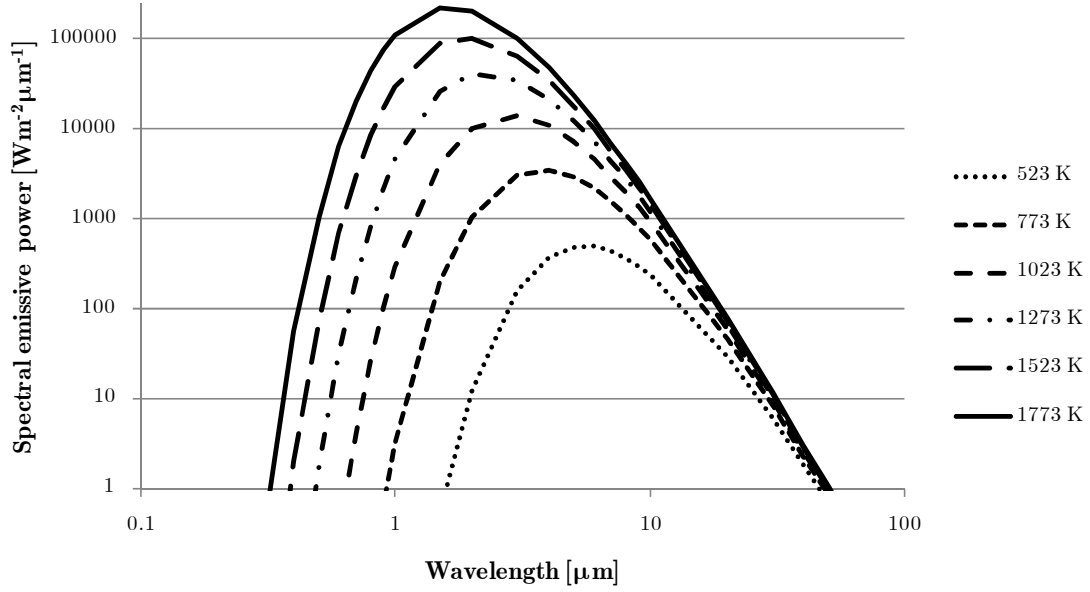


**Figure 3.10** – Spectral emissive power as a function of temperature and wavelength.

**Table 3.2** – Emitted radiation parameters

Temperature [K]	Emission Maximum [ $\mu\text{m}$ ]	80% Range [ $\mu\text{m}$ ]
523	5.54	14.23
773	3.75	9.63
1023	2.83	7.28
1273	2.28	5.85
1523	1.90	4.89
1773	1.63	4.20

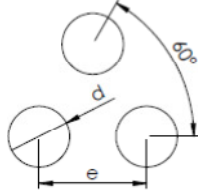
Transmission phenomena through solids with periodic apertures can be of very complex description and are especially studied in the range of frequencies relevant for radio and microwave applications. So, most of the applications encountered in the literature had to do precisely with the optimization of these phenomena in components where comparatively long wavelengths can interact with component features of similar dimensions according to fairly complex formulations. Given the fact that thermal radiation has a higher frequency (and shorter wavelength) than radio or microwaves, such interactions are not to be expected in the present case, as mentioned above. However, references for microwave applications do state that the transmission through

a perforated plate can be approximated by a geometrical consideration for the high frequency end of this range, as is the case for thermal radiation. For normal incidence the power transmittance is the geometrical ratio of opening to blockage, that is [Winnewisser *et al.* 1998]:

$$\tau_{\text{rad}\perp} = \frac{\text{Opening}}{\text{Blockage}}. \quad (3.14)$$

Opening and blockage areas will depend upon which particular unit cells are considered and these, in turn, are a function of the perforation parameters, the most usual perforated pattern using circular holes being the  $60^\circ$  staggered pattern used here. Unit cell parameters, namely hole diameters and their spacings that dictate opening and blockage areas are summarized in Table 3.3.

**Table 3.3** – Unit Cell Parameters

<b>Unit Cell</b>	
<b>Opening</b>	$\frac{\pi d^2}{8}$
<b>Blockage</b>	$\frac{e^2}{2} \sin(60) - \frac{\pi d^2}{8}$

where  $e$  is the distance between holes and  $d$  is their diameter. The selection of a  $60^\circ$  staggered pattern over a square pattern was already discussed in Chapter 2 and has to do with guaranteeing an isotropic distribution in the plane of the plate, as opposed to the orthotropic behaviour of a square pattern [Dowling 1999].

A variety of perforated patterns is thus defined in terms of hole diameter and spacing, and the resulting transmissivity can then be plotted as summarized in Table 3.4 and illustrated in Figure 3.11. The aforementioned limitations in the hole diameter-to-plate thickness must be remembered at this point, along with the selection

of a 0.1 mm thickness for the plate. This means that the hole diameter was set at the same value so that the transmissivity plot only takes into account this diameter and various hole spacings  $e$ .

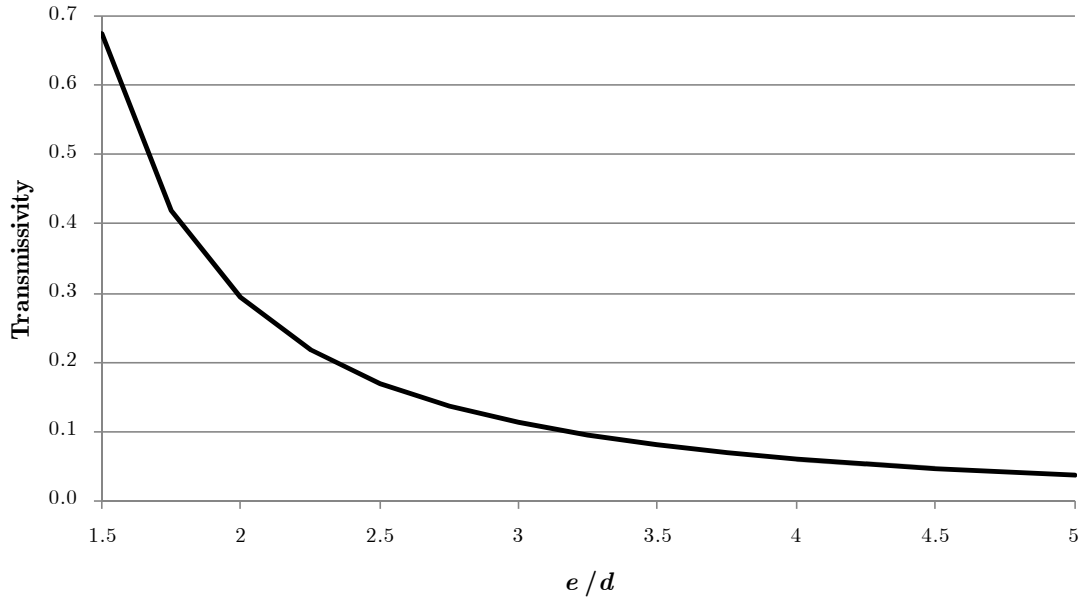


**Figure 3.11** – Plate transmissivity as a function of the hole diameter to spacing ratio of the perforated pattern.

A maximum acceptable transmissivity value was arbitrarily set at 20%. If a hole 0.1 mm in diameter is considered, a spacing of 0.233 mm between holes ensures the intended transmissivity, so that the final spacing was specified as 0.25 mm for a transmissivity of 17%, leading to the configuration illustrated in Fig. 3.1.

### 3.3.4 Cooling System

As mentioned earlier the relative importance of the external refrigeration system is lessened by the magnitude of the transpiration airflow and its cooling effect on the plate, given the airflow's direct contact with the bulk of the material of which the plate is made of and the admittedly rather small contact area between the porous medium and the rim of the plate.

The porous component is nevertheless important, if only as a means of containing, directing and ultimately handling the transpiration airflow. This function could arguably have been performed by a solid component. Temperatures could be minimized if the metal mass exposed to high heat fluxes was kept low by using small

outer tubing diameters, but this could be problematic from the strict point of view of system robustness. As mentioned earlier, the minimization of dimensions and the lessening of the thermal inertia of the overall system were never intended to be obtained at the expense of robustness, which meant that wall thicknesses of at least 1 mm had to be used for safety.

The idea of rendering the plate holder porous can be thought of merely as an additional benefit in terms of component safety in avoiding excessive temperatures by making use of this comparatively large wall thickness, and therefore volume, as a heat transfer surface.

The porous steel casing is thus intended to serve as a holder for the microperforated plate with some refrigeration around its outer diameter, the plate being welded to the top of the porous holder. The intention is to make use of the large specific area (defined as the ratio between the surface area available for heat transfer and the volume) of the porous parts to interact with a stream of cooling air.

An analytical description of heat transfer within a porous medium can be difficult to describe if some assumptions are not made in order to simplify the approach. It is indeed a field of study in its own right, with large numbers of articles being published every year and relevant studies being continuously carried out, so much that even well-established academic manuals have been in need of constant updating to take into account new analytical approaches, new porous medium morphologies such as metal foams (rather than the more conventional packed solid spheres) or the large number of empirical correlation for relevant parameters such as Nusselt numbers or convection coefficients that have been emerging [Kaviany 1995, Vafai 2005].

The one-equation equilibrium or the two-equation non-equilibrium models are commonly used. The first model assumes that there is no temperature difference between the local fluid and solid phase while the second model treats the fluid and solid separately, considering the local temperature difference between them. The latter is more difficult to apply because it requires information on the interfacial heat transfer coefficient, which is usually determined through a large number of experimental investigations [Kim 1993]. Owing to this difficulty, some investigators have used the

one-equation model for the analysis of convection heat transfer in a general porous medium. However, the one-equation model is only valid when the local temperature difference between fluid and solid is negligibly small. This will not be the case in heat exchanger applications where the difference in the thermal conductivities of the fluid and solid is significant and certainly not the case as far as the microperforated plate and the transpiration airflow are concerned, since no significant heating of the air flowing through the microperforated pattern is to be expected.

The most widely available models are for spherical media, that is materials where the porosity consists of the empty spaces between packed solid spheres. Other configurations are somewhat less well established and a large part of current work in the field focuses on other morphologies, such as spherical pores or open-cell metal foams [Boomsma *et al.* 2003].

Given the fact that the cooling system is a somewhat secondary component of the system in terms of the measurement process itself and that a proper analytical approach would for that reason be outside the main focus of the work described here, the emphasis was put merely on an adequate determination of its performance rather than on a comprehensive analytical formulation, commercial CFD software being used for the purpose, namely the *CFX* module of ANSYS 13.

As discussed in Chapter 4, the porous components that were eventually ordered consisted of porous steel with spherical pores. This required the definition of several parameters necessary to the simulation, especially as far as the porous medium morphology was concerned, namely its volume porosity and its interfacial area density. It was assumed that different porosity grades represented equally sized spherical voids of diameter  $d_p$ , the other important parameter being porosity, which can change for different types of packing and is a sufficient parameter to characterize the “packing” of the hollow spheres. The free volume  $V_{\text{void}}$  can be found from the number of pores and the volume of a single pore,  $V_{\text{void}} = NV_p$ . Defining porosity  $\phi$  as the ratio of free to total volumes:

$$\phi = \frac{V_{\text{void}}}{V_{\text{tot}}} \quad (3.15)$$



and the volume of a single spherical void  $V_p$ , the number of voids per volume can be calculated as:

$$\phi = \frac{NV_p}{V_{\text{tot}}}. \quad (3.16)$$

The number of voids per unit volume  $n_v$  is expressed as:

$$n_v = \frac{N}{V_{\text{tot}}} = \frac{\phi}{V_p}. \quad (3.17)$$

The specific interfacial surface area between the voids and the air can be defined as:

$$a_p = \frac{NA_p}{V_{\text{tot}}}, \quad (3.18)$$

with  $A_p$  being the surface area of a single spherical void, the SI unit of the specific area being  $\text{m}^2/\text{m}^3$  or  $\text{m}^{-1}$ . It then follows that:

$$a_p = \frac{A_p}{V_p} \phi, \quad (3.19)$$

where  $A_p/V_p$  is the specific surface area of a single void. The surface area-to-volume ratio can be calculated for every object and this ratio is the smallest for a sphere. This means that the interfacial area calculation used here is underestimating the real area of non-ideal voids:

$$\frac{A_p}{V_p} = \frac{4\pi \left(\frac{d_p}{2}\right)^2}{\frac{4}{3}\pi \left(\frac{d_p}{2}\right)^3} = \frac{6}{d_p}, \quad (3.20)$$

and finally:

$$a_p = \frac{6}{d_p} \phi. \quad (3.21)$$

As mentioned when the construction of prototypes is discussed, the parts were made using sintered steel with 25% porosity consisting of interconnected pores averaging 7  $\mu\text{m}$  in diameter dispersed throughout the material, thermal conductivity being similar to a 400-Series stainless steel for the solid matrix. These pore diameters, volume porosities and part total volumes led to an interfacial area density of about  $2.14 \times 10^5 \text{ m}^{-1}$ , but it should be noted that the aforementioned grossly underestimates interfacial area due to the fact that the assumption of uniform and spherical pores is overly simplified. A look at the SEM (Scanning Electronic Microscopy) image illustrated in Figure 3.12 clearly shows that the voids are very irregular and have a large variation in volume in any such materials.

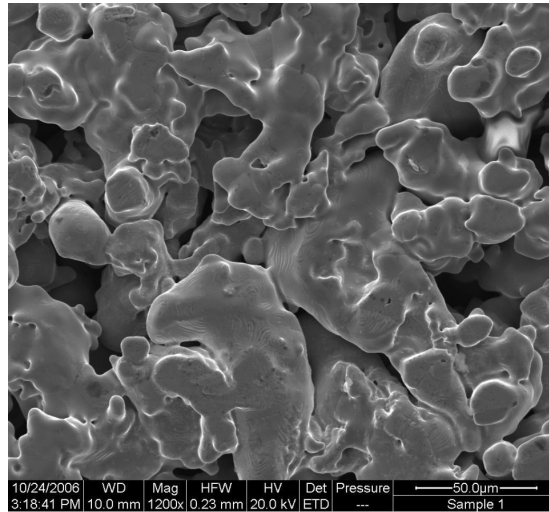


**Figure 3.12** – SEM image of the irregularity in void geometry and the significant variations in their volume (image courtesy of Applied Porous Technologies AB).

Another parameter was necessary in order to run the simulations, namely the heat transfer coefficient between the fluid and solid phases. Setting this value is notoriously difficult given the complexity of the matter, and the large number of numerical and experimental studies published in recent years on this specific topic has

to do with the determination of adequate correlations for particular porous morphologies, materials, fluids and component geometries, in this context especially as far as Nusselt numbers or Reynolds numbers based on Darcian flow velocities that are strongly dependant of the listed variables [Boomsma *et al.* 2003]. Given the relative importance of the porous medium in the overall performance of the system, at least when compared with the behaviour of the transpiration airflow interacting with the perforated plate, temperatures at the interface between the plate and the porous medium were evaluated by carrying out parametric studies in order to evaluate the variations that this parameter can have, rather than developing an approach with the same level of analytical detail as used for instance in the evaluation of critical transpiration flows or the interaction between incoming radiation and the perforated pattern. The CFD simulations where the relationships above were put into used will be described in the next section

Once the design principles stated above are used to determine some of the most important geometrical and dimensional features of the sensing element and to evaluate such important operational parameters as the transpiration airflows, the performance of the system as a whole must be studied, especially as far as the temperatures reached within the system for different incident radiation and transpiration airflow levels, as well as their variations in time, are concerned.

### **3.4 Parametric Studies**

The main parametric studies conducted using ANSYS *CFX* have to do with the central principle underlying the instrument under discussion, namely the correlation between the temperature measured by a thermocouple attached to the centre of the microperforated plate that serves as a sensing element, and the various incident heat fluxes and transpiration airflows to which the element is exposed, the latter being either a radiative heat flux if the transpiration mass flow is supercritical or otherwise a convective and radiative total heat flux. The various dimensioning procedures were discussed above, and the parametric studies to be conducted using *CFX* allow to some extent an evaluation of their adequacy as far as the instrument's overall thermal performance is concerned, especially regarding magnitude and time variation of the temperatures to be measured by the thermocouple. The reasonability of various

assumptions made in the development of the analytical model, for example ignoring the surface radiative emission term in the heat flux balance with hot surroundings, can also be validated in the numerical studies, since this emission term can be discounted if surface temperatures are comparatively low, as can be verified from the simulation results.

Besides the validation of design options and dimensioning procedures, the question of determining which operational conditions are most adequate must be kept in mind and discussed in terms of transpiration and refrigeration airflows and their impact on measurements. The fact that measured temperatures result from the balance between incident radiation and the cooling effect of various transpiration mass flows is especially relevant both in the context of operational conditions and in the verification of the assumption that the radiative emission from the plate is to be discounted.

The transient behaviour implied by the pulsed operation principle must also be adequately described for the various expected changes in incident heat fluxes and transpiration airflow. Of critical importance is the determination of acceptable limits to the thermocouple temperature when the transpiration airflow is significantly reduced or even switched off, in order to define adequate times for the induced pulsed behaviour.

Central to characterizing the instrument's performance is the relationship between the measured temperature (or the slope of its time variation curve), the incident heat flux and the various transpiration airflows. In order to proceed with such studies, some preparation is necessary in setting up the simulations.

The basic configuration of the system has already been established and discussed, and the process of obtaining adequate CAD models for importation onto *CFX* was straightforward. However, the large difference in size between features of the models could be troublesome because of implications in terms of specifying an adequate computational mesh. An example is the transition from the very fine mesh necessary to adequately represent each hole in the perforated pattern, which requires several elements on the perimeter of hundreds of holes 0.1 mm in diameter, to the mesh located in the air of fluid domains located on either side of the plate and that extend for several centimetres.

As mentioned in Chapter 2, all simulations and calculations were carried out on a computer equipped with an Intel Core i7 processor at 2.93 GHz clock frequency and 4 MB of RAM, on a Windows 7 64-bit operating system. As usual in applications of the kind, potential computational limitations arising from stringent mesh requirements can be alleviated by the possibility of making use of symmetries occurring in the system. In this particular case the overall geometry of the system consists of components with cylindrical components symmetrical in the angular direction, while at the level of the microperforated plate the pattern has an angular periodicity of  $60^\circ$ , as discussed above. This led to the specification of a geometry consisting of an angular sector of  $60^\circ$  with rotational symmetry boundary conditions specified on either side, as illustrated in Figure 3.13.

As a standard procedure in numerical studies, mesh independence was attempted by evaluating changes in the temperature at the centre of the sensing element between successive refinements and stopping the refinement process when no significant changes occurred. Although differences in the monitored variable were already low ( $< 5\%$ ), this process could not be continued due to a lack of memory in the system that caused the meshing program to exceed its limits in terms of memory allocation handling. Thus, the meshes used were the most refined usable ones resulting from this refinement process.

Figure 3.13a illustrates the solid component of the computational domain (in blue), with the limits of the fluid domain shown in wireframe. The rotational symmetry about the  $z$ -axis is readily apparent and the  $60^\circ$  section of the perforated plate is shown placed on top of the cone, with its outer section overhanging it. This surface will be set as an imposed temperature boundary condition, since it corresponds to the surface of the porous holder where the plate will be attached.

Symmetry and mass continuity require the specification of only one-sixth of the intended overall mass flow entering the inlet at the bottom at a specified pressure and temperature, while the upper part of the fluid domain is defined as an opening at atmospheric pressure and a set value of external blackbody temperature. The latter is defined as the effective blackbody temperature of any bodies beyond the boundary, which is exactly how the calibration furnace surfaces are intended to be represented.

Besides this external blackbody temperature the software also requires a local fluid temperature to be defined at the location of the boundary.

Simulations were conducted in order to find out if the earlier assumption of small values of heating for the overall airflow crossing the perforated plate under typical furnace temperatures and transpiration mass flows was valid, as was found to be the case. This meant that the airflow was considered to be entering the domain at 298 K (*i.e.* 25°C) and the local fluid temperature at the opening was set at 300 K for most simulated situations. The only exception was the simulation of situations where the transpiration airflow is cut and the steady-state response of the sensor to convection and radiation was sought, in which case the local fluid temperature was conservatively set at the same value as the external blackbody temperature. The intended transient operation mode means that such situations will not be encountered in practice but temperatures potentially reached in those cases were nevertheless studied as an indication of extreme bounds for thermal levels although, as will be discussed in the following chapter, the situation of gas temperatures reaching the same values as those of the furnace surfaces is unrealistic.

In this chapter the opening temperatures were set assuming a unitary emissivity, which is obviously not the case in the situations encountered in the experimental studies. Necessary adjustments to this parameter for comparison purposes will be discussed later in this text.

Figure 3.13b shows the type of imposed boundary conditions, while Figure 3.14 is a close-up view of the mesh at the level of the perforated pattern. Note that this configuration does not model the interaction of the refrigeration airflow with the porous medium. The integration of this factor into the simulation would require a less refined mesh to run due to system limitations encountered in the aforementioned refinement process.

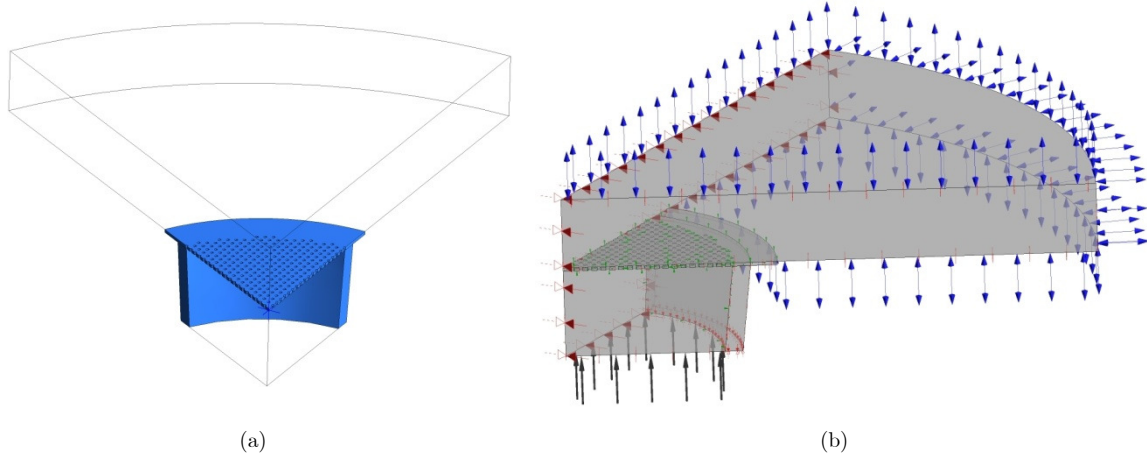


**Figure 3.13** – 60° unit cell geometry symmetry (a) and opening (blue), inlet (black), symmetry (red) and wall (green) boundary conditions (b).

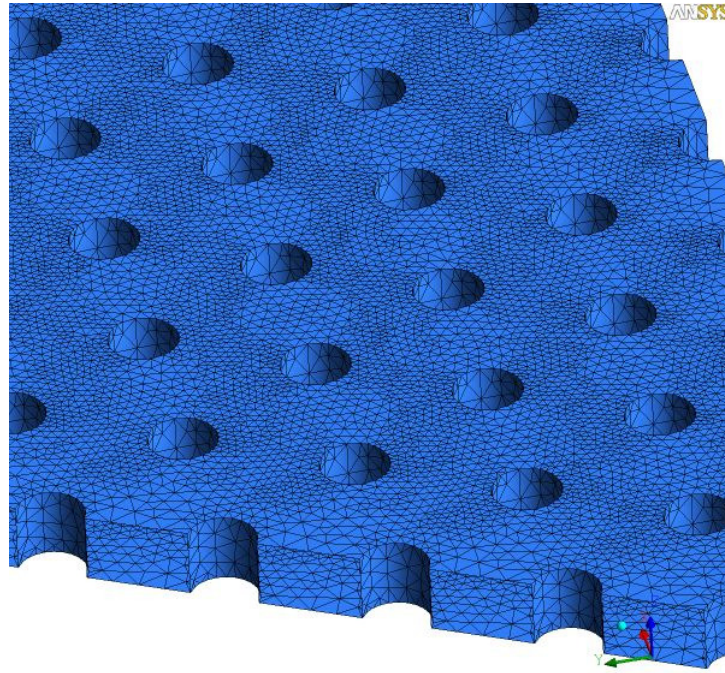


**Figure 3.14** – Close-up view of the perforated pattern mesh.

Furthermore, the presence of a swirling component in the refrigeration airflow, injected tangentially in the non-porous casing base and intended to augment its residence time in the space between the solid cone and the porous holder, invalidates the use of the 60° symmetry. So, the refrigeration airflow and its interaction with the porous medium needs to be addressed in a different model. Moreover, this other model

will provide simulated values for the temperatures achieved at the surface where the perforated plate will be attached to the porous holder, which only emphasises its importance even if, as discussed below, the essential contribution in terms of system refrigeration comes without surprise from the transpiration airflow.

The basic configuration of the model for studying the interaction of the refrigeration airflow with the porous medium is illustrated in Figure 3.15, where the tangential injection of the refrigeration airflow that provides the swirl component is visible. Both the transpiration and the refrigeration airflows can be seen in the form of streamlines, together with a plane showing the temperature distribution in the cone, the non-porous base and the porous holder. It should be noted how some of the streamlines actually cross the porous component. Results and implementation details of this model will be discussed further below.

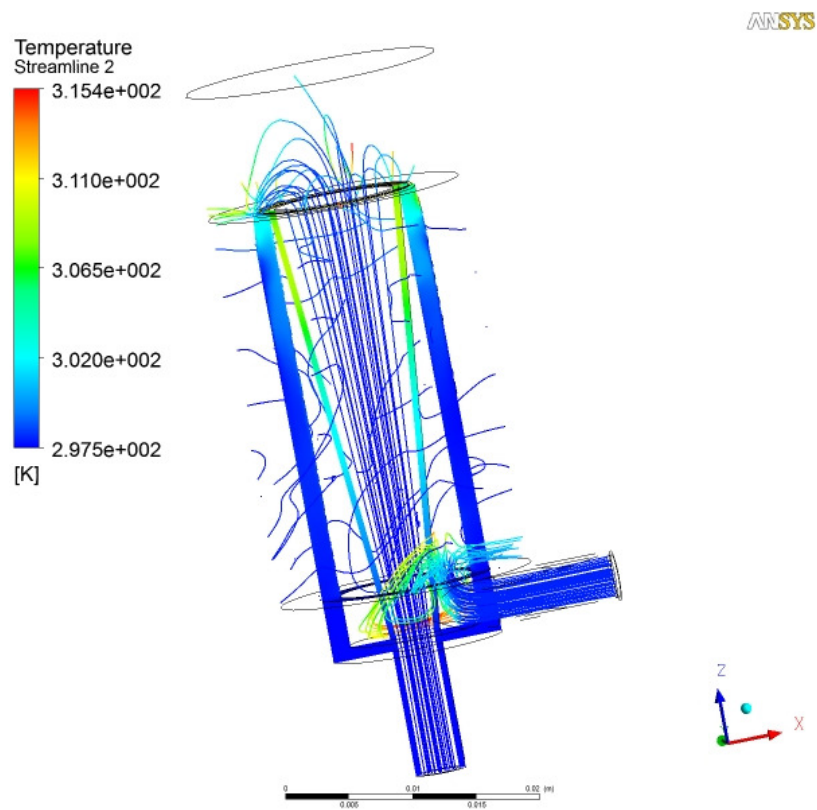


**Figure 3.15** – Basic configuration of the model studying the porous medium interacting with the refrigeration airflow.



Note that the microperforated pattern is not simulated in this model and understandably so considering the limitations encountered in simulating even one sixth of the perforated plate, as discussed above. This does not mean that this model does not consider the presence of the plate, but merely that the component was modelled as a porous medium for which an interfacial contact area between solid and fluid phases was calculated. This is a very straightforward process given the very well-ordered geometry of the perforated plate, where areas and volumes are easily calculated as discussed in the previous chapter, and heat transfer coefficients can likewise be calculated.

### ***3.4.1 Variations of Plate Temperatures with Incident Heat Fluxes***

The basic configuration illustrated in Figures 3.13 and 3.14 allows the simulation of a variety of situations. Of central interest within the framework under discussion is obviously the thermal response at the location where the thermocouple will be attached to the plate, that is, at its centre. This response must be evaluated as a function of a combination of incident heat fluxes and transpiration mass flows, but in order to understand the underlying influence of each of these factors their influence was studied separately, starting with a parametric study of the effect of incident heat fluxes.

These heat fluxes are ultimately the result of placing the system in a furnace that for the moment will be assumed to have a unitary emissivity, although this is not necessarily the case in practice, as will be discussed later. This means that heat flux coming from the cavity defined by the surrounding furnace walls is assumed to correspond to the emissive behaviour of a blackbody, where the spectral emissive power of Equation 3.13 is integrated over the entire wavelength spectrum to give the blackbody total emissive power:

$$E_b = \sigma T^4, \quad (3.22)$$

where  $\sigma$  is the Stefan-Boltzmann constant. This means that the system must be able to cope with thermal conditions that become comparatively more stringent as the temperature of the surroundings increases, leading to a need for strong refrigeration

requirements in order to keep superficial plate temperatures sufficiently low to allow a discounting of the emission component.

Since a significant amount of the plate refrigeration is provided by the transpiration airflow, this will lead to the use of comparatively high mass flows, as discussed below, but requires a study of the behaviour of plate temperatures under different incident heat fluxes for any given transpiration mass flow.

A variety of simulations was carried out by setting increasing values of furnace temperature for a range of transpiration mass flows, but in order to study the influence of the received radiation on the plate temperatures, a given mass flow must be set. A fixed outer refrigeration temperature was assumed for the moment at 200°C, although a more detailed study of this parameter will be performed and discussed later in the chapter when simulations on the porous medium are analyzed.

Some of the assumptions made during the discussion of the analytical models in the previous chapter and the dimensioning procedures discussed above were verified, namely the very small temperature gradients across the plate's thickness and the avoidance of choked flow conditions in the range of transpiration mass flows used in the simulations. The fact that these temperatures are also influenced by the sensing element's emissivity must also be kept in mind, so a parametric study for this variable is also desirable. Shown in Figure 3.16 are the results of simulations at a fixed transpiration mass flow ( $1 \times 10^{-3} \text{ kgs}^{-1}$ ) for increasing radiation source temperatures, with three different plate emissivities.

For the higher furnace temperatures, large differences in measured plate temperatures are apparent, which renders a precise determination of this parameter especially important.

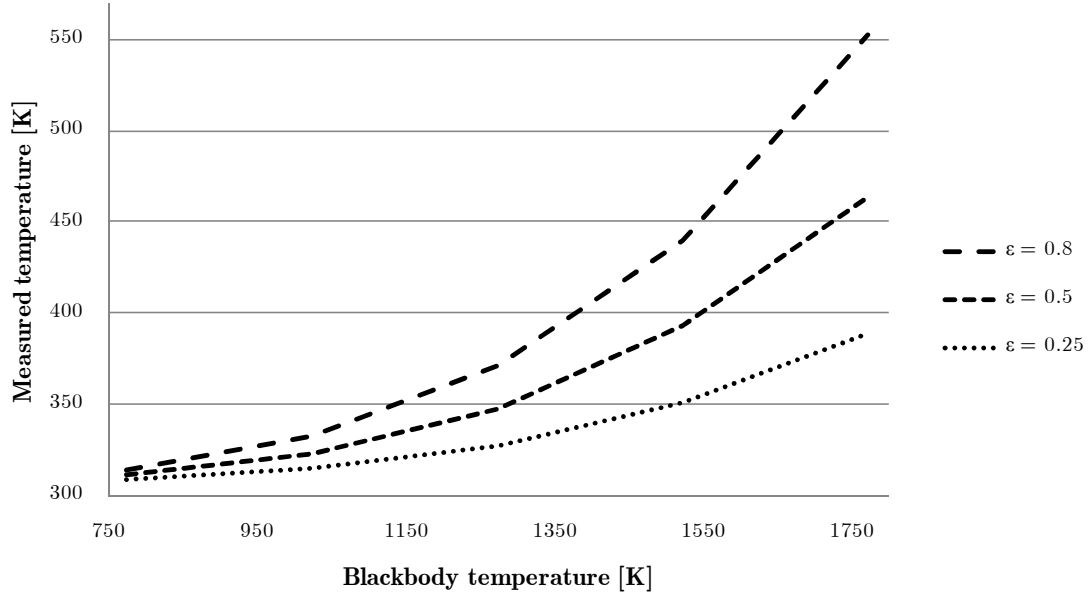


**Figure 3.16** – Plate temperatures as a function of furnace temperature and plate emissivity.

The aforementioned plate temperatures are also especially relevant regarding the underlying assumption that the emission component of the radiative balance between the plate and its hot surroundings can be ignored. Surface temperatures must be kept to low values (*e.g.* smaller than 100°C) in order not to invalidate this assumption. This in turn requires adequate plate cooling if the instrument is to work at high furnace temperatures, and most of the cooling will be provided by the transpiration airflow, as discussed in the next section. In any case, for low surroundings temperatures the radiative balance may not allow the convenient assumption of a non-significant emissive component for the plate. Consequently, if a model that relies on such an assumption is to be comfortably used, high surroundings temperatures must be assumed.

### ***3.4.2 Variations of Plate Temperatures with Transpiration Mass***

#### ***Flows***

In a similar fashion to the simulations discussed before for the variations of plate temperatures with various incoming heat fluxes caused by blackbodies at various temperatures, simulations of the thermal behaviour of the plates can also be set up in order to study the influence of increasing mass flows, for a given heat source temperature. Such a study is especially relevant in order to evaluate the mass flows

necessary to enable neglecting the radiative emission of the plate, by studying the temperature distribution over it.

Illustrated in Figure 3.17 is the variation of plate temperatures for the maximum furnace temperature of 1773 K and various transpiration mass flows and plate emissivities. Another less evident but nevertheless intuitive parameter must also be taken into account, and that is the temperature of the compressed air supply. While values measured in the laboratory in the months of August and September were typically between 20 and 25°C and most of the time closer to the latter value (which for that motive was used as a reference in simulations), values measured in December could be as low as 10°C, which rendered relevant a study of the influence of air supply temperature, since some differences are expected for lower heat flux levels and higher mass flows. This effect must be taken into account in practice for calibration and operation purposes, by specifying a correction coefficient for the airflow temperature that can take the form of the deviation percentage shown in Figure 3.18, where temperatures obtained at 10°C are divided by those obtained at 25°C.

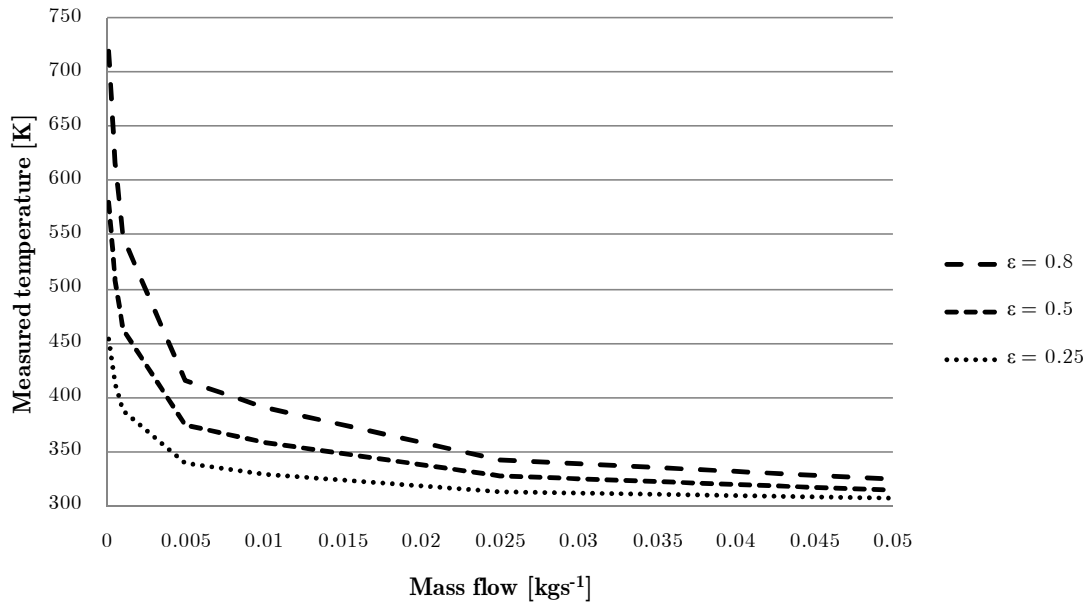


**Figure 3.17** – Plate temperatures as a function of transpiration mass flows and sensing element emissivities.

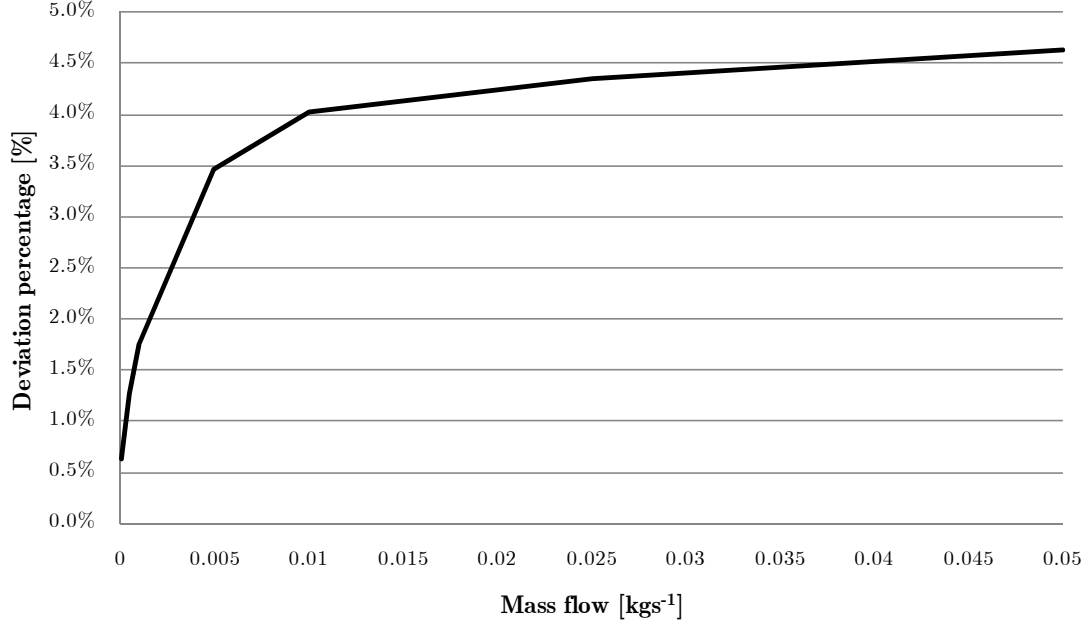


**Figure 3.18** – Percentage of deviation in measured temperatures for different supply temperatures.

These results emphasize the need of using relatively high transpiration mass flows for emission component minimization purposes. It should be kept in mind that higher mass flows could possibly lead to compressibility issues in the perforated plate. There is therefore a need to balance the sensitivity of the system with the assumption of insignificant emission values and the guarantee of boundary layer blow off.

Besides boundary layer blow-off and refrigeration considerations requirements that tend to dictate that mass flows be kept as high as possible in most situations, the effect of increasingly high mass flows, obviously bounded by the onset of compressibility and choked flow, is to diminish the dependence of the instrument output on the mass flow, and this effect is visible in the asymptotic behaviour of the sensor temperature curves, that flatten for increasing mass flows.

Attaining a temperature reading value independent of the mass flow may not be possible for the reasons mentioned above, but another effect of the high mass flows is to diminish the instrument's sensitivity for a given furnace temperature range, since the relative magnitude of values measured by the thermocouple will be compressed, so to speak, to a narrower temperature range.

A maximum plate temperature can be defined as the temperature that, resulting in an emission component:

$$q_{\text{em}} = \varepsilon \sigma T_{\text{max}}^4 \quad (3.23)$$

will lead to a relationship where emitted radiative flux will be a small percentage of the received flux, of the type:

$$q_{\text{em}} < 0.02 q_{\text{rec}} \quad (3.24)$$

or

$$T_{\text{max}} < \left( \frac{0.02 q_{\text{rec}}}{\varepsilon_{\text{plate}} \sigma} \right)^{0.25} = \left( \frac{0.02 \varepsilon_{\text{furnace}} T_{\text{furnace}}^4}{\varepsilon_{\text{plate}}} \right)^{0.25}. \quad (3.25)$$

Illustrated in Table 3.4 are the maximum admissible temperatures that satisfy the 2% requirement, listed for various plate emissivities and furnace temperatures, assuming blackbody behaviour for the furnace cavity. A comparison between the values in the table and the graphs in Figures 3.16 and 3.18 shows that the fulfilment of the requirement is not particularly troublesome, even for blackbody furnaces and expectably even less so for sources with smaller emissivities.

Likewise, a maximum value for the transpiration airflow can be defined for accuracy and sensitivity reasons, but while earlier transpiration radiometers relied on the measurement of a temperature difference that could be rendered too small for accuracy by high mass flows, the present instrument only measures one temperature. Its sensitivity over a range of temperatures is however strongly affected by the mass flow as mentioned above, but a mass flow value that would render the line slopes of Figure 3.18 too small to be meaningfully measured would be limited by the onset of choked flow conditions.

**Table 3.4** – Maximum admissible temperatures for emission component minimization.

<b>Furnace Temperature [K]</b>	<b>Plate Emissivity</b>		
	<b>0.8</b>	<b>0.5</b>	<b>0.25</b>
1773	705	793	943
1523	606	681	810
1273	506	569	677
1023	407	457	544
773	307	346	411

A sensitivity coefficient for the instrument can be defined as the ratio between its output signal and the received heat flux, the measured temperature also depending on the transpiration mass flow in addition to the received heat flux. The sensitivity coefficient can thus be plotted as the ratio  $T_{\text{measured}} / q_{\text{rec}}$  for the range of transpiration mass flows [Martins 1998].

A linear relationship will exist between the thermocouple reading and the fourth power of the furnace temperature, which multiplied by the Stefan-Boltzmann constant and the furnace cavity emissivity becomes the radiation emitted by the source. This linear relationship enables the determination of the heat flux for a given temperature reading, and can also be expressed in an inverse fashion, with the measured temperature as function of the incident heat flux. This alternate version represents the relationship between the instrument's output and the incident radiation and is useful because the linear relationship is preserved when the incident radiation is divided by the mass flow at which the curve was obtained. This allows a direct representation of the linearity of the steady-state instrument response, each instrument having its particular curve as an individual characteristic [Martins 1998]. These considerations apply for steady state conditions, while the intended pulsed transpiration mode is intrinsically transient. The simulation of transient conditions will be discussed later, but such considerations are nevertheless useful given the fact that the instrument under discussion can conceivably be used as a conventional, steady state transpiration

radiometer, although this is not its intended function and its calibration in such conditions was not carried-out.

### ***3.4.3 External Refrigeration System Temperatures***

As mentioned above the presence of a swirling component in the refrigeration airflow, injected tangentially in the non-porous casing base and intended to augment its residence time in the space between the solid cone and the porous holder, makes the use of the 60° symmetry more problematic, first of all because more mesh elements would be needed. Periodic boundary conditions could have been used in order to reproduce the swirling airflow but a less computationally burdensome solution was used instead. With the exception of the microperforated plate, the geometry of all components, including the porous holder, is fully modelled. The microperforated plate is modelled as a second porous medium for which an interfacial contact area between solid and fluid phases was easily calculated given the very well-ordered geometry of the plate.

Despite the fact that the bulk of the system refrigeration comes from the transpiration airflow, simulated values for the temperatures achieved at the surface where the perforated plate is attached to the porous holder were obtained in two distinct parametric studies. In all cases a heat transfer coefficient was set in the plate, with the same magnitude as discussed in Chapter 2 for the convection coefficient in the perforated pattern, but with a low, conservative value. Furnace temperatures were set at their maximum value of 1500°C. In the first, the refrigeration airflow is set to zero while various transpiration mass flows are simulated passing through the perforated plate, corresponding to a situation where all the plate refrigeration comes from transpiration. A conservative value for the convection coefficient in the porous medium was assumed, and the radiation source was set as a blackbody, which will not necessarily be the case in practice. Average temperatures on the interface between the plate and the porous medium can be determined, as illustrated in Figure 3.19. These temperature values are useful because they can serve as pessimistic estimates for the fixed outer refrigeration temperature assumed in the parametric studies of plate temperatures. Figure 3.19 shows that the value set at 200°C was indeed on the high side and that temperatures on the rim of the plate are lower.



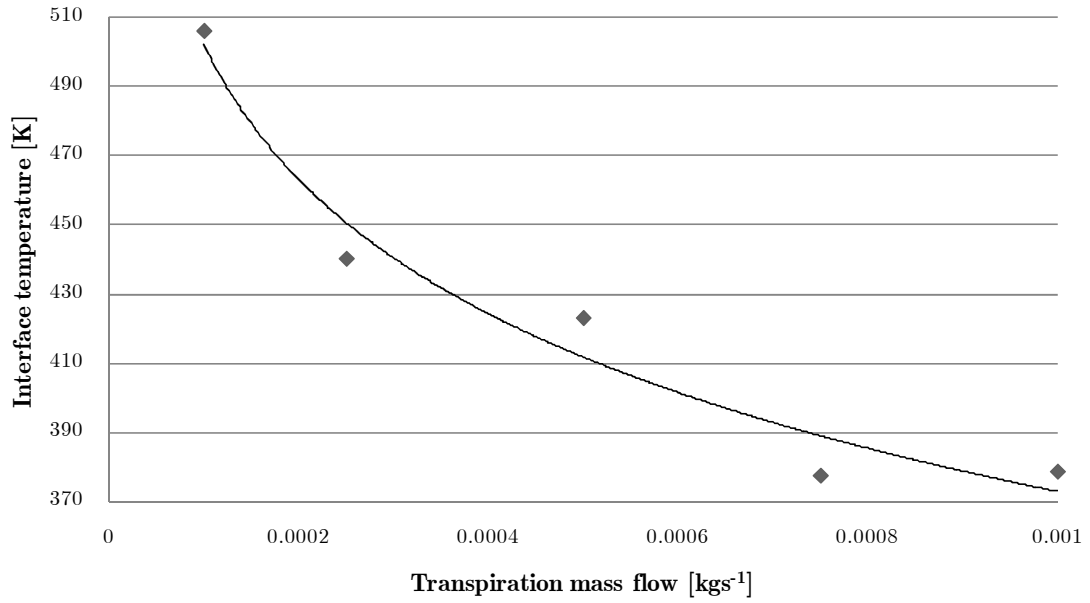


**Figure 3.19** – Average temperatures on the interface between the plate and the porous medium for various transpiration mass flows.

In the second study the transpiration and refrigeration airflows were both set at  $0.0005 \text{ kgs}^{-1}$  and the same temperatures as above were determined and are illustrated in Figure 3.20. The same conclusion as above regarding the fixed outer refrigeration temperature applies.

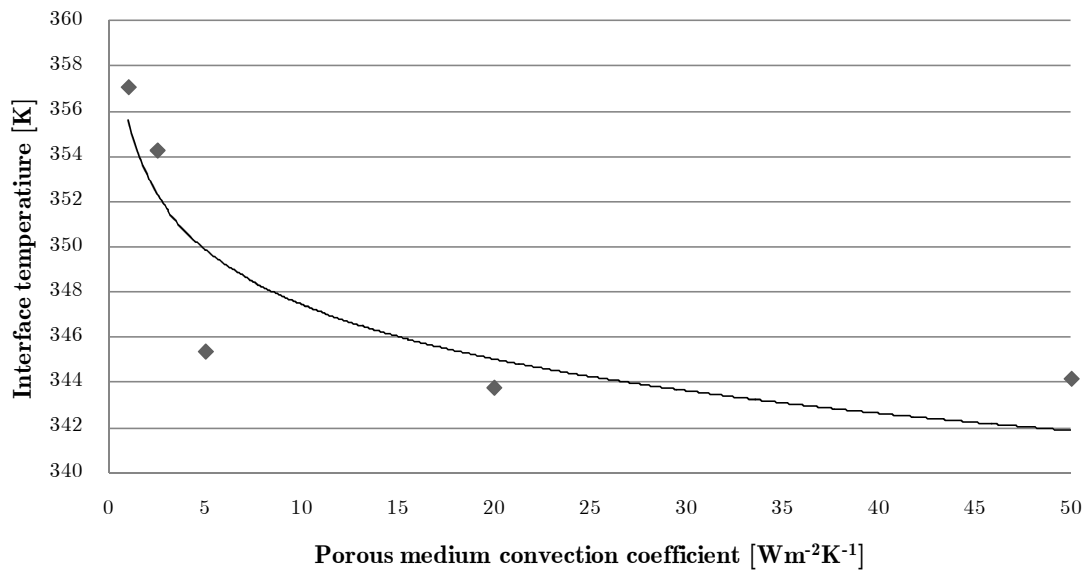


**Figure 3.20** – Average temperatures on the interface between the plate and the porous medium for various convection heat transfer coefficients.

#### ***3.4.4 Transient Temperature Curves***

The intended pulsed operation mode for the instrument dictates that the transient behaviour of its sensing element be studied, when exposed to variations in incident heat flux, or more particularly in this context when variations occur in the transpiration airflow.

Besides the matter of ascertaining whether the default airflow is supercritical or not and the implications of this fact on the nature of the heat flux being measured, the intensity of the pulses must be adjusted to ensure that temperature levels in the plate are kept within reasonable limits. Besides the obvious requirement of avoiding excessive temperatures that could damage the components of the system, the plate emission component of the radiative heat balance must be must once again be considered.

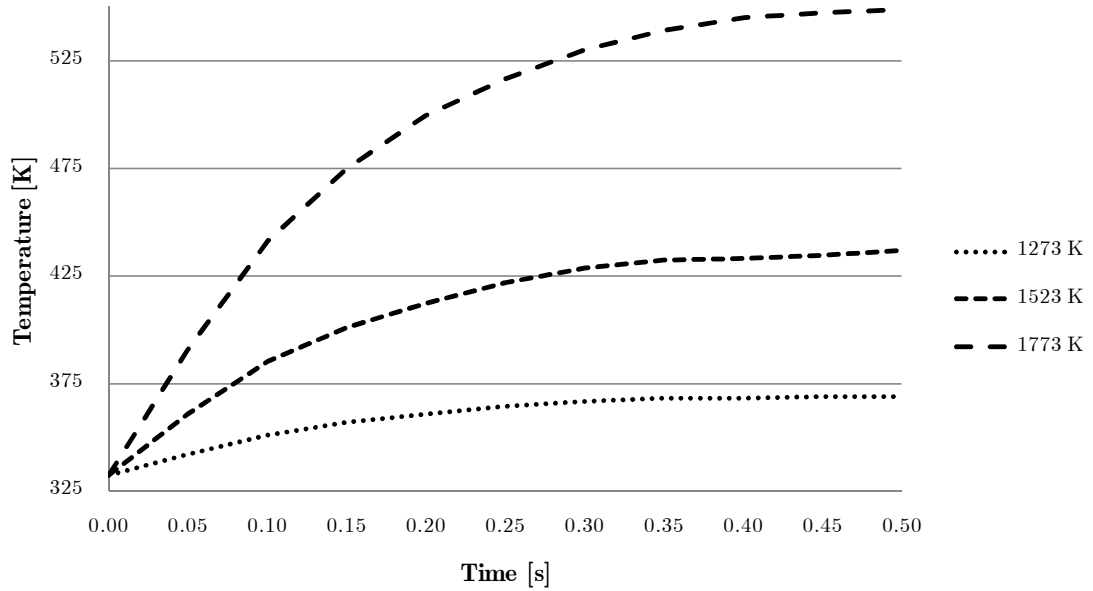
A steady-state first approach to the problem will result in temperature profiles such as those illustrated in Figures 3.16 and 3.17, and temperature levels for the instrument operating purely as a radiometer can be evaluated in this way. Once the transpiration airflow is reduced or even shut down, temperatures will rapidly rise to high values, so it is impractical to keep the airflow at low levels for significant times. This is nevertheless an improvement over previous transpiration radiometers, where the transpiration airflow had to be kept at high values at all times in order not to compromise the sensing element's cooling, transient behaviours being induced using mechanical shutters in front of the furnace openings.

Various transient simulations were therefore conducted in order to gain some insight into the sensing element's thermal behaviour when subjected to sudden variations in incident heat fluxes or transpiration mass flows. Such simulations were set up using the results of steady-state simulations as initial values and were especially intended to evaluate the slopes of the transient temperature curves to be expected in practice.

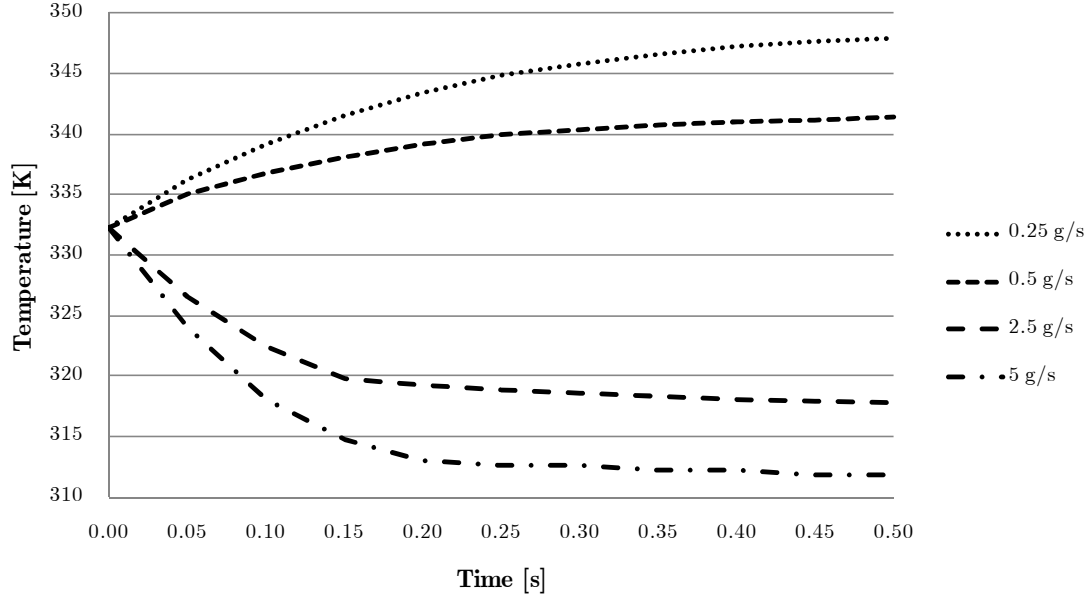
The effect of increased furnace temperatures starting from a moderate initial value were simulated first, in a process akin to that described for the transient testing of earlier transpiration radiometers where the transient behaviours were obtained through the use of a mechanical shutter placed between the sensing element and the furnace. Illustrated in Figure 3.21 are transient temperature curves at the centre of the

plate for a situation where a  $0.001 \text{ kgs}^{-1}$  transpiration mass flow crosses the sensing element, initially for a blackbody cavity temperature of 1023 K and then subjected to steps in furnace temperature to 1273, 1523 and 1773 K. The surface emissivity of the sensing element was set at 0.8.

Simulated next were more relevant situations where the transient behaviour is obtained by variations in the transpiration mass flow. The same initial situation as above was used, and steps in the initial  $1 \text{ gs}^{-1}$  mass flow were specified at 0.25, 0.5, 2.5 and  $5 \text{ gs}^{-1}$  and no variation in the furnace temperature, with the resulting transient temperature curves at the centre of the plate illustrated in Figure 3.22.



**Figure 3.21** – Transient temperature curves at the centre of the plate for various steps in furnace temperature and a constant transpiration mass flow.



**Figure 3.22** – Transient temperature curves at the centre of the plate for various steps in transpiration mass flow and a constant furnace temperature.

In all cases differences in the slopes of the transient temperature curves are evident, depending of the intensity of the driving force for the temperature variation, *i.e.* higher temperatures or more or less refrigeration, and as expected the intensity of the rate of change, materialized in the slopes, is higher for larger steps in temperature, positive for lessened transpiration airflows and negative (reflecting a cooling process) for heightened transpiration airflows.

Notice that in all cases the transpiration airflow was never shut off, while the intended pulsed transpiration operation mode will demand such conditions, or at least will require significantly lower transpiration mass flows in order to enable the measurement of the convective component of the incident heat flux.

As mentioned earlier, such situations where the transpiration airflow is cut are simulated by setting the local fluid temperature at the same value as the external blackbody temperature, to get a sense of the magnitude of the slopes of the resulting temperature curves, that would never be allowed in practice but that could conceivably be encountered and dictate such transient responses before the transpiration mass flow was reset at its initial value.

The pulsed transpiration operation mode means that the stabilized temperature values shown above will never be reached due to a continuous switching on and off of the transpiration airflow. In practical terms this means that the temperature must be monitored and the electrovalve that controls the transpiration airflow must open when temperatures above a specified value are detected. On the other hand, as mentioned earlier, the valve does not have to stay shut until stable readings are obtained for the total heat flux, since measuring the slope of the transient temperature curve allows the anticipation of this steady-state value because of its proportionality to the incident heat flux [Hit 2004, Martins *et al.* 2006].

The use of short duration pulses is also relevant because if the on/off cycles are short enough, it can be assumed that conditions in the surroundings have not changed significantly and heat flux partitioning is achieved because both components of the total heat flux are measured, radiation directly and convection by difference between successive total flux and radiation measurements. This is possible provided that the data acquisition system has enough time resolution for the purpose and places challenges in terms of temporal resolution and noise levels that must be adequately addressed.

The new element's much lower thermal inertia makes for much faster temperature curve responses, which in turn allow the switching off of the transpiration airflow for very brief times that nevertheless allow sufficient temperature increases for curve slope calculation and total heat flux determination, although it is conceivable that in some situations it may be practical to wait for steady-state values if variations are sufficiently rapid, as would be the case in high temperature and high transpiration mass flows situations.

The software does not allow the direct specification of two different alternate mass flows, so a step function (set either at a zero or one value) controlled by a sine function using the intended period as an argument was implemented to control the airflow value as a function of time.

The adjustment of the periodicity of the mass flow pulses will be dictated by the instrument response as a function of prevalent temperatures and mass flow

combinations and will require some level of adjustment and calibration in any case to keep temperatures within reasonable bounds, as discussed further in Chapter 4.

Illustrated in Figure 3.23 are *CFX* output graphs two different furnace temperature-transpiration airflow combinations where the measured temperature values are kept roughly within the same range by adjusting the pulse period. Temperatures rise when the airflow is set to zero by the step function and decreases when the mass flow is reset at its default specified value. Mass flows and furnace temperatures were in these cases set to moderate values in order to illustrate curves with equally moderate slopes. As discussed in Chapter 4, very steep variations are encountered in practice.

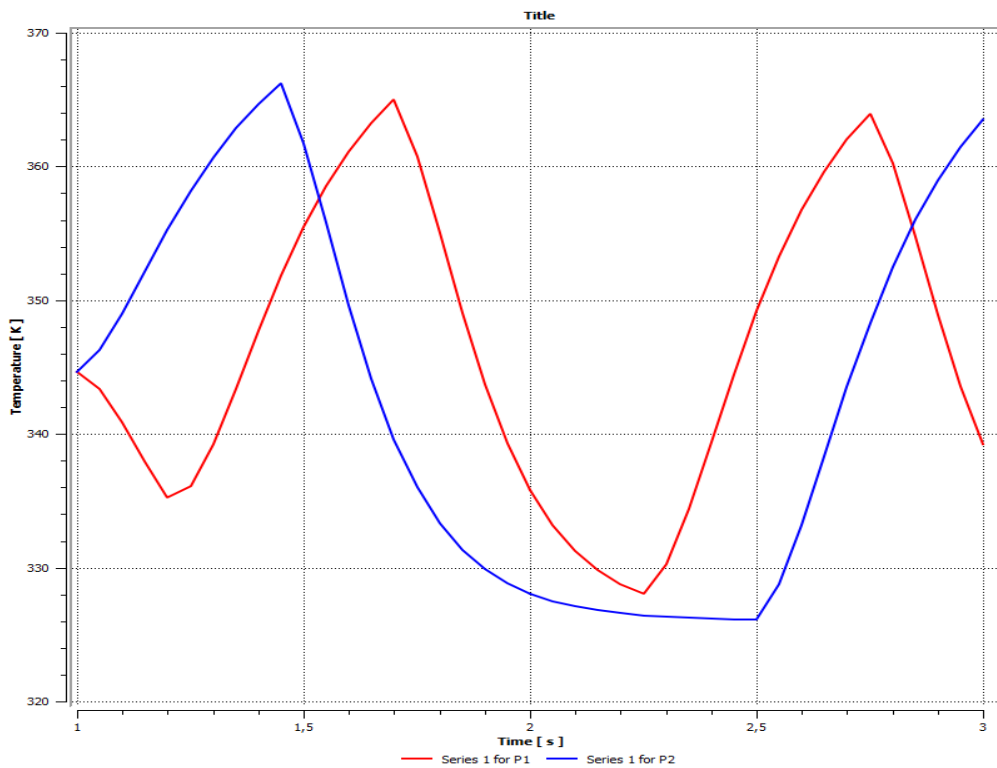


**Figure 3.23** – Transient temperatures in the plate.

The intended transient transpiration mode means that the instrument calibration is not to be carried out as for conventional transpiration radiometer, but rather by determining the variation in slope of the transient temperature curves for a variety of conditions.

Since a large number of on/off cycles (within limitations imposed by a minimum temperature interval necessary for slope determination and by the electrovalve

response) is expected to occur for any given time interval, a calibration process will consist of the analysis of response curve slopes with the intention of establishing a quantitative linear relationship between furnace set points, transpiration airflows and transient temperature curves slopes, as discussed in detail in Chapter 4.

### **3.5 Concluding Remarks**

The dimensional and operational parameters that influence sensor performance were determined and discussed, based both on established analytical principles and on the simulation software that was compared to the analytical models discussed in the previous chapter.

Assumptions and simplifications made in the process of developing the analytical model were discussed and found to be reasonable.

Ranges for the relevant mass flow values to be used for the intended range of furnace working temperatures could also be identified in order to guarantee the simplification of the radiative balance between the plate and its surroundings and to ensure proper boundary layer control while avoiding compressibility phenomena. The instrument's transient behaviour was also found to be within expectations and the proposed external cooling system was likewise found satisfactory in theory.

These procedures in turn led to the building of the prototypes discussed in the following chapter and provided the framework to evaluate their performance, by comparison with simulated values determined using the methodologies discussed above, although necessary adjustments naturally had to be made in order to accommodate differences dictated by laboratory conditions.





## CHAPTER 4

# EXPERIMENTAL STUDY

A detailed discussion of the experimental setup is presented along with the presentation and discussion of data acquisition and control setups.

The specifications of the various components that were used in the course of the experimental work are presented and their integration into the data acquisition and control system are detailed along with implemented methodologies and procedures. Special relevance is given to the data processing flow and operations. Measurements carried out with the discussed setup are described and relevant comparisons with previously developed analytical and numerical models are made against experimental data. Instrument calibration procedures are also proposed, described and discussed, together with the experimental uncertainty analysis.

### 4.1 Introduction

In the previous chapter design strategies based on the use of analytical and numerical models for the heat and mass transfer phenomena in the sensing element were presented, discussed and used to build design rules in order to meet requirements, prototypes of the instrument being built based on those design rules.

These prototypes are identical as far as their principal physical features are concerned, although small differences resulting from the various manufacturing and assembly processes cannot be ruled out and will be addressed later in order to verify if significant biases are induced. In the present chapter the experimental verification of the instrument prototypes is presented and discussed.

The chapter starts with a discussion of the experimental setup and of the equipment selection procedures, along with the presentation and discussion of data acquisition and control setups. The various components that were used in the course of the experimental work are presented, while their integration into the data acquisition and control system is detailed along with implemented methodologies and procedures,

including the data processing flow and operations. Measurements carried out with the discussed setup are described and relevant comparisons with previously developed analytical and numerical models are made against experimental data. Instrument calibration procedures are also discussed.

## 4.2 Integrated Hardware and the Prototype

The essential components of the experimental set-up comprise the above-described flux meter instrument, a radiation source and a data acquisition and processing system, as illustrated in Figure 4.1. Characteristics of the various components are given in detail in the next paragraphs.

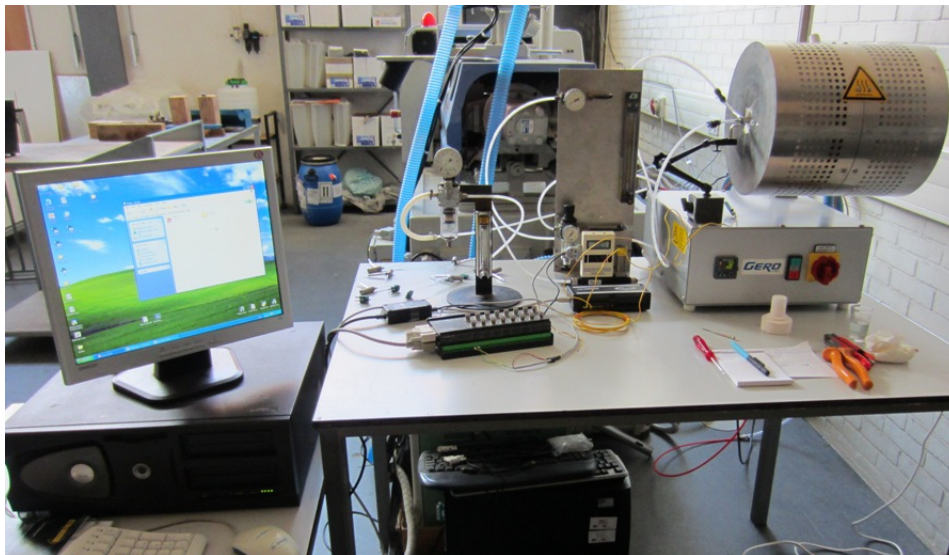


**Figure 4.1** – Experimental System.

The transpiration gas mass flow rate control and measurement is a fundamental aspect in the operation the present instrument, and accurate heat flux measurements are dependent not only of an accurate measurement of the temperature in the microperforated plate but also of a precise control and measurement of the transpiration gas mass flow rate.

As mentioned earlier, compressed air was chosen as the transpiration gas. A pressure regulator, a gas filter, a rotameter and two manometers compose the TG control unit. The pressure regulator has the function of uncoupling the pressure in the

instrument air circuit from that in the air supply line. Without this regulator, any pressure fluctuation in the line would be transmitted to the instrument circuit resulting in TG mass flow fluctuations affecting the instrument readings. The filter was chosen so that its grade efficiency is higher to that of the porous disc material, filtering particles as small as 5  $\mu\text{m}$ .

The rotameter (and its associated needle valve) has the function of controlling and measuring the TG mass flow rate. Depending on the TG mass flow rate, different pressure levels are obtained downstream, so that a manometer is required to calculate the actual mass flow rate. Figure 4.2 shows a photograph of the TG control unity panel together with the corresponding diagram. A digital mass flow meter was also available and was tested, showing similar readings to those of the rotameter. Since the latter caused lesser pressure losses and was easier to control, it was used preferentially.

The pressure regulator and the filter are standard pneumatic devices from Parker Hannifin Co. with a maximum input pressure of 10 bar and a maximum output pressure of 6 bar. The rotameter is an Omega Engineering instrument (FL-3840ST model) with maximum output of 40 SLPM of air at 20°C and 1.013 bar, an accuracy of  $\pm 2\%$  FS and a repeatability of  $\pm 0.25\%$  FS. The manometers are manufactured by VDO and have a maximum output of 4 bar and an accuracy of  $\pm 2.5\%$  FS. Only the transpiration airflow is connected to this setup, the refrigeration airflow being connected to the same compressed air supply but without any control besides preliminary checks that were sufficient to ensure that the refrigeration mass flow values employed in the simulations discussed in Chapter 3 were actually exceeded in practice, although in part due to some leakage within the sensor casing, as discussed further below.

The overall configuration of the instrument was discussed in Chapter 3, along with the dimensioning of the main features of the most important system components, namely the microperforated plate, the airflow separation cone, the porous outer casing and the non-porous base on top of which the porous holder is placed. The aforementioned components are illustrated and briefly discussed below.

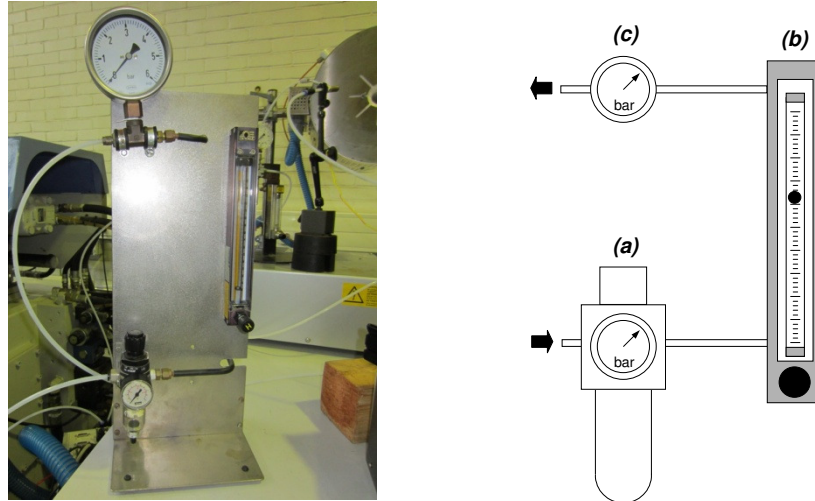


**Figure 4.2** – Photograph and diagram of the TG measurement and control unit, showing the pressure regulator (a), the rotameter (b) and the manometer (c).

Each component was ordered in a total of 12 units with the available budget, except for the perforated plates, of which 50 were purchased. It was at first thought to keep some components in reserve but the decision was eventually taken to incorporate all available parts into prototypes, since some level of damage to the parts was to be expected during testing and valuable time could be lost waiting for the assembly of new prototypes.

A major concern was the robustness, or lack thereof, of the attachment of the thermocouple to the perforated plate. While some of the weldings eventually broke, mainly due to some rough handling such as being dropped, others resisted quite well, which indicates a need to improve both the robustness of the joint itself and the repeatability of the welding process, transforming it from an artisanal task into an industrial process.

The microperforated plate is arguably the most important component given its function as a sensing element and as fundamental in preserving the transpiration principle. As discussed earlier a survey of providers, manufacturing technologies and prices for obtaining the plates resulted in the selection of photo-etched components that made holes with diameters smaller than the plate thickness extremely difficult to obtain, thus placing limits on hole diameter to plate thickness ratios.

The stainless steel plates were provided by a leading photoetched component manufacturer, Precision Micro Ltd of Birmingham, UK. As illustrated in Figure 4.3 the process require some adjustments but did eventually result in the intended perforated pattern. In order to increase their emissivity, an oxidisation procedure consisting in keeping their temperature at 850°C for approximately 8 hours was performed, although a totally uniform matte black colour for the whole surface was not achieved. Figure 4.4 shows an oxidized plate after it was mated to the porous holder and with the thermocouple laser-welded on, together with a non-oxidized sample. A difference in surface colour is apparent but the surface is still highly specular, so this treatment probably had little effect and the surface emissivity is probably close to that of the original non-oxidized stainless steel.

The determination of surface emissivities is a field of its own and has given rise to a large number of publication, including detailed studies for relevant emissivity measurement methodologies in materials of interest such as different types of steel at comparatively low temperatures [Carpenter and Sewell 1962], or for much higher temperature values [Paloposki and Liedquist 2005], as well as for other metallic alloys [Maynard 2011]. In any case it is apparent that the emissivity values usually encountered in technical tables are consistent and generally accurate, and indicate that emissivities for polished, non-oxidized stainless steel such as the one received from the manufacturer typically has a surface emissivity lower than 0.2 and potentially as small as 0.1.

The temperature and time of this oxidization process could have been increased, but given the plate's very low thickness and small hole diameters there were some concerns that stronger oxidization could weaken the component and render it unable to withstand the air pressure from the transpiration airflow, so the matter was not pursued further.

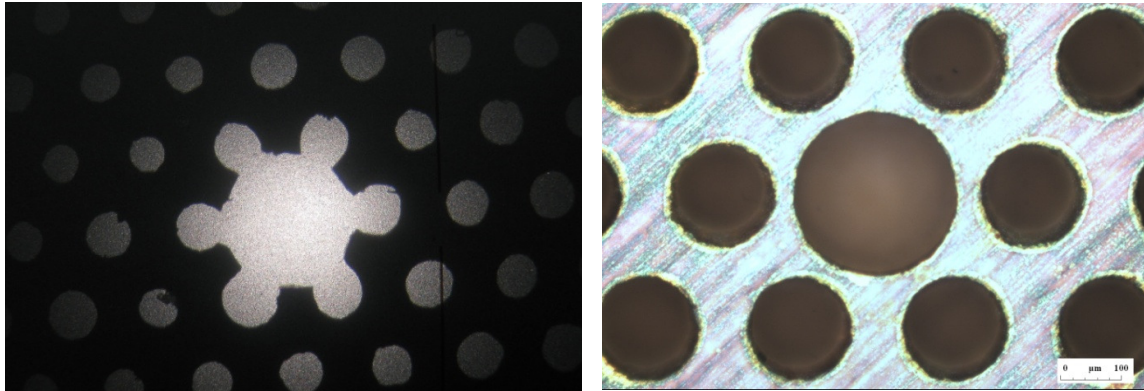


**Figure 4.3** – Microperforated plate: early unsuccessful attempt and detailed view of the intended microperforated pattern.

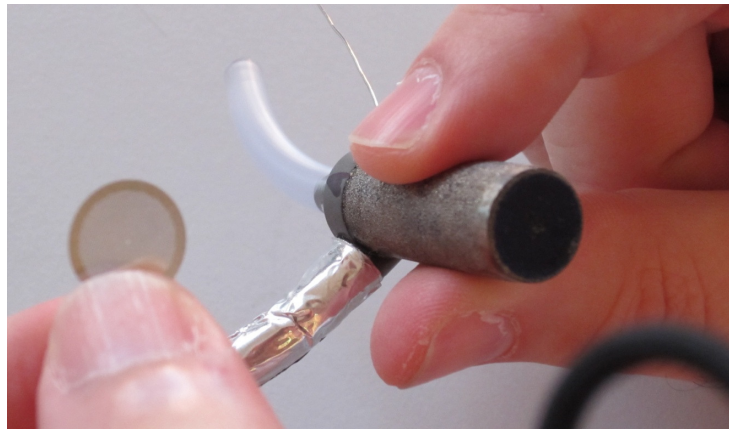


**Figure 4.4** – Non-oxidized plate sample and oxidized unit mounted on instrument.

Illustrated next in Figures 4.5 and 4.6 are the stainless steel non-porous base (including the refrigeration airflow tubing) and airflow separation cone (including the small hole where the thermocouple is passed). Both components were machined using standard turning and milling equipment, and sourced from local manufacturers. The cone was the more difficult of the two to obtain, given the need of long and thin turning cutting tools for the machining of its inner cavity. This capability was not as easy to find locally as expected but was nevertheless found at an injection moulds manufacturing company in the Aveiro region, without the need of purchasing special tools for the purpose.

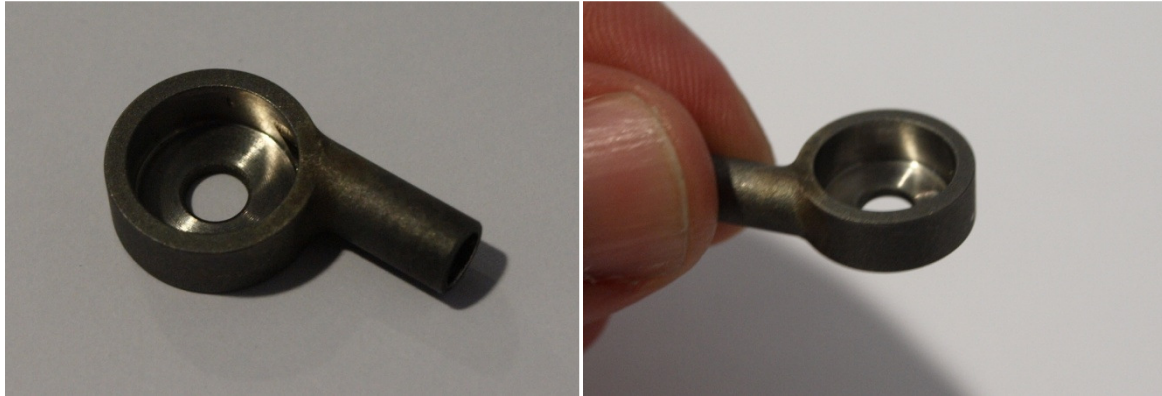


**Figure 4.5** – Non-porous base and refrigeration airflow tubing.

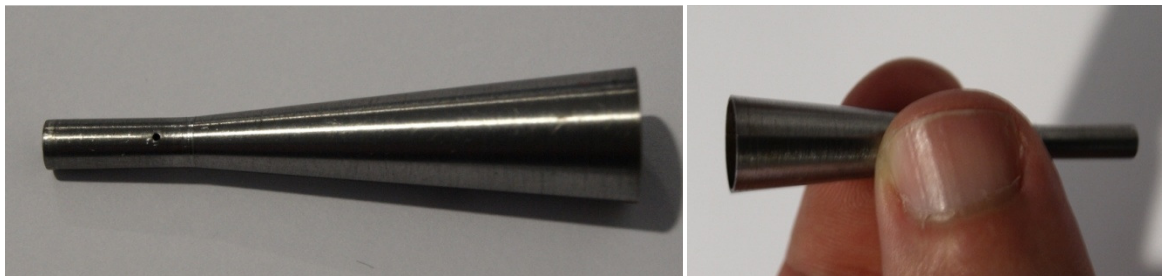


**Figure 4.6** – Non-porous cone for airflow separation.

Illustrated next is the porous holder (Figure 4.7). This component was somewhat more difficult to obtain, for various reasons.

Some companies specializing in porous components were contacted in order to ascertain their capabilities in terms of part specifications, both in terms of porosity parameters and achievable dimensional tolerances. The latter item was especially relevant because of the small dimensions of some parts of the components. These were typically obtained by building moulds which were then filled with small diameter metal spheres that were subsequently sintered. Given the fact that a relatively small number of components was to be ordered for the prototypes, delivery times and most of all prices were regarded as being unreasonable because they represented a significant portion of the available budget. Smaller unit prices could only have been obtained for much larger orders that would have been too costly to consider, especially as far as early prototypes are concerned, since lessons learned during this study could not have been incorporated. There was therefore a need to find a viable alternative.



Some industries rely on porous steel components that are machined from porous blocks rather than moulded. Plastic injection mould manufacturers, for instance, use porous steel in some parts of the moulds for degassing purposes, and such parts could be machined from commercially available porous blocks. The porosity parameters were not necessarily optimal regarding the porous medium performance but some compromise was necessary if components were to be obtained at a reasonable cost for an adequate performance. This less optimal solution meant that there was not as much freedom of choice in terms of unit cell and pore configurations as for a custom made porous medium. This in turn did not for instance allow the selection of better studied porous structures for which more analytical and empirical relationships would have been available for use in the numerical studies mentioned in the previous chapter.

The parts were thus made using metal manufactured by International Mould Steel, Inc. of Florence, Kentucky, USA. Porcerax II comes as sintered steel blocks with 25% porosity, consisting of interconnected pores averaging 7 microns in diameter, dispersed throughout the material. Thermal conductivity is similar to a 400 Series stainless steel.



**Figure 4.7** – Porous holder.

Several processing technologies for obtaining the final components can be used, although EDM (Electrical Discharge Machining) is recommended in order to maximize venting. This was done but in turn led to the occurrence of another potentially serious problem. Component specifications were provided to a local company with EDM



equipment and manufacturing proceeded without problems until the final step, where an employee polished the parts in order to make them look better. This obviously led to concerns regarding the maintenance of the surface porosity. Another EDM passage was then performed and the components duly exhibited the rough surfaces typically obtained with EDM, but the extent to which polished could have affected porosity along the component's thickness remained.

Once the prototypes were assembled and the compressed air lines were connected, very little airflow was apparent by touch through the porous medium, which was not completely unexpected considering the results of the CFD simulations described in Chapter 3.

A very simple test was nevertheless carried out in order to illustrate the passage of the refrigeration airflow through the porous medium, using a drop of dishwashing liquid detergent dissolved in water. By dipping a fingertip in that water and then touching the porous component, thus leaving a small amount of water on top of it, a foaming of the detergent could immediately be observed, proving the passage of the airflow, as illustrated in Figure 4.8.



**Figure 4.8** – Porosity verification.

The matter of assembling the aforementioned components naturally came about next. One of the interesting aspects of the proposals received from the porous component manufacturers was the option of having all components built, assembled and factory-tested for airtightness. The greater part of the costs was that of the porous

components themselves, and as mentioned earlier was in itself sufficient to make finding another option necessary, but such an option would have been the most interesting from a strictly technical point of view, if financially unpractical. It should nevertheless be considered in future versions of the instrument, especially if the patenting process proceeds further.

Since all components, including the central sheathed thermocouple, were metallic in nature, some form of welding and brazing process was envisaged for their assembly. Local industries and workshops with welding capabilities were contacted but replied that they were not up to the task of handling such small components, especially the thermocouple.

Watchmakers or jewellers with the ability to carry out repairs were then sought but such capabilities were found to be not as widespread as they once were. Watches are nowadays much more reliable than several decades ago, while typically either much cheaper and not worth repairing, or expensive but usually sent back to the manufacturer for repairs. Jewellery is another matter and repairs must indeed take place, usually being subcontracted to specialists that recommended contacting the institution where most of them get their training.

The Portuguese Professional Training Centre for the Jewelry and Watchmaking Industries (*CINDOR - Centro de Formação Profissional da Indústria de Ourivesaria e Relojoaria*) was therefore contracted and one of the teachers at the institution proved able and willing to provide the necessary assembly services for a very reasonable fee. The thermocouple was thus laser welded to the plate and the remaining components were brazed to each other. This artisanal method proved sufficient in this early prototype phase of development but more systematic and repeatable industrial processes are necessary if and when commercial instruments are to be built, this matter and its implications being addressed in greater detail later on.

Temperature measurements in the microperforated plate are made using ungrounded 0.25 mm diameter, stainless steel sheathed, K-Type Omega thermocouples (KMQSS-IM025U-300) that are passed inside the conic element through a sealed hole in its lower tube and are then laser-welded to the centre of the microperforated plate. Shown in Figure 4.9 is a close-up of the thermocouple attachment to the plate, once the

later has been brazed into place at the top of the porous holder. The temperature probes' output was verified for 273.15°C and 373.15°C and a maximum relative error of  $\pm 0.2 \%$  was found, both using the thermocouple calibration hardware available in the laboratory and the traditional boiling water/melting ice method.



**Figure 4.9** – Thermocouple attachment.

As discussed earlier one of the most important objectives was to significantly diminish the overall dimensions of the system, when compared with earlier transpiration radiometers. The achievement of this objective is readily visible in Fig. 4.10, where the proposed instrument is compared with an earlier, water cooled system [Martins 1998]. Shown are the water inlet, outlet and circulation system, the transpiration airflow conduit and the two thermocouples required by the older instrument. The newer system is much smaller thanks to its lower refrigeration necessities, which allow the use of a much more compact air refrigeration system. The difference in frontal area between systems is shown, being a potential issue in the installation of the sensors in systems where dimensions are restrictive factors. The earlier system is however more robust in actual operation, but this fact was a foregone conclusion evident from the start and was not the central issue.

Visible are the transpiration and refrigeration compressed air tubes. The latter is wrapped in aluminium adhesive foil in order to reflect radiative heat coming from the calibration furnace and avoid damage to the plastic tubing, given its proximity to the

furnace aperture and the fact that unlike the transpiration tubing it is not shielded by the instrument body. A more detailed view of the prototype can be seen in Figure. 4.11.

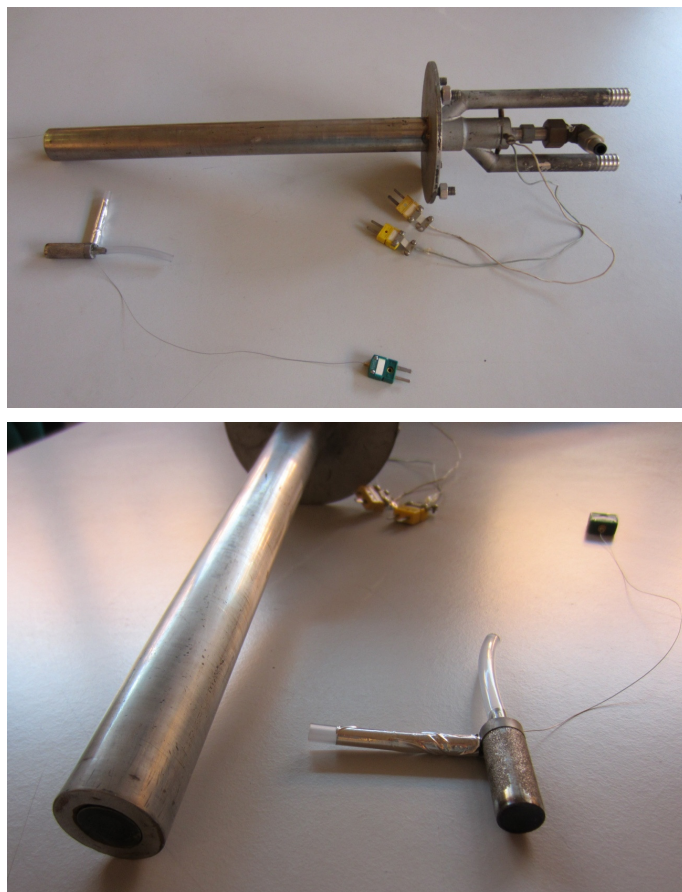


**Figure 4.10** – Size comparison between the proposed instrument and an earlier, water cooled system.

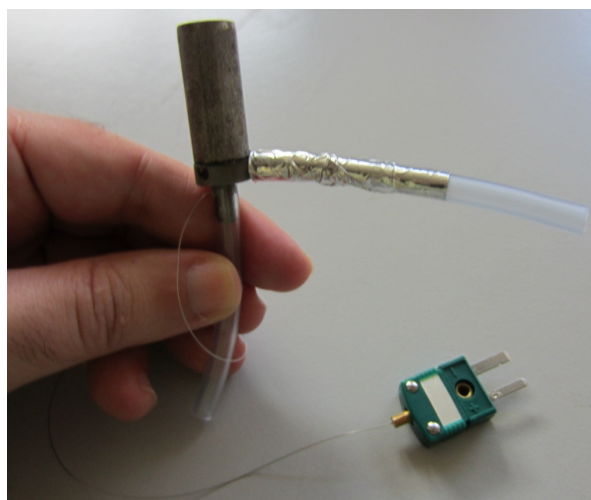


**Figure 4.11** – Assembled prototype.

Some other problems became apparent during testing. It was found that the aluminium adhesive foil intended to avoid damage to the plastic tubing by reflecting radiation coming from the furnace was not sufficient for the purpose. The plastic tubing was not affected directly, but the adhesive that was used to glue it to the metal tube was degraded, leading to its detachment under operation. Additional shielding was therefore needed and provided as illustrated in Figure 4.12. It consists of a thin metal plate coated with reflective material that is fitted to the front of the furnace using adjusting and spacing nuts. The plate has a central opening with a diameter such that only the instrument body can be fitted through it, leaving the refrigeration tubing on the outside.

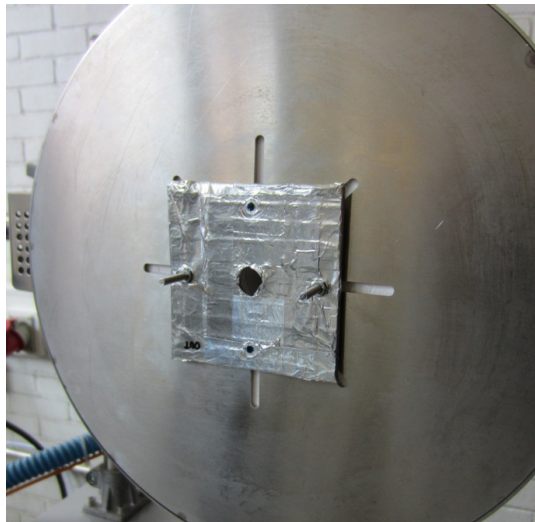


**Figure 4.12** – Additional tubing shielding.

Even this shielding was not sufficient depending of the configuration of the radiation source, which brings us to the matter of discussing its nature.

The primary radiation source, located in the laboratory of the Mechanical Engineering Department of the University of Aveiro, is a GERO RO 30-200 tubular furnace capable of reaching temperatures up to 1500°C. The furnace cavity is 30 mm in diameter, 350 mm in length and is heated over the central 200 mm of its length. The heating module consists of electric resistance  $\text{MoSi}_2$  wire coiled around a ceramic tube, integrated in light ceramic fibre insulation with a perforated stainless steel sheet

housing. The cavity's aspect ratio does not, however, insure that the radiating cavity can be considered as a black body, given verified temperature non-uniformities along the tube, as summarized in Table 4.1.

**Table 4.1** – Furnace axial temperature profiles

<b>Set Point</b>	<b>Position [cm]</b>					
<b>Temperature</b> [°C]	5	10	15	20	25	30
500	305	485	525	500	405	275
750	610	740	780	757	650	326
1000	808	986	1025	1000	890	580

If the furnace was to be reliably used for calibration purposes, its cavity's emissivity needed to be determined in order to quantify the amount of thermal radiation that exits the cavity as a function of the furnace controller set point. A NEC TH-9100 infrared camera was used to measure the temperature of the cavity, averaged over its whole area and assuming a unitary emissivity. The apparent emissivity can be defined as the ratio between the measured temperature value and the furnace set point:

$$\varepsilon_{\text{app}} = \frac{T_{\text{cav}}}{T_{\text{set}}} \quad (4.1)$$

Measurements were carried out over 4 days with ambient temperatures ranging between 21 and 25°C for furnace set points of 750, 1000, 1250 and 1500°C. These measurements lead to the calculated apparent cavity emissivities shown in Figure 4.13 along with the underlying linear relationship, plotted using the averages of the cavity temperatures and displaying the associated linear regression parameters.

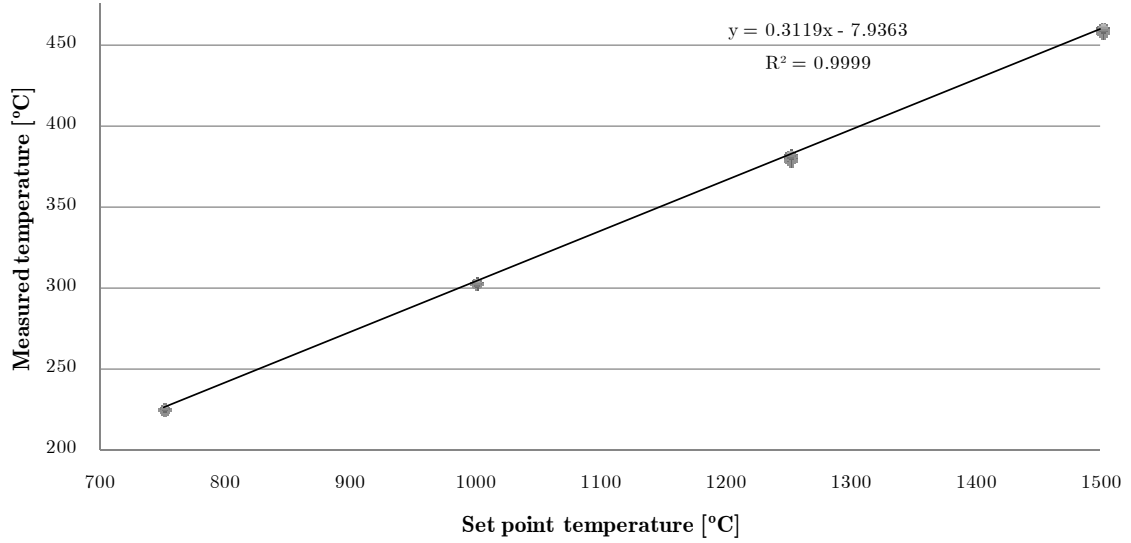


**Figure 4.13** – Relationship between furnace set point and cavity temperatures.

For a 95% confidence interval, the apparent emissivity distributions yield the relationship shown below:

$$\varepsilon_{\text{app}} = 0.305 \pm 1.4 \times 10^{-3} \quad (4.2)$$

This emissivity is for a situation where the end of the tubular furnace opposite to the instrument location is not fitted with the ceramic plug provided precisely for this purpose, as illustrated in Figure 4.14, where both options are shown.

This open-end configuration had to be used because of the interaction between the transpiration airflow and the furnace, especially at high set point temperatures. With the other end closed, the transpiration airflow heated up significantly inside the furnace cavity and was blown back towards the instrument, degrading the integrity of the compressed air tubes and their gluing to the sensor casing, and degrading the aluminium foil coatings of the shielding shown in Figure 4.12.

Tests could thus not proceed in such conditions and the plug had to be removed to avoid the problem of the hot gas blowback. The use of the plug would have been beneficial from the point of view of the apparent furnace emissivity, since it would have reflected some radiation directly to the surface across the length of the cavity and certainly heated significantly and emitted a large amount of radiation, since it becomes



visibly red-hot. Apparent emissivities measured at the sensor location were shown to be much higher with the plug fitted. The plug can be modified by performing an oblique perforation that would enable the hot transpiration airflow to exit the cavity, without allowing radiation to directly escape the cavity.

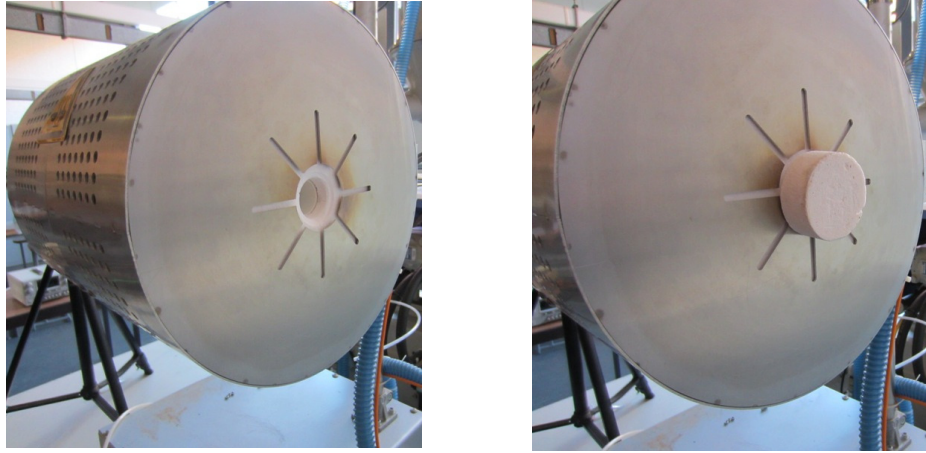


**Figure 4.14** – End of the tubular furnace opposite to the instrument location, with and without the ceramic plug fitted.

The absence of the plug opens a significant area to cold surroundings, causing a large radiative transfer due to a large temperature difference even for surfaces where the radiative view factor is not very large, as is the case of the central, heated portion of the cavity. Without surprise, the apparent emissivity for the configuration where the plug is fitted is:

$$\varepsilon_{\text{app}} = 0.88 \pm 1.82 \times 10^{-4} \quad (4.3)$$

As discussed below, this must be taken into account when measurements are compared with the simulations discussed in Chapter 3, since those were set up using unitary emissivities.

Once the emissivity can be safely dealt with, other measurements can take place. More particularly, some contamination of the transpiration airflow by the refrigeration airflow was detected, in the sense that some refrigeration compressed air



crossed the sensing element due to perfectible welded joints between the porous holder and the interior cone. Given the fact that the measurement of the transpiration mass flow is a central element in the instrument's operation principle it was fundamental to quantify the magnitude of this contamination.

This was measured, for various refrigeration mass flows, by tightly fitting each sensor to a tube linked to a Omega FMA 1816 digital gas mass flowmeter while plugging the transpiration air inlet in order to ensure that all the possible leakage flows through the sensing element. The flowmeter has a 0-2 SLPM range with an accuracy of  $\pm 1.5\%$  FS. This setup is illustrated in Fig. 4.15.



**Figure 4.15** – Transpiration airflow contamination measurement.

The instruments were connected directly to the compressed air system and tested at various pressures up to 5 bar. Measurements were repeated three times for each instrument and the mean value at each pressure was determined with the objective of determining the three units with the smaller contamination values, to be used in subsequent tests, where one of these eventually suffered damage in consequence.

As expected beforehand, airflow contamination was found to increase linearly with pressure to a maximum at 5 bar. The highest contamination airflow registered was 1.43 SLPM but even at 5 bar the selected instruments registered an average contamination airflow of 0.67 SLPM. This is a very small value when compared to the

transpiration airflows, meaning that in practice the measured transpiration mass flows do not require an adjustment taking this contamination into account.

The output of the thermocouple was read using an Omega Engineering Inc. instruNET series INET-100b acquisition and control system. InstruNet provides microvolt-range absolute accuracy, using a topology where the analogue electronics are close to the sensor in electrically quiet boxes outside the PC, and noisy digital electronics are left inside the computer. The external box contains signal conditioning amplifiers for each channel and can be directly attached to sensors such as thermocouples, returning engineering units to the PC (e.g. °C or volts). The controller contains a 32 bit microprocessor with 256KB of RAM that manages the external “network” of devices and all real-time tasks are off-loaded to this processor, not burdening the host computer with real-time issues. The instruNet iNET-100 box provides 16 single-ended/8 differential analogue inputs, 8 analogue outputs and 8 digital I/O lines. The instruNet system supports the digitizing of multiple channels at a maximum aggregate sample rate of 166Ks/sec, where each channel can be digitized at its own rate. According to specifications, K-type thermocouples connected to the system have accuracies (including cold junction compensation, voltage measurement and linearization errors) of  $\pm 0.6^{\circ}\text{C}$  in the temperature range of interest.

Regarding the analysis of the instrument’s transient response, the setup only had to be slightly adjusted. A bifurcation in the compressed air supply before the manometers and the rotameter provides the non-controlled refrigeration airflow, while the remainder of the air supply proceed to these control units in order to allow the control and measurement of the transpiration airflow using an electrovalve that is commanded by the data acquisition system that monitors the instrument’s output.

Upper and lower temperature limits can be defined for switching on and off the airflow, or varying it between upper and lower values if the option of switching it off completely is not retained. The easiest way of implementing a complete elimination of the airflow in its off position is merely disconnecting the tubing from the regulator on the adequate side of the valve.

This can be implemented by feeding the transpiration airflow through two previously adjusted flow regulators, depending of the position of the electrovalve,

resulting in the configuration illustrated in Figure 4.16, while Figure 4.17 illustrated the electrovalve and the flow regulators themselves.

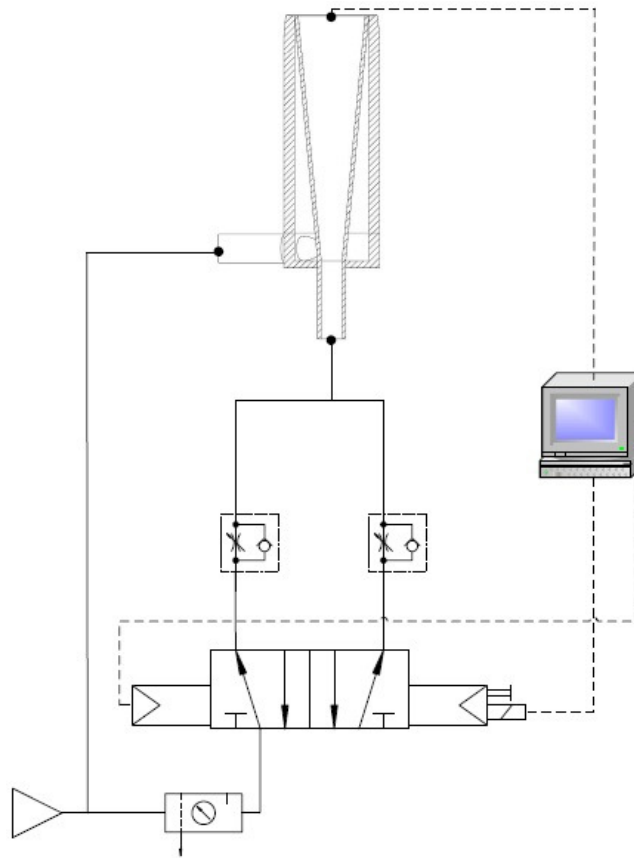


**Figure 4.16** – Transient airflow control setup.

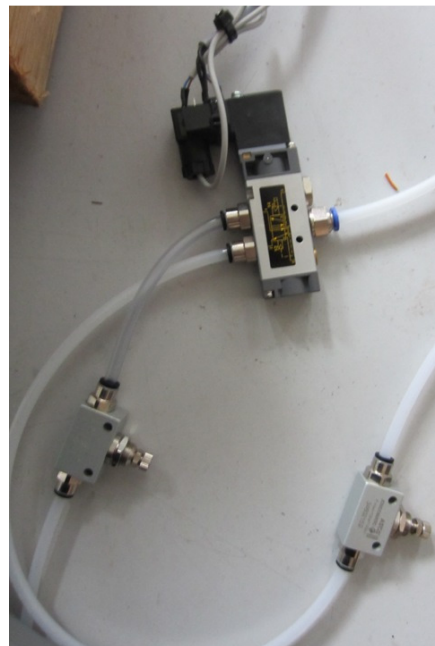


**Figure 4.17** – Control electrovalve and flow regulators.

### 4.3 Experimental Results

The experimental testing of the instrument included cool and hot experiments, the latter being carried out both in steady state and in transient conditions. Broadly speaking, such tests can be said to have the following objectives:

- To confirm previously discussed mathematical and especially physical assumptions;
- To test the instrument's repeatability;
- To establish a calibration procedure and calibrate the instruments;
- To seek possible additional relevant and unforeseen phenomena and effects.

For that purpose the instrument's output as a function of various transpiration mass flows and incident heat fluxes was studied, especially regarding the transient experiments in order to establish the calibration of the instrument working as a transient transpiration heat flux meter.

The aforementioned three units with lesser airflow contamination values were tested in order to verify the repeatability of the experimental results and establish the instrument calibration curve. The tested instruments will henceforth be designated as Sensor 1, Sensor 2 and Sensor 3.

During cool experiments the radiation heat flux is negligible because the instrument is exposed to room temperature, while in for the hot experiments the instrument output is monitored for different known heat flux levels. These steady state experiments were followed by a study of the transient response of the instruments, namely the determination of the slopes associated with their temperature response curves, and their calibration.

The cool experiments are intended to establish a reference output for a null input that can be used to check and correct possible bias errors. The hot experiments, on the other hand, are meant to verify the instrument performance in comparison with numerical predictions obtained earlier. Despite the fact the instrument is intended to have an intrinsically transient operation mode, steady-state calibration curves could be obtained at this point. This was not done given the intended transient operation, but

the instrument can always be looked upon as a steady-state instrument if the pulsed airflow is maintained at a constant value.

The transient experiments are foremost in importance since they are meant to establish the instrument's transient operation mode calibration curves, *i.e.* when the pulsed operation principle is used, where a linear relationship between the slope of the transient temperature curve at the start of the pulse and the incoming heat flux is anticipated, as stated in Equation 2.1.

During the setting up of the experiment, special care was required in order to reduce the noise associated to the thermocouple readings. This aspect was particularly important due to the low temperature levels to be measured, given the fact that the surface temperatures of the sensing element were to be kept relatively low, as mentioned earlier. For that purpose, sheathed thermocouples were used and the sheaths were connected to a common ground.

In the steady-state mode experiments, after each temperature or airflow level variation, 5 minutes were allowed in order to let readings stabilize and the temperature measurements were then conducted during another 5 minutes at a 10 Hz sampling rate. The averaged temperature value for one second was taken as representative of the instantaneous temperature, and the variation of this instantaneous value was then analyzed over the whole sampling time. No need was found to make further adjustments since the observed fluctuations in signal fell within the range of thermocouple error, obviously unlike the situation described below regarding the setup for transient measurements.

For the cool experiments, the instrument output was registered for different TG mass flow rates similar to those later considered for the hot experiments. The cooling system was active but the sensing surface was not receiving any relevant incident heat flux, while for the hot experiments the source furnace was heated up to the various set points and staged at that temperature until stable temperature levels were attained. The transpiration and refrigeration airflows were then set to the appropriate levels and the heat flux meter was placed into the furnace cavity, at a position and depth where the temperature measured by the thermocouple stabilises at the highest level, in order to minimize edge effects from the furnace cavity.

The radiation source temperature was continuously monitored and the temperature readings from the flux meter thermocouples were taken after a stable condition in the radiation source was obtained, as explained above. For each radiation flux level, different transpiration gas mass flows were considered and the corresponding flux meter output temperatures were read. Each measurement condition, defined by the radiation source temperature and the TG mass flow rate was repeated five times.

The values considered for the radiation source temperature are listed in Table 4.2 together with the corresponding blackbody radiation fluxes. As mentioned earlier, care must be taken when analyzing results given the fact that these values are for blackbody emission and as mentioned earlier correction factors must be introduced depending of the experimental setup used. In the case under discussion the furnace emissivity was corrected using Equation 4.2 and the emitted radiation was calculated accordingly, as described in Table 4.2. It is readily visible that the low apparent emissivity of the furnace to be employed has strongly detrimental effects as far as reachable heat flux levels are concerned, thereby limiting the testing range of the instruments under discussion.

**Table 4.2** – Furnace set points

<b>Set Point Temperature</b> [°C]	<b><math>q_{\text{rad}}</math></b> [kW/m <sup>2</sup> ]	<b><math>q_{\text{corr}}</math></b> [kW/m <sup>2</sup> ]
500	20.25	6.17
750	62.10	18.94
1000	148.90	45.42
1250	305.06	93.04
1500	560.30	170.89

Regarding transpiration mass flows, a rotameter was used in order to set 6 volumetric flow levels (measured in the rotameter linear scale at 50, 70, 90, 110, 130 and 150mm) for each run, airflow pressures and temperatures being registered and used to compute mass flow rates from the volumetric rates using the calibration curve provided by the manufacturer.

Considering the number of set points for the radiation source temperature (5) and transpiration mass flows (6) above, thirty different steady-state operation

conditions were verified for each prototype. In addition, each working condition was verified five times, resulting in one hundred and twenty independent measurements for the experimental verification of each instrument.

The setup for the transient experimental is the same from the point of view of the use of the basic hardware, except for the fundamental issue of the implementation of the pulsed transpiration airflow. As discussed above this requires the use of the setup illustrated in Figures 4.15 and 4.16 and different procedures in terms of signal acquisition and processing, as discussed below in the relevant section.

The instrument output should ideally be zero for a null incident flux but there are a number of phenomena that may induce deviations from such an ideal scenario, resulting in bias errors. The output signal for a null heat flux can thus be useful in order to correct such errors. The same overall behaviour is apparent for all three instruments and the example of Sensor 1 is illustrated in Figure 4.18, showing measured temperatures in five runs for each instrument where mass flows were gradually increased.

The temperature scale shows that differences are negligible but an underlying physical phenomenon is nevertheless evident. Similar effects were observed in earlier applications of transpiration radiometers [Martins 1998]. Different phenomena may contribute for the results shown but it is not possible obtain a conclusion with the available data. A global cooling effect due to the gas expansion after it passes through the perforated pattern may be present, and the slight increase in temperature observed for low mass flows can be due to some heating due to some amount of compression as the air passes through the perforated pattern that is overwhelmed by the expansion cooling process at higher mass flows. The relatively low velocities involved, even within the holes, are not expected to lead to a heat generation due to friction to play an important role.

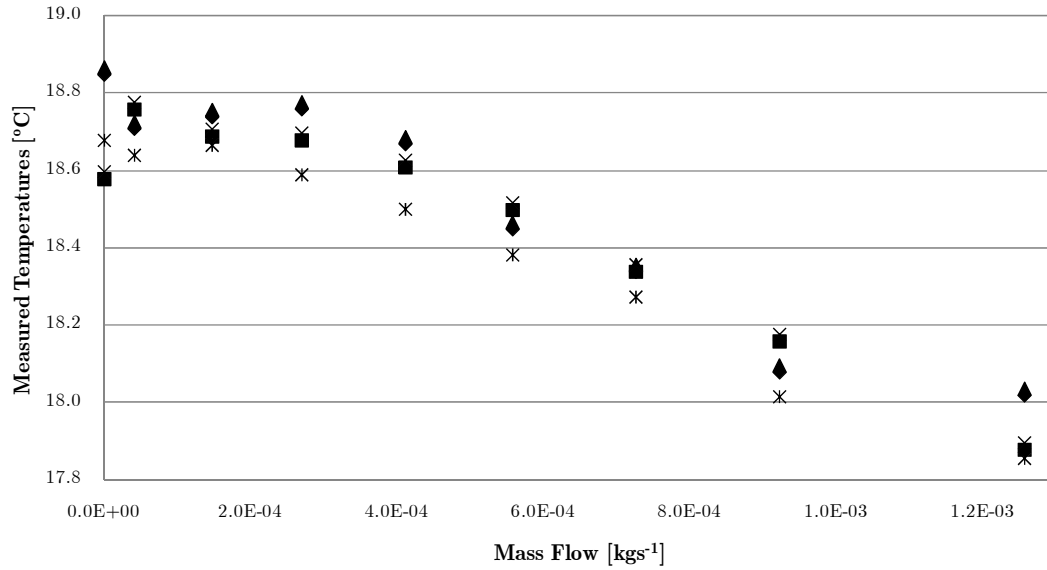


**Figure 4.18** – Sensor 1 cool experiment measured temperatures.

The matter is somewhat irrelevant for the intended transient conditions, due to the large number of cycles occurring in very short times that lead to comparatively higher plate temperatures and especially because in the transient mode the heat flux is determined based on the sensing element temperature variation with time and not on its absolute value, as would be the case in the steady state mode.

As mentioned earlier the hot experiments are intended to verify the instrument's response to different heat flux levels, under different operating conditions defined by various transpiration mass flows. The results for the upper attainable furnace temperatures of 1500°C must be taken with some caution due to the cooling load of the transpiration gas in the furnace cavity together with the latter's power limitation, resulting in an effective lower temperature in the furnace cavity and consequently in a lower heat flux.

When the higher mass flows where used the furnace visibly struggled to achieve the required set point temperature, so that the aforementioned ceramic plug was placed in a partially closed position to enable some of the hot gas blowback discussed above to allow the furnace to reach higher temperatures. This in turn led to a need to use even more tubing shielding on the compressed air feed lines.



This procedure was tried but the variation induced in the furnace's apparent emissivity was felt to render the measured temperatures unreliable, so the values for the 1500°C set point in the furnace were left out of the steady-state experimental analysis.

Curves such as those illustrated in the previous chapter, where measured plate temperatures are shown to be a function of furnace temperatures and transpiration mass flows, were obtained and show the same overall behaviour with one notable exception: the measured temperature scale is expectedly lower than the values simulated for blackbody sources due to the lower apparent emissivity of the cavity of the furnace employed in the laboratory experiment.

The curves obtained for blackbody sources discussed in Chapter 3 must be adapted for comparison purposes between the numerical model and the experimental values, so new curves were obtained by correcting the blackbody temperature using the apparent emissivity in Equation 4.3. As in Chapter 3 and for model validation purposes, these curves were obtained for a range of plate emissivities that allow a comparison with the experimental response curve, as shown in Figure 4.19, where the means of the values obtained in the five runs conducted for each of the 3 sensors are also displayed with 2% error bars on the lower simulated values. A mass flow of  $0.001 \text{ kgs}^{-1}$  was considered and the corrected heat fluxes are those of Table 4.2.

The experimental values are consistent with a sensor surface emissivity of around 0.25, indicating that the oxidization process did not lead to the intended high emissivities. This is nevertheless somewhat irrelevant given the intended transient operation mode where the heat flux is determined based on the sensing element temperature variation with time.

The instrument's performance over long times was evaluated by placing one of the tested instruments in a larger furnace than the one discussed above, made available for a limited time at the Department of Ceramics and Glass Engineering of the University of Aveiro. Two 8 hour runs at its maximum temperature of 1300°C on two consecutive days were conducted in a closed furnace with a circular opening in its door, rendering the emissivity much higher than for the tubular furnace discussed above and thus exposing the sensing element to much higher radiative heat fluxes.

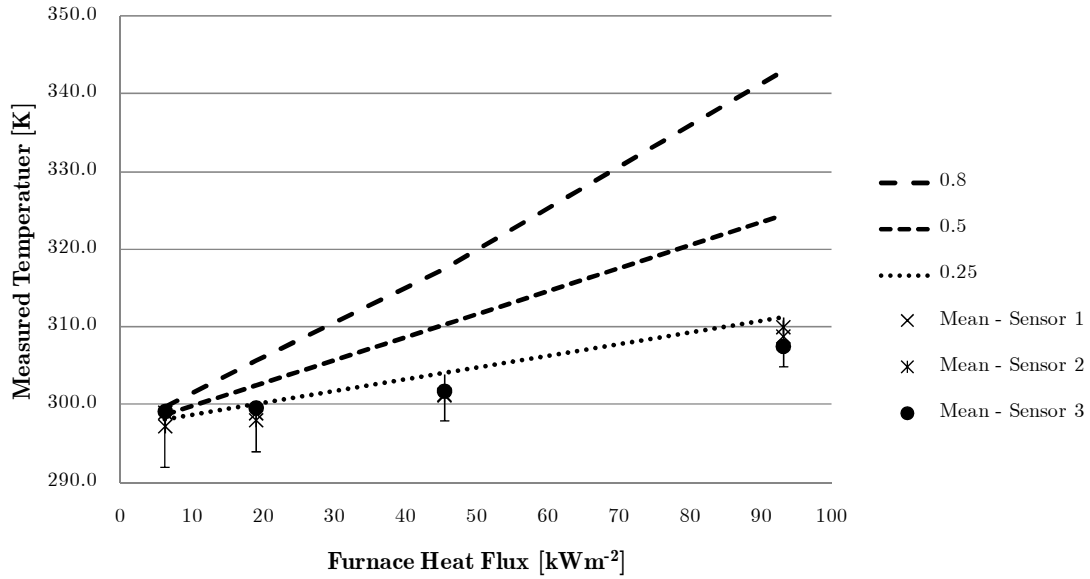


**Figure 4.19** – Numerical temperatures for the corrected furnace emissivity, various element emissivities and experimentally measured values for the same operational conditions.

The small diameter and large thickness of the opening in the furnace's door rendered impossible the use of the refrigeration airflow tubing, so that the instrument was used with only the transpiration airflow switched on, with glass wool placed around the instrument in order to close the gap with the opening. The interior of the furnace had significant amounts of ceramic dust particles that were stirred by the transpiration airflow, thus replicating the aggressive and dirty environments where the instrument is expected to perform. The configuration of the furnace and the placement of the instrument in its door are illustrated in Figure 4.20.

No damage was apparent after the 16 hours of these tests, indicating that the instrument has the potential to withstand adverse conditions over long periods of time, although further testing is desirable. These steady experiments provide added confidence for the crucial component of the work under discussion, namely the analysis of the transient response.



**Figure 4.20** – Closed furnace for 8 hour runs.

As mentioned earlier the hot experiments are intended to verify the instrument's response to different heat flux levels, under different operating conditions defined by various transpiration mass flows. As discussed above these experiments were conducted both in steady-state but especially in transient conditions, in order to quantify the instrument's transient response, since this will be the basis of its transient mode operation.

The transient conditions were induced using the pulsed transpiration mass flow working principle, meaning that when the airflow is turned on at a supercritical mass flux level the instrument will behave like a conventional transpiration radiometer, and the temperature measured by the thermocouple attached to the perforated plate would be a steady-state equilibrium value dictated by the incoming radiation heat flux and the cooling provided by the transpiration airflow, if such conditions were allowed to be reached. This also means that although it was not the intent behind its development, the instrument under discussion can also be used as a traditional transpiration radiometer.

The situation where the airflow is eliminated and the boundary layer is no longer blown off will present a dramatic increase in measured temperature driven not only by the presence of a convective component in addition to the radiative component

that was already present, but also by the absence of transpiration cooling in the sensing element.

As discussed earlier such a process would eventually lead to a steady-state value that would be reached if temperatures were allowed to increase and stabilize, and would indeed be proportional to the total received heat flux, according to the relationship shown earlier in Equation 2.1:

$$q_{\text{total}} = \beta \left. \frac{dT}{dt} \right|_{t=0} \quad (4.4)$$

where the slope of the transient temperature curve at the start of the pulse (hence the zero value for time) would be proportional to the incoming heat flux.

An adequate analysis of the sensing element's transient response is precisely intended to avoid reaching such high temperatures, allowing the resetting of the supercritical transpiration mass flow once the proportionality constant  $\beta$  is established. This would enable the convenient assumption of a comparatively insignificant plate emission term and most importantly would avoid severe damage to the components and their welding and attachments.

Furthermore, if the process is carried out in a sufficiently rapid way, the radiative component of the heat flux can be treated as constant and the convective component can be estimated based on the radiative heat flux measured for a supercritical transpiration mass flow. A calibration of the transient transpiration radiometer would thus involve the determination of the proportionality constant  $\beta$  for various incident heat fluxes, with temperature curves slopes being quantified in degrees per second ( $^{\circ}\text{Cs}^{-1}$  or  $\text{Ks}^{-1}$ ).

A previous attempt to verify the proposed formulation was developed within this research team [Martins 1998, Martins *et al.* 1998, Martins *et al.* 2000], including experimental studies using a different heat flux instrument, operated at a constant blow off mass flow rate, and using a diaphragm between the sensor and the radiation source to create the transient. The performed studies showed a direct proportionality between the slope of the line tangent to the temperature response curve and the

incident heat flux, the same slope being observed in the linear portion of the curve for the same heat fluxes regardless of the initial temperature, establishing the soundness of the transient transpiration principle [Hit 2004].

The latter reference mentioned the difficulty of identifying the exact moment  $t = 0$  mentioned in Equation 2.1, with a precision sufficient to decide the exact starting point for slope determination purposes, and suggested higher data acquisition frequencies as a remedy. This problem is compounded by the noisy nature of the output signal from the thermocouple, since even when the sensing element is experiencing heating or cooling, as discussed earlier when its transient behaviour was simulated, fluctuations in the temperature curve will manifest themselves and small variations from one instant to the next can even be contrary to the overall heating or cooling tendency, rendering necessary some form of filtering to account for fluctuations in the signal, as discussed below.

The output of the thermocouple was read using the same data acquisition system, connecting its terminals to the external box that contains the signal conditioning amplifiers that convert millivolt readings to  $^{\circ}\text{C}$ , with the  $\pm 0.6^{\circ}\text{C}$  accuracies for K-type thermocouples. The acquisition and control system was programmed to control the electrovalve open and close cycles based on maximum and minimum cycle temperatures rather than on a time period. This option was retained in order to ensure that a possibly less than judicious period selection does not result in excessive temperatures in the sensing element, due to the valve being closed for too long. The valve opens when the maximum cycle temperature is reached, letting the transpiration airflow eliminate the convection heat transfer and cool the sensing element until the lower cycle temperature is reached and the valve closes again. Some measured temperature overshoot is always to be expected at both ends of the temperature spectrum, due to some delay in the response of the valve and some controller drift.

An acquisition frequency must also be defined, at a value sufficiently high to capture the transient temperature variations occurring in the element, so that care must be taken to ensure that the frequency is sufficiently high in order not to miss possible temperature curve inflexions. This parameter was duly taken into account in the experimental study, as discussed below.

The system was also programmed to register the valve position (0 for closed and 1 for open), writing results as standard *csv* (comma separated values) files that can be open and processed in software such as *Excel*, *Mathematica* or *Matlab*. A real-time interface is available and allows a continuous monitoring of the measurements, as illustrated in Figure 4.21. The noisy nature of the temperature signals is evident in most measurement runs and the interface allows some magnification in terms both of time and temperature. Such an interface is always useful, if only for interrupting a measurement run if something is visibly wrong with the process. It also allows a visualisation of the signal stabilization, since some transient adjustment must always be considered at the start of each experiment.

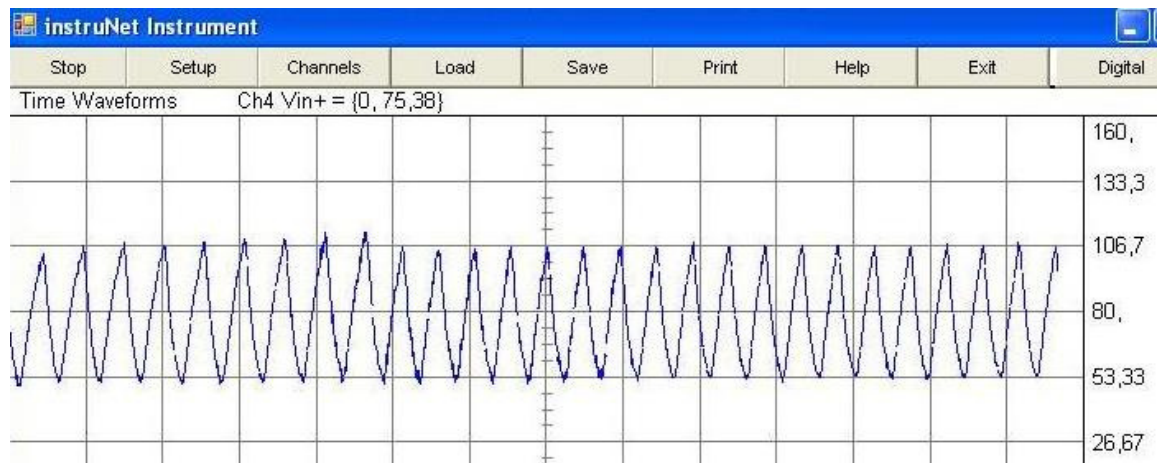


**Figure 4.21** – Data acquisition system real-time interface.

Files resulting from the described procedure contain information about the instant of measurement, the position of the valve and measured temperatures. When plotted the files show the same basic information, as illustrated in Figure 4.22, displaying “raw” values, before any data processing procedures are applied. Noise in the temperature signal is not usually perceptible unless a certain degree of magnification is used (which is not necessarily practical in most situations where an entire experimental run is to be visualized for analysis purposes), but is nevertheless always present and should be dealt with either by reducing its magnitude or by processing the obtained data. Another phenomenon can also be noticed in the lower values of the temperature cycles, namely a variation over time. As can be seen by the

time values the graph plots temperatures at the start of the run, where the instrument output has not stabilized. Care was therefore taken in the calibration runs, starting measurements only after such effects were no longer apparent, which occurred after a few minutes.

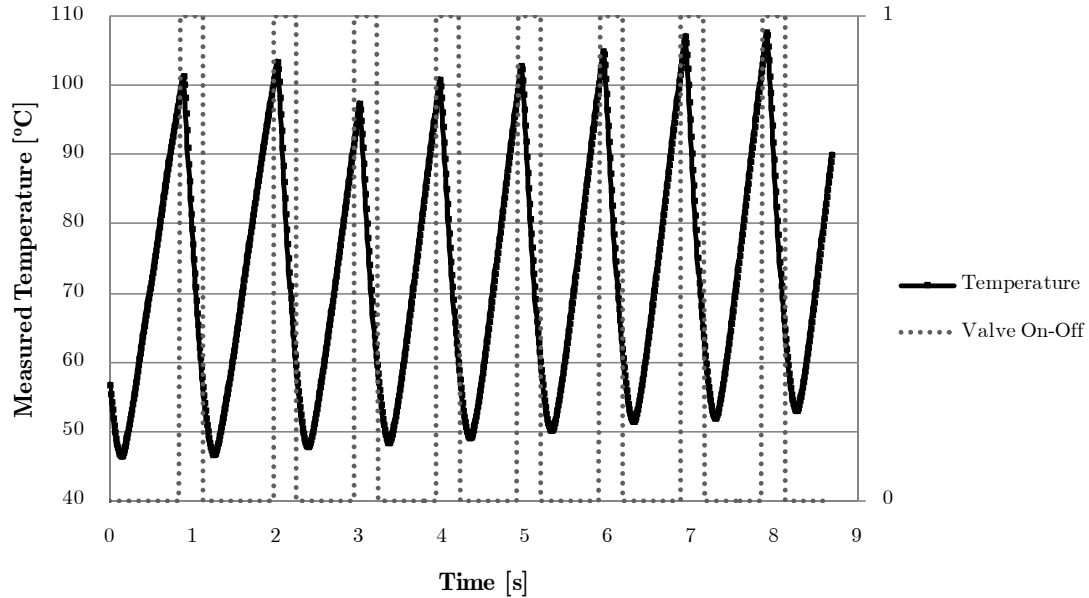


**Figure 4.22** – Raw data plots.

While the data acquisition procedures should be tailored to reduce as much as possible the noise levels in the signal, and although the transient data found in the work under discussion are not particularly noisy when compared to those found in other applications, some form of data filtering is desirable in order to make the trends in the data stand out from background noise. Furthermore, when seeking a calibration curve for the instrument, these noisy data must be adequately processed for a correct calculation of transient temperature curve slopes.

For the case under discussion, the use of the Savitzky-Golay smoothing algorithm for data filtering purposes was decided upon, for a variety of reasons. It is a well established and widely used tool that is nowadays available in most scientific computation software packages (such as *Mathematica* or *Matlab*) and therefore does not have to be specifically programmed to be used. Furthermore, Savitzky-Golay smoothing is very easy to apply and can be used to calculate inherently smoothed first and second derivatives of the signal, which is especially relevant in this context given the stated need to calculate the slope of the transient temperature curve.

A FIR is a filter with an impulse response (or response to any finite length input) is of finite duration, settling to zero in finite time in contrast to infinite impulse response (IIR) filters that may have internal feedback and continue to respond indefinitely (although usually decaying). FIR filters are inherently stable and require no feedback, meaning that any rounding errors are not compounded by summed iterations and the same relative error occurs in each calculation. This also makes implementation simpler, but typically comes at a higher computational cost when compared with IIR filters.

The Savitzky–Golay FIR smoothing filter essentially performs a local polynomial regression (of degree  $k$ ) on a series of values (of at least  $k + 1$  points which are treated as being equally spaced in the series) to determine the smoothed value for each point. The main advantage of this approach is that it tends to preserve features of the distribution such as relative maxima, minima and width, which are usually 'flattened' by other adjacent averaging techniques like moving averages [Savitzky and Golay 1964].

Given a set of data containing both signal and noise, the objective of the Savitzky-Golay method is to replace the raw data by a smoother set of data representing the true signal responsible for the recorded intensities. For a constant underlying signal, the most natural means of estimating the true signal from a set of measurements would be to average the values. Spectral data, such as the periodic temperature signals imposed by the transient transpiration operation, typically contain peaks superimposed on a background signal and therefore a more subtle use of averaging is required if the essential structure in the data set is to be retained.

The smoothed time series is obtained by replacing each value of the series with a new value which is obtained from a polynomial fit to  $2n+1$  neighbouring points (including the point to be smoothed), with  $n$  being equal to, or greater than the order of the polynomial.

Illustrated in Figure 4.23 are calculated first derivatives curves for a run with the furnace at 1500°C, where higher slope values occur.



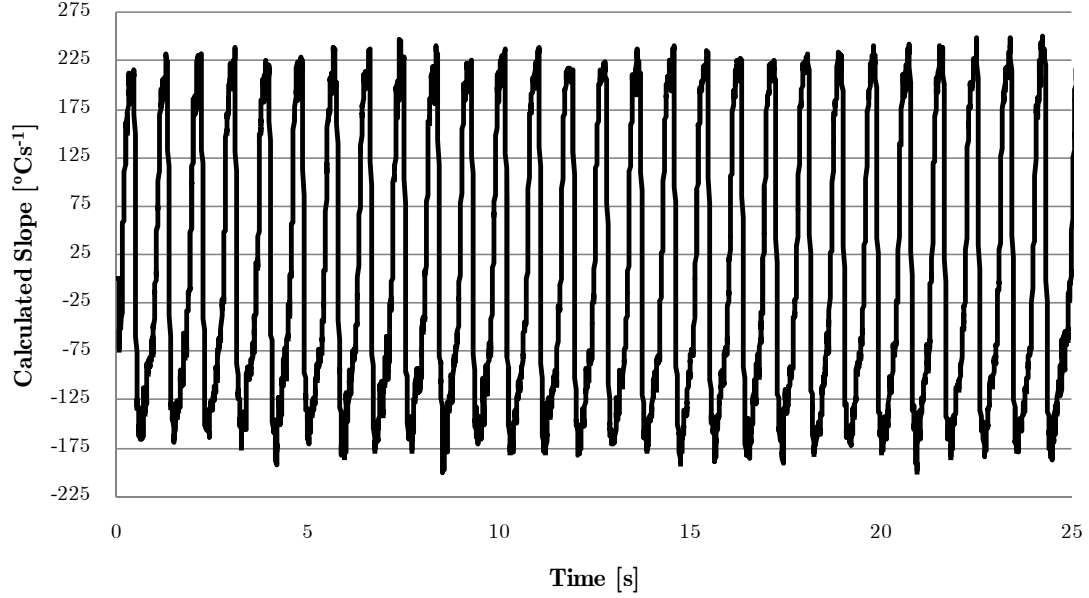


**Figure 4.23** – Calculated first derivatives.

An important conclusion was reached in the course of this experimental and analytical process, and the graph above is helpful in making the point, since it readily indicates that a more easily measureable indication of the instrument's transient response can be the maximum value of the first derivative of the temperature curve, rather than its value at instant  $t = 0$  when each airflow pulse begins and ends:

$$q_{\text{total}} = \beta \left. \frac{dT}{dt} \right|_{\text{max}} \quad (4.5)$$

The identification of this instant  $t = 0$  is extremely difficult for the case when the airflow is turned off and the temperature curve rises, even at high data acquisition frequencies (which were tested up to 500 Hz and could conceivably have been set at even higher values since the hardware allowed it) and with adequate filtering. The uncertainty associated with the specification of a particular instant for curve slope calculation purposes would lead to significant variations in the calculated slope value and render the use of this value hazardous for calibration purposes.

This strategy can also be justified from the point of view of the data acquisition systems available in practice, where the available hardware may not enable very high

acquisition frequencies. In the studies presented here, a 250 Hz acquisition frequency was used, although in practice frequencies as low as tens of Hz can be encountered in acquisition systems deployed in industrial applications.

Parametric tests were performed at various transpiration mass flows (0.001, 0.002 and 0.003  $\text{kg s}^{-1}$ ) and as expected it was found that higher measured slopes are encountered at higher mass flows, leading to greater correlation coefficients in the linear relationships between heat fluxes and measured slopes. Since greater transpiration mass flows values not only increase the sharpness of variations but also provide greater protection from incoming particles as mentioned earlier, transpiration mass flows should be set as high as possible and the higher tested mass flow value was subsequently used in all tests. Furthermore, the calibration procedure was carried out using this constant value and the fact that different calibration curves would be obtained at other values must be kept in mind.

Given the results of the 8 hour runs described above where the refrigeration airflow was shut down without any detrimental effect, the later was set at only 20% of its maximum value.

Switching the transpiration mass flow on and off will lead to two distinct situations, the temperature rising when the airflow is shut down due to the absence of refrigeration and the addition of an admittedly small convective component (a “total” incident heat flux thus being present) and falling when the airflow is restored, cooling is present and convection is eliminated.

Defining an operational mode where the airflow valve is controlled by setting a maximum temperature above which the valve opens and minimum value at which it closes, the temperatures measured by the thermocouple will overshoot the maximum set temperature due to the inherent delay introduced by the valve-opening process, and this overshoot will increase with increasing furnace set point temperatures. The restoration of the airflow, which is kept constant between experiments, will likewise result in higher cooling curve slopes for higher furnace set points, due to the greater difference in temperature between the plate and the airflow.

In any case a linear relationship between the two aforementioned incident heat flux situations and the temperature curve slopes is expected. Given the fact that

several heating and cooling cycles occur every second (with more cycles at higher furnace temperatures given the proposed operational mode) due to the sensing element's low thermal inertia, several slope measurements per second can be carried out for both heating and cooling and the correspondent incident heat fluxes will be determined using the following relationships:

$$q_{\text{total}} = \beta_{\text{heating}} \left. \frac{dT}{dt} \right|_{\text{max,heating}} \quad (4.6)$$

$$q_{\text{rad}} = \beta_{\text{cooling}} \left. \frac{dT}{dt} \right|_{\text{max,cooling}} \quad (4.7)$$

Equation 4.4 embodies a proportional relationship between the incoming heat flux and the slope of the transient temperature curve at the start of the pulse (hence the zero value for time) and where the linear calibration curve has a zero intercept value, meaning that no slope is measured for a non-existent incoming heat flux.

Given the aforementioned difficulty in determining instant  $t = 0$  and the proposed use of the maximum slope in each cycle, it should be kept in mind that while for higher heat fluxes maximum slope values are expected to be reached very rapidly, slower responses are to be expected at lower incident heat flux values where the maxima are not reached at quite the same speed, meaning that a bias resulting from the experimental conditions can be expected to lead to non-zero intercept values. This in turn means that Equations 4.6 and 4.7 must be adapted in order to include non-zero intercepts  $K_{\text{heating}}$  and  $K_{\text{cooling}}$ :

$$q_{\text{total}} = \beta_{\text{heating}} \left. \frac{dT}{dt} \right|_{\text{max,heating}} + K_{\text{heating}} \quad (4.8)$$

$$q_{\text{rad}} = \beta_{\text{cooling}} \left. \frac{dT}{dt} \right|_{\text{max,cooling}} + K_{\text{cooling}} \quad (4.9)$$

The relationships themselves can be established by determining a large number of slopes at each heat flux level and performing a standard statistical analysis of the obtained values, especially as far as their mean values and standard deviations are concerned, allowing the determination of slope uncertainties at a given confidence interval. This is especially relevant regarding the calibration of the instrument, as discussed below.

Plots of mean measured slopes (calculated with 500 samples each) versus furnace heat fluxes can be presented for each instrument, as shown in Figures 4.24 to 4.29, with radiative heat fluxes corresponding to furnace set point temperatures of 1000 to 1500°C, with 100°C increments, as illustrated in Table 4.3 after correction with the apparent emissivity described in Equation 4.2.

**Table 4.3** – Furnace set points for transient runs

<b>Set Point Temperature [°C]</b>	<b><math>q_{\text{corr}}</math> [kW/m<sup>2</sup>]</b>
1000	45.42
1100	61.40
1200	81.42
1300	105.88
1400	135.49
1500	170.89

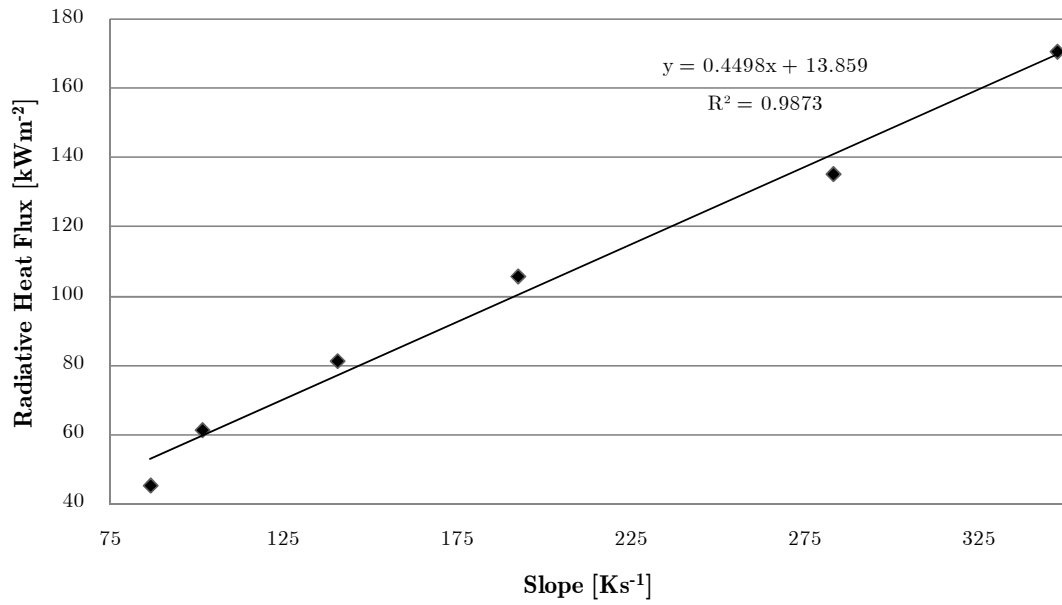


**Figure 4.24** – Sensor 1 linear relationship between mean temperature curve slopes and furnace heat fluxes, in the heating situation.

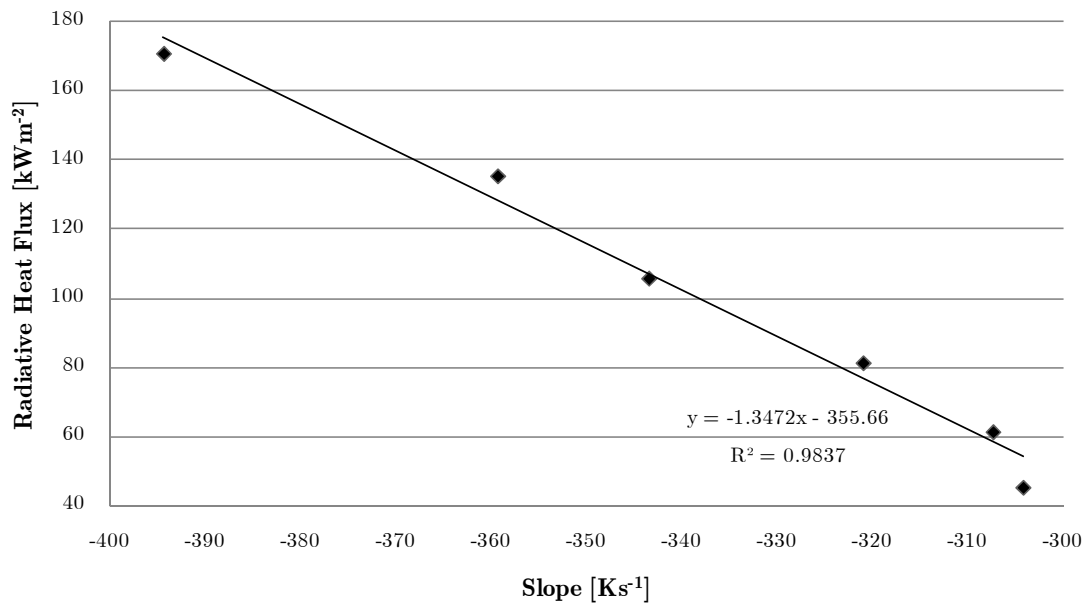


**Figure 4.25** – Sensor 1 linear relationship between mean temperature curve slopes and furnace heat fluxes, in the cooling situation.

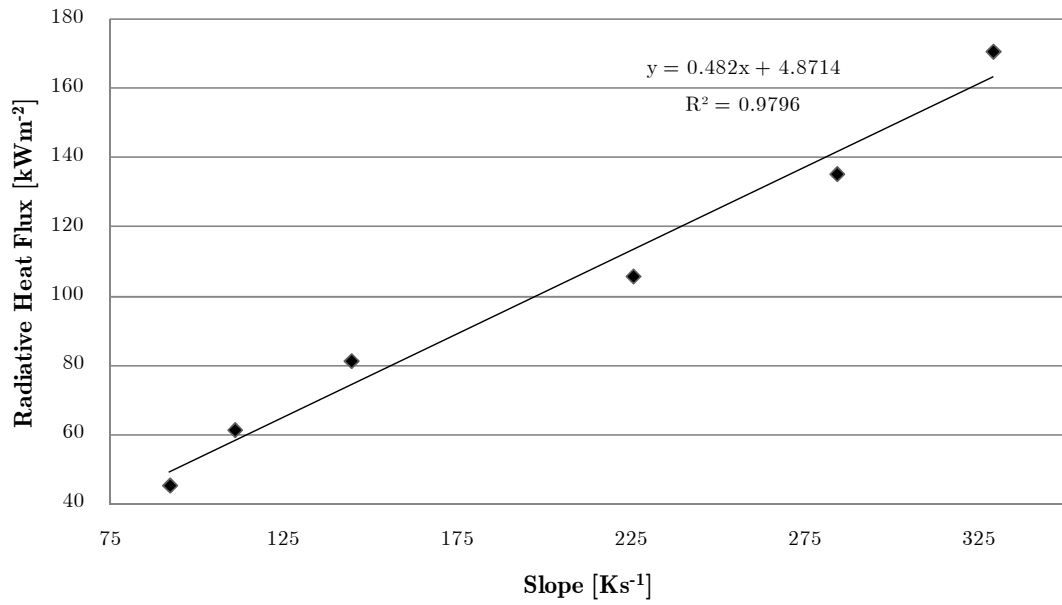


**Figure 4.26** – Sensor 2 linear relationship between mean temperature curve slopes and furnace heat fluxes, in the heating situation.

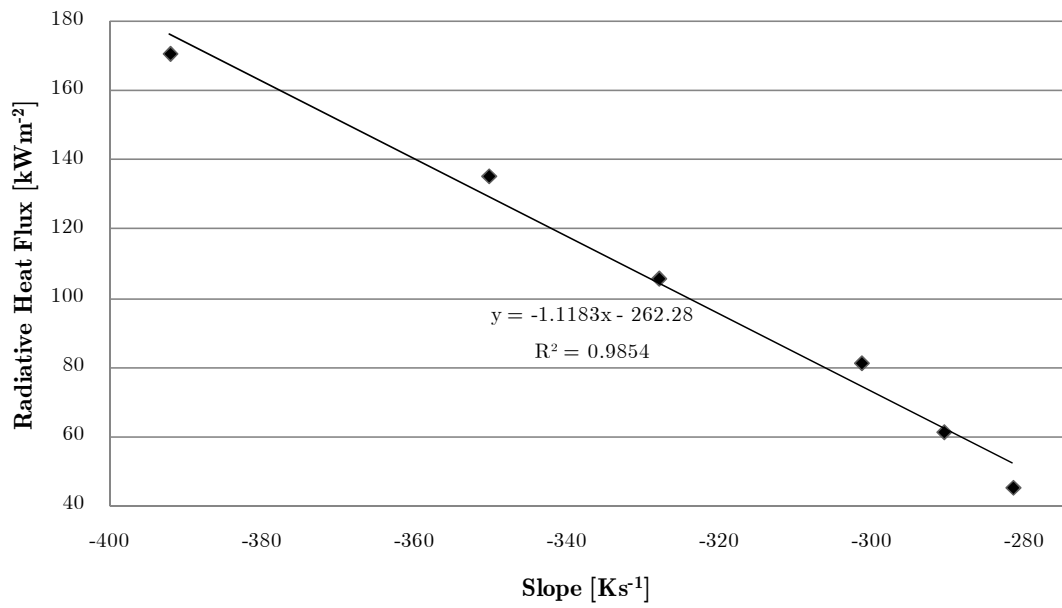


**Figure 4.27** – Sensor 2 linear relationship between mean temperature curve slopes and furnace heat fluxes, in the cooling situation.

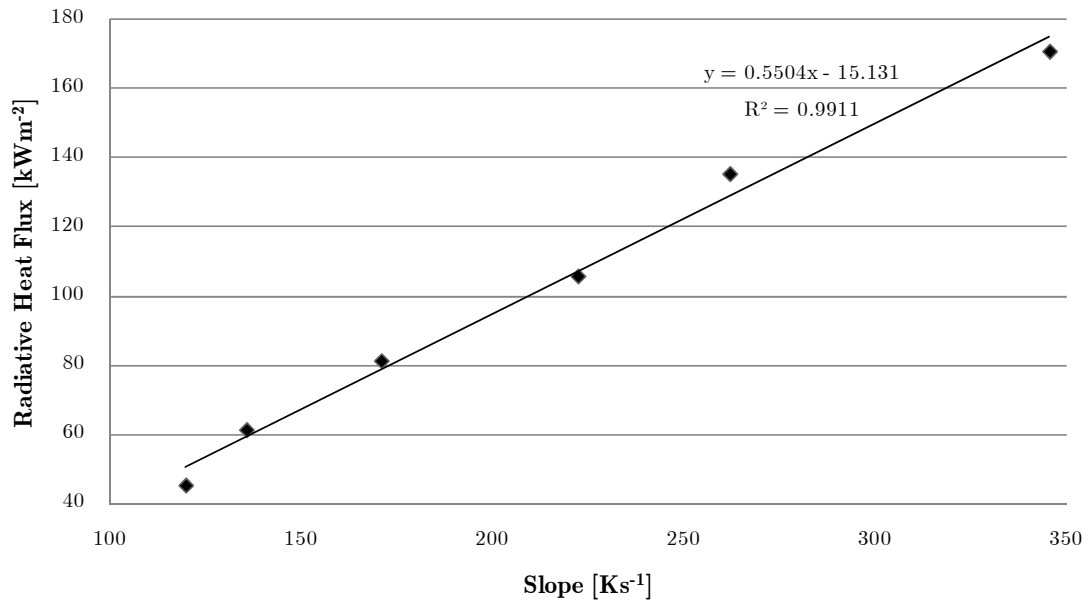


**Figure 4.28** – Sensor 3 linear relationship between mean temperature curve slopes and furnace heat fluxes, in the heating situation.

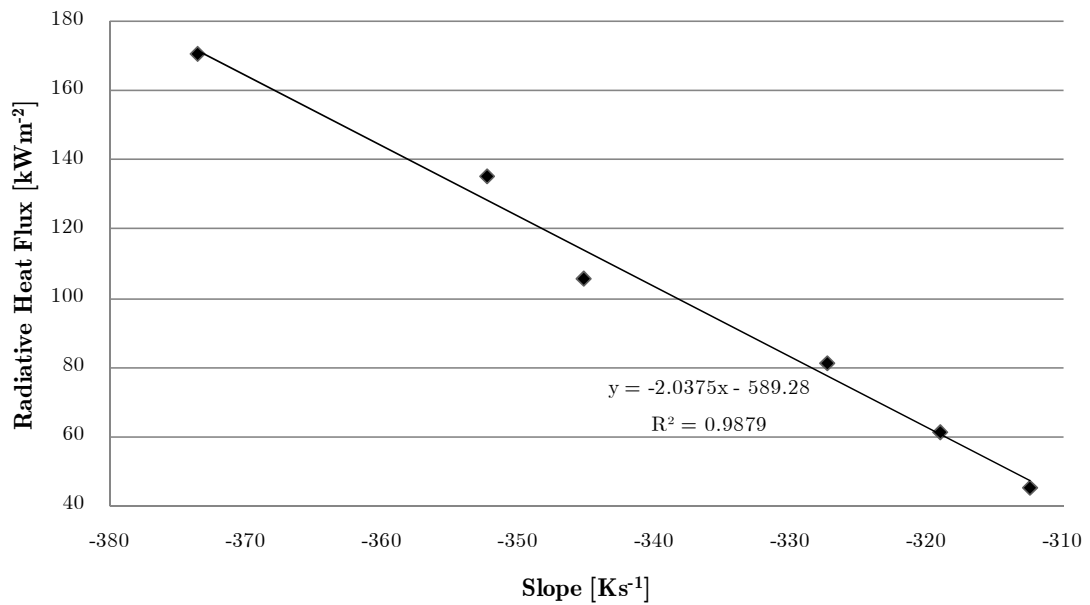


**Figure 4.29** – Sensor 3 linear relationship between mean temperature curve slopes and furnace heat fluxes, in the cooling situation.

It was hoped that the greater dimensional control of the various features of all system components would lead to instruments with very similar behaviours when

compared among themselves, but Figures 4.24 to 4.29 show that although the instruments' response is linear, albeit with admittedly perfectible correlation coefficients, considerable differences remain between them. This renders an individual calibration for each instrument indispensable. The main justification for the verified differences may be the artisanal nature of the instrument's production, namely the welding processes that must evolve into an automated procedure if full-scale production ever takes place.

It should be noted that the linear equations displayed in Figures 4.24 to 4.29 are not instrument calibration curves since no measurement uncertainties and resulting instrument uncertainty ranges are indicated. These will be determined below where the instrument calibration procedures are discussed, but the expected linear relationship between curve slopes and incident heat fluxes is nevertheless apparent.

Another interesting and expected effect given the temperature-controlled operational mode was observed regarding the magnitudes of the measured heating and cooling temperature curve slopes at the various furnace set points: each instrument also displays a linear relationship between the heating and cooling temperature curve slopes, as illustrated in Figures 4.30 to 4.32.

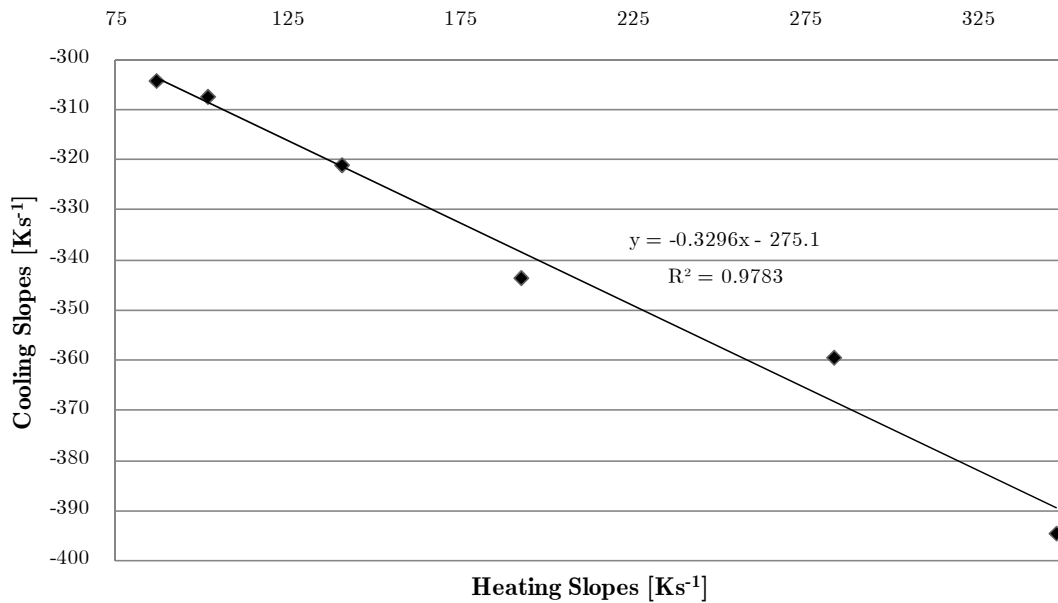


**Figure 4.30** – Sensor 1 linear relationship between heating and cooling temperature curve slopes.



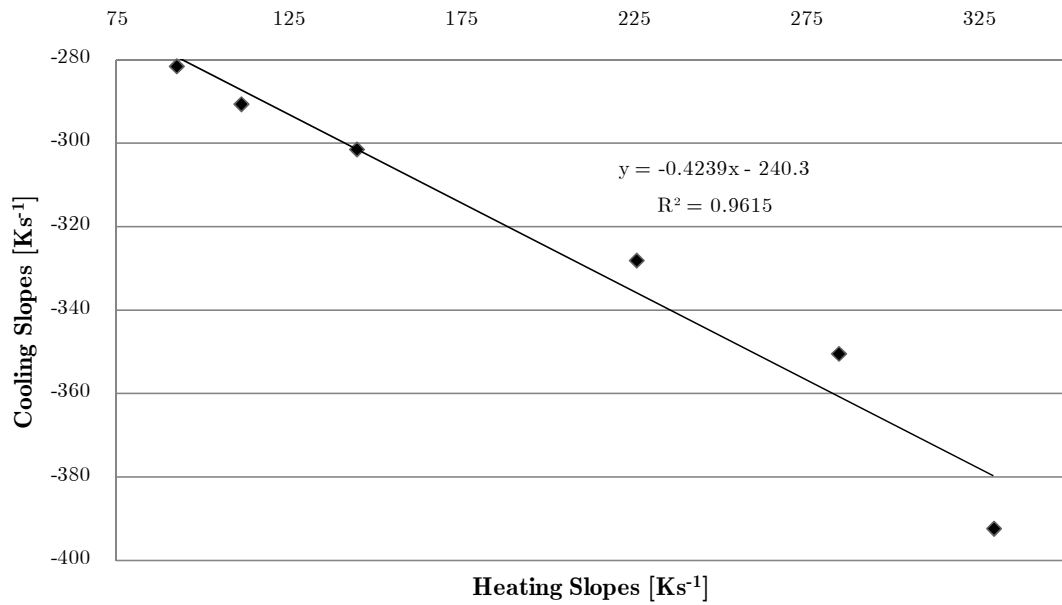


**Figure 4.31** – Sensor 2 linear relationship between heating and cooling temperature curve slopes.

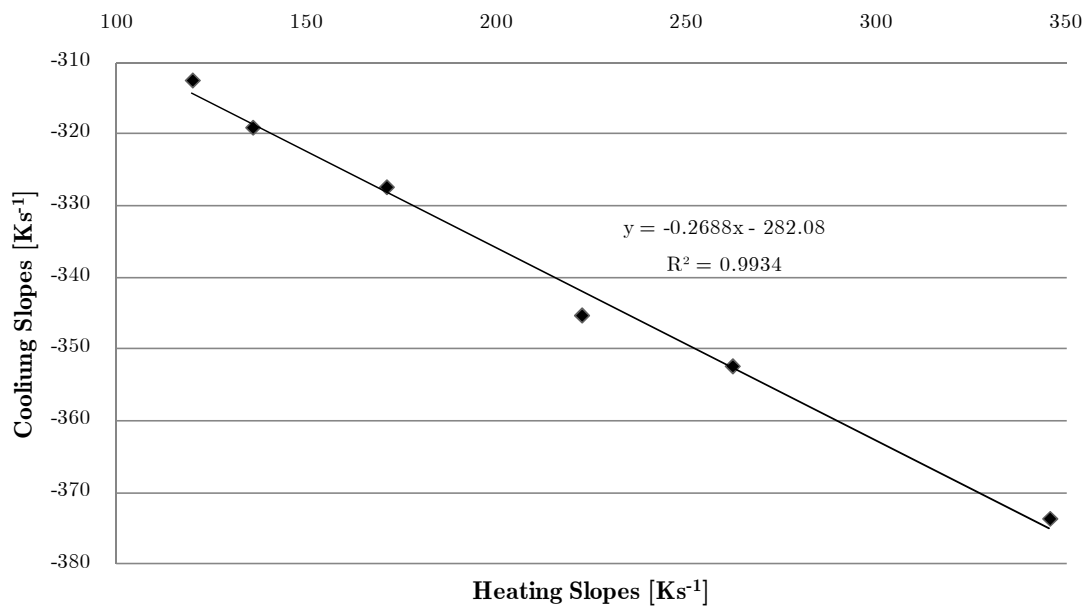


**Figure 4.32** – Sensor 3 linear relationship between heating and cooling temperature curve slopes.

Differences in instrument performance are clear in the obtained correlation coefficients, Sensor 3 displaying higher correlation values while Sensor 2 visibly performs worse than the other two. The calibration procedures discussed below will show the uncertainties associated the relationship between measured slope and the heat flux to be determined.

## 4.4 Calibration of the Transient Heat Flux Meter

Calibration curves are experimentally obtained rules, relating the instrument output and the quantity to be measured as a function of the instrument operating conditions with a defined accuracy.

For the present application the instrument output is the sensing element temperature and time, expressed as temperature curve slopes, during a transient condition created by pulsed air jet, while the quantity to be measured is the incident heat flux.

Calibration of heat flux sensors is a complex issue because some heat flux sensors respond differently to different modes and conditions of heat flux. As in other types of measurement, the major problem with heat flux measurement is the error caused by the disruption due to the presence of the sensor itself.

For sensors based on spatial temperature gradient methods, a larger signal implies a larger temperature difference and a larger temperature disruption. For sensors based on the transient temperature change, the surface temperature is changing while the measurement occurs. The larger the temperature change, the easier the determination of the sensor heat flux, but the larger the error from the sensor temperature disruption. The error caused by this disruption is fairly easy to estimate for conduction but for convection, however, the effect of the surface temperature disruption on the developing thermal boundary layer is much more difficult to estimate and the effect on the heat flux can be much larger than the percentage change of the temperature [Robertson and Ohlemiller 1995]. It is therefore imperative, in convection measurements, to keep the thermal disruption of the sensor to a minimum. This is somewhat less relevant in the case under discussion since radiation will clearly be predominant.

Calibration of differential heat flux sensors can be achieved by conduction, convection or radiation methods, either on their own or in combination. One-dimensional conduction calibration can be carried out by mounting the sensor in a good thermal insulator with known heat addition and removal at each end. Problems with this method arise from the need of knowing the thermal conductivity of the different materials and also the interfacial contact resistances.

A well-established and therefore common laboratory method is the calibration of sensors against a well-defined convection correlation such as for jet impingement [Martin 1977]. In this technique a sensor mounted flush with the surface is exposed to a fluid jet of known geometry, velocity and temperature; the expected value of the local flux is determined from an established correlation for this geometry and for given flow conditions. This is then used for the calibration against the electrical signal from the sensor.

A variety of references exist for calibration methodologies and facilities, from simple layered gauges [Hager et al. 1994], to round robin studies of the calibration of various sensors using different methods [Pitts *et al.* 2006] or radiative calibration procedures of heat flux sensors [Murthy *et al.* 2000], including the determination of and radiative heat flux measurement uncertainty [Bryant *et al.* 2003].

Also widely discussed are fire testing situations where the convective component can be significant, rendering necessary proper heat flux partition experimental setups [Lennon and Silcock 2006]. Specific heat flux meter calibration procedures for fire testing laboratories are also available [Filtz *et al.* 2002].

Alternatively, the sensor can be irradiated to a known intensity by, for example, quartz lamps. Thermal radiation sources such as a laser are well suited for the transient calibration where a mechanical shutter can be used to modulate the heat flux. A comprehensive review of high-temperature radiation reference sources for calibration purposes was recently published [Hartmann 2009].

As mentioned earlier one of the problems encountered during the present study was the cooling of the furnace inner surfaces induced by the cold transpiration airflow and the small amount of contamination coming from the lack of airtightness with the refrigeration airflow. The problem had already been encountered in earlier transpiration radiometers' development and to the best knowledge of the author there are no purpose-developed calibration furnaces that take this problem into account, requiring keeping it in mind when analysing results. This only compounds the problem that lies in the fact that the furnace cannot be taken as a primary calibration standard, which means that an uncertainty in the radiative heat flux at each furnace set point should

also be taken into account, namely by estimating it based on the uncertainties in the furnace emissivity and the temperature values, as explained below.

#### ***4.4.1 Calibration Procedure***

As mentioned above, the calibration procedure of the instrument will involve the determination of the uncertainties associated with each calibration curve, *i.e.* the relationship between measured slope and the heat flux to be determined.

Bearing in mind some of the discussion of results above, the calibration process can be broadly described as follows:

1. Mass flow and acquisition frequency are set at constant values;
2. Maximum and minimum temperatures for the opening and closing of the electrovalve controlling the transpiration mass flow are set;
3. Once initial transient behaviours stabilize, data acquisition is performed;
4. Transient temperature curves are processed using Savitzky-Golay filtering;
5. Mean values for the slopes at each heat flux level are calculated, together with the respective uncertainty;
6. The uncertainty in the furnace heat flux is calculated;
7. Calibration curves, including uncertainties in slope and intercept, are obtained through linear regression.

As discussed above measurements were performed at an arbitrary constant transpiration mass flow of  $0.003 \text{ kg s}^{-1}$ , corresponding to the higher value considered in the transient tests when various mass flows were used, since it was found, as expected, higher measured slopes and higher correlation coefficients in the linear relationships between heat fluxes and measured slopes are encountered at higher mass flow rates. Higher transpiration mass flows values also provide more effective protection against incoming particles. The data acquisition frequency was likewise set at a constant value of 250 Hz, previously proven to be sufficient for the task at hand.

Maximum and minimum temperatures for the opening and closing of the electrovalve that controls the transpiration mass flow rate were set at 120 and 90°C respectively for tests carried out at furnace temperatures ranging between 1000 and 1500°C, with 100°C increments. These temperatures were kept the same for all tests since they have implications in terms of response times materialized in the number of measurement cycles per time unit. Higher heat fluxes lead to sharper temperature variations, enabling faster cycles, with average cycle times ranging from 1.7 s at 1000°C to 0,75 s at 1500°C, using the aforementioned maximum and minimum temperatures.

This temperature interval was selected for two reasons, the least of which was producing clear maximum slope values, which might be more difficult to identify for smaller temperature ranges than the specified 30°C, although smaller temperature intervals obviously allow faster heating and cooling cycles.

The main reason for the specified range was however providing valve opening and closing temperature values that would be common to the entire operation range, in order to establish the expected linear variation pattern. At high heat flux levels a low measured temperature might not be reached even after the transpiration airflow was restored, while at lower heat flux levels the higher measured temperatures might not be reached given the fact that for temperature control safety reasons the cycle was programmed to always start from a situation where the transpiration airflow is on.

Numerous transient temperature curves slopes were determined for calibration purposes, 500 values being used to calculate mean values and standard deviations for each furnace set point, after the aforementioned stabilization times. These mean values and respective standard deviations, together with the sample size and a specified confidence interval (in this case, 95%), allowed the calculation of the uncertainties in the heating and cooling slopes. The values used to calculate the slope mean values were themselves obtained after the implementation of Savitzky-Golay filtering, as described earlier.

The aforementioned cooling of the furnace by the cold transpiration airflow means that the furnace cannot be taken as a primary calibration standard and renders the quantification of the uncertainty in the radiative heat flux at each furnace set point

necessary, based on the uncertainties in the furnace emissivity and the temperature values. Writing the corrected heat flux as:

$$q = \varepsilon_{\text{app}} \sigma T^4 \quad (4.10)$$

its uncertainty due to uncertainties in the temperature and the apparent emissivity can be written as:

$$\omega_q = \sqrt{\left(\frac{\partial q}{\partial \varepsilon_{\text{app}}}\right)^2 \omega_{\varepsilon_{\text{app}}}^2 + \left(\frac{\partial q}{\partial T}\right)^2 \omega_T^2} \quad (4.11)$$

or

$$\omega_q = \sqrt{(\sigma T^4)^2 \omega_{\varepsilon_{\text{app}}}^2 + (4\varepsilon_{\text{app}} \sigma T^3)^2 \omega_T^2} \quad (4.12)$$

The uncertainty in the apparent emissivity can be found in Equation 4.2, while the uncertainty in temperature was set at 0.75% of each temperature, as per NIST reference tables [NIST 1999]. This value is for standard K-type thermocouples, rather than the sheathed thermocouple used here, but is nevertheless a reasonable upper estimate.

Obtaining uncertainty values both for the furnace heat fluxes and the temperature curve slopes enables the calculation of calibration curves by performing linear regressions. Despite its seeming simplicity, the problem of finding the best straight line through an experimentally determined set of points on the  $x$ - $y$  plane has triggered the publication of hundreds of papers in a host of fields since Gauss' original development of the method of least-squares estimation (LSE). Although the traditional regression of  $y$  on  $x$  is widely used and included in most hand calculators and spreadsheets, only rarely are the  $x$  values actually error-free. In reality, both  $x$  and  $y$  errors may be significant, and may vary from point to point. Furthermore, the errors in

the two coordinates may be highly correlated, although in the present case the correlation was assumed to be nonexistent.

The approaches to fitting straight lines to collections of  $x$ - $y$  data pairs can be broadly grouped into two categories: the “standard” least-squares methods in which the distances between the fitted line and the data in the  $y$ -direction are minimized, and the “bivariate” least-squares methods in which the perpendicular distances between the fitted line and the data are minimized. In all of these methods, weights may be also applied to the data to account for the differing uncertainties in the individual points. In “standard” least-squares, the weighting pertains to the  $y$ -variables only, whereas in “bivariate” methods, weights can be assigned for the  $x$ - and  $y$ -variables independently.

A variety of references are available listing available linear least-squares data fitting methods [Cantrell 2008], one of the most widespread being developed by York, first giving the general solutions for the LSE best straight line in terms of its slope and  $y$  intercept and errors in these two parameters, when both observables ( $X_i$ ,  $Y_i$ ) are subject to errors which vary from point to point [York 1966]. A more general solution also allowed for the possible correlation between the  $x$  and  $y$  errors at each point [York 1968]. A compact set of equations for the slope, intercept, and standard errors was proposed [York *et al.* 2004] and implemented in an iterative function available at the *Matlab* website [Wiens 2010], used here.

This methodology enables the calculation of the same type of linear relationship between temperature curve slopes and heat fluxes as displayed in Figures 4.24 to 4.29, but taking into account the aforementioned  $x$ - and  $y$ -variables uncertainties.

Figures 4.33 and 4.34 are examples of the plots resulting from the application of the *Matlab* function, where the calibration curves obtained using standard least-squares estimation are compared with the method proposed by York [York *et al.* 2004]. The function represents errors in  $x$  (slope) and  $y$  (heat flux) as error bars around the mean values.

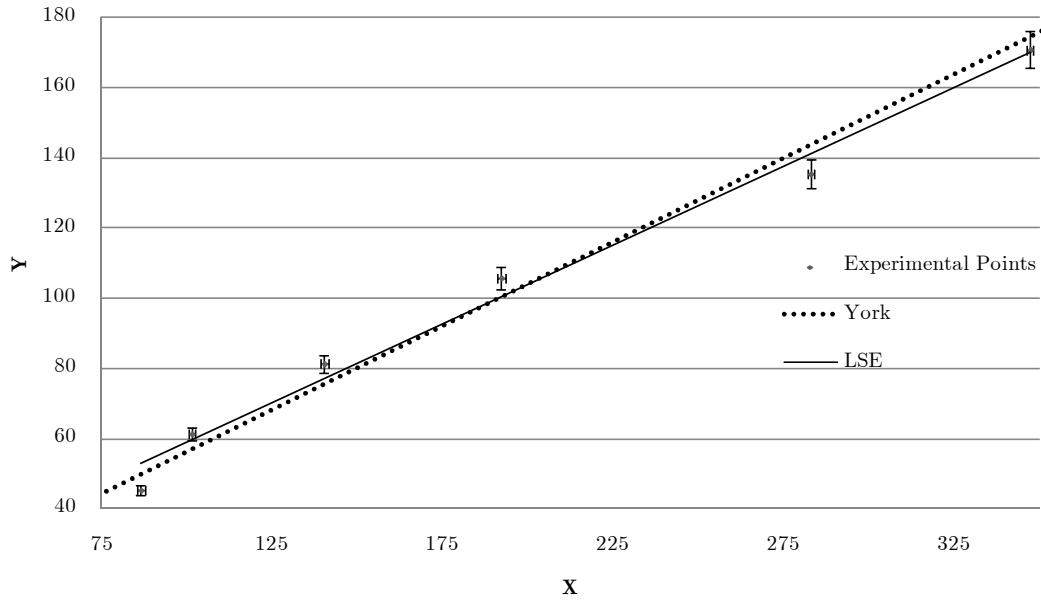


**Figure 4.33** – Comparison of LSE and York-method linear regressions for the heating situation in Sensor 1.

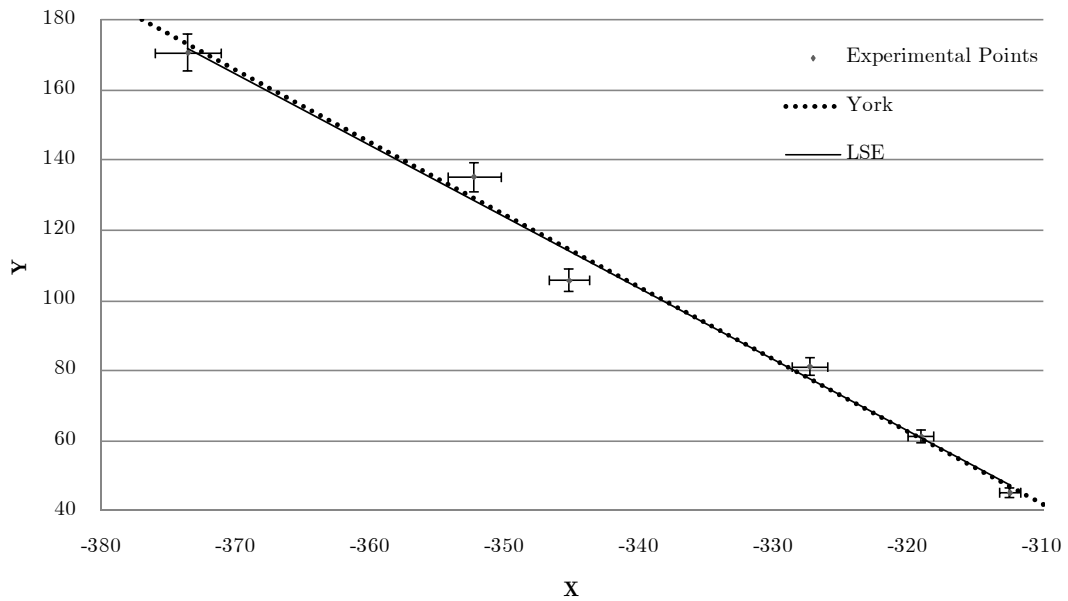


**Figure 4.34** – Comparison of LSE and York-method linear regressions for the cooling situation in Sensor 3.

Regression results, regarding parameters such as calibration curve slopes, intercepts and respective standard errors, are summarized in Table 4.4. Errors were not computed for LSE but the regression slopes and intercepts are displayed for comparison purposes. Differences are slight but undeniable.



It is readily visible that taking into account errors in both temperature curve slopes and heat fluxes, as per the York method, increases slopes in all cases, reflecting the “weighting” induced by the larger “error clouds” around higher heat flux values, as visible for instance in Figure 4.33. Intercept values are “driven” by this increase in slope and decrease as expected given the higher slopes.

The uncertainties in slopes lead to less than 5% variations of its value in all cases, reflecting adequate relative accuracy in the absence of reliable calibration references. It should be stressed that given the experimental setup the convective component of the heat flux is probably always too small to have a significant impact on measurements even for the heating situation where the total heat flux is received by the sensing element.

**Table 4.4** – Linear regression results summary

		<b>Method</b>	<b>Slope</b>	<b>Error</b>	<b>Intercept</b>	<b>Error</b>
<b>Sensor 1</b>	<i>Heating</i>	LSE	0.450	-	13.859	-
		York	0.479	$\pm 0.015$	8.423	$\pm 2.076$
	<i>Cooling</i>	LSE	-1.347	-	-355.657	-
		York	-1.462	$\pm 0.054$	-394.815	$\pm 17.204$
<b>Sensor 2</b>	<i>Heating</i>	LSE	0.482	-	4.871	-
		York	0.485	$\pm 0.015$	3.389	$\pm 2.221$
	<i>Cooling</i>	LSE	-1.118	-	-262.282	-
		York	-1.212	$\pm 0.044$	-292.240	$\pm 13.104$
<b>Sensor 3</b>	<i>Heating</i>	LSE	0.550	-	-15.131	-
		York	0.580	$\pm 0.018$	-21.088	$\pm 2.948$
	<i>Cooling</i>	LSE	-2.037	-	-589.282	-
		York	-2.062	$\pm 0.089$	-597.063	$\pm 28.792$

Using the results summarized in Table 4.4, Equations 4.8 and 4.9 can be rewritten as:

$$q_{\text{total,sensor 1}} = (0.479 \pm 0.015) \left. \frac{dT}{dt} \right|_{\text{max,heating}} + (8.423 \pm 2.076) \text{ [kWm}^{-2}\text{]} \quad (4.13)$$

$$q_{\text{rad,sensor 1}} = (-1.462 \pm 0.054) \left. \frac{dT}{dt} \right|_{\text{max,cooling}} - (394.81 \pm 17.20) \text{ [kWm}^{-2}\text{]} \quad (4.14)$$

$$q_{\text{total,sensor 2}} = (0.485 \pm 0.015) \left. \frac{dT}{dt} \right|_{\text{max,heating}} + (3.389 \pm 2.221) \text{ [kWm}^{-2}\text{]} \quad (4.15)$$

$$q_{\text{rad,sensor 2}} = (-1.212 \pm 0.044) \left. \frac{dT}{dt} \right|_{\text{max,cooling}} - (292.24 \pm 13.10) \text{ [kWm}^{-2}\text{]} \quad (4.16)$$

$$q_{\text{total,sensor 3}} = (0.480 \pm 0.018) \left. \frac{dT}{dt} \right|_{\text{max,heating}} - (21.088 \pm 2.948) \text{ [kWm}^{-2}\text{]} \quad (4.17)$$

$$q_{\text{rad,sensor 3}} = (-2.062 \pm 0.089) \left. \frac{dT}{dt} \right|_{\text{max,cooling}} - (597.06 \pm 28.8) \text{ [kWm}^{-2}\text{]} \quad (4.18)$$

True heat flux partitioning potential is demonstrated but can only be really achieved once reliable test and calibration facilities are available. Given the aforementioned lack of calibration sources that are not affected by the transpiration airflow, this means that further work is necessary regarding the facilities themselves, besides improvements to the instruments themselves.

Observed standard deviation were higher in the cooling cases and translate into absolute higher error values in this process in comparison with the heating process, reflecting the complex interaction encountered when the transpiration airflow meets plate and thermocouple.

As mentioned above it was hoped that a precise dimensional control of the geometric features of the various components would result in instruments with very

similar behaviours when compared with each other, which could potentially make individual calibration for each instrument indispensable. This is clearly not the case, considerable differences existing between instruments as materialized in the differing calibration curve parameters, especially slopes and their uncertainties.

The linearity of the transient responses of all three instruments is nevertheless satisfactory, as can be judged by the correlation coefficients shown in Figures 4.24 to 4.29, and their reasonable accuracy was also established above for the transpiration mass flow and range of temperatures used in this particular calibration. The reason for that undesirable behaviour, namely in an industrial production framework, was already discussed in a previous section.

Providing a plate central zone with holes placed at a slightly greater distance from the thermocouple attachment point should diminish the risk of disruption of the perforated pattern while rendering the welding itself easier to execute and more robust, without significantly coming to the detriment of the sensor's thermal inertia.

The issue of weldings quality and variability is relevant not also from the pure thermal point of view but also in terms of overall instrument robustness. While some units withstood all tests without any visible changes, including the two 8 hour runs, one unit broke during operation (the thermocouple coming loose from the plate but still being capable of temperature measurements) while two others broke due to clumsy handling, being dropped to the ground and breaking the thermocouple attachment.

These facts emphasize the need to revise the thermocouple attachment method, which is far from being a trivial matter given its small size, and attachment location free space, as well as the low plate thickness. These challenging requirements led to some unusual options that resulted in functioning prototypes with some handicaps that must be addressed in future versions of the instrument.

From the analytical point of view, the fact that the calibrations above took place at a single, arbitrary transpiration mass flow must be remembered. Now that the basic principle is established and was shown to be viable, tests at other mass flows would enable the establishment of a range of calibration curves for various situations potentially more suited to other possible working conditions, bearing in mind that in

terms of transient operation sensitivity higher mass flow rates were shown to lead to greater temperature curve slopes.

## 4.5 Concluding Remarks

The present chapter was devoted to the description of the experimental verification and calibration of the transient transpiration heat flux meter prototypes.

Three flux meters were built and tested. A description of the constructed prototypes and of the experimental setup was presented along with a discussion of the experimental procedure followed in the experimental study of the instrument's performance.

A reasonable agreement was found between the steady experimental data and the numerical model predictions, despite the uncertainty regarding the sensing element's surface emissivity. Measured steady temperatures were the same in all cases to a very small difference and the instrument output is linear with heat fluxes. Truly long terms tests could not be performed with the available equipment but runs lasting several hours at high temperatures indicate a basic soundness of the design and its potential for full scale applications, despite some concerns in terms of robustness if some changes are not introduced.

A calibration procedure for the instrument's transient behaviour was described and discussed. Calibrated relationships between measured maximum temperature curve slopes and furnace heat fluxes are discussed, namely in terms of the effect of uncertainties in their magnitudes on the calibration curves. Conclusions regarding operational aspects are also presented.

## CHAPTER 5

# GLOBAL CONCLUSIONS AND PROPOSED DEVELOPMENTS

A summary of all the work described within this thesis is provided and the main conclusions are listed and discussed. Proposed developments to be carried out in the future are also presented.

### 5.1 Summary

The present document presents a new embodiment of the transpiration radiometer principle, intended to maintain established features of previous instruments of the same type while diminishing their dimensions and response time, the purpose of such instruments remaining the measurement of the total hemispherical radiation and its separation into radiative and convective heat fluxes being proposed.

The proposed concept is particularly suitable and intended for high temperature, harsh environments. The transpiration principle implies the possibility of eliminating the convective component of the heat flux, hence the transpiration radiometer designation.

A bibliographic review covering existing techniques heat flux measurements made clear that no instrument exists with the particular combination of features proposed here. This assumption was embodied in a patent request and supported by the fact that the relevant issuing organization (*Instituto Nacional de Propriedade Industrial* – Portuguese National Institute of Industrial Property) approved the preliminary report, having found no impediments to patentability, and issued a provisional patent application that must be converted into a definitive patent application, pending a decision to carry on by the administration of the University of Aveiro, as patent co-proprietor, to be taken until August 1st, 2013

A chapter was devoted to the description of the instrument's working principle and of possible formulations for the study of the sensing element's behaviour.

The problem requirements and subsequent simplifications were discussed and implemented as necessary. The need to take into account a non-homogeneous transient problem was foremost, especially given the presence of the interaction between a perforated plate being heated by radiation and a colder transpiration airflow crossing the pattern of holes, leading to the analytical treatment of such an interaction as a heat sink term.

The GF method was recognized as being well suited to the task of providing an analytical solution and a proper methodology was established in order to implement it in order to obtain temperature values for all locations and times of interest. A concurrent finite differences approach was also found to be adequate for the same purpose, with added benefits in terms of implementation in situations where boundary conditions vary in space and time. Other relationships necessary to describe phenomena that needed to be integrated into the model were obtained and implemented.

A comparison of results of both approaches with those of equivalent CFD simulations of the same physical problems showed good approximation and simultaneously provided both increased confidence in the results provided by the GFSE and validation for the simulations to be carried out for dimensioning purposes using CFD software.

The dimensional and operational parameters that influence sensor performance were determined and discussed, based both on established analytical principles and on the simulation software that was compared to the analytical models discussed in the previous chapter.

Ranges for the relevant mass flow values to be used for the intended range of furnace working temperatures were also identified in order to guarantee the simplification of the radiative balance between the plate and its surroundings and to ensure proper boundary layer control while avoiding compressibility phenomena. The instrument's transient behaviour was also found to be within expectations and the proposed external cooling system was likewise found satisfactory in theory.

The procedures developed earlier led to the building of the prototypes and provided the framework to evaluate their performance, by comparison with simulated values, although necessary adjustments naturally had to be made in order to accommodate differences dictated by laboratory conditions.

Three flux meters were built and tested. A description of the constructed prototypes and of the experimental setup was presented along with a discussion of the experimental procedure followed in the experimental study of the instrument's performance.

A reasonable agreement was found between the experimental data and the numerical model predictions, Runs lasting several hours at high temperatures indicate a basic soundness of the design and its potential for full scale applications.

A calibration procedure for the instrument's transient behaviour was described and discussed. Calibrated relationships between measured maximum temperature curve slopes and furnace heat fluxes were discussed, namely in terms of the effect of uncertainties in their magnitudes on the calibration curves. Conclusions regarding operational aspects were also presented.

## **5.2 Conclusions**

The various tasks summarized above resulted in an operational heat flux meter that was shown to have significantly lessened dimensions, geometrical complexity and response times when compared with earlier transpiration radiometers.

The much-reduced thermal inertia and cooling needs of the sensing element developed for the present instrument furthermore enabled a switching off of the transpiration mass flow, enabling the possibility of performing heat flux partitioning given the small times associated with the transient measurement cycles, meaning that sufficiently fast consecutive measurements of total and radiative heat fluxes render the estimation of the convection component by difference realistic. This feature was not present in earlier instruments because of the refrigeration needs, which made transpiration airflows indispensable at all times. Given the experimental setup the convective component of the heat flux is probably always too small to have a significant impact on measurements, and the heat flux partitioning potential

demonstrated can only be really achieved once reliable test and calibration facilities are available.

The satisfactory linearity and accuracy displayed by the instruments can be attributed to the precise control of dimensional parameters in the sensing elements, and the option of using such components is considered to be validated. However, it was hoped that this precise dimensional control would result in instruments with identical behaviours when compared with each other, potentially rendering individual calibration for each instrument necessary. This is not the case, considerable differences existing between instruments as materialized in the differing calibration curve parameters, especially slopes and their respective uncertainties.

The linearity of the transient responses of all three instruments is nevertheless satisfactory as indicated by the correlation coefficients of their regression curves, and their reasonable accuracy was also established for the transpiration mass flow and range of temperatures used in this particular calibration, the uncertainties in slopes leading to less than 5% variations of their values.

Better control and repeatability in the various welding processes would partially overcome verified differences and are essential if full-scale industrial is ever to take place, since issues regarding the quality of the weldings were identified.

The lack of quality of some weldings was first of all visible in the existence of the contamination leakage between airflows and must also be present at the junction of the thermocouple to the plate, where the microperforated pattern can be more or less damaged by the welding process and change the local interaction between the transpiration airflow and the plate, as well as the temperature distribution in the plate itself, influencing the thermocouple output and potentially causing the observed differences, especially during the cooling process when the airflow actually crosses the plate and causes a somewhat more erratic observed cooling process behaviour.

Experience in handling of the prototypes during the testing procedures also showed that the sensing elements are sufficiently sturdy to handle some level of mishandling without measurable harm and can withstand shocks and impacts greater than those to be expected in aggressive high temperature environments with large



amounts of soot and dust particles. More extensive long term tests are however necessary in order to conclude if these positive traits are retained over time.

The microperforated plate was shown to be easy to refrigerate, while initial concerns regarding the lack of robustness both of the 0.25 mm thermocouples themselves and their welding to the perforated plate were not wholly verified in practice, so their use can be recommended for the intended purpose. Truly long terms tests could not be performed with the available equipment but runs lasting several hours at high temperatures indicate a basic soundness of the design and its potential for full scale applications.

The fact that most of the sensing element refrigeration actually comes from the transpiration airflow was corroborated to a large extent by the 8 hour runs described above, where the refrigeration airflow was shut down without any detrimental effect. This means that the option for a porous holder can be re-examined and compared with the possibility of providing a thin-walled holder that could be maintained at acceptable temperatures purely by being refrigerated by the transpiration airflow, resulting in a much less complex and cheaper system.

Cost considerations are fundamental for several reasons, both in this prototype stage and especially in possible later production versions where this academic discussion will need to move into much more practical considerations. Possible reductions in system complexity such as those arising from doing without a porous holder can also have a significant impact in terms of price and must therefore be investigated, but in any case the high unit prices and building/assembly costs encountered in the work described here would be brought down by ordering larger batches of components. These reduced costs would in turn increase the likelihood of an actual operational deployment of the proposed instruments.

While troublesome, the artisanal and perfectible welding processes used were not an obstacle in establishing the potential of the type of proposed instrument but rather an identified area of further refinement in future improved versions.

The fact that the relevant issuing organization (*Instituto Nacional de Propriedade Industrial* – Portuguese National Institute of Industrial Property) issued a provisional patent application, having found no impediments to patentability, indicates

the novelty of the work described here and helps putting into perspective an eventual commercial interest in optimized and more thoroughly tested instruments of the same type, given the potential demonstrated here.

### 5.3 Future Developments

The work started with the present study may proceed in different directions, especially since the developed instrument may be improved in various ways. Bearing in mind some the conclusions discussed in each chapter and above, the following research topics are recommended for future work:

- Given the aforementioned lack of calibration sources that are not affected by the transpiration airflow, further work is necessary regarding the calibration heat sources, besides improvements to the instruments themselves;
- A calibration setup capable of adequately producing measurable convective heat fluxes usable for calibration purposes is fundamental in fulfilling the potential shown here in terms of heat flux partitioning implementation;
- Truly long term testing must be carried out in order to prove the soundness of the retained design options embodied in the present version of the instrument;
- Providing a plate central zone with holes placed at a slightly greater distance from the thermocouple attachment point should diminish the risk of disruption of the perforated pattern while rendering the welding itself easier to execute and more robust, without significantly coming to the detriment of the sensor's thermal inertia;
- The capability to implement all necessary weldings in a reliable fashion will have to be developed through a combination of purpose built equipment and revised design. This is relevant in terms of building ease and reliability but especially so in terms of operational robustness and measurement accuracy;
- Crystal growth techniques such as laser-heated pedestal growth (LHPG) could be used to obtain thermocouple junctions grown directly onto the intended emplacement on the microperforated plate [Feigelson 1985, Andreeta and Hernandez 2010]. Such techniques are becoming more widespread and the machinery necessary to their implementation is steadily decreasing in cost,

rendering it potentially interesting in circumventing thermocouple welding issues;

- The problems encountered in the refrigeration airflow tubing due to the hot gas blowback from the furnace also indicate that the present solution must be changed, the most obvious solution being to change the inlet from its present tangential location to an inlet concentric (*i.e.* annular) with that of the transpiration airflow, in order to let the body of the instrument provide it with the same shielding from direct radiation;
- Standard tubing dimensions and fittings should be used as much as possible, lessening some problem encountered in the present version;
- The sensing element spectral sensitivity can be optimized or even tailored to specific wavelengths both by superficial treatments for emissivity adjustment and by adjusting microperforated plate parameters such as thickness or hole diameter and spacing;
- The transient transpiration principle implemented here can be extended to more complex geometries besides the cylindrical components studied here, especially in systems where air cooling is already used, as is the case in the cooling of some gas turbine blades.

All of the aforementioned points would be important both in the validation of the work described within this document but especially as contributions to an improved commercial version based on the design proposed herein



## REFERENCES

- [Afgan and Leontiev 1995] N. H. Afgan and A. I. Leontiev. Instrument for Thermal Radiation Flux Measurement in High Temperature Gas Flow (Cuernavaca Instrument). *Heat Recovery Systems and CHP*, **15**(4):347-350, 1995.
- [Alekseev 1997] A. K. Alekseev. The Heat Flux Measurement Method Based on Isotherm Registration. *International Journal of Heat and Mass Transfer*, **40**(7):1643-1646, 1997.
- [Andreeta and Hernandez 2010] M. R. B. Andreeta and A. C. Hernandez. Laser-Heated Pedestal Growth of Oxide Fibers. In *Springer Handbook of Crystal Growth*. Springer, 2010.
- [Andrews *et al.* 1988] G. E. Andrews, M. Alikhanizadeh, F. Bazdidi-Tehrani, C. I. Hussain and M. S. K. Azari. Small Diameter Film Cooling Holes - the Influence of Hole Size and Pitch. *International Journal of Turbo and Jet-Engines*, **5**:61-71, 1988.
- [Andrews *et al.* 1991] G. E. Andrews, F. Bazdidi-Tehrani, C. I. Hussain and J. P. Pearson. Small Diameter Film Cooling Hole Heat Transfer - The Influence of the Hole Length. *36th International Gas Turbine and Aeroengine Congress and Exposition, American Society of Mechanical Engineers*. June 3-6. Orlando, FL, USA, 1991.
- [Anson and Godridge 1967] D. Anson and A. M. Godridge. A Simple Method for Measuring Heat Flux. *Journal of Scientific Instruments*, **44**(7):541-544, 1967.
- [Arai *et al.* 1996] N. Arai, A. Matsunami and S. W. Churchill. A Review of Measurements of Heat Flux Density Applicable to the Field of Combustion. *Experimental Thermal and Fluid Science*, **12**(4):452-460, 1996.
- [Arpaci 1966] V. S. Arpaci. *Conduction Heat Transfer*. Addison-Wesley, 1966.
- [Astarita *et al.* 2006] T. Astarita, G. Cardone and G. M. Carlomagno. Infrared Thermography: An Optical Method in Heat Transfer and Fluid Flow Visualisation. *Optics and Lasers in Engineering*, **44**(3-4):261-281, 2006.

- [Astarita *et al.* 2000] T. Astarita, G. Cardone, G. M. Carlomagno and C. Meola. A Survey on Infrared Thermography for Convective Heat Transfer Measurements. *Optics & Laser Technology*, **32**(7-8):593-610, 2000.
- [ASTM 1988a] ASTM Standard E457-72. *Standard method for measuring heat transfer rate using a thermal capacitance (slug) calorimeter*. American Society for Testing and Materials, 1988.
- [ASTM 1988b] ASTM Standard E598-77. *Standard method for measuring extreme heat-transfer rates from high-energy environments using a transient null-point calorimeter*. American Society for Testing and Materials, 1988.
- [Atkinson *et al.* 1983] W. Atkinson, H. F. Hobart and R. R. Strange. Advanced High Temperature Heat Flux Sensors. *International Conference of the Instrument Society of America (ISA '83)*, October 10-13, Houston, TX, USA, 1983.
- [Atkinson *et al.* 1988] W. H. Atkinson, R. R. Strange and R. J. Moffat. Development of Porous Plug Radiometers for Use in Advanced Gas Turbine Programs. *AIAA/ASME/SAE/ASEE 24th Joint Propulsion Conference*, 1988.
- [Baker and Ryder 1975] H. D. Baker and E. A. Ryder. *Temperature Measurement in Engineering*. Omega Press, 1975.
- [Ballestrín *et al.* 2006] J. Ballestrín, C. A. Estrada, M. Rodríguez-Alonso, C. Pérez-Rábago, L. W. Langley and A. Barnes. Heat Flux Sensors: Calorimeters or Radiometers? *Solar Energy*, **80**(10):1314-1320, 2006.
- [Ballestrín and Monterreal 2004] J. Ballestrín and R. Monterreal. Hybrid Heat Flux Measurement System for Solar Central Receiver Evaluation. *Energy*, **29**(5-6):915-924, 2004.
- [Ballintijn and Ginsel 1968] C. M. Ballintijn and L. A. Ginsel. Shell Develops New Heat-Flowmeter. *The Oil and Gas Journal*, 121-125, July 1968.
- [Baughn 1995] J. W. Baughn. Liquid Crystal Methods for Studying Turbulent Heat Transfer. *International Journal of Heat and Fluid Flow*, **16**:365-375, 1995.
- [Beck 1984] J. V. Beck. Green's Function Solution for Transient Heat Conduction Problems. *International Journal of Heat and Mass Transfer*, **27**:1235-1244, 1984.
- [Beck 1986] J. V. Beck. Green's Function and Numbering System for Transient Heat Conduction. *American Institute of Aeronautics and Astronautics Journal*, **24**:327-333, 1986.

- [Beck and Keltner 1987] J. V. Beck and N. R. Keltner. Green's Function Partitioning Procedure Applied to Foil Heat Flux Gauges. *Journal of Heat Transfer*, **109**:274-280, 1987.
- [Beck and Litkouhi 1985] J. V. Beck and B. Litkouhi. Heat Conduction Numbering System. *American Society of Mechanical Engineers Paper 85-WA/HT-63*, 1985.
- [Beirão *et al.* 2006] S. Beirão, M. Ramires, M. Dix and C. Nieto de Castro. A New Instrument for the Measurement of the Thermal Conductivity of Fluids. *International Journal of Thermophysics*, **27**(4):1018-1041, 2006.
- [Bethe 1944] H. A. Bethe. Theory of Diffraction by Small Holes. *Physical Review*, **66**:163-182, 1944.
- [Bhattacharya *et al.* 2007] A. Bhattacharya, R. Srinivasa Rao and M. Ghanashyam Krishna. Characterization of  $\text{Yb}_2\text{O}_3$  Based Optical Temperature Sensor for High Temperature Applications. *Sensors and Actuators A: Physical*, **134**(2):348-356, 2007.
- [Bizzak and Chyu 1995] D. J. Bizzak and M. K. Chyu. Use of Laser-Induced Fluorescence Thermal Imaging System for Local Jet Impingement Heat Transfer Measurement. *International Journal of Heat and Mass Transfer*, **38**:267-274, 1995.
- [Blanchat *et al.* 2009] T. Blanchat, T. O'Hern, S. Kearney, A. Ricks and D. Jernigan. Validation Experiments to Determine Radiation Partitioning of Heat Flux to an Object in a Fully Turbulent Fire. *Proceedings of the Combustion Institute*, **32**(2):2511-2518, 2009.
- [Boomsma *et al.* 2003] K. Boomsma, D. Poulikakos and F. Zwick. Metal Foams as Compact High Performance Heat Exchangers. *Mechanics of Materials*, **35**(12):1161-1176, 2003.
- [Bouwkamp 1950] C. J. Bouwkamp. On the Diffraction of Electromagnetic Waves by Small Circular Disks and Holes. *Philips Research Reports*, **5**:401-422, 1950.
- [Brajskovic and Afgan 1991] B. Brajskovic and N. Afgan. A Heat Flux-Meter for Ash Deposit Monitoring Systems – II. "Clean" Heat Flux-Meter Characteristics. *International Journal of Heat and Mass Transfer*, **34**(9):2303-2315, 1991.
- [Brajskovic *et al.* 1991] B. Brajskovic, M. Matovic and N. Afgan. A Heat Flux-Meter for Ash Deposit Monitoring Systems - I. Ash Deposit Prevention. *International Journal of Heat and Mass Transfer*, **34**(9):2291-2301, 1991.

- [Bryant *et al.* 2003] R. Bryant, C. Womeldorf, E. Johnsson and T. Ohlemiller. Radiative Heat Flux Measurement Uncertainty. *Fire and Materials*, **27**(5):209-222, 2003.
- [Butler *et al.* 1994] B. W. Butler, M. K. Denison and B. W. Webb. Radiation Heat Transfer in a Laboratory-Scale, Pulverized Coal-Fired Reactor. *Experimental Thermal and Fluid Science*, **9**(1):69-79, 1994.
- [Calisto and Martins 2012] H. Calisto and N. Martins. *Gas-Cooled Compact Transient Transpiration Heat Flux Meter*. Portugal patent application, Instituto Nacional de Propriedade Industrial, INPI - PT 106.475. 2012.
- [Calisto *et al.* 2008] H. Calisto, N. Martins and N. Afgan. Diagnostic System for Boilers and Furnaces Using CFD and Neural Networks. *Expert Systems with Applications*, **35**(4):1780-1787, 2008.
- [Camci 1996] C. Camci. Liquid Crystal Thermography. In *Temperature Measurements*, Von Karman Institute Lecture Series, 1996.
- [Canpean and Astilean 2009] V. Canpean and S. Astilean. Interaction of Light with Metallic Nanohole Arrays. *Nuclear Instruments and Methods in Physics Research Section B: Beam Interactions with Materials and Atoms*, **267**(2):397-399, 2009.
- [Cantrell 2008] C. A. Cantrell. Technical Note: Review of Methods for Linear Least-Squares Fitting of Data and Application to Atmospheric Chemistry Problems. *Atmospheric Chemistry and Physics Discussions*, **8**(2):6409 - 6436, 2008.
- [Carpenter and Sewell 1962] W. G. D. Carpenter and J. H. Sewell. *Thermal Emissivities of Some Metallic and Non-Metallic Surfaces over the Range of 70°C to 250°C*. Royal Aircraft Establishment - Farnborough, 1962.
- [Carslaw and Jaeger 1959] H. S. Carslaw and J. C. Jaeger. *Conduction of Heat in Solids* - 2nd Edition. Oxford University Press, 1959.
- [Çengel 2006] Y. A. Çengel. *Heat and Mass Transfer: A Practical Approach*. McGraw-Hill Higher Education, 2006.
- [Chander and Ray 2005] S. Chander and A. Ray. Flame Impingement Heat Transfer: A Review. *Energy Conversion and Management*, **46**(18-19):2803-2837, 2005.



- [Chao-Chun 1973] C. Chao-Chun. Transmission of Microwave through Perforated Flat Plates of Finite Thickness. *IEEE Transactions on Microwave Theory and Techniques*, **21**(1):1-6, 1973.
- [Chedaille and Braud 1972] J. Chedaille and Y. Braud. *Measurements in Flames*. Edward Arnold Ltd, 1972.
- [Childs *et al.* 1999] P. R. N. Childs, J. R. Greenwood and C. A. Long. Heat Flux Measurement Techniques. *Proceedings of the Institution of Mechanical Engineers Part C - Journal of Mechanical Engineering Science*, **213**(7):655-677, 1999.
- [Childs *et al.* 2000] P. R. N. Childs, J. R. Greenwood and C. A. Long. Review of Temperature Measurement. *Review of Scientific Instruments*, **71**(8):2959-2978, 2000.
- [Cho *et al.* 1997] H. H. Cho, M. Y. Jabbari and R. J. Goldstein. Experimental Mass (Heat) Transfer in and near a Circular Hole in a Flat Plate. *International Journal of Heat and Mass Transfer*, **40**(10):2431-2443, 1997.
- [Cole 2000] K. D. Cole. *Green's Function Library*. Available: <http://www.greensfunction.unl.edu> [Accessed January 2012], 2000.
- [Cole 2004] K. Cole. Fast-Converging Series for Heat Conduction in the Circular Cylinder. *Journal of Engineering Mathematics*, **49**(3):217-232, 2004.
- [Cole *et al.* 2010] K. Cole, J. V. Beck, A. Haji-Sheikh and B. Litkouhi. *Heat Conduction Using Green's Functions* - 2nd Edition. Taylor & Francis, 2010.
- [Cook and Felderman 1966] W. J. Cook and E. M. Felderman. Reduction of Data from Thin Film Heat-Transfer Gages: A Concise Numerical Technique. *American Institute of Aeronautics and Astronautics Journal*, **4**:561-562, 1966.
- [Diller *et al.* 1993] T. E. Diller, J. P. Hartnett and T. F. Irvine. Advances in Heat Flux Measurements. In *Advances in Heat Transfer*. Elsevier, 1993.
- [Diller and Kidd 1997] T. E. Diller and C. T. Kidd. Evaluation of Numerical Methods for Determining Heat Flux with a Null Point Calorimeter. *Proceedings of the 43rd International Instrumentation Symposium*, 1997.
- [Doorly 1988] J. E. Doorly. Procedures for Determining Surface Heat Flux Using Thin Film Gauges on a Coated Metal Model in a Transient Test Facility. *Journal of Turbomachinery*, **110**:242-250, 1988.

- [Dorignac *et al.* 2005] E. Dorignac, J. J. Vullierme, M. Broussely, C. Foulon and M. Mekkadem. Experimental Heat Transfer on the Windward Surface of a Perforated Flat Plate. *International Journal of Thermal Sciences*, **44**(9):885-893, 2005.
- [Dowling 1999] N. E. Dowling. *Mechanical Behavior of Materials*. Prentice-Hall, 1999.
- [Duffy 2001] D. G. Duffy. *Green's Functions with Applications*. Chapman and Hall, 2001.
- [Ebbesen *et al.* 1998] T. W. Ebbesen, H. J. Lezec, H. F. Ghaemi, T. Thio and P. A. Wolff. Extraordinary Optical Transmission through Sub-Wavelength Hole Arrays. *Nature*, **391**(6668):667-669, 1998.
- [Eckert and Goldstein 1976] E. R. G. Eckert and R. J. E. Goldstein. *Measurements in Heat Transfer*. Hemisphere, 1976.
- [Edwards 1970] D. K. Edwards. Thermal Radiation Measurements. *AGARDograph Nr. 130 - Measurement Techniques in Heat Transfer*. NATO Advisory Group for Aerospace Research and Development (AGARD), 1970.
- [Englund and Seasholtz 1988] D. R. Englund and R. G. Seasholtz. Advanced High Temperature Instrumentation for Hot Section Research Applications. *Toward improved durability in advanced aircraft engine hot sections*, June 5-9 1988 Amsterdam, Netherlands. 5-21.
- [Escriba *et al.* 2005] C. Escriba, E. Campo, D. Estève and J. Y. Fourniols. Complete Analytical Modeling and Analysis of Micromachined Thermoelectric Uncooled Ir Sensors. *Sensors and Actuators A: Physical*, **120**(1):267-276, 2005.
- [Estrada *et al.* 2007] C. A. Estrada, O. A. Jaramillo, R. Acosta and C. A. Arancibia-Bulnes. Heat Transfer Analysis in a Calorimeter for Concentrated Solar Radiation Measurements. *Solar Energy*, **81**(10):1306-1313, 2007.
- [Feigelson 1985] R. S. Feigelson. Growth of fiber crystals. In *Crystal Growth of Electronic Materials*. Elsevier, 1985.
- [Fenot *et al.* 2005] M. Fenot, J. J. Vullierme and E. Dorignac. Local Heat Transfer Due to Several Configurations of Circular Air Jets Impinging on a Flat Plate with and without Semi-Confinement. *International Journal of Thermal Sciences*, **44**(7):665-675, 2005.

- [Filipczak *et al.* 2005] R. Filipczak, S. Crowley and R. E. Lyon. Heat Release Rate Measurements of Thin Samples in the OSU Apparatus and the Cone Calorimeter. *Fire Safety Journal*, **40**(7):628-645, 2005.
- [Filipczak and Lyon 2002] R. Filipczak and R. E. Lyon. Heat Flux Measurements in the OSU Rate of Heat Release Apparatus. *Fire Safety Journal*, **37**(6):591-604, 2002.
- [Filtz *et al.* 2002] J.-R. Filtz, M. Lièvre, T. Valin, J. Hameury, I. Wetterlund, B. Persson, P. Andersson, R. Jansson, T. Lemaire, M. Öhlin and J. Myllymäki. *Improving Heat Fluxmeter Calibration for Fire Testing Laboratories (HFCAL)*. Report 9012453 C360W03. European Commission, 2002.
- [Franca *et al.* 1998] G. A. C. Franca, P. Pagnier and A. Lallemand. Simulation des Transferts de Masse et de Chaleur par Modélisation à Bas Nombres de Reynolds dans un Écoulement avec Effusion Locale en Canalisation. *Revue Générale de Thermique*, **37**(3):205-222, 1998.
- [Frankel *et al.* 2008] J. I. Frankel, R. V. Arimilli, M. Keyhani and J. Wu. Heating Rate  $dT/dt$  Measurements Developed from in-Situ Thermocouples Using a Voltage-Rate Interface. *International Communications in Heat and Mass Transfer*, **35**(8):885-891, 2008.
- [Fried and Idelchik 1989] E. Fried and I. E. Idelchik. *Flow Resistance: A Design Guide for Engineers*. Hemisphere Publishing Corporation, 1989.
- [Garcia and de Schor 1990] J. Garcia and B. B. de Schor. A Fast Gauge for Energy Flux Density Measurement. *Review of Scientific Instruments*, **61**(1):165-170, 1990.
- [Gardon 1953] R. Gardon. An Instrument for the Direct Measurement of Intense Thermal Radiation. *Review of Scientific Instruments*, **24**(5):366-370, 1953.
- [Gardon 1960] R. Gardon. A Transducer for the Measurement of Heat Flow Rate. *Journal of Heat Transfer*, **82**:396-398, 1960.
- [Genix *et al.* 2009] M. Genix, P. Vairac and B. Cretin. Local Temperature Surface Measurement with Intrinsic Thermocouple. *International Journal of Thermal Sciences*, **48**(9):1679-1682, 2009.
- [George *et al.* 1991] W. K. George, W. J. Rae, P. J. Seymour and J. R. Sonnenmeier. An Evaluation of Analog and Numerical Techniques for Unsteady Heat Transfer Measurement with Thin Film Gages in Transient Facilities. *Experimental Thermal and Fluid Science*, **4**(333-342), 1991.

- [Godefroy *et al.* 1990] J. C. Godefroy, M. Cléry, C. Gageant, D. François and Y. Servouze. Thin Film Temperature Heat Fluxmeters. *Thin Solid Films*, **193-194** (Part 2):924-934, 1990.
- [Goldstein 1970] R. J. Goldstein. Optical Measurement of Temperature. *AGARDograph Nr. 130 - Measurement Techniques in Heat Transfer*. NATO Advisory Group for Aerospace Research and Development (AGARD), 1970.
- [Goldstein and Chiang 1985] R. J. Goldstein and H. D. Chiang. Measurement of Temperature and Heat Transfer. In *Handbook of Heat Transfer Applications*. McGraw-Hill 1985.
- [Goldstein and Cho 1995] R. J. Goldstein and H. H. Cho. A Review of Mass Transfer Measurements Using Naphthalene Sublimation. *Experimental Thermal and Fluid Science*, **10**:416-434, 1995.
- [Green and Yi 2004] M. Green and F. Yi. Light Transmission through Perforated Metal Thin Films Made by Island Lithography. *Thin Solid Films*, **467**(1-2):308-312, 2004.
- [Grey 1970] J. Grey. Probe Measurements in High-Temperature Gases and Dense Plasmas. *AGARDograph Nr. 130 - Measurement Techniques in Heat Transfer*. NATO Advisory Group for Aerospace Research and Development (AGARD), 1970.
- [Hager *et al.* 1991] J. M. Hager, S. Simmons, D. Smith, S. Onishi, L. W. Langley and T. E. Diller. Experimental Performance of a Heat Flux Microsensor. *Journal of Engineering for Gas Turbines and Power*, **113**(2):246-250, 1991.
- [Hager *et al.* 1993] J. M. Hager, L. W. Langley, S. Onishi and T. E. Diller. Microsensors for High Heat-Flux Measurements. *Journal of Thermophysics and Heat Transfer*, **7**(3):531-534, 1993.
- [Hager *et al.* 1994] J. M. Hager, J. P. Terrell, E. Sivertson and T. E. Diller. In-Situ Calibration of a Heat Flux Microsensor Using Surface Temperature Measurements. *Vatell Corporation, Christiansburg, VA, USA, Paper 0227-7576/94*:261-270, 1994.
- [Hager 1965] N. E. Hager. Thin Foil Heat Meter. *Review of Scientific Instruments*, **36**:1564-1570, 1965.
- [Hakenesch 1999] P. R. Hakenesch. Thin Layer Thermography - a New Heat Transfer Measurement Technique. *Experiments in Fluids*, **26**:257-265, 1999.

- [Hartmann 2009] J. Hartmann. High-Temperature Measurement Techniques for the Application in Photometry, Radiometry and Thermometry. *Physics Reports*, **469**(5-6):205-269, 2009.
- [Hartnett and Eckert 1957] J. P. Hartnett and E. R. G. Eckert. Mass Transfer Cooling in a Laminar Boundary Layer with Constant Fluid Properties. *American Society of Mechanical Engineers Transactions*, **79**:247-254, 1957.
- [Hayes *et al.* 2001] R. R. Hayes, S. Brewster, B. W. Webb, M. Q. McQuay and A. M. Huber. Crown Incident Radiant Heat Flux Measurements in an Industrial, Regenerative, Gas-Fired, Flat-Glass Furnace. *Experimental Thermal and Fluid Science*, **24**(1-2):35-46, 2001.
- [Heitor and Moreira 1993] M. V. Heitor and A. L. N. Moreira. Thermocouples and Sample Probes for Combustion Studies. *Progress in Energy and Combustion Science*, **19**(3):259-278, 1993.
- [Hencky 1915] K. Hencky. Untersuchungen Zur Isolation Von Kühlräumen (Investigation of Insulation in Cold-Stores). *Zeitschrift für die Gesamte Kälte-Industrie (Journal for the Cold Storage Industry)*, **22**(8):79-84, 1915.
- [Hit 2004] S. Hit. *Estudo de Sensor de Fluxo de Calor em Regime Transitório*. MSc Thesis, Universidade de Aveiro, 2004.
- [Holman 1986] J. P. Holman. *Heat Transfer* - 6th Edition. McGraw-Hill, 1986.
- [Holmberg and Diller 1995] D. G. Holmberg and T. E. Diller. High-Frequency Heat Flux Sensor Calibration and Modelling. *American Society of Mechanical Engineers Journal of Fluids Engineering*, **117**:659-664, 1995.
- [Hoogendoorn *et al.* 1970] C. J. Hoogendoorn, C. M. Ballintijn and W. R. Dorrestijn. Heat-Flux Studies in Vertical Tube Furnaces. *Journal of the Institute of Fuel*, **43**:511-516, 1970.
- [Hukseflux 2009] *RC01 Radiation/Convection Heat Flux Sensor Version 0616 - Specifications*. Hukseflux Thermal Sensors - Delft, Netherlands, 2009.
- [Incropera and DeWitt 1996] F. P. Incropera and D. P. DeWitt. *Fundamentals of Heat and Mass Transfer* - 4th Edition. John Wiley & Sons, 1996.

- [Ingason and Wickström 2007] H. Ingason and U. Wickström. Measuring Incident Radiant Heat Flux Using the Plate Thermometer. *Fire Safety Journal*, **42**(2):161-166, 2007.
- [Ireland and Jones 1987] P. T. Ireland and T. V. Jones. The Response Time of a Surface Thermometer Employing Encapsulated Thermochromic Liquid Crystals. *Journal of Physics E: Scientific Instruments*, **20**:1195-1199, 1987.
- [Ishizuka et al. 2005] M. Ishizuka, S. Nakagawa, K. Koizumi and E. Takegoshi. Measurement of Flow Resistance Coefficients for Wire Nets in Natural Air Convection Flow. *Sixteenth International Symposium on Transport Phenomena (ISTP-16)*, Prague, Czech Republic, 2005.
- [Jaremiewicz et al. 2009] M. Jaremiewicz, D. Taler and T. Sobota. Measuring Transient Temperature of the Medium in Power Engineering Machines and Installations. *Applied Thermal Engineering*, **29**(16):3374-3379, 2009.
- [Kaviany 1995] M. Kaviany. *Principles of Heat Transfer in Porous Media*. Springer, 1995.
- [Kidd 1990a] C. T. Kidd. Coaxial Surface Thermocouples: Analytical and Experimental Considerations for Aerothermal Heat Flux Measurement Applications. 1990.
- [Kidd 1990b] C. T. Kidd. Recent Developments in High Heat Flux Measurement Techniques at the AEDC. *Proceedings of the 36th Instrument Society of America International Instrumentation Symposium*, May 6-10, Denver, CO, USA, **36**:477-492, 1990.
- [Kidd and Nelson 1995] C. T. Kidd and C. G. Nelson. How the Schmidt-Boelter Gauge Really Works. *Proceedings of the 41st Instrument Society of America International Instrumentation Symposium*, May 7-11, Aurora, CO, USA, **41**: 347-368, 1995.
- [Kim 1993] L. V. Kim. Determination of the Heat Transfer Coefficients in Porous Media. *Journal of Engineering Physics and Thermophysics*, **65**(6):1168-1172, 1993.
- [Kolodzie and Van Winkle 1957] P. A. Kolodzie and M. Van Winkle. Discharge Coefficients through Perforated Plates. *American Institute of Chemical Engineers Journal*, **3**(3):305-312, 1957.
- [Kostkowski and Burns 1970] H. J. Kostkowski and G. W. Burns. Thermocouple and Radiation Thermometry above 900K. *AGARDograph Nr. 130 - Measurement*

*Techniques in Heat Transfer*. NATO Advisory Group for Aerospace Research and Development (AGARD), 1970.

- [Kumada *et al.* 1990] M. Kumada, S. Kume, I. Mabuchi, Y. Watanabe and M. Hirata. Characteristics of Dynamic Behavior and Local Heat Transfer around Single Row Tubes Immersed in Floating Particles. *Experimental Thermal and Fluid Science*, **3**(3):272-279, 1990.
- [Kuo and Kulkarni 1991] C. H. Kuo and A. K. Kulkarni. Analysis of Heat Flux Measurement by Circular Foil Gages in a Mixed Convection/Radiation Environment. *American Society of Mechanical Engineers Journal of Heat Transfer*, **113**:1037-1040, 1991.
- [Kutateladze and Leontiev 1964] S. S. Kutateladze and A. I. Leontiev. *Turbulent Boundary Layers in Compressible Gases*. Academic Press, 1964.
- [Langley *et al.* 1999] L. W. Langley, A. Barnes, G. Matijasevic and P. Gandhi. High-Sensitivity, Surface-Attached Heat Flux Sensors. *Microelectronics Journal*, **30**(11):1163-1168, 1999.
- [Lennon and Silcock 2006] P. F. Lennon and G. W. H. Silcock. A Preliminary Investigation into the Partitioning of the Convective and Radiative Incident Heat Flux in Real Fires. *Fire Technology*, **42**(2):109-129, 2006.
- [Leontiev 1966] A. I. Leontiev. Heat and Mass Transfer in Turbulent Boundary Layers. *Advances in Heat Transfer*, **3**:33-99, 1966.
- [Letrou and Gheudin 1992] C. Letrou and M. Gheudin. Dichroic Diplexer Design for Millimeter Waves. *International Journal of Infrared and Millimeter Waves*, **13**(1):27-42, 1992.
- [Liebert 1994] C. H. Liebert. Miniature Convection Cooled Plug-Type Heat Flux Gages. *Proceedings of the 40th Instrument Society of America International Instrumentation Symposium*, May 1-5, Baltimore, MD, USA, **40**: 289-302, 1994.
- [Lourenço *et al.* 2000] M. J. Lourenço, S. C. S. Rosa, C. A. Nieto de Castro, C. Albuquerque, B. Erdmann, J. Lang and R. Roitzsch. Simulation of the Transient Heating in an Unsymmetrical, Coated, Hot-Strip Sensor with a Self-Adaptive Finite-Element Method (SAFEM). *International Journal of Thermophysics*, **21**(2):377-384, 2000.

- [Lourenço *et al.* 1998] M. J. Lourenço, J. M. Serra, M. R. Nunes, A. M. Vallêra and C. A. Nieto de Castro. Thin-Film Characterization for High-Temperature Applications. *International Journal of Thermophysics*, **19**(4):1253-1265, 1998.
- [Marinoski *et al.* 2007] D. L. Marinoski, S. Güths, F. O. R. Pereira and R. Lamberts. Improvement of a Measurement System for Solar Heat Gain through Fenestrations. *Energy and Buildings*, **39**(4):478-487, 2007.
- [Marner *et al.* 1989] W. J. Marner, K. S. MacDavid and L. J. Muzio. Development of a Gas-Side Fouling Measuring Device. In *Heat Transfer Equipment Fundamentals, Design, Applications and Operating Principles*. American Society of Mechanical Engineers, 1989.
- [Martín-Moreno *et al.* 2001] L. Martín-Moreno, F. J. García-Vidal, H. J. Lezec, K. M. Pellerin, T. Thio, J. B. Pendry and T. W. Ebbesen. Theory of Extraordinary Optical Transmission through Subwavelength Hole Arrays. *Physical Review Letters*, **86**(6):1114, 2001.
- [Martin 1977] H. Martin. Heat and Mass Transfer between Impinging Gas Jets and Solid Surfaces. *Advances in Heat Transfer*, **13**:1-59, 1977.
- [Martins 1998] N. Martins. *A New Heat Flux Meter for High Temperature Harsh Environments*. PhD Thesis, Instituto Superior Técnico - Universidade Técnica de Lisboa, 1998.
- [Martins *et al.* 1998] N. Martins, M. G. Carvalho, N. H. Afgan and A. I. Leontiev. Experimental Verification and Calibration of the Blow-Off Heat Flux Sensor. *Applied Thermal Engineering*, **18**(6):481-489, 1998.
- [Martins *et al.* 2000] N. Martins, M. G. Carvalho, N. Afgan and A. I. Leontiev. A Radiation and Convection Fluxmeter for High Temperature Applications. *Experimental Thermal and Fluid Science*, **22**(3-4):165-173, 2000.
- [Martins *et al.* 2006a] N. Martins, H. Calisto, N. Afgan and A. I. Leontiev. The Transient Transpiration Heat Flux Meter. *Applied Thermal Engineering*, **26**(14-15):1552-1555, 2006.
- [Martins *et al.* 2006b] N. Martins, S. Hit, H. Calisto and N. Afgan. The Transient Transpiration Radiometer: Analysis and Parameter Selection. *Applied Thermal Engineering*, **26**(17-18):2247-2254, 2006.



- [Matthews and Longenbaugh 1989] L. Matthews and R. Longenbaugh. Radiative Flux Measurements in a Sooty Pool Fire. *Experimental Heat Transfer*, **2**(3):189-199, 1989.
- [Maynard 2011] R. K. Maynard. *Total Hemispherical Emissivity of Very High Temperature Reactor (VHTR) Candidate Materials: Hastelloy X, Haynes 230 and Alloy 617*. PhD Thesis, University of Missouri, 2011.
- [McGee 1988] T. McGee. *Principles and Methods of Temperature Measurement*. Wiley, 1988.
- [Moffat *et al.* 1971] R. J. Moffat, B. D. Junn and J. F. Ayers. Development of a Transpiration Radiometer. *Advances in Instrumentation*, **26**(2), Paper #613, 1971.
- [Moffat 1988] R. J. Moffat. Describing the Uncertainties in Experimental Results. *Experimental Thermal and Fluid Science*, **1**(1):3-17, 1988.
- [Moffat 1990] R. J. Moffat. Some Experimental Methods for Heat Transfer Studies. *Experimental Thermal and Fluid Science*, **3**(1):14-32, 1990.
- [Moffat 1998] R. J. Moffat. What's New in Convective Heat Transfer? *International Journal of Heat and Fluid Flow*, **19**(2):90-101, 1998.
- [Murthy *et al.* 2000] A. V. Murthy, B. K. Tsai and R. D. Saunders. Radiative Calibration of Heat Flux Sensors at NIST - Facilities and Techniques. *Journal of Research of the National Institute of Standards and Technology*, **105**(2):293-305, 2000.
- [Murthy *et al.* 2003] A. V. Murthy, I. Wetterlund and D. P. DeWitt. Characterization of an Ellipsoidal Radiometer. *Journal of Research of the National Institute of Standards and Technology*, **108**(2):115-124, 2003.
- [Neal *et al.* 1980] S. B. H. C. Neal, E. W. Northover and R. J. Preece. The Measurement of Radiant Heat Flux in Large Boiler Furnaces - Ii. Development of Flux Measuring Instruments. *International Journal of Heat Mass Transfer*, **23**:1023-1031, 1980.
- [Neuer *et al.* 2001] G. Neuer, J. Fischer, F. Edler and R. Thomas. Comparison of Temperature Measurement by Noise Thermometry and Radiation Thermometry. *Measurement*, **30**(3):211-221, 2001.

- [Neumann 1989] R. D. Neumann. Aerothermodynamic Instrumentation. *AGARD Report Nr.761 - Special Course on Aerothermodynamics of Hypersonic Vehicles*. NATO Advisory Group for Aerospace Research and Development (AGARD), 1989.
- [Neumann *et al.* 1988] R. D. Neumann, P. J. Erbland and L. O. Kretz. Instrumentation of Hypersonic Structures: A Review of Past Applications and Needs of the Future. *American Institute of Aeronautics and Astronautics Thermophysics, Plasmadynamics and Lasers Conference*, June 27-29, San Antonio, TX, USA, 1988.
- [Nieto de Castro *et al.* 1991] C. Nieto de Castro, R. Perkins and H. Roder. Radiative Heat Transfer in Transient Hot-Wire Measurements of Thermal Conductivity. *International Journal of Thermophysics*, **12**(6):985-997, 1991.
- [NIST 1999] National Institute of Standards and Technology. *ITS-90 Thermocouple Database*. Available: <http://srdata.nist.gov/its90/main> [Accessed September 2012], 1999.
- [Oh *et al.* 2006] S. H. Oh, S. H. Lee, J. C. Jeon, M. H. Kim and S. S. Lee. Bulk-Micromachined Circular Foil Type Micro Heat-Flux Sensor. *Sensors and Actuators A: Physical*, **132**(2):581-586, 2006.
- [Oliveira and Yanagihara 2004] A. R. Oliveira and J. I. Yanagihara. Parametric and Performance Analysis of an Ellipsoidal Radiometer. *10th Brazilian National Congress of Thermal Sciences and Engineering*. Rio de Janeiro, Brazil, 2004.
- [Oliveira and Yanagihara 2008] A. R. Oliveira and J. I. Yanagihara. A Semi-Ellipsoidal Cavity Radiometer for Measurement of Emissive Power. *5th European Thermal-Sciences Conference*. Netherlands, 2008.
- [Ortolano and Hines 1983] D. J. Ortolano and F. F. Hines. A Simplified Approach to Heat Flow Measurement. *Advances in Instrumentation*, **38**(2):1449-1456, 1983.
- [Özisik 1968] M. N. Özisik. *Boundary Value Problems of Heat Conduction*. International Textbook Company 1968.
- [Özisik 1993] M. N. Özisik. *Heat Conduction* - 2nd Edition. John Wiley & Sons, 1993.
- [Paloposki and Liedquist 2005] T. Paloposki and L. Liedquist. *Steel Emissivity at High Temperatures*. VTT Technical Research Centre of Finland, 2005.
- [Pitts *et al.* 2006] W. M. Pitts, A. V. Murthy, J. L. de Ris, J.-R. Filtz, K. Nygård, D. Smith and I. Wetterlund. Round Robin Study of Total Heat Flux Gauge Calibration at Fire Laboratories. *Fire Safety Journal*, **41**(6):459-475, 2006.

- [Ploteau *et al.* 2007] J. P. Ploteau, P. Glouannec and H. Noel. Conception of Thermoelectric Flux Meters for Infrared Radiation Measurements in Industrial Furnaces. *Applied Thermal Engineering*, **27**(2-3):674-681, 2007.
- [Poloniecki *et al.* 1995] J. G. Poloniecki, A. Vianou and E. Mathioulakis. Steady-State Analysis of the Zero-Balance Heat-Flux Meter. *Sensors and Actuators A: Physical*, **49**(1-2):29-35, 1995.
- [Porro *et al.* 1991] A. R. Porro, T. G. Keith Jr. and W. R. Hingst. A Laser Induced Heat Flux Technique for Convective Heat Transfer Measurements in High Speed Flows. *International Congress on Instrumentation in Aerospace Simulation Facilities*, October 27-31, Rockville, MD, USA, pp. 146-155, 1991.
- [Robertson and Ohlemiller 1995] A. F. Robertson and T. J. Ohlemiller. Low Heat-Flux Measurements: Some Precautions. *Fire Safety Journal*, **25**(2):109-124, 1995.
- [Saidi and Kim 2004] A. Saidi and J. Kim. Heat Flux Sensor with Minimal Impact on Boundary Conditions. *Experimental Thermal and Fluid Science*, **28**(8):903-908, 2004.
- [Sanz *et al.* 2008] A. Sanz, J. Ballester, R. Hernández and L. M. Cerecedo. Advanced Monitoring of Industrial Burners Based on Fluctuating Flame Signals. *Fuel*, **87**(7):1063-1075, 2008.
- [Savitzky and Golay 1964] A. Savitzky and M. J. E. Golay. Smoothing and Differentiation of Data by Simplified Least Squares Procedures. *Analytical Chemistry*, **36**(8):1627-1639, 1964.
- [Saxena *et al.* 1989] S. C. Saxena, K. K. Srivastava and R. Vadivel. Experimental Techniques for the Measurement of Radiative and Total Heat-Transfer in Gas-Fluidized Beds - A Review. *Experimental Thermal and Fluid Science*, **2**(3):350-364, 1989.
- [Schulte and Kohl 1970] E. H. Schulte and R. F. Kohl. A Transducer for Measuring High Heat Transfer Rates. *Review of Scientific Instruments*, **41**(12): 1732-1740, 1970.
- [Schultz and Jones 1973] D. L. Schultz and T. V. Jones. Heat Transfer Measurements in Short Duration Hypersonic Facilities. *AGARDograph Nr.165*. NATO Advisory Group for Aerospace Research and Development (AGARD), 1973.

- [Scott 1970] C. J. Scott. Transient Experimental Techniques for Surface Heat Flux Rates. *AGARDograph Nr.130 - Measurement Techniques in Heat Transfer*. NATO Advisory Group for Aerospace Research and Development (AGARD), 1970.
- [Shah 1979] N. G. Shah. *New Method of Computation of Radiation Heat Transfer in Combustion Chamber*. PhD Thesis, Imperial College of Science and Technology, 1979.
- [Shepherd 1985] J. E. Shepherd. Stagnation Point Heat Transfer from Jet Plumes. In: *Heat Transfer in Fires and Combustion Systems*. American Society of Mechanical Engineers, 1985.
- [Shewan *et al.* 1989] E. C. Shewan, K. G. T. Hollands and G. D. Raithby. The Measurement of Surface Heat Flux Using the Peltier Effect. *Journal of Heat Transfer*, **111**:798-803, 1989.
- [Siegel 1998] R. Siegel. Transient Effects of Radiative Transfer in Semitransparent Materials. *International Journal of Engineering Science*, **36**(12-14):1701-1739, 1998.
- [Silvani and Morandini 2009] X. Silvani and F. Morandini. Fire Spread Experiments in the Field: Temperature and Heat Fluxes Measurements. *Fire Safety Journal*, **44**(2):279-285, 2009.
- [Souza Mendes 1991] P. R. Souza Mendes. The Naphthalene Sublimation Technique. *Experimental Thermal and Fluid Science*, **4**:510-523, 1991.
- [Sparrow and Gurdal 1981] E. M. Sparrow and U. Gurdal. Heat Transfer at an Upstream-Facing Surface Washed by Fluid En Route to an Aperture in the Surface. *International Journal of Heat and Mass Transfer*, **24**(5):851-857, 1981.
- [Sparrow and Ortiz 1982] E. M. Sparrow and M. C. Ortiz. Heat Transfer Coefficients for the Upstream Face of a Perforated Plate Positioned Normal to an Oncoming Flow. *International Journal of Heat and Mass Transfer*, **25**(1):127-135, 1982.
- [Stakgold 1967] I. Stakgold. *Boundary Value Problems of Mathematical Physics*. Macmillan 1967.
- [Talati and Jalalifar 2009] F. Talati and S. Jalalifar. Analysis of Heat Conduction in a Disk Brake System. *Heat and Mass Transfer*, **45**(8):1047-1059, 2009.
- [Tedeschi *et al.* 1995] G. Tedeschi, G. A. C. Franca and A. Lallemand. Refroidissement d'une Paroi Plane par Transpiration: Comparaison de Différents Modèles pour le

Calcul des Échanges Thermiques. *Congrès de la Société Française des Thermiciens*, Poitiers, pp.206-211, 1995.

- [Terrel 1996] J. P. Terrel. New High Sensitivity, Low Thermal Resistance Surface Mounted Heat Flux Transducer. *Proceedings of the 42nd Instrument Society of America International Instrumentation Symposium*, May 5-9, San Diego, CA, USA, **42**:235-249, 1996.
- [Thibault and Hoffman 1979] J. Thibault and T. W. Hoffman. A Heat Flux Meter to Determine the Local Boiling Heat Flux Density During a Quenching Experiment. *International Journal of Heat and Mass Transfer*, **22**(2):177-184, 1979.
- [Thompson and Emrich 1981] W. P. Thompson and R. J. Emrich. Heat Transfer Gauges. In *Methods in Experimental Physics*. Academic Press, 1981.
- [Travkin and Catton 2001] V. S. Travkin and I. Catton. Transport Phenomena in Heterogeneous Media Based on Volume Averaging Theory. In *Advances in Heat Transfer*. Elsevier, 2001.
- [Tsai and Strieder 1986] D. S. Tsai and W. Strieder. Radiation Across and Down a Cylindrical Pore Having Both Specular and Diffuse Reflectance Components. *Industrial & Engineering Chemistry Fundamentals*, **25**(2):244-249, 1986.
- [Vafai 2005] K. Vafai (ed.). *Handbook of Porous Media*. Taylor & Francis, 2005.
- [van der Graaf 1989] F. van der Graaf. Heat Flux Sensors. In *Sensors*. VCH Publishers, 1989.
- [van Dorth *et al.* 1983] A. C. van Dorth, F. van Der Graaf and G. K. Steenvoorden. Thick Film Heat Flux Sensor. *Sensors and Actuators*, **4**:323-331, 1983.
- [Wang *et al.* 2005] Z.-H. Wang, S. K. Au and K. H. Tan. Heat Transfer Analysis Using a Green's Function Approach for Uniformly Insulated Steel Members Subjected to Fire. *Engineering Structures*, **27**(10):1551-1562, 2005.
- [Wang and Tan 2007a] Z.-H. Wang and K.-H. Tan. Temperature Prediction for Contour-Insulated Concrete-Filled CHS Subjected to Fire Using Large Time Green's Function Solutions. *Journal of Constructional Steel Research*, **63**(7):997-1007, 2007.

- [Wang and Tan 2007b] Z.-H. Wang and K. H. Tan. Temperature Prediction of Concrete-Filled Rectangular Hollow Sections in Fire Using Green's Function Method. *Journal of Engineering Mechanics*, **133**(6):688-700, 2007.
- [Wehrspohn 2005] R. B. Wehrspohn (ed.). *Ordered Porous Nanostructures and Applications*. Springer Science+Business Media, 2005.
- [White 1998] F. M. White. *Fluid Mechanics*. McGraw-Hill, 1998.
- [Wiens 2010] T. Wiens. *Linear Regression with Errors in X and Y*. Available: <http://www.mathworks.com/matlabcentral/fileexchange/26586-linear-regression-with-errors-in-x-and-y> [Accessed January 2013], 2010.
- [Winnewisser *et al.* 1998] C. Winnewisser, F. Lewen and H. Helm. Transmission Characteristics of Dichroic Filters Measured by THz Time-Domain Spectroscopy. *Applied Physics A: Materials Science & Processing*, **66**(6):593-598, 1998.
- [Yang *et al.* 2012] C.-Y. Yang, C.-W. Chen, T.-Y. Lin and S. G. Kandlikar. Heat Transfer and Friction Characteristics of Air Flow in Microtubes. *Experimental Thermal and Fluid Science*, **37**:12-18, 2012.
- [York 1966] D. York. Least-Squares Fitting of a Straight Line. *Canadian Journal of Physics*, **44**(5):1079-1086, 1966.
- [York 1968] D. York. Least Squares Fitting of a Straight Line with Correlated Errors. *Earth and Planetary Science Letters*, **5**:320-324, 1968.
- [York *et al.* 2004] D. York, N. M. Evensen, M. L. Martinez and J. D. B. Delgado. Unified Equations for the Slope, Intercept, and Standard Errors of the Best Straight Line. *American Journal of Physics*, **72**(3):367-375, 2004.
- [Young *et al.* 1984] M. F. Young, J. C. LaRue and J. E. Koency. Effect of Free-Stream Velocity Vector on the Output of a Circular Disk Heat Gauge. *American Society of Mechanical Engineers Journal of Heat Transfer*, **106**:229-233, 1984.

## APPENDIX A – *MATHEMATICA* CODE

```
(*STATIONARY MODEL*)

Clear[Nnos, Nelem, L, dz, xr, PP, Are, Vol, Tsurf, T, Nmax, tol,
Resinic, niter, Tant, Tmed, ki, Qgi, qini, qouti, Rmax, Rmin, invR,
QQvol, qgsurf, sigma, epsil, Tinfirad, invRrad, hconv, Tinfirconv,
invRconv, Tinfirad2]

(*MESH & GEOMETRY*)

Number of nodes; Nnos = 6;

Nelem = Nnos - 2; (*number of elements*)

Radius [m]; L = 0.0022/2;

Width [m]; dz = .0001;

PP = L/Nelem; (*incremental step [m]*)

For[i = 1, i < Nelem + 1, i++, xr[i] = (i - 0.5)*PP]; (*intermediate
nodal positions [m]*)

For[i = 1, i < Nelem + 1, i++, Are[i] = xr[i]*PP*2*Pi]; (*element
areas*)

For[i = 1, i < Nelem + 1, i++, Vol[i] = xr[i]*PP*2*Pi*dz]; (*element
volumes*)

(*INITIAL AND BOUNDARY CONDITIONS*)

Superficial temperature [K]; Tsurf = 473.;

Initial temperature [K]; For[i = 1, i < Nelem + 1, i++, T[i] = 473.];

(*CONVERGENCE CONTROL*)

Maximum number of iterations; Nmax = 1000000;

Convergence tolerance; tol = .000000000001;

Resinic = 1000.; (*initial residual*)

(*RADIATION AND CONVECTION PROPERTIES*)

Sigma [W/(m2 K4)]; sigma = 5.6697/100000000;

Emissivity; epsil = 1.0*0.8549;

Radiative medium temperature [K]; Tinfirad = 1023.;

Radiative medium temperature 2 [K]; Tinfirad2 = 298.;

Convection coefficient [W/(m2 K)]; hconv = 1590.3*2.29;
```

```

Convective medium temperature [K]; Tinfconv = 298.;

(*CYCLE OF GAUSS-SEIDEL METHOD*)

niter = 0; While[niter < Nmax, If[Resinic < tol, Break[],

{

(*DEFINITION OF INITIAL ITERATIVE TEMPERATURE FIELD*)

For[i = 1, i < Nelem + 1, i++, Tant[i] = T[i]];

(*DETERMINATION OF MEAN TEMPERATURE FIELD*)

For[i = 1, i < 2, i++, Tmed[i] = T[i]];

For[i = 2, i < Nelem, i++, Tmed[i] = (T[i + 1] + T[i])/2];

For[i = Nelem, i < Nelem + 1, i++, Tmed[i] = (T[i] + Tsurf)/2];

(*DEFINITION OF K, Q, QIN AND QOUT*)

Thermal conductivity [W/(m°C)]; For[i = 1, i < Nelem + 1, i++,
ki[i] = 60.5];

Body heat generation [W/m3]; For[i = 1, i < Nelem + 1, i++,
Qgi[i] = 0*500000000.];

Surface heat influx [W/m2]; For[i = 1, i < Nelem + 1, i++,
qini[i] = 0.];

Surface heat outflux [W/m2]; For[i = 1, i < Nelem + 1, i++,
qouti[i] = 0.];

(*DETERMINATION OF THERMAL RESISTANCES*)

For[i = 1, i < Nelem, i++, Rmax[i] = PP/((xr[i] +
PP/2)*2*Pi*ki[i]*dz)];

For[i = Nelem, i < Nelem + 1, i++, Rmax[i] = PP/2/((xr[i] +
PP/4)*2*Pi*ki[i]*dz)];

For[i = 2, i < Nelem + 1, i++, Rmin[i] = PP/((xr[i] -
PP/2)*2*Pi*ki[i]*dz)];

(*DETERMINATION OF THE INVERSES OF CONVECTIVE THERMAL
RESISTANCES*)

For[i = 1, i < Nelem + 1, i++, invRconv[i] = hconv*Are[i] ];

(*DETERMINATION OF THE INVERSES OF CONDUCTIVE THERMAL
RESISTANCES*)

For[i = 1, i < 2, i++, invR[i] = 1/Rmax[i] + invRconv[i]];

```



```
For[i = 2, i < Nelem + 1, i++, invR[i] = 1/Rmax[i] + 1/Rmin[i] +
invRconv[i]];
```

```
(*DETERMINATION OF BODY HEAT GENERATION AND SURFACE HEAT
FLUXES*)
```

```
For[i = 1, i < Nelem + 1, i++, QQvol[i] = Qgi[i]*Vol[i]];
```

```
For[i = 1, i < Nelem + 1, i++, qqsurf[i] = Are[i]*(qini[i] -
qouti[i])];
```

```
(*TEMPERATURE FIELD UPDATE*)
```

```
For[i = 1, i < 2, i++,
```

```
T[i] = (Tinfinrad2*sigma*epsil*Are[i]*(Tant[i]*Tant[i] +
Tinfinrad2 * Tinfinrad2)*(Tant[i] + Tinfinrad2) +
Tinfinrad*sigma*epsil* Are[i]*(Tant[i]*Tant[i] + Tinfinrad *
Tinfinrad)*(Tant[i] + Tinfinrad) + Tinfinconv*invRconv[i] +
QQvol[i] + qqsurf[i] + T[i + 1]/Rmax[i])/(invR[i] +
sigma*epsil* Are[i]*(Tant[i]*Tant[i] + Tinfinrad * Tinfinrad)*
(Tant[i] + Tinfinrad) + sigma*epsil* Are[i]*(Tant[i]*Tant[i] +
Tinfinrad2 * Tinfinrad2)*(Tant[i] + Tinfinrad2))];
```

```
For[i = 2, i < Nelem, i++,
```

```
T[i] = (Tinfinrad2*sigma*epsil* Are[i]*(Tant[i]*Tant[i] +
Tinfinrad2 * Tinfinrad2)*(Tant[i] + Tinfinrad2) +
Tinfinrad*sigma*epsil* Are[i]*(Tant[i]*Tant[i] + Tinfinrad *
Tinfinrad)*(Tant[i] + Tinfinrad) + Tinfinconv*invRconv[i] +
QQvol[i] + qqsurf[i] + T[i - 1]/Rmin[i] + T[i +
1]/Rmax[i])/(invR[i] + sigma*epsil* Are[i]*(Tant[i]*Tant[i] +
Tinfinrad * Tinfinrad)*(Tant[i] + Tinfinrad) + sigma*epsil*
Are[i]*(Tant[i]*Tant[i] + Tinfinrad2 * Tinfinrad2)*(Tant[i] +
Tinfinrad2))];
```

```
For[i = Nelem, i < Nelem + 1, i++,
```

```
T[i] = (Tinfinrad2*sigma*epsil* Are[i]*(Tant[i]*Tant[i] +
Tinfinrad2 * Tinfinrad2)*(Tant[i] + Tinfinrad2) +
Tinfinrad*sigma*epsil* Are[i]*(Tant[i]*Tant[i] + Tinfinrad *
Tinfinrad)*(Tant[i] + Tinfinrad) + Tinfinconv*invRconv[i] +
QQvol[i] + qqsurf[i] + Tsurf/Rmax[i] + T[i -
1]/Rmin[i])/(invR[i] + sigma*epsil* Are[i]*(Tant[i]*Tant[i] +
Tinfinrad * Tinfinrad)*(Tant[i] + Tinfinrad) + sigma*epsil*
Are[i]*(Tant[i]*Tant[i] + Tinfinrad2 * Tinfinrad2)*(Tant[i] +
Tinfinrad2))];
```

```
(*DETERMINATION OF ITERATION'S RESIDUAL*)
```

```
For[i = 1, i < Nelem + 1, i++, res[i] = T[i] - Tant[i]];
```

```
Resinic = Max[Table[Abs[res[i]], {i, 1, Nelem}]];
```

```
]]; niter++];
```

```

(*TRANSIENT MODEL*)

Clear[Nnos, Nelem, L, dz, xr, PP, Are, Vol, Tsurf, T, niter, Ttot,
rho, cimax, kimax, mindt, npace, Rmax2, Rmin2, invR2, CT2, Tmed, ki,
Qgi, qini, qouti, QQvol, qqsurf, Ci, CT, Rmax, Rmin, sigma, epsil,
Tfinrad, hconv, Tfinconv, invRrad, invRconv, Maxtempfix,
Tfinrad2]

(*MESH & GEOMETRY*)

Number of nodes; Nnos = 37;

Nelem = Nnos - 2; (*number of elements*)

Radius [m]; L = 0.0011;

Width [m]; dz = .0001;

PP = L/Nelem; (*incremental step [m]*)

For[i = 1, i < Nelem + 1, i++, xr[i] = (i - 0.5)*PP]; (*nodal
intermediate positions [m]*)

For[i = 1, i < Nelem + 1, i++, Are[i] = xr[i]*PP*2*Pi]; (*elements'
areas*)

For[i = 1, i < Nelem + 1, i++, Vol[i] = xr[i]*PP*2*Pi*dz]; (*elements'
volumes*)

(*INITIAL AND BOUNDARY CONDITIONS*)

Superficial temperature [K]; Tsurf = 473.;

Initial temperature [K]; For[i = 1, i < Nelem + 1, i++, T[i] = 473.];

(*RADIATION AND CONVECTION PROPERTIES*)

Sigma [W/(m2 K4)]; sigma = 5.6697/100000000;

Emissivity; epsil = 1.0*0.8549;

Radiative medium temperature [K]; Tfinrad = 1023.;

Radiative medium temperature2 [K]; Tfinrad2 = 298.;

Convection coefficient [W/(m2 K)]; hconv = 1590.3*2.2902 ;

Convective medium temperature [K]; Tfinconv = 298.;

Maximum fixed temperature [K]; Maxtempfix = Max[Tsurf, Tfinrad,
Tfinconv]

```

```

(*ANALYSIS TIME AND PROPERTIES*)

Total analysis time [s]; Ttot = 0.005;

rho = 7854.;(*steel density [kg/m3]*)

cimax = 432.;(*Maximum thermal capacity [J/(kg°C)]*)

kimax = 60.5;(*Maximum thermal conductivity [W/(m°C)]*)

(*DETERMINATION OF STABLE INCREMENTAL STEP*)

mindt = 0.;

npace = 0.;

For[i = 1, i < Nelem, i++, Rmax2[i] = PP/((xr[i] +
PP/2)*2*Pi*kimax*dz)];

For[i = Nelem, i < Nelem + 1, i++, Rmax2[i] = PP/2/((xr[i] +
PP/4)*2*Pi*kimax*dz)];

For[i = 2, i < Nelem + 1, i++, Rmin2[i] = PP/((xr[i] -
PP/2)*2*Pi*kimax*dz)];

For[i = 1, i < 2, i++,

    invR2[i] = 1/Rmax2[i] + sigma*epsil*xr[i]*PP*2*
    Pi*(Maxtempfix*Maxtempfix + Tfinrad2 * Tfinrad2)*(Maxtempfix +
    Tfinrad2) + sigma*epsil*xr[i]*PP*2*Pi*(Maxtempfix*Maxtempfix +
    Tfinrad * Tfinrad)*(Maxtempfix + Tfinrad) +
    hconv*xr[i]*PP*2*Pi];

For[i = 2, i < Nelem + 1, i++,

    invR2[i] = 1/Rmax2[i] + 1/Rmin2[i] + sigma*epsil*xr[i]*PP*2*
    Pi*(Maxtempfix*Maxtempfix + Tfinrad2 * Tfinrad2)*(Maxtempfix +
    Tfinrad2) + sigma*epsil*xr[i]*PP*2*Pi*(Maxtempfix*Maxtempfix +
    Tfinrad * Tfinrad)*(Maxtempfix + Tfinrad) +
    hconv*xr[i]*PP*2*Pi];

For[i = 1, i < Nelem + 1, i++, CT2[i] = rho*cimax*Vol[i]];

For[i = 1, i < Nelem + 1, i++, CT2[i]/invR2[i]];

mindt = Min[Table[CT2[i]/invR2[i], {i, 1, Nelem}]];

npace = IntegerPart[20*Ttot/mindt];

mindt = Ttot/npace;

(*INCREMENTAL EXPLICIT CYCLE*)

niter = 0; While[niter < npace,

    (*DETERMINATION OF MEAN TEMPERATURE FIELD*)

    For[i = 1, i < 2, i++, Tmed[i] = T[i]];

    For[i = 2, i < Nelem, i++, Tmed[i] = (T[i + 1] + T[i])/2];

```

```

For[i = Nelem, i < Nelem + 1, i++, Tmed[i] = (T[i] + Tsurf)/2];

(*DEFINITION OF K, Q, QIN AND QOUT*)

Thermal conductivity [W/(m°C)]; For[i = 1, i < Nelem + 1, i++,
ki[i] = 60.5];

Body heat generation [W/m3]; For[i = 1, i < Nelem + 1, i++,
Qgi[i] = 500000000.];

Surface heat influx [W/m2]; For[i = 1, i < Nelem + 1, i++,
qini[i] = 0.];

Surface heat outflux [W/m2]; For[i = 1, i < Nelem + 1, i++,
qouti[i] = 0.];

(*DETERMINATION OF BODY HEAT GENERATION AND SURFACE HEAT
FLUXES*)

For[i = 1, i < Nelem + 1, i++, QQvol[i] = Qgi[i]*Vol[i]];

For[i = 1, i < Nelem + 1, i++, qqsurf[i] = Are[i]*(qini[i] -
qouti[i])];

(*DETERMINATION OF THERMAL CAPACITIES*)

For[i = 1, i < Nelem + 1, i++, Ci[i] = 432.*0.8549];

For[i = 1, i < Nelem + 1, i++, CT[i] = rho*Ci[i]*Vol[i]];

(*DETERMINATION OF THE INVERSES OF CONVECTIVE THERMAL
RESISTANCES*)

For[i = 1, i < Nelem + 1, i++, invRconv[i] = hconv*xr[i]*PP*2*Pi
];

(*DETERMINATION OF CONDUCTIVE THERMAL RESISTANCES*)

For[i = 1, i < Nelem, i++, Rmax[i] = PP/((xr[i] +
PP/2)*2*Pi*ki[i]*dz)];

For[i = Nelem, i < Nelem + 1, i++, Rmax[i] = PP/2/((xr[i] +
PP/4)*2*Pi*ki[i]*dz)];

For[i = 2, i < Nelem + 1, i++, Rmin[i] = PP/((xr[i] -
PP/2)*2*Pi*ki[i]*dz)];

(*DETERMINATION OF TEMPERATURE FIELD*)

{For[i = 1, i < 2, i++,

T[i] = mindt/ CT[i]*(sigma*epsil*xr[i]*PP*2*Pi*(T[i]*T[i]+
Tfinrad2 * Tfinrad2)* (T[i] + Tfinrad2)*(-T[i] +
Tfinrad2) + sigma*epsil*xr[i]*PP*2*Pi*(T[i]*T[i] +
Tfinrad * Tfinrad)* (T[i] + Tfinrad)*(-T[i] +

```

```

Tinfinrad) + invRconv[i]*(-T[i] + Tinfinconv) + QQvol[i] +
qqsurf[i] + (T[i + 1] - T[i])/Rmax[i]) + T[i]];

For[i = 2, i < Nelem, i++,

T[i] = mindt/ CT[i]*(sigma*epsil*xr[i]*PP*2*Pi*(T[i]*T[i] +
Tinfinrad2 * Tinfinrad2)* (T[i] + Tinfinrad2)*(-T[i] +
Tinfinrad2) + sigma*epsil*xr[i]*PP*2*Pi*(T[i]*T[i] +
Tinfinrad * Tinfinrad)* (T[i] + Tinfinrad)*(-T[i] +
Tinfinrad) + invRconv[i]*(-T[i] + Tinfinconv) + QQvol[i] +
qqsurf[i] + (T[i - 1] - T[i])/Rmin[i] + (T[i + 1] - T[i])/
Rmax[i]) + T[i]];

For[i = Nelem, i < Nelem + 1, i++,

T[i] = mindt/ CT[i]*(sigma*epsil*xr[i]*PP*2*Pi*(T[i]*T[i] +
Tinfinrad2 * Tinfinrad2)* (T[i] + Tinfinrad2)*(-T[i] +
Tinfinrad2) + sigma*epsil*xr[i]*PP*2*Pi*(T[i]*T[i] +
Tinfinrad * Tinfinrad)* (T[i] + Tinfinrad)*(-T[i] +
Tinfinrad) + invRconv[i]*(-T[i] + Tinfinconv) + QQvol[i] +
qqsurf[i] + (Tsurf - T[i])/Rmax[i] + (T[i - 1] - T[i])/
Rmin[i]) + T[i]];

}; niter++;

```